NIST CENTER FOR NEUTRON RESEARCH

2018
ACCOMPLISHMENTS AND OPPORTUNITIES

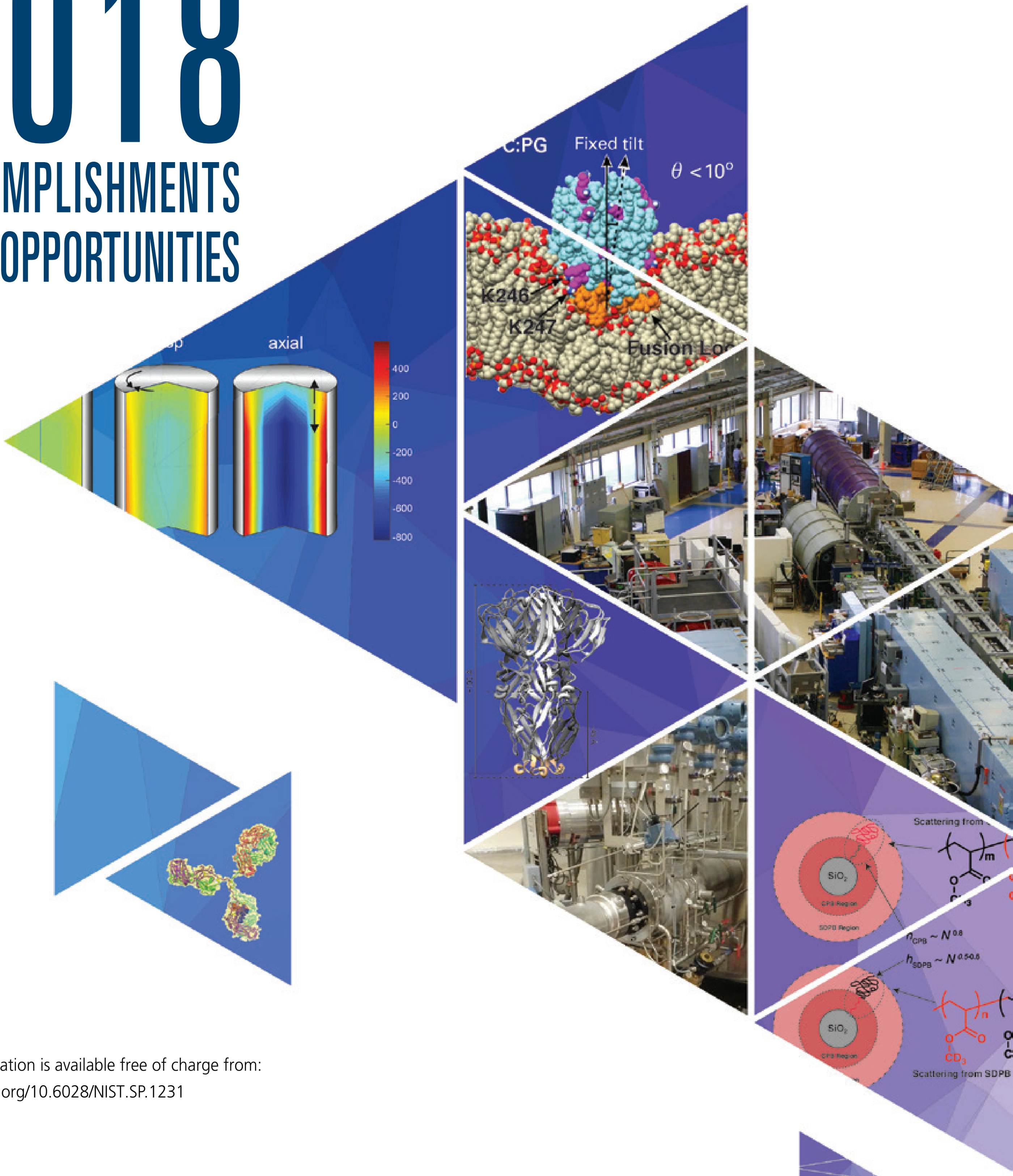

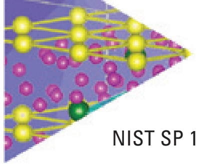

This publication is available free of charge from:
https://doi.org/10.6028/NIST.SP.1231

National Institute of Standards and Technology
U.S. Department of Commerce

NIST SP 1231

ON THE COVER

The NCNR's neutron source provides a valuable research tool for a wide variety of scientific fields from biological systems, engineering materials, to magnetic structures, and more. The cover features data from only a few of the experiments highlighted in this report.

NIST Special Publication 1231

2018 NIST Center for Neutron Research Accomplishments and Opportunities

Robert M. Dimeo, Director

Steven R. Kline, Editor

This publication is available free of charge from:
https://doi.org/10.6028/NIST.SP.1231

February 2019

U.S. Department of Commerce
Wilbur L. Ross, Jr., Secretary

National Institute of Standards and Technology
*Walter Copan, NIST Director and Undersecretary of
Commerce for Standards and Technology*

DISCLAIMER

National Institute of Standards and Technology
Special Publication 1231, 100 pages
(February 2019)
CODEN: NSPUE2

This publication is available free of charge from:
https://doi.org/10.6028/NIST.SP.1231

Table of Contents

HIGHLIGHTS

BIOLOGY

CHEMICAL PHYSICS

CONDENSED MATTER

CULTURAL HERITAGE

ENGINEERING PHYSICS

GEOLOGY

NEUTRON PHYSICS

SOFT MATTER

ADVANCES IN MEASUREMENT

Foreword

It is my pleasure to present to you this year's Accomplishments and Opportunities for the NIST Center for Neutron Research. This year we celebrated the 50th anniversary of the reactor. Though the historical reliability of the reactor has been very good, we are striving to improve the reactor's operational reliability via a robust aging reactor management program. As part of this effort, we had an extended outage of the reactor to perform several major upgrades to the reactor plant (primary cooling pumps and safety shim arm drives) and we brought online the new, higher-capacity cold source refrigerator in anticipation of installation of the liquid D_2 cold source in the early 2020s. Details of these reliability enhancements can be found in the section on facility developments in this report.

Considerable progress was also made in our instrument development program with the commissioning of VSANS and its entry into the user program. As of this writing, the first paper containing VSANS data has been submitted and we expect the scientific productivity of this instrument to rapidly increase. Major assembly work on CANDOR is underway and we are looking forward to detecting "first neutrons" in CY 2019. In addition, the thermal neutron imaging station was upgraded, now enabling simultaneous X-ray and neutron radiography. As we complete VSANS and CANDOR, design work continues for the next set of instrument ideas discussed at the 2014 instrument development meeting. The design of a new cold neutron triple-axis spectrometer to replace SPINS on NG-5 is underway.

As we look to the long-term future of the NCNR, it is essential that we make improvements that assure the availability of neutron measurement capabilities and a reliable source of neutrons to the U.S. scientific community. A recent report by the American Physical Society titled "Neutrons for the Nation," recommended increasing investments in neutron instrumentation development. In accordance with the report, we are planning several future improvements to the NCNR. Most importantly, we will replace our current liquid hydrogen cold source with one based on liquid deuterium thereby enhancing our cold neutron flux by about a factor of two at long wavelengths. We will take the opportunity to install the guide for the SPINS replacement, upgrade our cold neutron imaging station, and replace the NG-7 guide and relocate the α–γ instrument to NG-7 resulting in a significant performance gain for this instrument.

Our continuing goal is to provide the scientific community with the best tools to perform research with a reliable source of neutrons. The research produced by the users of the NCNR was outstanding as evidenced by the high quality of science results contained in this report. I am delighted to share with you this report containing a cross-section of the impressive research from the past year.

The NIST Center for Neutron Research

Neutrons provide a uniquely effective probe of the structure and dynamics of materials ranging from water moving near the surface of proteins to magnetic domains in memory storage materials. The properties of neutrons (outlined below) can be exploited using a variety of measurement techniques to provide information not otherwise available. The positions of atomic nuclei in crystals, especially of those of light atoms, can be determined precisely. Atomic motion can be directly measured and monitored as a function of temperature or pressure. Neutrons are especially sensitive to hydrogen, so that hydrogen motion can be followed in H-storage materials and water flow in fuel cells can be imaged. Residual stresses such as those deep within oil pipelines or in highway trusses can be mapped. Neutron-based measurements contribute to a broad spectrum of activities including engineering, materials development, polymer dynamics, chemical technology, medicine, and physics.

The NCNR's neutron source provides the intense, conditioned beams of neutrons required for these types of measurements. In addition to the thermal neutron beams from the heavy water moderator, the NCNR has two liquid hydrogen moderators, or cold sources which supply neutrons to three-fourths of the instruments. One is a large area moderator and the other is smaller, but with high brightness. These moderators provide long wavelength guided neutron beams for industrial, government, and academic researchers.

There are currently 29 experiment stations: 12 are used for neutron physics, analytical chemistry, or imaging, and 17 are beam facilities for neutron scattering research. The subsequent pages provide a schematic description of our instruments. More complete descriptions can be found at www.ncnr.nist.gov/instruments/. The very small angle neutron scattering instrument (VSANS) was commissioned in 2017, and a quasi-white beam neutron reflectometer (CANDOR) is under development.

The Center supports important NIST measurement needs but is also operated as a major national user facility with merit-based access made available to the entire U.S. technological community. Each year, about 2000 research participants from government, industry, and academia from all areas of the country are served by the facility (see p. 59). Beam time for research to be published in the open literature is without cost to the user, but full operating costs are recovered for proprietary research. Access is gained mainly through a web-based, peer-reviewed proposal system with user time allotted by a beamtime allocation committee twice a year. For details see www.ncnr.nist.gov/beamtime.html. The National Science Foundation and NIST co-fund the Center for High Resolution Neutron Scattering (CHRNS) that currently operates five of the world's most advanced instruments (see p. 62). Time on CHRNS instruments is made available through the proposal system. Some access to beam time for collaborative measurements with the NIST science staff can also be arranged on other instruments.

Why Neutrons?

Neutrons reveal properties not readily probed by photons or electrons. They are electrically neutral and therefore easily penetrate ordinary matter. They behave like microscopic magnets, propagate as waves, can set particles into motion, losing or gaining energy and momentum in the process, and they can be absorbed with subsequent emission of radiation to uniquely fingerprint chemical elements.

WAVELENGTHS – in practice range from ≈ 0.01 nm (thermal) to ≈ 1.5 nm (cold) (1 nm = 10 Å), allowing the formation of observable interference patterns when scattered from structures as small as atoms to as large as biological cells.

ENERGIES – of millielectronvolts, the same magnitude as atomic motions. Exchanges of energy as small as nano-electronvolts and as large as tenths of electronvolts can be detected between samples and neutrons, allowing motions in folding proteins, melting glasses and diffusing hydrogen to be measured.

SELECTIVITY – in scattering power varies from nucleus to nucleus somewhat randomly. Specific isotopes can stand out from other isotopes of the same kind of atom. Specific light atoms, difficult to observe with X-rays, are revealed by neutrons. Hydrogen, especially, can be distinguished from chemically equivalent deuterium, allowing a variety of powerful contrast techniques.

MAGNETISM – makes the neutron sensitive to the magnetic moments of both nuclei and electrons, allowing the structure and behavior of ordinary and exotic magnetic materials to be detailed precisely.

NEUTRALITY – of the uncharged neutrons allows them to penetrate deeply without destroying samples, passing through walls that condition a sample's environment, permitting measurements under extreme conditions of temperature and pressure.

CAPTURE – characteristic radiation emanating from specific nuclei capturing incident neutrons can be used to identify and quantify minute amounts of elements in samples as diverse as ancient pottery shards and lake water pollutants.

NIST Center for Neutron Research Instruments *(as of December 2018)*

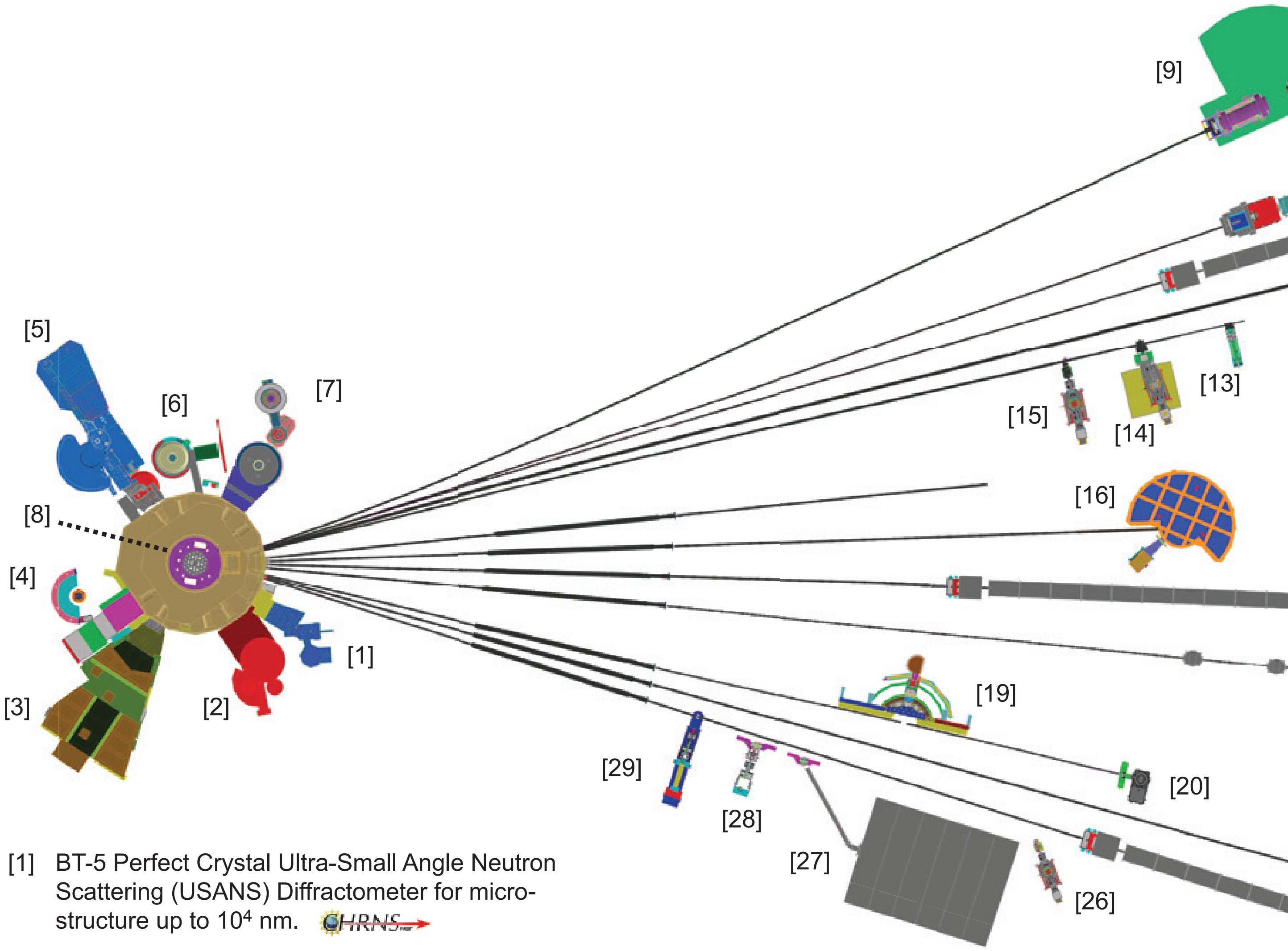

[1] BT-5 Perfect Crystal Ultra-Small Angle Neutron Scattering (USANS) Diffractometer for microstructure up to 10^4 nm. CHRNS

[2] BT-4 Filter Analyzer Neutron Spectrometer with cooled Be/Graphite filter analyzer for chemical spectroscopy and thermal triple axis spectrometer.

[3] BT-2 Neutron Imaging Facility for imaging hydrogenous matter in large components such as water in fuel cells and lubricants in engines, in partnership with General Motors and DOE.

[4] BT-1 Powder Diffractometer with 32 detectors; incident wavelengths of 0.208 nm, 0.154 nm, and 0.120 nm, with resolution up to $\Delta d/d \cong 8 \times 10^{-4}$.

[5] BT-9 Multi Axis Crystal Spectrometer (MACS II), a cold neutron spectrometer for ultra high sensitivity access to dynamic correlations in condensed matter on length scales from 0.1 nm to 50 nm and energy scales from 2.2 meV to 20 meV. CHRNS

[6] BT-8 Residual Stress Diffractometer optimized for depth profiling of residual stresses in large components.

[7] BT-7 Thermal Triple Axis Spectrometer with large double focusing monochromator and interchangeable analyzer/detectors systems.

[8] VT-5 Thermal Neutron Capture Prompt Gamma-ray Activation Analysis Instrument used for quantitative elemental analysis of bulk materials including highly hydrogenous materials (≅ 1 % H) such as foods, oils, and biological materials.

[9] NG-A Neutron Spin-Echo Spectrometer (NSE) for measuring dynamics from 5 ps to 100 ns. CHRNS

[10] NG-B 10 m SANS for macromolecular structure measurements. nSoft

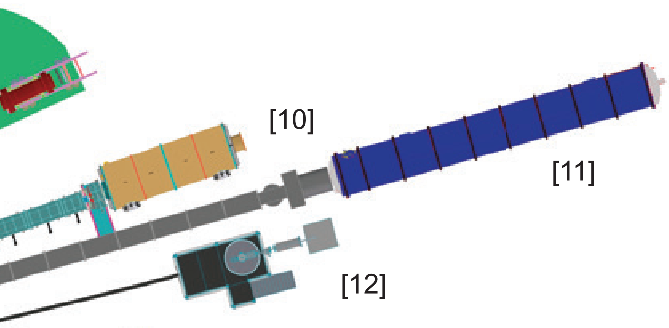

The Center for High Resolution Neutron Scattering (CHRNS) is a partnership between NIST and the National Science Foundation that develops and operates neutron scattering instrumentation for use by the scientific community. The following instruments are part of the Center: 1 (USANS), 5 (MACS II), 9 (NSE), 11 (NG-B 30m SANS), 16 (HFBS), and 17 (VSANS).

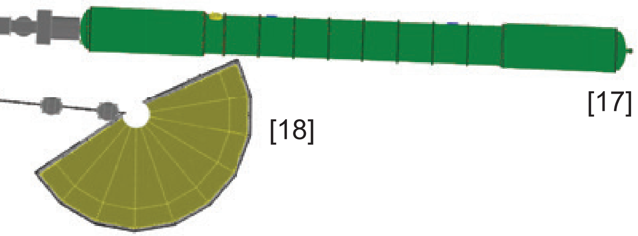

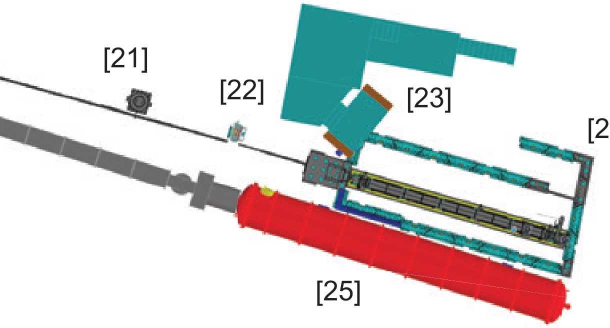

[11] NG-B 30 m SANS for microstructure measurements.

[12] NG-C Neutron lifetime experiment.

[13] NG-D Cold neutron capture Prompt Gamma Activation Analysis, for quantitative elemental analysis of bulk materials.

[14] NG-D MAGIK off-specular reflectometer for studies of thin-film samples with in-plane structure.

[15] NG-D Polarized Beam Reflectometer (PBR) for measuring reflectivities as low as 10^{-8} to determine subsurface structure.

[16] NG-2 Backscattering Spectrometer (HFBS) high intensity inelastic scattering instrument with energy resolution < 1 μeV, for studies of motion in molecular and biological systems.

[17] NG-3 VSANS Single measurement investigation of lengths from 1 nm to 2 micron.

[18] NG-4 Disk Chopper Time-of-Flight Spectrometer for diffusive motions and low energy dynamics. Wavelengths from $\cong$ 0.18 nm to 2.0 nm and energy resolutions from $\cong$ 2 meV to < 10 μeV.

[19] NG-5 Spin-Polarized Triple Axis Spectrometer (SPINS) using cold neutrons with position sensitive detector capability for high-resolution studies.

[20] NG-5 Cold Neutron Depth Profiling for profiling of subsurface elemental composition.

[21] NG-6 Precision measurement of the magnetic dipole moment of the neutron.

[22] NG-6 Precision measurement of neutron flux.

[23] NG-6 LAND detector development, neutron source calibration, and neutron cross section measurement.

[24] NG-6 Cold Neutron Imaging Facility for imaging hydrogenous matter in large components such as water in fuel cells and lubricants in engines.

[25] NG-7 30 m SANS for microstructure measurements, in partnership with ExxonMobil and University of Minnesota's IPrime.

[26] NG-7 PHADES Cold neutron test station.

[27] NG-7 Neutron Interferometry and Optics Station with perfect crystal silicon interferometer. A vibration isolation system provides exceptional phase stability and fringe visibility.

[28] NG-7 Neutron Physics Interferometry Test Bed for quantum information science.

[29] NG-7 Horizontal Sample Reflectometer allows reflectivity measurements of free surfaces, liquid/vapor interfaces, as well as polymer coatings.

NCNR Images 2018

NCNR Health Physicist Susan Deeb re-enlisting for another tour of duty in the U.S. Navy Reserves.

Taufique Hassan (NCNR) and SURF student Hannah Burrall testing a new solenoid for NSE.

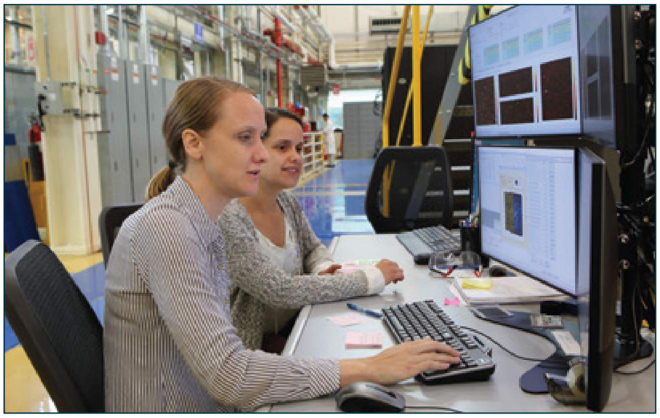

NCNR instrument scientists Grethe Jensen and Liz Kelley setting up a measurement at VSANS.

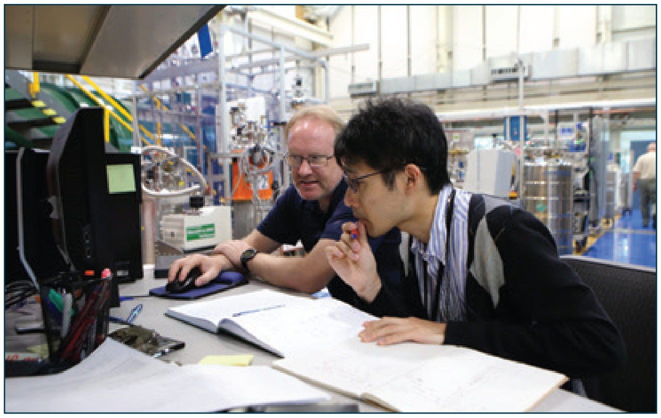

Craig Brown (NCNR) and Takafumi Yamamoto (Kyoto University, Japan) at DCS studying dynamics of hydrides.

Scott Dewey (NCNR) supervising Ripan Biswas (Tulane University) as he replenishes liquid Helium for the neutron lifetime experiment at NG-C.

SURF student Temi Okusolubo preparing a sample of lipid vesicles for measurement on SANS.

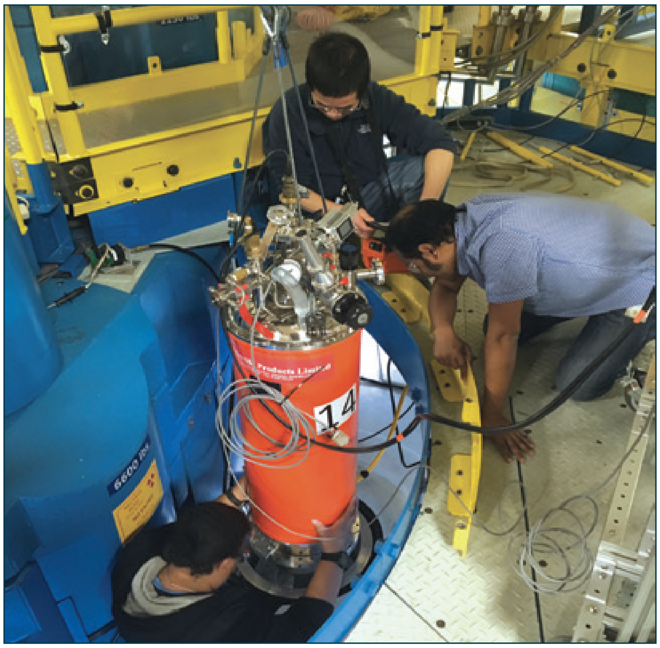

Shannon Watson, Yiming Qiu, and Taufique Hassan of the NCNR testing the ^{3}He horseshoe cell and the new orange cryostat at MACS.

Tim Reeder from the Institute for Quantum Matter at Johns Hopkins University installing a microwave device on the 10 T magnet in preparation for a MACS experiment.

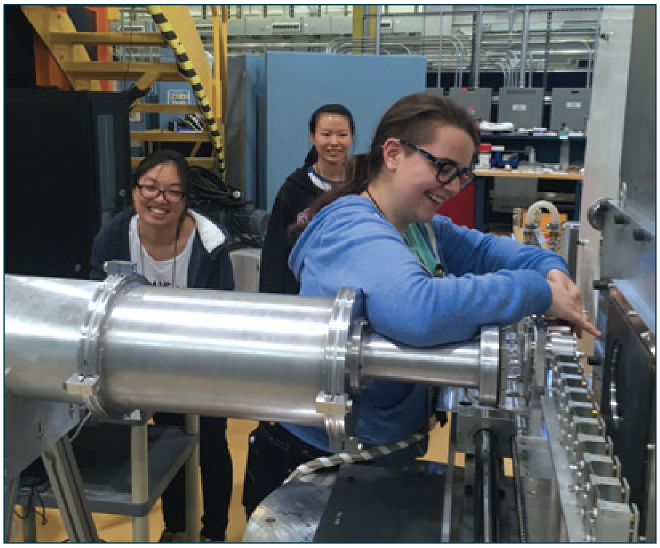

In May, Bing Zheng, Xiaoxi Yu, and Amanda Carr from SUNY-Stony Brook became the first external users on VSANS.

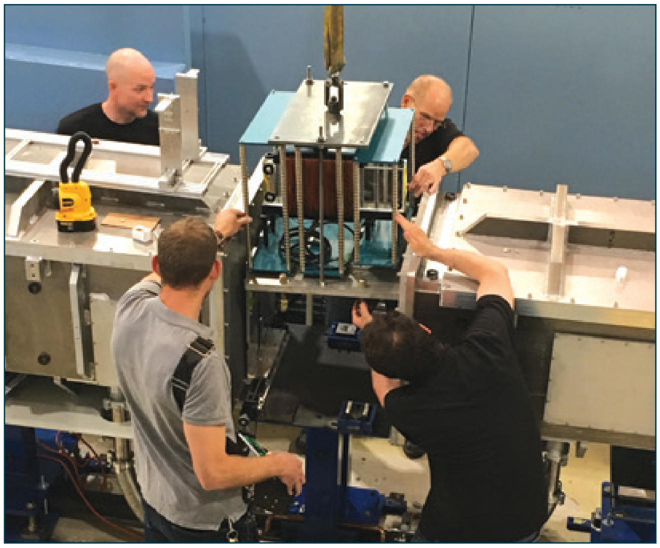

NCNR technicians Sean Mullendore, Doug Ogg, Doug Johnson, and Mark O'Brien installing the RF flipper at CANDOR.

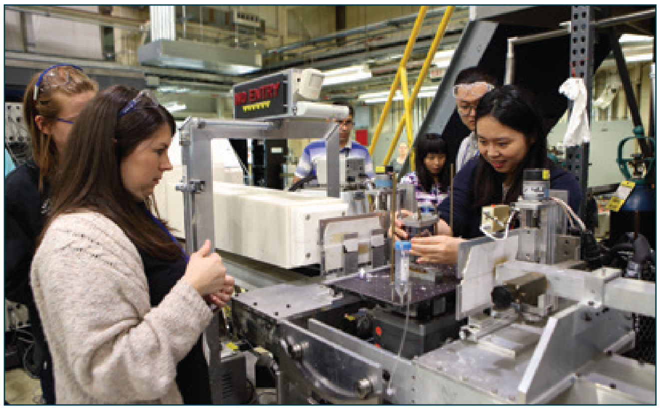

Summer school students aligning a sample at the NG-7 reflectometer.

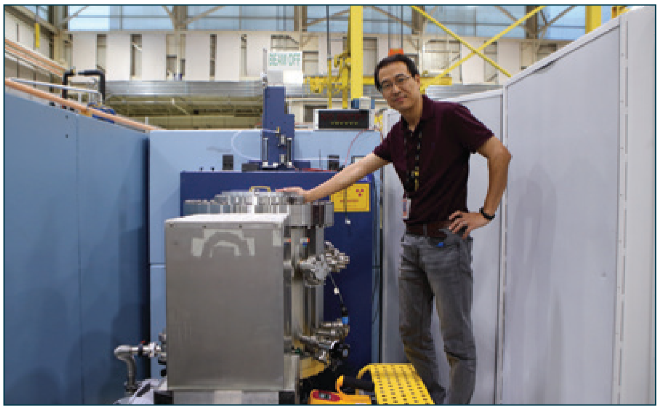

Howard Wang (SUNY Binghamton) studying a new battery material at CNDP.

Small-angle neutron scattering proves crucial for characterizing the structures of (poly)ubiquitin complexes with small-molecule inhibitors

D. Fushman[1] and S. Krueger[2]

Eukaryotic cells which have a cell nucleus containing DNA are the basis of multicellular organisms including plants and animals. Essentially every aspect of cell biology in eukaryotes, including protein turnover, DNA repair, signal transduction, cell division, and differentiation is regulated by a critical post-translational covalent attachment of a small 76 amino-acid protein called ubiquitin (Ub) to other cellular proteins [1]. The most well studied and vital ubiquitin-mediated signaling pathway involves the ubiquitin-proteasome system (UPS), which is the principal negative regulatory mechanism for short-lived cytosolic proteins [2]. Deficiencies in components of the UPS – such as mutations in the enzymes, receptors, and the Ub molecule itself – have severe consequences, including cell death and the onset of disease. Proteins destined for degradation are post-translationally tagged with Ub or a chain of Ub molecules (polyUb) attached to a lysine side chain on a modified protein through the action of a cascade of enzymes. Provided the protein is appropriately modified with Ub, shuttling factors facilitate its transport to the 26S proteasome where dedicated receptors initiate its degradation (Figure 1) [3].

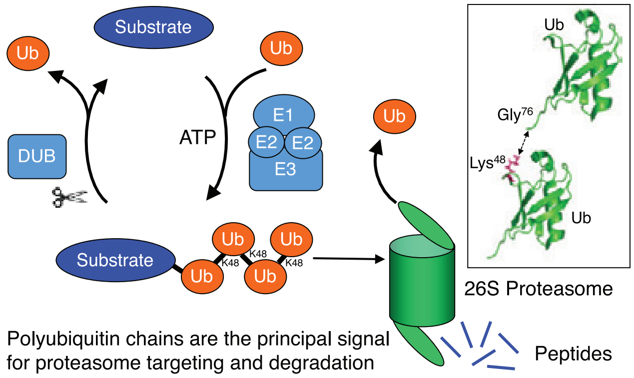

FIGURE 1: Degradation of a protein via the Ubiquitin Proteasome System (UPS) involves covalent attachment of one or more Ub molecules to the substrate protein followed by degradation of the (poly)Ub-tagged substrate protein by the 26S proteasome. Tagging with Ub – ubiquitination – is achieved through a cascade of chemical reactions catalyzed and controlled by several enzymes (E1, E2, E3) and can be reverted by deubiquitinating enzymes (DUBs). Ubiquitin is covalently attached through an isopeptide bond between its C-terminal glycine (G76) and the side chain of a lysine on the target protein or another Ub in a polyUb chain. (The inset illustrates the isopeptide bond between G76 of one Ub and the side chain of lysine K48 of another Ub.) This K48-linked polyUb tag acts as the principal signal for proteasomal degradation. The tagged substrate protein is either directly recognized by the proteasome or transferred to the proteasome by several shuttle proteins. The Ub tag is removed by proteasomal DUBs prior to the substrate's degradation, such that Ub molecules can be re-used by the cell for the next rounds of ubiquitination.

Thus far, peptide-based proteasome inhibitors (such as bortezomib and carfilzomib) which bind to the proteolytic β-subunits in the 20S core of the proteasome are the only clinically approved therapeutics targeting the UPS. Because malignancies such as multiple myeloma require enhanced UPS function, these cells are particularly susceptible to proteasome inhibitors [4]. However, through mechanisms that are not clear, some patients relapse as the cancer becomes resistant to these inhibitors [5]. Unlike the enzymatic components of the UPS, ubiquitin is significantly less likely to tolerate mutations and therefore is potentially a more robust drug target.

Ubistatins are a family of small molecules that inhibit degradation of polyubiquitinated proteins by the UPS [6]. Ubistatins act upstream of the proteasome by directly binding to (poly)Ub and preventing its recognition by downstream receptors. The discovery of ubistatins has made Ub itself a potential therapeutic target. Although ubistatins have the potential for drug development and clinical applications, the lack of structural details of Ub-ubistatin interactions has impeded their development. To address this deficiency, in this study [7], a panel of ubistatin derivatives was synthesized and examined using a combination of functional and NMR-based binding assays. Based on this screening we focused our structural efforts on ubistatin B (ubiB) as the most promising one (inset, Figure 2 (A)). UbiB binds preferentially to Ub chains linked via the lysine at the 48th amino acid position (K48), so the results described here apply to K48-linked Ub chains.

The molecular symmetry of ubiB necessitated the synthesis and use of a half-ubistatin B compound (hemi-ubiB), to enable unambiguous assignment of the NMR-derived interatomic contacts between ubiquitin and ubiB. Our NMR structure of the Ub:hemi-ubiB complex revealed direct interactions of hemi-ubiB with the hydrophobic patch on Ub's surface and the basic/polar residues surrounding it; these interactions were then confirmed by site-directed mutagenesis. Furthermore, using NMR, we found that both ubiB and hemi-ubiB bind to the same surface on Ub, suggesting that hemi-ubiB is the fundamental Ub-binding

---

[1] University of Maryland, College Park, MD 20742
[2] NIST Center for Neutron Research, National Institute of Standards and Technology, Gaithersburg, MD 20899

unit in full ubiB. However, scaling up the structure from half- to full ubistatin presented a number of challenges. Specifically, both ^{15}N relaxation and small-angle neutron scattering (SANS) data revealed that Ub:ubiB complex comprises two Ubs bound to the same ubiB molecule. With two Ub-binding units, each having two surfaces/sides capable of binding, there are a number of possible arrangements. NMR-based docking analysis was unable to discriminate between two possibilities depicted in Figure 2 (C and E). SANS data shown in Figure 2 (D and F) are consistent with only one of these two complexes.

Extending the studies to di-ubiquitin (Ub_2) and longer chains, one would expect that the presence of two Ub-binding units/halves in ubiB could result in even more complicated binding scenarios. In fact, both NMR (^{15}N relaxation) and SANS data indicated that K48-linked Ub_2 binds ubiB in at least 2:1 stoichiometry. Importantly, our SANS data suggest that the structural arrangement of di-Ubs in this complex might resemble that in the compact form of K48-linked tetra-ubiquitin (Ub_4) [7, 8].

These results demonstrate the sensitivity of SANS data to the global arrangement of individual components of a complex. This feature nicely complements the local inter-atomic contact information attainable by NMR. Combined NMR and SANS data allow both the spatial arrangement of individual components as well as their orientations with respect to each other to be determined. When NMR data produce multiple possible models involving different global arrangement of the components, SANS data can often distinguish between them.

The structural details of ubiB interactions with (poly)Ub revealed by our studies will guide future development of small-molecule inhibitors targeting UPS and other ubiquitin-signaling pathways. By binding to the functionally critical hydrophobic patch on Ub's surface, ubiB can outcompete high-affinity Ub receptors from proteasomal shuttles and shields polyUb chains from disassembly by a range of DUBs including the proteasome itself. Furthermore, we found that ubiB penetrates cancer cells and causes accumulation of polyubiquitinated substrates, thus altering the cellular ubiquitin landscape. Ubistatins present many advantages over other existing synthetic Ub-binding molecules: the ubistatins are highly specific for Ub, bind Ub tightly, penetrate cells, have well characterized *in vitro* and *in vivo* outcomes, and provide a fluorescent readout. Moreover, the chemical properties of ubistatins combined with resistance to proteases offer advantages compared to the peptide-based drugs targeting the UPS. Even if some other factors limit ubistatins as therapeutics, the intrinsic fluorescence and the ability of ubistatins to accommodate modular substituent groups will allow them to serve as powerful reagents in biochemical studies.

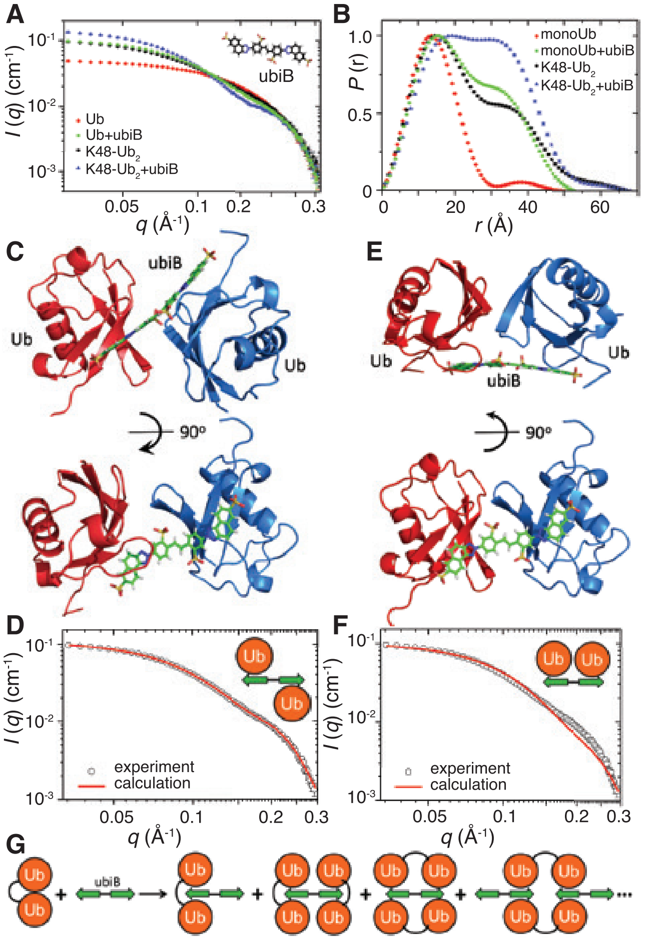

FIGURE 2: SANS intensity (A) and pair distribution function (B) for Ub or K48-Ub_2 alone and in the presence of an equimolar amount of ubiB. (D) Agreement between the $I(q)$ calculated (solid line) for the structure shown in (C) and the experimental SANS intensity ($I(q)$, open circles). (F) Agreement between the $I(q)$ calculated (solid line) for the structure shown in (E) and the experimental SANS intensity ($I(q)$, open circles). (G) Possible structural arrangements of K48-linked Ub_2 in complexes with ubiB that could lead to SANS data in (A) (B).

References

[1] D. Fushman, K. D. Wilkinson, F1000 Biol Rep **3**, 26 (2011).

[2] A. Hershko, A. Ciechanover, Annu Rev Biochem **67**, 425 (1998).

[3] C. M. Pickart, FASEB J. **11**, 1055 (1997).

[4] A. L. Goldberg, J Cell Biol **199**, 583 (2012).

[5] A. M. Ruschak, M. Slassi, L. E. Kay, A. D. Schimmer, J Natl Cancer Inst **103**, 1007 (2011).

[6] R. Verma et al., Science **306**, 117 (2004).

[7] M. A. Nakasone et al., Structure **25**, 1839-1855 e1811 (2017).

[8] M. J. Eddins, R. Varadan, D. Fushman, C. M. Pickart, C. Wolberger, J Mol Biol **367**, 204 (2007).

Insertion of Dengue E into lipid bilayers studied by neutron reflectivity and molecular dynamics simulations

J. M. Vanegasa,[1] F. Heinrich,[2,3] D. M. Rogers,[1] B. D. Carson,[1] S. La Bauve,[1] B. C. Vernon,[1] B. Akgun,[2] S. Satija,[2] A. Zheng,[4] M. Kielian,[4] S. B. Rempe,[1] and M. S. Kent[1]

Dengue virus is a flavivirus that is endemic to tropical and subtropical regions of the world. Dengue is an enveloped virus having a dedicated protein that promotes fusion between viral and host membranes. Fusion proteins are critical for infectivity and are therefore targets of therapeutic intervention. All fusion proteins have a hydrophobic peptide sequence that inserts into the host membrane although the sequences and structures vary considerably among the different enveloped viruses. The precise roles of fusion proteins and their hydrophobic peptides are under considerable debate. Possible functions include anchoring into the host membrane strongly enough to support the high membrane bending that must occur to form a fusion stalk; promoting positive curvature in the target membrane and dimple formation or promoting negative curvature in the target membrane as required to form a fusion stalk; and disrupting the local ordering of the host membrane to facilitate mixing with the viral membrane. With regard to the latter, prior studies have shown that fusion peptides lower the rupture tension of membranes. Molecular simulations have suggested that the fusion peptide of influenza promotes splaying of lipid tails, such that one tail protrudes from the host membrane, thereby promoting fusion. Substantial work is needed to understand fully the detailed mechanisms by which such proteins promote fusion and the roles of the fusion peptides.

The characterization of membrane proteins under physiologically relevant conditions remains a difficult problem in structural biology. Neutron scattering techniques and in particular neutron reflectometry, have unique advantages as they allow the study of this class of proteins in a biomimetic, fluid-immersed state using model membrane systems. The disadvantage of neutron reflectometry is the comparatively low resolution and a spatial sensitivity along one axis only, which is typically the membrane normal. Therefore, neutron reflectometry data is routinely combined with atomistic MD simulations to overcome these experimental limitations (integrative modeling). Here we demonstrate this approach in an application to a biomedically relevant problem – the membrane association of the Dengue virus fusion protein (see Figure 1), which represents the first step in viral infection [1].

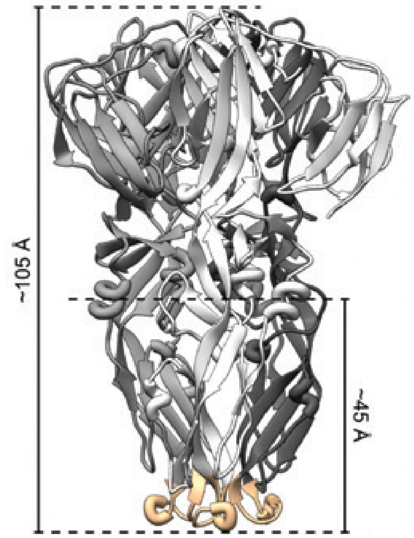

FIGURE 1: Crystal structure of the Dengue envelope protein trimer. In MD simulations, a shorter truncated form of the protein was used. The fusion loops are shown in tan.

The envelope protein of the Dengue virus is comprised of three domains and is arranged as a head-to-tail dimer in the mature virus but reorganizes into head-to-head trimers upon exposure to low pH within endosomes. A small number of residues at the tip of the trimer that inserts into the target membrane form a fusion loop (see Figure 1). The NR results show that the tip of the envelope protein containing the fusion loop is located at the interface of the headgroups and acyl chains of the outer leaflet of the lipid bilayers, in good agreement with prior predictions. The results also indicate that E tilts with respect to the membrane normal upon insertion, promoted by either the anionic lipid POPG or CHOL (see Figure 2).

MD simulations demonstrated that tilting of the protein correlates with hydrogen bond formation between lysine and arginine residues located on the sides of the trimer close to the tip and nearby lipid headgroups (see Figure 3). These hydrogen bonds provide a major contribution to the membrane anchoring and may help to destabilize the target membrane. While much prior work has focused on the importance of the FL, we have shown that those residues are important in the interaction of Dengue E with the target membrane. Our simulations indicate that hydrogen bonds formed between these residues and phosphates in the lipid headgroups provide substantially more binding energy than the interaction of the fusion loop with the membrane.

---

[1] Sandia National Laboratories, Albuquerque, NM 87185
[2] NIST Center for Neutron Research, National Institute of Standards and Technology, Gaithersburg, MD 20899
[3] Carnegie Mellon University, Pittsburgh, PA 15213
[4] Albert Einstein College of Medicine, Bronx, NY 10461

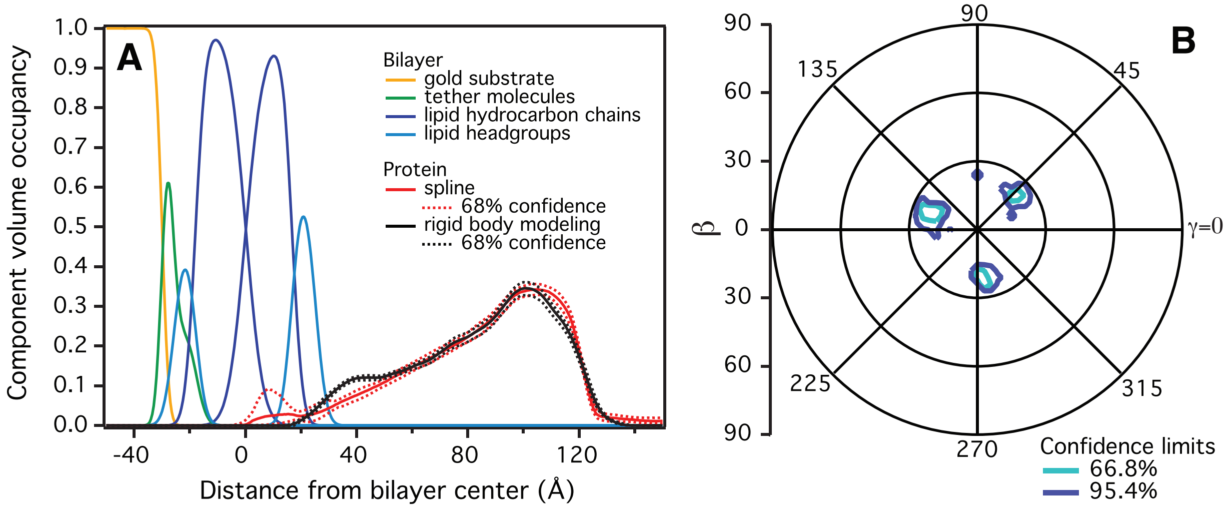

FIGURE 2: A) Composition-space modeling result for the NR data for Dengue E bound to a cholesterol-containing tethered lipid bilayer. Volume occupancy profiles are shown for molecular components of the lipid bilayer and the protein. Protein occupancy profiles were obtained from a free-form spline model (red trace) and a rigid body modeling approach using a high-resolution X-ray structure of the Dengue envelope protein (PDB 1OK8) (black trace). Composition-space modeling directly parameterizes the real-space volume occupancy distributions of sub-molecular groups of a biological interfacial structure, such as the one shown here [2]. This model provides significant advantages over traditional slab models in that it allows for overlapping molecular groups, such as a protein penetrating a lipid membrane. Further, it is more efficient in utilizing available external information such as molecular volumes, chemical connectivity, and molecular stoichiometries across the interface. B) Orientation probability plot from the fit using the X-ray structure (see black trace on the left) parameterized using two Euler angles: the tilt (β) and a rotation along the long axis of the protein (γ). The protein assumes an approximately 20º tilt from a fully upright position and either one of three identical sites faces the membrane plane. The trifold symmetry is a consequence of the envelope protein forming a trimer.

In summary, we have shown how the Dengue envelope protein interacts with the lipid membrane under biomimetic, fluid-immersed conditions. Contrary to previous knowledge, the protein does not associate with the membrane head-on, but rather at an angle leveraging additional interactions between peripheral lysine and arginine residues and the membrane. We propose that these interactions play the dominant role in membrane anchoring and may also play a role in initiating mixing of the outer leaflets during the fusion process. At the same time, our results indicate avenues for future research. Our simulations show a propensity of the Dengue envelope protein to bend the membrane (see Figure 3). While most likely biologically relevant, such a deformation is greatly suppressed in the planar solid-supported model membranes used for the neutron reflectometry experiments that are optimized for a high spatial resolution. Other scattering techniques and model systems that do not rely on lipid membranes this close to a solid substrate should be used to characterize the effect of the Dengue envelope protein on membrane bending. Further, the protein in the simulation shows a much larger variability in tilt angles than observed in the experiment, which indicates either a subtle mismatch of experimental and simulation parameters, or an imperfect description of the atomistic and molecular forces in the simulation. As this is a rather common problem, steered MD simulations in which the experimental data directly affects the simulation trajectory are under development.

References

[1] J. M. Vanegas et al. Biochimica Et Biophysica Acta (BBA)-Biomembranes, **1860** (5), 1216 (2018).

[2] F. Heinrich, M. Lösche, Biochimica Et Biophysica Acta (BBA)-Biomembranes, **1838** (9), 2341 (2014).

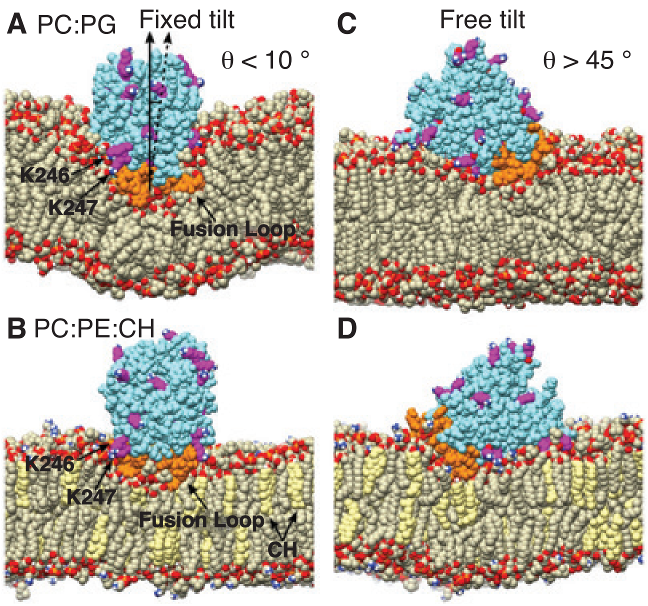

FIGURE 3: Simulation cross-section of truncated trimers interacting with (A) PC:PG and (B) PC:PE:CH membranes while fixing the protein vertical orientation (θ < 10º) with respect to the membrane normal. PC:PG system simulated for 700 ns and PC:PE:CH system simulated for 600 ns. Lipid carbon atoms are shown in tan color, cholesterol atoms in yellow, protein atoms in cyan except fusion loop (orange) and Lys residues (magenta). Panels on the right (C) and (D) show cross-sections for the analogous systems without orientational restraint (free to tilt).

Protein adsorption on stainless steel

C. K. Kalonia,[1,2] F. Heinrich,[3,4] J. E. Curtis,[3] S. Raman,[2] M. A. Miller,[2] and S. D. Hudson[1]

Monoclonal antibodies are a major class of therapeutic proteins, often administered as solutions. Such solutions sometimes destabilize, and a small fraction of the protein forms aggregates known as subvisible particles (SVP, 2 µm to 100 µm in size). This instability can be exacerbated by material incompatibility, which is not well understood. We therefore seek to know what happens to protein that adsorbs to material surfaces. The NIST mAb (shown schematically in Fig. 1) is an extensively studied reference material (RM 8671) with excellent stability in solution, and we measured its adsorption to stainless steel, a material commonly used for pistons and nozzles during the final "fill/finish" step of product manufacture. In addition to standard biophysical and analytical approaches, we applied neutron reflectometry and a flow-cell sample environment to investigate adsorption and particle formation, testing the effect of shear and different interface materials [1].

To obtain nm resolution of the adsorbed film, the roughness of the substrate surface must be at most of comparable scale. Smooth and ultrathin (approximately 15 nm) layers of the test materials (stainless steel and alumina) were thus sputtered onto silicon wafer (111, roughness Ra ≈ 0.5 nm) by the NanoFab group at the NIST Center for Nanoscale Science and Technology. The sputtered layers were characterized by X-ray reflectivity. The sample environment was assembled with these wafers as shown schematically in Fig. 2.

The test surface is somewhat less than half of the total surface in contact with the protein solution, and so one wonders if particle generation might also occur from any of these other surfaces. Nevertheless, the number of SVP was largely governed by the test surface; for example, more than five times as many particles were produced consistently by flow past the stainless steel when compared to flow past alumina under the identical flow conditions and protein concentration. SVP concentration increased with protein concentration in each case. The test surfaces could be used and cleaned repeatedly without degradation, demonstrating that particle formation here occurred by shedding protein only and did not occur by shedding substrate material. We only measured SVP (2 µm to 100 µm in size). Smaller particles and the total amount of protein shed were not measured. The total amount of SVP produced is smaller than the amount of material adsorbed to the surface at any given moment. The mass of the protein in the monolayer adjacent to the interface (measured by quartz crystal microbalance with dissipation monitoring (QCM-D) and neutron reflectivity, see Fig. 3) is roughly (200 to 350) ng/cm^2. A few cm^2 has sufficient adsorbed mass to account for the total mass of SVP generated during flow. The total test surface area is 33 cm^2.

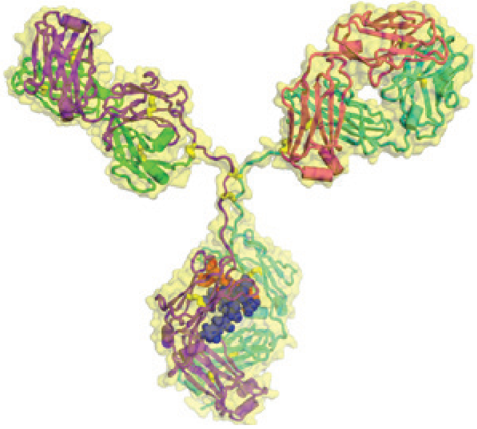

FIGURE 1: NIST mAb reference material (RM 8671).

The NISTmAb antibody adsorbs readily to stainless steel and alumina. Even at very low protein concentration (0.1 g/L), a substantial monolayer adsorbs (see Fig. 3). At 0.1 g/L mAb solution concentration, a simple, ≈ 6 nm thick layer was observed (Fig. 3). The thickness and neutron scattering length density (nSLD) profile of the layer was like a monolayer of mAb molecules oriented flat at the interface. Surface coverage (area occupied) for this layer, however, was well below the surface coverage of a densely-packed, native monolayer. At 50 g/L mAb solution concentration, the volume fraction and structure of the adsorbed layer changed noticeably with the % area occupied substantially increasing near the stainless steel interface. Interestingly, the thickness remained ≈ 6 nm which suggests that the conformation of the adsorbed mAb changed rather than the molecules adopting a new orientation such as standing upright. Thus, the structure of the adsorbed mAb was no longer comparable to the modeled native mAb monolayer

---

[1] Material Measurement Laboratory, National Institute of Standards and Technology, Gaithersburg, MD 20899
[2] MedImmune Inc., Gaithersburg, MD 20878
[3] NIST Center for Neutron Research, National Institute of Standards and Technology, Gaithersburg, MD 20899
[4] Carnegie Mellon University, Pittsburgh, PA 15213

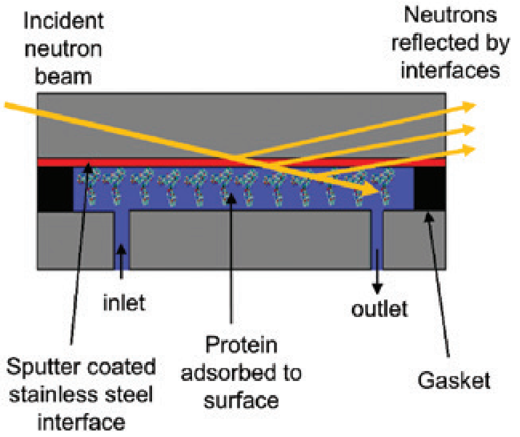

FIGURE 2: The shearing flow cell sample environment: protein solution in contact with a thin smooth model interface, which is probed by neutron reflectometry.

and the shape of the antibody must be distorted. At 100 g/L mAb, the resulting structure and thickness of the adsorbed mAb layer was similar to the layer formed at 50 g/L bulk mAb solution concentration. The structure of the primary layer was therefore found to vary with mAb solution concentration.

At these higher solution concentrations, the nSLD profile hints of additional protein adsorbed further from the interface. QCM-D detects this additional, much lower density, viscoelastic layer in contact with the adsorbed monolayer. Since the volume fraction of bulk protein solution is approximately (3.5 and 7) % at (50 and 100) g/L, respectively, reflectivity results indicate that the volume fraction of the secondary layer must be like the volume fraction of the mAb solution. If the volume fraction of the secondary layer was only a few percent more than the solution concentration and the secondary layer was very thick (e.g., > 100 nm), it would be challenging to capture through neutron reflectivity.

Neutron reflectivity measured the structure of the protein layer that adsorbs onto stainless steel. At even modest protein concentrations (50 g/L), the shape of the antibody adsorbed is distorted, providing a likely mechanism or path to particle formation. Significant differences of particle production were observed when solution flows over different surfaces. This sample environment is thus advantageous to measure protein adsorption and to produce protein particles derived from the surface, making it an important tool to study surface interactions, as a function of surface and/or solution chemistry. These results are relevant to the biopharmaceutical formulation sciences and process engineering communities because solid-liquid interfaces play a critical role in protein stability, particularly in the presence of shear or other external forces.

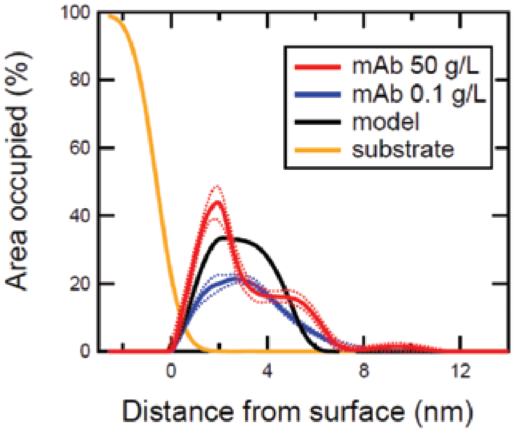

FIGURE 3: Structure of the antibody adsorbed, expressed as a relative concentration, as a function of distance from the interface with stainless steel. The curve in black is the profile expected for a close-packed (albeit hydrated) undistorted monolayer of the antibody lying flat with Fc and Fab domains adjacent to the interface. When the antibody concentration in solution is low (0.1 g/L), the profile (blue curve) indicates substantial (yet not close-packed) adsorption and is consistent with well-spaced undistorted molecules lying flat. When the antibody concentration is higher (50 g/L and above, red curve), adsorption increases, and the profile is no longer consistent with undistorted molecules; the highest concentration of protein segments is within approximately 2 nm from the surface.

Reference

[1] C. K. Kalonia, F. Heinrich, J. E. Curtis, S. Raman, M. A. Miller, and S. D. Hudson, Molecular Pharmaceutics **15** (3), 1319 (2018).

Perovskite nickelates as electric-field sensors in salt water

D. Schwanz,[1] Z. Zhang,[1] B. Narayanan,[2] M. Kotiuga,[3] J. A. Dura,[4] M. Cherukara,[2] H. Zhou,[5] J. W. Freeland,[5] J. Li,[6] R. Sutarto,[7] F. He,[7] C. Wu,[8] J. Zhu,[9] Y. Sun,[1] K. Ramadoss,[1] S. S. Nonnenmann,[9] N. Yu,[8] R. Comin,[6] K. M. Rabe,[3] S. K. R. S. Sankaranarayanan,[2] and S. Ramanathan[1]

Designing materials to function in harsh environments, such as conductive aqueous media, is a problem of broad interest to a range of technologies, including energy, ocean monitoring, and biological applications. The main challenge is to retain the stability and morphology of the material as it interacts dynamically with the surrounding environment. Materials that respond to mild stimuli through collective phase transitions and amplify signals could open up new avenues for sensing. On the other hand, some marine organisms such as sharks have evolved naturally to detect their environment through various sensory organs, positioning them as apex predators [1]. The electroreceptive sensor organ, popularly known as Ampullae of Lorenzini (AoL), enables sharks to detect bioelectric fields emitted by prey fish.

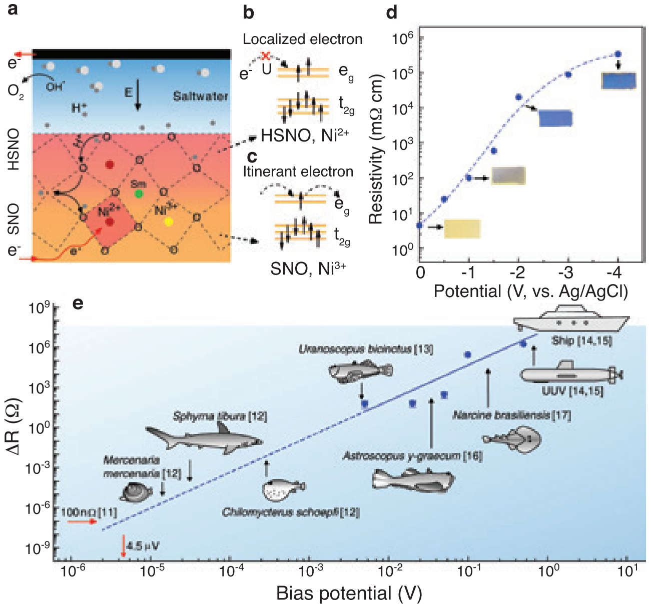

FIGURE 1: (a) Schematic of the saltwater-mediated phase transition in $SmNiO_3$ (SNO). Under bias, the protons intercalate and diffuse into the SNO lattice accompanied by electron transfer from the counter electrode. (b) and (c) Schematics of the electronic structure of the Ni 3*d* orbital in pristine (c) and H-doped SNO (b). (d) Electrical resistivity and color change of SNO thin film after applying various bias potentials in 0.6 mol/L NaCl for 60 s. (e) The change in the electrical resistance (ΔR) for bias potentials ranging from 0.5 V to 5 mV. The resistance change beyond the present measurement window is estimated by linear extrapolation. UUV, unmanned underwater vehicle. Adapted from Ref [2].

In this study, the discovery of an electric-field driven, water-mediated phase transition in a prototypical, strongly correlated semiconductor, $SmNiO_3$ (SNO), which enables direct mimicking of the mechanism of AoL is reported [2]. Fig. 1(a) illustrates SNO submerged in water in the presence of an electric bias generated by a counter electrode. Under negative electric potentials, the protons intercalate into the SNO lattice, which is accompanied by an uptake of electrons from oxidation at the counter electrode. As a result, a saltwater-mediated transition from pristine SNO to the hydrogenated phase (HSNO) occurs under bias. Accompanied with this proton influx is an entire modification of the electronic configuration of the Ni 3*d* orbitals. As Figs. 1(b) and 1(c) show, the partially filled e_g orbital, which has a low transport gap for charge carriers in SNO, becomes half-filled in HSNO where strong Mott-Hubbard electron-electron interactions localize the charge carriers. Figure 1(d) shows the electrical resistivity of SNO after applying negative electric potentials up to – 4.0 V (vs. Ag/AgCl) in 0.6 mol/L NaCl. Upon application of a negative electric potential, the electrical resistivity of SNO increases more than 5 orders of magnitude and exhibits a noticeable color change, indicating the occurrence of a water-mediated phase transition. We find that the electrical resistivity of SNO can change consistently following the switching of the bias potential ranging from ± 0.5 V to ± 0.005 V over multiple cycles, indicating their capability to act as sensors. Figure 1(e) shows the modulation of the electrical resistance of SNO when the bias potential is lowered to the level of millivolts to evaluate the sensitivity of SNO to numerous documented sources of electric signals in oceans. The sensitivity of the present SNO device can

---

[1] Purdue University, West Lafayette, IN 47907
[2] Argonne National Laboratory, Argonne, IL 60439
[3] Rutgers University, Piscataway, NJ 08854
[4] NIST Center for Neutron Research, National Institute of Standards and Technology, Gaithersburg, MD 20899
[5] Advanced Photon Source, Argonne National Laboratory, Argonne, IL 60439
[6] Massachusetts Institute of Technology, Cambridge, MA 02139
[7] Canadian Light Source, University of Saskatchewan, Saskatoon, Saskatchewan S7N 2V3, Canada
[8] Columbia University, New York, NY 10027
[9] University of Massachusetts Amherst, Amherst, MA 01003

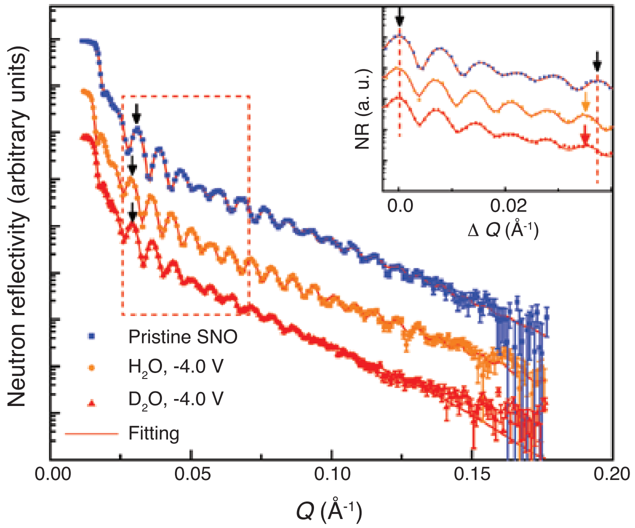

FIGURE 2: Neutron reflectivity, error bars, and associated fits for pristine, hydrogenated, and deuterated SNO thin films. The inset shows an enlarged area comparing oscillations normalized to the peak at $Q \approx 0.03$ Å^{-1}. Adapted from Ref [2].

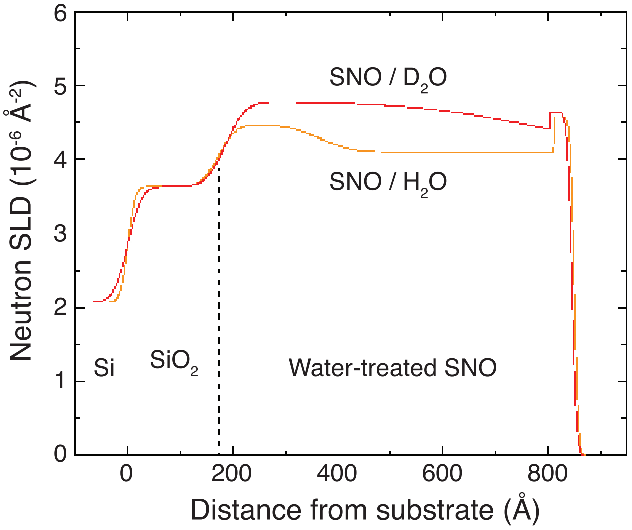

FIGURE 3: Neutron scattering length density profiles of heavy-water-treated SNO. The scattering length density (SLD) was fitted to the data shown in Fig. 2 for the SNO/SiO_2/Si thin film devices. The isotope contrast between water and heavy-water treated sample indicates the intercalation of D^+ from D_2O into the lattice after the treatment. Adapted from Ref [2].

be extrapolated further to show its ability to detect signals in oceans down to microvolts, which spans the bioelectric potentials generated by numerous marine species all the way up to galvanic potentials from ship and unmanned underwater vehicles (UUV).

To investigate the microscopic mechanism of environmental sensing, neutron scattering, which is sensitive to hydrogen isotopes, was utilized to detect protons in solids. The neutron reflectometry (NR) measurements [3] were performed in air with procedures similar to those found in the literature [4]. The samples were characterized over the Q range (0 to 0.18) Å^{-1}. The NR data fitting was performed with the NIST Refl1d software package [5]. For the NR isotope substitution measurement, an ≈ 70 nm thick SNO sample was grown on a Si (100) substrate. The sample was cleaved into two pieces. One piece was characterized first in the pristine state as a reference. This sample was then treated at -4.0 V (vs. Ag/AgCl) for 30 s in 0.01 mol/L KOH/H_2O solution. To observe the contrast from isotope substitution, the other piece of SNO was treated at -4.0 V (vs. Ag/AgCl) for 30 s in 0.01 mol/L KOH/D_2O solution. After the treatment, both samples were cleaned in isopropanol and dried in ambient conditions before measurements.

Neutron reflectivity (NR) curves of SNO are shown in Fig. 2 for the pristine film as well as after treatment in D_2O (heavy water) and H_2O solutions respectively. The surface roughness fitted from the NR results remains at 0.7 nm for both pristine and water-treated SNO, which indicates the absence of corrosion and morphological degradation during treatment. The decrease in oscillation period in the NR results after either H_2O or D_2O treatment (Fig. 2 inset) corresponds to ≈ 6.9 % film expansion and a decrease of the scattering length density from 5.4×10^{-6}Å^{-2} in pristine SNO to 4.6×10^{-6}Å^{-2} in deuterated SNO and 4.1×10^{-6}Å^{-2} in hydrogenated SNO. The fitted neutron scattering length density (SLD) profiles (Fig. 3) show significant increase in the SNO region when H_2O is replaced with D_2O, consistent with the larger coherent neutron scattering cross section of D relative to H. The isotopic substitution results therefore show clearly the intercalation and transport of H (or D) from the solution to SNO, which is similar to the ion transfer process observed in naturally occurring AoL membranes.

In conclusion, our work reveals the potential of strongly correlated nickelate perovskites as tunable hydronic devices, operable in saltwater and oceanic environments, capable of measuring a wide range of electric fields due to proton intercalation. The material stability coupled with environmental and bioelectric potential sensing capability open up new frontiers in deep-sea explorations and may provide new insights into the marine world.

References

[1] R. D. Fields, Sci. Am. **297**, 74 (2007).

[2] Z. Zhang, D. Schwanz, B. Narayanan, M. Kotiuga, J. A. Dura, M. Cherukara, H. Zhou, J. W. Freeland, J. Li, R. Sutarto, F. He, C. Wu, J. Zhu, Y. Sun, K. Ramadoss, S. S. Nonnenmann, N. Yu, R. Comin, K. M. Rabe, S. K. R. S. Sankaranarayanan, S. Ramanathan, Nature **553**, 68 (2018).

[3] J. A. Dura et. al. Rev. Sci. Instrum. **77**, 74301 (2006).

[4] S. C. DeCaluwe, P. A. Kienzle, P. Bhargava, A. M. Baker, J. A. Dura, Soft Matter **10**, 5763 (2014).

[5] P. A. Kienzle, K. V. O'Donovan, J. F. Ankner, N. F. Berk, C. F. Majkrzak, http://www.ncnr.nist.gov/reflpak, 2000-2006.

In-situ neutron reflectometry reveals structure-property relationships at Nafion thin-film interfaces

S. C. DeCaluwe,[1] A. M. Baker,[2] P. Bhargava,[3] J. E. Fischer,[4] and J. A. Dura[5]

Due to its high ionic conductivity and stability, Nafion is the polymer electrolyte material of choice for a range of electrochemical energy devices, including polymer electrolyte membrane fuel cells (PEMFCs). Its properties depend on the phase segregation of its constituent groups (Teflon-like backbone and sulfonic-acid side chains), the nature of which is sensitive to Nafion's chemical environment. However, commercialization of PEMFC for clean electric vehicles is currently impeded by the poor understanding of these properties in the PEMFC catalyst layer (CL), where many limiting processes occur. This understanding is hindered by the complex, nano-scale CL structure, where thin Nafion layers coat clusters of carbon-supported Pt particles, and by the influence of material interfaces and operating conditions on Nafion's properties.

Here, we highlight the use of neutron reflectometry (NR) to study structure-property relationships at Nafion thin film interfaces [1]. Because transport in Nafion is driven by *local* species gradients, composition depth profiles are required to correlate structures within the thin film to resulting transport properties. Nafion forms alternating water-rich and water-poor lamellae (i.e., extended planar features) at SiO_2 substrate interfaces with composition variations that decay toward an average composition [2]. More than 12 nm from the substrate, planar features are no longer observed; instead an "outer layer" forms in which the nano-scale compositional variations are oriented randomly in three dimensions. In this study, NR for a series of 10 films with thicknesses ranging from 5 nm to 153 nm, coated onto SiO_2 substrates, was measured at the NCNR on the MAGIK and PBR reflectometers and fit using Refl1D software.

The fitted SLD profiles for the 10 films (Figure 1) show that water uptake in the outer layer increases (indicated by a decreasing SLD) with increasing thickness for equivalent Nafion thickness, $t_{\mathrm{Naf}} < 60$ nm, but above 60 nm these layers have constant water uptake, similar to bulk membranes. Our results also show variations in the lamellae with varying Nafion thickness, as seen in the Figure 1 inset for selected samples. Of particular note, the average SLD of the lamellae drops significantly for films with $t_{\mathrm{Naf}} \geq 60$ nm, indicating an increase in water uptake.

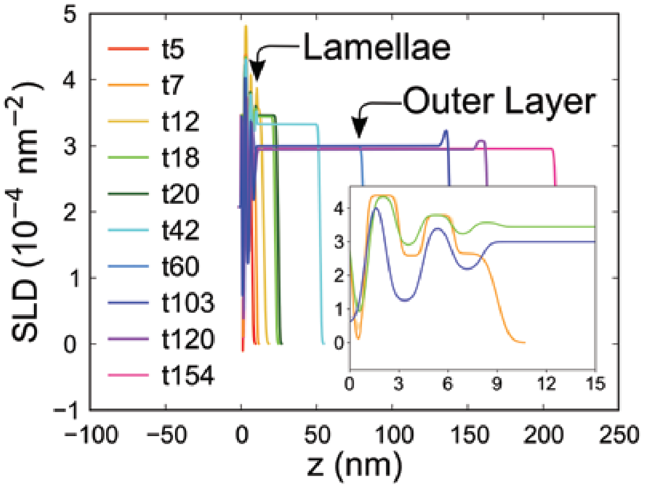

FIGURE 1: SLD profiles for Nafion thin films. Sample name 'tXX' indicates the equivalent Nafion thickness (i.e., thickness if all water were removed), in nm, e.g., sample t18 has an equivalent Nafion thickness of 18 nm. Inset focuses on the lamellar region, including best fits (solid lines) and 68 % confidence intervals (shaded regions) for select samples.

Figure 2 shows the water volume fraction as a function of film thickness, averaged over three different regions of the sample: (*i*) $V_{\mathrm{water,lamellae}}$: the lamellar region, (*ii*) $V_{\mathrm{water,outer}}$: the outer layer, and (*iii*) $V_{\mathrm{water,average}}$: the entire sample (i.e., regions *i* and *ii*). The Nafion water uptake falls into three distinct regimes of sample thickness. In the truncated regime, for $t_{\mathrm{Naf}} \leq 7$ nm, the entire film consists of lamellae. For the thin-film regime, with 7 nm $< t_{\mathrm{Naf}} <$ 60 nm, a thin outer layer is added between the lamellae and the vapor environment, which has a low water uptake that increases approximately linearly with increasing thickness. The upper boundary of this regime roughly corresponds to when the outer layer thickness equals the Nafion radius of gyration. Thus, the suppressed but increasing water uptake of the outer layer is likely due to decreasing confinement effects. Furthermore, this outer layer significantly suppresses the water uptake in the lamellae, which tracks slightly above that of the outer layer. In the thick-film regime for $t_{\mathrm{Naf}} \geq 60$ nm, both $V_{\mathrm{water,bulk\text{-}like}}$ and $V_{\mathrm{water,lamellae}}$ are roughly constant with

---

[1] Colorado School of Mines, Golden, CO 80401
[2] Los Alamos National Laboratory, Los Alamos, NM 87545
[3] University of California, Berkeley, CA 94720
[4] Tesla Motor Company. Fremont, CA, 94538
[5] NIST Center for Neutron Research, National Institute of Standards and Technology, Gaithersburg, MD 20899

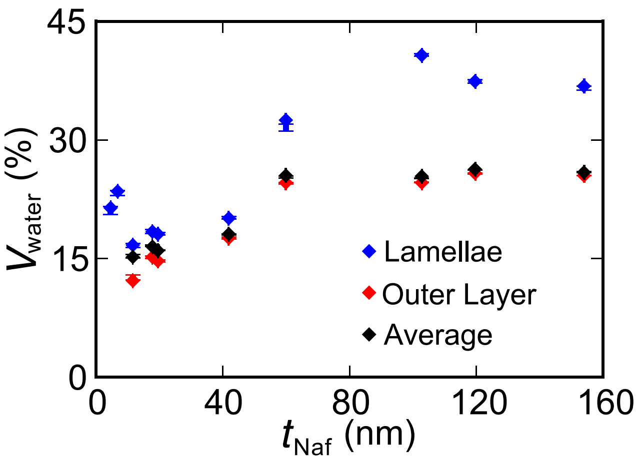

FIGURE 2: Water volume fraction as a function of equivalent Nafion thickness t_{Naf}, including the lamellae, outer layer, and whole-film average. Results show increasing influence of the water-rich lamellae as the total film thickness decreases. Error bars represent 68 % confidence intervals and do not include systematic error or sample-to-sample variations.

thickness, the former leveling off at the amount consistent with the linear trend in the thin-film regime but the lamellar water uptake abruptly increasing, indicating a decoupling of the influence of the outer layer on the lamellae as the radius of gyration is reached. These results demonstrate the importance of depth profiles to explain the variations in total water uptake with Nafion film thickness. For example, the added information of knowing how the water is distributed throughout the film helps to explain previous counter-intuitive results such as the increase in water uptake for films thinner than 20 nm.

To understand how these observed interfacial structures might affect species transport and PEMFC performance, we calculated the effective in-plane ionic conductivities. $\sigma_{parallel}$, for the Nafion thin films, taking the interfacial lamellae into account. These conductivities were fit to experimental results on similar thicknesses, published by Karan and colleagues (Paul, et al. [3]). While standard models for Nafion describe a linear relationship between the water uptake and the ionic conductivity, fits to the experimental data required a model where, additionally, the conductivity of individual layers decreases with proximity to the SiO_2 interface. These in turn were used to predict the conductivity in the through-plane direction (σ_{normal}). Figure 3 shows the individual layer and sample average conductivities fitted to the experimental data at T = 50 °C for samples t5, t7, and t42. The individual layer conductivities help to explain the measured total sample conductivity trends with increasing thickness and show the importance of the composition depth profile when predicting Nafion conductivity in the CL. For samples t5 and t7, in the 'truncated' regime, we observe high conductivities in the water-rich lamellae, and very low conductivities in the water-poor lamellae. In the 'thin-film' regime (sample t42), the water-rich layer adjacent to the SiO_2 retains a high conductivity, but the conductivities of the subsequent water-rich layers quickly decay toward that of the outer layer. While the water-rich layer conductivities for t42 are generally less than those in the 'truncated' regime (which has greater water uptake in the lamellae), we observe that for t42, $\sigma_{parallel}$ is similar to and σ_{normal} exceeds those in the truncated regime, owing to the dominating influence of the thick outer layer.

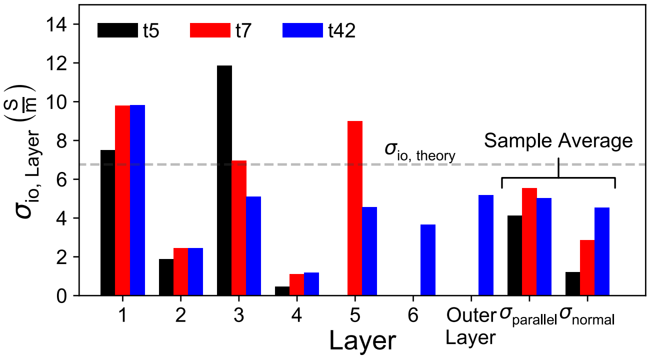

FIGURE 3: Predicted layer and sample average ($\sigma_{parallel}$ and σ_{normal}) conductivities for samples t5, t7, and t42, at T = 50 °C. The results explain the non-monotonic conductivity trends with increasing thickness and the significant anisotropy in sample t5. $\sigma_{io,theory}$ is the conductivity for bulk Nafion membranes at RH = 92 % and T = 50 °C.

These results provide new insights into the evolution of Nafion interfacial morphology as a function of film thickness. At thicknesses relevant to PEMFC catalyst layers (< 60 nm), a re-entrant behavior is observed where water uptake is initially reduced for thinner films but increases again below 12 nm. This can be explained by the presence of interfacial lamellae and the influence of the outer layer with vastly different water uptake and coupling to the lamellae for thicknesses below vs. above the radius of gyration of Nafion. Fitting against experimental conductivity measurements establishes the effect of the interfacial lamellae and the re-entrant water uptake on ionic conductivities. Calculations demonstrate how the thickness, interfacial morphology, and water uptake influence anisotropic conductivity in the PEMFC catalyst layer. These results motivate further accurate measurements of Nafion properties and structure-property relationships as a function of thickness, substrate, and chemical environment relevant to operating PEMFCs.

References

[1] S. C. DeCaluwe, A. M. Baker, P. Bhargava, J. E. Fischer, J. A. Dura, Nano Energy **46**, 91 (2018).

[2] J. A. Dura, V. S. Murthi, M. Hartman, S. K. Satija, C. F. Majkrzak, Macromolecules **42** (13), 4769 (2009).

[3] D. K. Paul, R. Mccreery, K. Karan, J. Electrochem. Soc. **161**, 1395 (2014).

Elucidating the nature of high methane uptake in porous coordination cages via neutron powder diffraction

C. A. Rowland,[1] G. R. Lorzing,[1,2] E. J. Gosselin,[1,2] B. A. Trump,[4] G. P. A. Yap,[1] C. M. Brown,[3,4] and E. D. Bloch[1,2]

Natural gas, which is primarily comprised of methane, has recently been touted as an alternative to gasoline as a fuel in the transportation sector. Since methane is the most gravimetrically energy dense hydrocarbon fuel, its combustion releases less carbon dioxide, carbon monoxide, nitrogen oxides, and particulates than more typical fossil fuels. Additionally, its abundance makes it a promising fuel across power generation and transportation sectors. However, for the latter, the low volumetric energy density of methane has prevented its widespread usage. Adsorbed natural gas (ANG) systems, where methane is stored in a cylinder packed with a high-capacity adsorbent material, have shown promise as an alternative to cryogenic or ultra-high-pressure storage strategies. The challenge with ANG systems is the development of the appropriate high-capacity adsorbent material. Metal-organic frameworks (MOFs) are a relatively new class of porous adsorbent materials that have been widely investigated for methane storage applications. These materials are three-dimensional solids composed of metal ions connected with organic linkers and can display surface areas approaching 10,000 m^2/g. Although MOFs display the highest methane capacities reported to date, their structures contain significant pore space that is not advantageous for adsorbing methane at relevant pressures. Porous molecular solids represent a new class of adsorbents that may show promise for high-pressure methane storage, as they are molecular versions of the pores found within metal-organic frameworks. This could potentially endow them with favorable properties, such as tailored syntheses, flexibility upon adsorption, cooperative binding, and increased ease of processability. However, they have remained relatively unexplored as compared to MOFs, and their gas adsorption properties are poorly understood [1].

In designing the optimal molecular adsorbent material, carbazoledicarboxylate (cdc^{2-}) cages were targeted, as MOFs based on these types of building units have shown interesting high-pressure H_2 and CH_4 adsorption properties (Figure 1) [2]. Carbazole-based Metal$_{12}$Ligand$_{12}$ molecular cages have been reported, although they displayed no porosity. However, as chromium(II) cages have recently shown high surface areas [3], $Cr_{12}(cdc)_{12}$ was targeted. The resulting material, which was synthesized via air-free reactions, displayed high surface areas upon solvent evacuation. Its Brunauer–Emmett–Teller (BET) surface area of 1235 m^2/g represents a record for molecular metal-organic materials. Adapting the precise synthesis, solvent exchange, and activation procedures used on the chromium(II) material similarly afforded high surface area $Cu_{12}(cdc)_{12}$ and $Mo_{12}(cdc)_{12}$ with BET surface areas of 657 m^2/g and 1108 m^2/g, respectively.

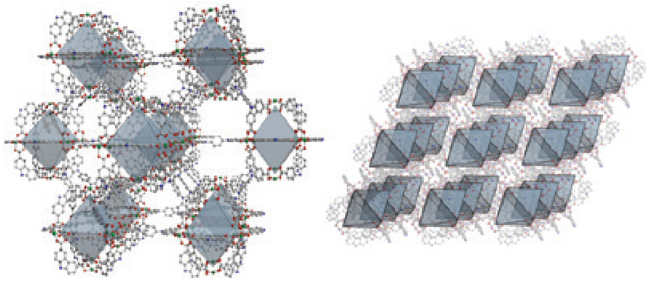

FIGURE 1: (Left) Structure of PCN-81, a metal-organic framework based on covalently linked carbazoledicarboxylic (cdc) acid cages. (Right) Structure of $M_{12}(cdc)_{12}$ (where M = Cr, Cu, or Mo), a molecular adsorbent based on similar coordination cages. Notable in this material is the lack of three-dimensional connectivity leading to less unusable void space. For both solids the polygons represent potentially gas-accessible pore volume.

The record surface areas of these materials prompted high-pressure methane measurements. All three materials display high methane adsorption capacities from 0 bar to 65 bar at 298 K. At 35 bar the total gravimetric uptakes follow the surface area trends with capacities of 148 cm^3/g, 135 cm^3/g, and 81 cm^3/g for $Cr_{12}(cdc)_{12}$, $Mo_{12}(cdc)_{12}$, and $Cu_{12}(cdc)_{12}$, respectively (Figure 2). Methane uptake increases up to at least 65 bar with the $Cr_{12}(cdc)_{12}$ displaying the highest gravimetric capacity of 194 cm^3/g while $Mo_{12}(cdc)_{12}$ has the highest volumetric capacity (150 cm^3/cm^3). Both the gravimetric and volumetric capacities are the highest observed for a porous molecular assembly. The carbazole-based metal-organic framework (PCN-81) similarly displays high methane capacity. As a result of its significantly increased surface area of 4050 m^2/g, the MOF has a CH_4 capacity at 35 bar and 298 K of 305 cm^3/g, which increases to 449 cm^3/g at 65 bar, exceeding that of HKUST-1. Given the low density of the material, its volumetric capacity at 35 bar is significantly lower at 147 cm^3/cm^3. For adsorption/desorption conditions relevant to natural gas storage, PCN-81 has a

---

[1] Department of Chemistry and Biochemistry, University of Delaware, Newark, DE 19716
[2] Center for Neutron Science, University of Delaware, Newark, DE 19716
[3] Department of Chemical and Biomolecular Engineering, University of Delaware, Newark, DE 19716
[4] NIST Center for Neutron Research, National Institute of Standards and Technology, Gaithersburg, MD 20899

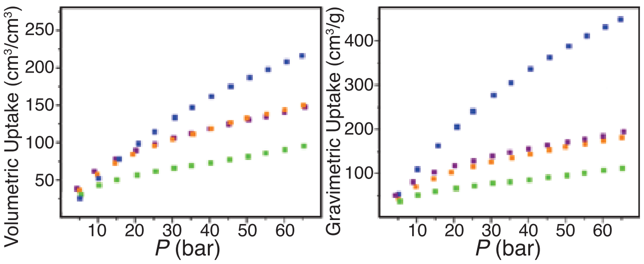

FIGURE 2: (left) Total volumetric methane adsorption in the MOF PCN-81 (blue) and the molecular clusters of $M_{12}(cdc)_{12}$ (Cr = purple, Mo = orange, Cu = green). At lower pressures the molecular materials display higher volumetric uptake than does the MOF as a result of minimal void space in their structures. (right) High pressure methane adsorption plotted as total gravimetric uptake.

deliverable capacity of 190 cm^3/cm^3, which is comparable to the highest values reported for any solid adsorbent.

Neutron powder diffraction offers a unique opportunity to gain insight into the nature of CH_4 adsorption in these materials. Although the porous coordination cages retain crystallinity upon solvent removal, it is decreased during activation to the point of precluding the use of diffraction studies to interrogate binding sites. PCN-81, however remains highly crystalline upon degassing. At a CD_4:Cu loading of 1:1 three main adsorption sites are apparent in the framework. Although the framework is comprised of three types of pores, the methane is exclusively adsorbed in the $M_{12}(cdc)_{12}$ cage. A primary adsorption site is the open copper(II) center with a Cu–C distance of 2.777 Å and an occupancy of 0.63(3). A site with similar occupancy (0.64(3)) is at the edge of a carbazole ligand with $C_{methane}$–C_{ligand} distances of 3.27 Å and 3.69 Å. Together, these two adsorption sites form the basis for the lowest occupancy site (0.28(3)) in a triangular pocket between two of the metal bound CD_4 and a carbazole-bound CD_4 with methane-methane distances of 2.79 Å - 4.13 Å. (Figure 3). At 2.0/Cu a number of additional sites are populated. At this loading the final two triangular windows of the cage are populated at their three corners. An additional adsorption site on the inside of the cage and the copper on the exterior bind methane at this loading. Increasing the methane dose to 4.0/Cu reveals no additional CD_4 binding sites, although the overall occupancy increases.

Interestingly, at this loading the small cage in PCN-81 remains the only one that is occupied. Nine methane adsorption sites are related by symmetry to afford a total methane capacity of 49 molecules per cage. This corresponds to a methane adsorption capacity of approximately 260 cm^3/g, a value PCN-81 reaches by 35 bar. At this pressure the two additional pores in the material remain unoccupied but would allow for additional storage at higher pressures. At lower pressures the two other pores are essentially empty space that is detrimental to the density, and thus volumetric capacity of the material. This is consistent with the nearly equal volumetric adsorption capacities of PCN-81, $Cr_{12}(cdc)_{12}$, and $Mo_{12}(cdc)_{12}$ at 35 bar and 298 K.

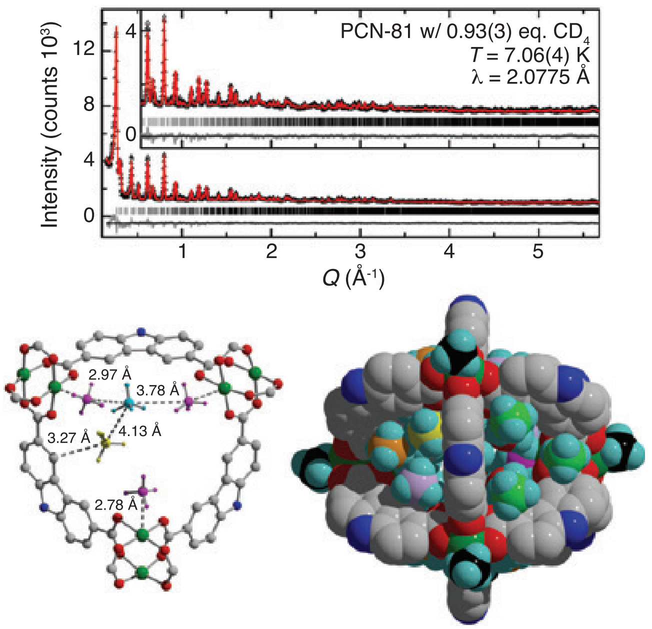

FIGURE 3: (Top) Neutron powder diffraction data (black triangles) along with Rietveld fit (red line) from the structural model of PCN-81 with adsorbed methane. (Bottom left) Three individual methane adsorption sites (pink, yellow and cyan) are coordinated to the copper paddlewheel, benzene ring, and bridging between methane molecules, respectively, are identified. (Bottom right) A space-filling representation of the packing inside the pore.

In conclusion, this work shows that with precise synthesis, solvent exchange, and activation procedures, high surface areas are attainable for porous coordination assemblies. Although the surface areas displayed by these materials currently fall short of the record values displayed by metal-organic frameworks, porous cages show potential utility for the high-pressure storage of natural gas. Neutron diffraction experiments suggest that the $M_{12}(cdc)_{12}$ cage, which is also present in PCN-81 and a number of related MOFs ,may be the optimal pore environment for high-pressure methane storage. An ideal methane storage material may consist nearly entirely of $M_{12}(cdc)_{12}$ cages, whether it is molecular or an extended solid.

References

[1] C. A. Rowland, G. R. Lorzing, E. J. Gosselin, B. A. Trump, G. P. A. Yap, C. M. Brown, E. D. Bloch, J. Am. Chem. Soc. Just Accepted Manuscript, DOI: 10.1021/jacs.8b05780.

[2] U. Stoeck, S. Krause, V. Bon, I. Senfovska, S. Kaskel, Chem. Commun. **48**, 10841 (2012).

[3] G. R. Lorzing, B. A. Trump, C. M. Brown, E. D. Bloch, Chem. Mater. **29** (20), 8583 (2017).

A local quantum phase transition in YFe_2Al_{10}

W. J. Gannon,[1] L. S. Wu,[2] I. A. Zaliznyak,[3] W. H. Xu,[3] A. M. Tsvelik,[3] Y. Qiu,[4] J. A. Rodriguez-Rivera,[4,5] and M. C. Aronson[1]

One of the great triumphs of theoretical physics has been the development of a phenomenology of classical phase transitions between a phase where there is long-ranged order, and one where there is not. The central paradigm has the ordered phase growing within the disordered phase. At temperatures that are large compared to the critical temperature T_C where the phase transition occurs, the ordered phase only exists over a limited length scale and has a limited lifetime. The length scale and lifetime of the ordered phase diverge as $T \rightarrow T_C$, where the ordered phase spans the sample and becomes static. This scenario has received extensive experimental support in a variety of systems hosting phase transitions that are as diverse as the onset of magnetic or superconducting order, structural modifications, or even liquid-solid or liquid-gas phase transformations. We report here [1] the first direct experimental evidence for an entirely new type of phase transition where the ordered phase is limited to the shortest length scales, while the fluctuations of individual magnetic moments become perfectly correlated in time.

This local phase transition has been observed in inelastic neutron scattering measurements carried out on the compound YFe_2Al_{10}, whose structure can be visualized as layers of square nets of Fe atoms, each of which bears a moment of $\approx 0.5\ \mu_B$ (Fig. 1A). No ordering of these moments is found at temperatures as low as 0.07 K, and the divergence of the magnetic susceptibility $\chi(T) \sim T^{-1.4}$ is evidence that the associated phase transition happens exactly at $T = 0$ (Fig. 1B), and so the dynamics associated with this phase transition necessarily reflect quantum, not thermal, fluctuations.

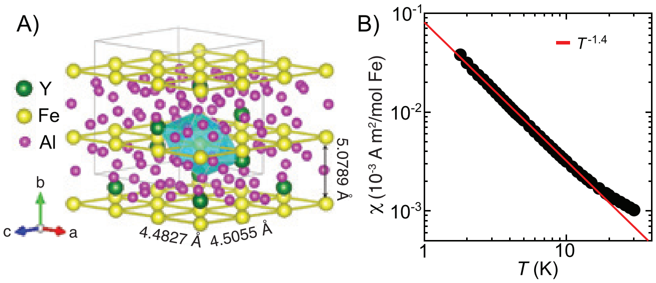

FIGURE 1: (A) The layered crystal structure of YFe_2Al_{10}. (B) The dc magnetic susceptibility of YFe_2Al_{10} diverges as $T \rightarrow 0$, $\chi(T) \sim T^{-1.4}$ when the 40 x 10^3 A/m measuring field is oriented within the Fe planes.

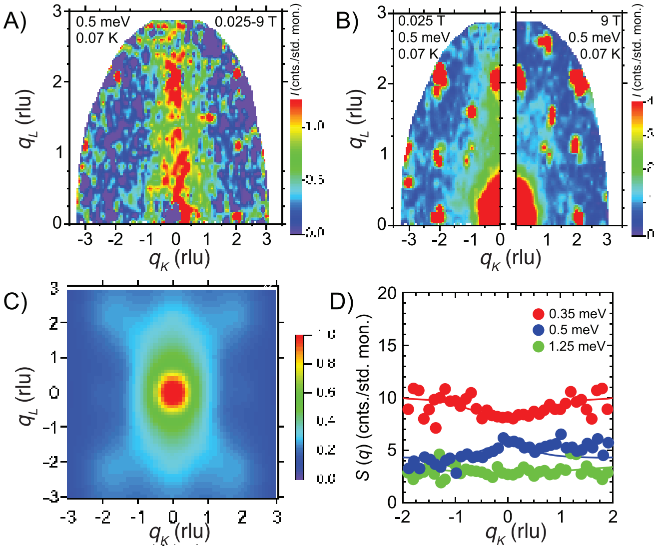

FIGURE 2: The scattered neutron intensity S measured at 0.07 K and a fixed energy transfer of 0.5 meV, with similar data measured at 9 T subtracted (A) and the 9 T background (B). (C) The form factor for the d_{xz} Fe orbital in YFe_2Al_{10} computed using Density Functional Theory. (D) Once the scattered intensity is corrected for the form factor in (C) it no longer has any significant wave vector dependence.

Proximity to a conventional magnetic phase transition involves a growth of scattered neutron intensity near wave vectors that are associated with the spatial periodicity of the magnetic moments in the ordered phase. As shown in Fig. 2A, the situation is very different in YFe_2Al_{10}. A broad ridge of scattered neutron intensity $S(q_K)$ is observed for wave vectors q_K that lie in the plane of the Fe moments. The suppression of this scattering by magnetic fields (Fig. 2B) confirms its intrinsically magnetic character. Comparing $S(q_K)$ to the form factor of an isolated Fe^{2+} ion, or alternatively to theoretical computations of the Fe d_{xz} orbitals (Fig. 2C) reveals that this very broad wave vector dependence arises only from the spatial distribution of the Fe moment itself, and in YFe_2Al_{10} they provide no evidence for the spatial correlations that accompany magnetic order. Indeed, once the form factor is divided from $S(q_K)$, the result is entirely independent of wave vector (Fig. 2D), indicating that, within the accuracy of the neutron scattering experiment, each magnetic moment acts independently of every other moment.

---

[1] Texas A&M University, College Station, TX 77843-4242
[2] Oak Ridge National Laboratory, Oak Ridge, TN 37831
[3] Brookhaven National Laboratory, Upton, NY 11973
[4] NIST Center for Neutron Research, National Institute of Standards and Technology, Gaithersburg, MD 20899
[5] University of Maryland, College Park, MD 20740

The $T = 0$ phase transition in YFe_2Al_{10} involves only the *temporal* correlation of individual Fe moments. Evidence that these local magnetic dynamics correspond to a phase transition comes from the energy dependence of the scattered intensity $S(q_K)$ (Fig. 3). Taking advantage of the very small background signal and the significant signal intensification available in the multi-axis spectrometer MACS, we are able to show that $S(E)$ exhibits a strong divergence as $E \rightarrow 0$, i.e., $S(E) \sim E^{-1.4}$. This buildup of spectral weight at the lowest energies is a universal feature of phase transitions that is referred to as `critical slowing down', where the dynamics of Fe moments are increasingly occurring on the longest time scales that can be experimentally probed. A remarkable picture of a local phase transition emerges from our neutron scattering observations, where the spectrum of excitations for each Fe moment is exactly the same, but that this occurs without the individual Fe moments developing any spatial correlations. Unlike conventional phase transitions, our experiments find no evidence that this phase transition is related to a broken symmetry, such as time reversal symmetry.

What physics could lead to a local phase transition? In the absence of long-range magnetic order, it is appealing to think that it is the emergence of the Fe moments themselves that drives this purely dynamical transition. The unusually small magnitude of the Fe moments may suggest that, YFe_2Al_{10} is on the verge of a Mott-like transition where the Hund's and Coulomb interactions are just the right strength to localize a d_{xz} orbital, introducing a magnetic moment on the Fe atoms. In this scenario, the quantum critical dynamics correspond to fluctuations between two different electronic configurations: one where the underlying Fermi surface is small, and the localized d-electron is excluded, and another where the Fermi surface is large, and the d-electron is delocalized. An alternate suggestion is that YFe_2Al_{10} is very close to a topological phase transition, where its layered nature could justify its description within the quantum 2DXY model [2,3]. In this case, the relationship between correlation length and correlation time that is central to conventional phase transitions is largely broken, and the fundamental excitations are vortices whose dynamics can be described as warps, or `wrinkles in time'.

Our neutron scattering measurements on the model compound YFe_2Al_{10} provide the first experimental evidence for the existence of a new type of phase transition that does not involve the growth of long-range spatial correlations that culminate in a broken symmetry at T_C. Such phase transitions have previously been theoretically proposed within the contexts of different models and Hamiltonians appropriate for quantum electronic matter, although there was no certainty that the localized aspects of the physics truly dominate in real materials. Increasingly, it is understood that quantum phase transitions involve the interplay of broken symmetries, electronic confinement, and also topological character and protection. The new results that we have outlined here remind us that the possibilities are vast, both for the types of order that can be realized in theory and experiment, but also for the way in which real systems transition among these different phases at $T = 0$.

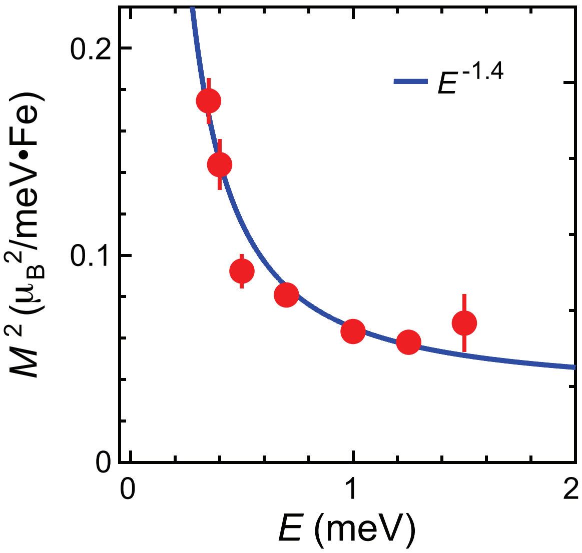

FIGURE 3: The energy dependence of the magnetization squared M^2 of the fluctuating moments at 0.07 K and magnetic field $B = 0.025$ T. The solid blue line shows $E^{-1.4}$.

References

[1] W. J. Gannon, L. –S. Wu, I. A. Zaliznyak, W. H. Xu, A. M. Tsvelik, Y. Qiu, J. A. Rodriguez-Rivera, and M. C. Aronson, Proc. Nat. Acad. Sci. **115**, 6995 (2018).

[2] C. Hou and C. M. Varma, Phys. Rev. B **94**, 201101 (2016).

[3] Chandra M. Varma, W. J. Gannon, M. C. Aronson, J. A. Rodriguez-Rivera, Y. Qiu, Phys. Rev. B **97**, 085134 (2018).

Screened moments and extrinsic in-gap states in samarium hexaboride

W. T. Fuhrman,[1] J. R. Chamorro,[1,2] P. Alekseev,[3,4] J.-M. Mignot,[5] T. Keller,[6,7] P. Nikolić,[1,8] T. M. McQueen,[1,2,9] and C. L. Broholm[1,9]

While condensed matter physics has long encompassed technologically relevant materials, the recent incorporation of ideas from topology has led to surprising insights with tantalizing future applications. Strong electron-electron correlations are a well-known driver of exotic physics, yet our understanding of topological materials with strongly interacting electrons is in its infancy. Kondo insulators have strongly interacting, localized 4*f* electrons hybridized with conduction electrons. The resultant correlated, insulating state and the potential for topological non-triviality present an ideal confluence in the search for novel topological phenomena [1]. Samarium hexaboride (SmB_6) is the first proposed topological Kondo insulator. With an experimental description that has stoked curiosity for decades, SmB_6 is a paramount compound in the emerging class of topological materials.

Topological insulators have protected metallic surface states that become apparent at low temperatures as bulk carriers are depleted. As the surface begins to dominate conduction channels, the temperature dependence of the resistance flattens (typically below about 5 K in SmB_6). This energy scale has naturally come under renewed scrutiny in SmB_6. Quantum oscillations, anomalous optical conductivity, large linear specific heat, and more form a myriad of perplexing experimental results below 10 K that seem to belie an insulating ground state. These low-energy phenomena are found below the bulk electronic gap (≈ 20 meV) and commonly referred to as in-gap states. The surface states are themselves a manifestation of the bulk band structure, which defines the electronic gap. Understanding these in-gap states is crucial to a comprehensive understanding of both the bulk and surface of SmB_6.

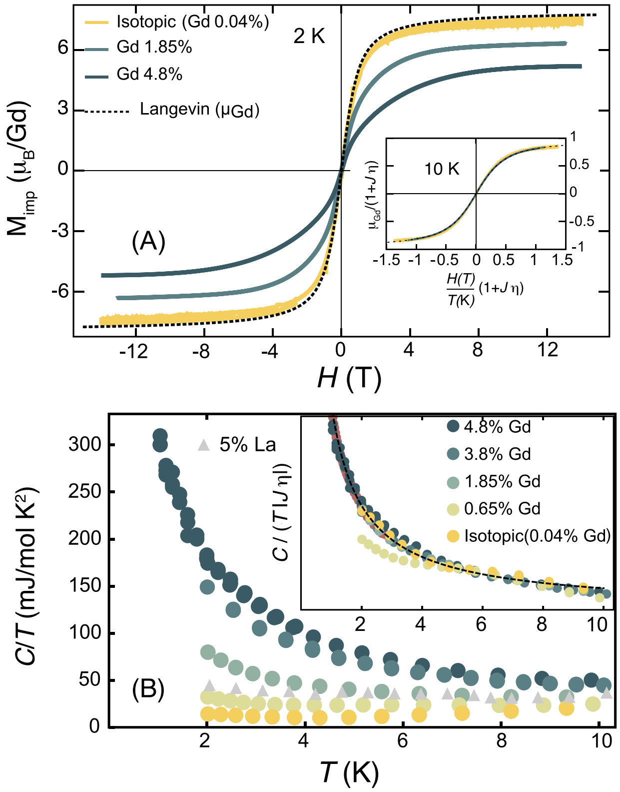

FIGURE 1: Magnetization and heat capacity of Gd-doped SmB_6. (A) Van Vleck component has been removed and magnetization scaled by impurity concentration to reveal a reduced effective paramagnetic Gd moment. Inset shows that scaling by the effective moment collapses magnetization. (B) Specific heat of variously doped SmB_6. Inset shows specific heat after removal of lattice contribution and scaling by reduction in moment $|J\eta|$ from (A).

The unconventional phenomenology of SmB_6 has been difficult to explain in part because of differences between samples. Rare-earth purification is exceedingly difficult, and impurities are a natural suspect for the sample dependency in SmB_6. Isotopic purification greatly reduces contaminants, but due to isotopic mass overlap, dilute quantities of Gd-154 remain even in highly-purified samples of $^{154}Sm^{11}B_6$. We used an isotopically purified sample as well as moderately doped samples to examine the heat capacity and magnetization over more than two orders of magnitude of impurity concentration [2]. These results indicate that magnetic impurities introduce a magnetic low-energy density of states (LEDOS). Our neutron scattering

---

[1] Institute for Quantum Matter and Department of Physics and Astronomy, The Johns Hopkins University, Baltimore, MD 21218
[2] Department of Chemistry, The Johns Hopkins University, Baltimore, MD 21218
[3] National Research Centre “Kurchatov Institute,” 123182 Moscow, Russia
[4] National Research Nuclear University “MEPhI,” 115409 Moscow, Russia
[5] Laboratoire Leon Brillouin, CEA-CNRS, CEA/Saclay, France
[6] Max Planck-Institut fur Festkörperforschung, Heisenbergstrasse 1, D-70569 Stuttgart, Germany
[7] Max Planck Society Outstation at the Forschungsneutronenquelle Heinz Maier-Leibnitz (MLZ), D-85747 Garching, Germany
[8] George Mason University, Fairfax, VA 22030
[9] Department of Materials Science and Engineering, The Johns Hopkins University, Baltimore, MD 21218

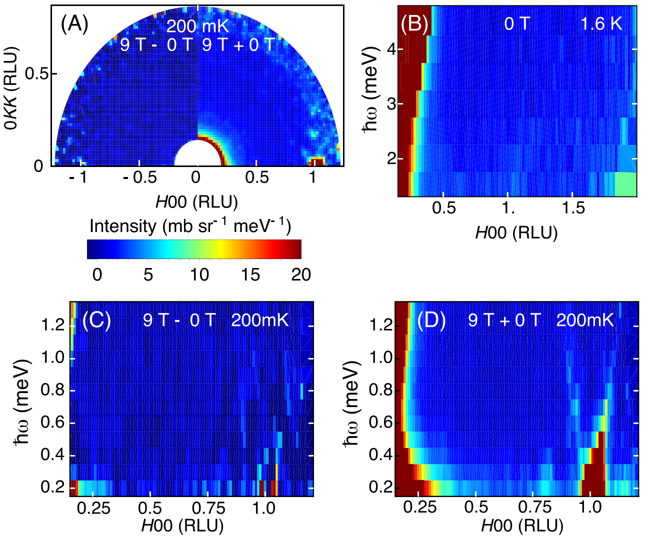

FIGURE 2: Low-energy neutron scattering of SmB_6 taken at 1.6 K and 200 mK in zero field and 9 T. Only residual Bragg scattering is seen in both zero-field and high-field measurements. (A) Energy integrated from 0.2 meV to 1.3 meV. Left shows 9 T data with the 0 T data subtracted (9T - 0T). Right, averaged (9 T + 0 T). (B) 0 T data from 1.5 meV to 5 meV. (C) 9 T - 0 T data along *H*00 (D) Average of 9 T and 0 T data along *H*00.

experiments furthermore show no intrinsic excitations below the well-established 13 meV spin-exciton.

The relationship between magnetic impurities and the LEDOS is made clear by comparing the magnetization and specific heat of variously doped samples, as shown in Figure 1. Subtracting the linear Van Vleck magnetization that arises from non-magnetic Sm^{2+} reveals a paramagnetic-like component in the magnetization (Fig. 1(A)). Fitting the residual magnetization with a paramagnetic Langevin function extracts both an effective moment size ($\mu_{Eff} = \mu_{Gd}(1-|J\eta|)$) and impurity concentration. Meanwhile, the specific heat of Gd-doped samples exhibits a dramatic enhancement at low-temperatures, far greater than that from doping the non-magnetic lanthanum (Fig. 1(B)). By scaling the specific heat with the reduction in effective Gd moment obtained by fitting the magnetization ($|J\eta|$), we achieve a data collapse. This indicates that the LEDOS is associated with a screening of the impurity magnetic moments, accounting for the specific heat of our samples. Impurities in the Kondo lattice are distinct from those typical of semiconductors. The dynamic screening effect we observe demonstrates the importance of the magnetic character of the impurities. The consequences of magnetic impurities in a Kondo insulator bear resemblance to the well-known Kondo impurity effect in metals, now exhibited in a small-gap semiconductor.

In addition to the thermo-magnetic relationship described above, we used neutron scattering to probe directly the low-energy magnetism of SmB_6. We found no indications of magnetism in the low energy regime of the doubly-isotopic sample at both zero and high field (9 T). Figure 2 shows the scattering in the *HKK* plane of the doubly-isotopic sample. Aside from residual nuclear Bragg scattering due to the spectrometer resolution, no momentum, energy, or field dependence of the neutron scattering cross section is observed.

Our neutron scattering results provide crucial constraints on theories of the intrinsic low energy magnetism in SmB_6 as well as help to interpret other experimental results. Magnetic neutron scattering is well-suited for probing magnetic excitations such as those proposed for SmB_6 (e.g., spinons, excitons, etc.), and our experiments place a tight upper limit on any low-energy excitations with a $4f$ electron form factor. Given the absence of magnetic neutron scattering, as well as the continued trend to lower heat capacity with improved sample quality, it is reasonable to assign most if not all of the low energy DOS typically observed in SmB_6 to extrinsic origins. The variety of metal-like properties induced by impurities that we have documented even in nominally pure samples is an important part of the phenomenology of this cornerstone Kondo insulator.

Following these results, along with our previous neutron scattering work [3], the bulk low-energy regime of SmB_6 can be succinctly understood as a Kondo insulator with a gap to a collective bound state extracted from the continuum of particle-hole excitations. The experiments described here reveal an absence of intrinsic low-energy magnetism as well as a stark sensitivity of this insulating state to even dilute quantities of impurities. Defects and impurities are certainly not unique to SmB_6, and so it is natural to wonder why such impurity effects are not noted in other similar compounds. The most dramatic difference between SmB_6 and other heavy fermion materials is that SmB_6 has a truly insulating bulk ground state. As such, the density of states at low energies introduced by impurities is unmuffled by the typically large contribution from heavy electrons, themselves often on the brink of magnetism. In SmB_6, instead of low energy degrees of freedom approaching critically, the magnetism is manifested in the gapped spin exciton, which is readily marred. Our results help to explain the seemingly paradoxical metal-like bulk phenomena and indicate that SmB_6 has the prerequisite Kondo insulator ground state of a putative topological Kondo insulator.

References

[1] M. Dzero, K. Sun, V. Galitski, P. Coleman, Physical Review Letters **104**, 106408 (2010).

[2] W. Fuhrman, J. Chamorro, P. Alekseev, J.-M. Mignot, T. Keller, J. Rodriguez-Rivera, Y. Qiu, P. Nikolic, T. McQueen, C. Broholm, Nat. Comm. **9**, 1539 (2018).

[3] W. T. Fuhrman, J. Leiner, P. Nikolic, G. E. Granroth, M. B. Stone, M. D. Lumsden, L. DeBeer-Schmitt, P. A. Alekseev, J.-M. Mignot, S. M. Koohpayeh, P. Cottingham, W. A. Phelan, L. Schoop, T. M. McQueen, C. Broholm, Physical Review Letters **114**, 036401 (2015).

Proximity to a quantum spin liquid state in the pyrochlore $Er_2Pt_2O_7$

A. M. Hallas,[1] J. Gaudet,[1] N. P. Butch,[2] Guangyong Xu,[2] M. Tachibana,[3] C. R. Wiebe,[1,4,5,6]
G. M. Luke,[1,5] and B. D. Gaulin[1,5,6]

The quantum spin liquid is a much sought-after magnetic state of matter that exists in the limit where quantum effects dominate [1]. Whereas a typical magnetic material will tend to order or freeze at sufficiently low temperatures, a quantum spin liquid will remain disordered and dynamic even at absolute zero temperature. Much in the way that quantum mechanical zero-point fluctuations suppress solidification in liquid helium-3, quantum spin liquids are unable to order magnetically because of intense quantum mechanical spin fluctuations. Herein lies a major dilemma: so long as the temperature is above zero, it is always possible that the spins may order or freeze at some still lower temperature. Thus, there is currently no indisputable experimental proof of the quantum spin liquid ground state. However, to bolster the candidacy of a putative quantum spin liquid, one can look for a key signature with inelastic neutron scattering: fractionalized excitations. In a typical ordered magnet, the spin excitations are quantized as magnons, which carry $S = 1$. In contrast, the elementary spin excitation of a quantum spin liquid is called a spinon and carries a fractional quantum number, $S = ½$. In an inelastic neutron scattering experiment, pairs of spinons are created which divide the energy and momentum transferred by the neutron and thus manifest themselves as a continuum of scattering.

Rare-earth pyrochlore materials, with the chemical formula $R_2M_2O_7$ (R = rare earth, M = transition or post-transition metal) are amongst the most successful platforms for the study of exotic magnetism, such as the quantum spin liquid state [2]. The reasons for this are numerous and include: (i) chemical versatility and flexibility; the pyrochlore structure can host a large fraction of the elements on the periodic table, (ii) many of these materials are insulating, allowing their magnetism to be studied independently from electronic degrees of freedom, and (iii) the R and M atoms in this structure each form a network of corner-sharing tetrahedra. This lattice is imbued with a special property known as geometric frustration: the connectivity often makes it more challenging for the material to find a favourable ordered state, resulting in the suppression of magnetic order. Frustration is thus a crucial characteristic for a quantum spin liquid candidate [1]!

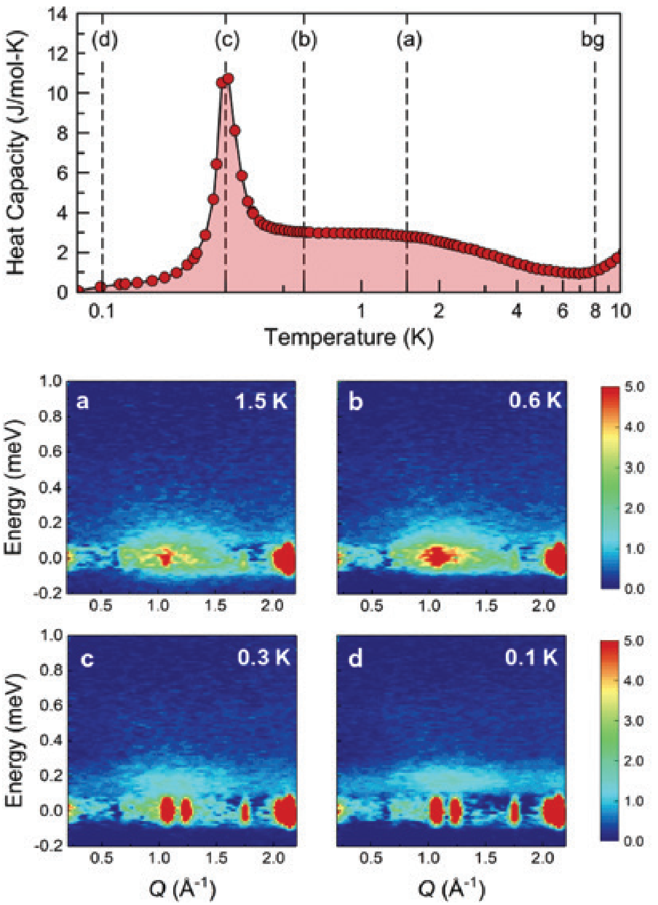

FIGURE 1: Inelastic neutron scattering measurements were performed on powder samples of $Er_2Pt_2O_7$ at the DCS. Measurements were performed at (a) 1.5 K (b) 0.6 K (c) 0.3 K and (d) 0.1 K, where in each case an 8 K background has been subtracted. The temperatures of these data sets are indicated with respect to the low temperature heat capacity, reproduced from Ref. [3]. (a-b) Above the ordering transition, short-range spin correlations are observed to build up at the elastic line. (c-d) Then, below T_N = 0.3 K, this scattering segregates into magnetic Bragg peaks and a gapped spin excitation.

$Er_2Pt_2O_7$ is a rare earth pyrochlore in which the magnetism is carried by Er^{3+} and Pt^{4+} is non-magnetic. The synthesis of platinum-based oxides is challenging due to the propensity of platinum to reduce into its base metal form. Thus, the preparation of this material requires high-pressure methods, which we performed at the National Institute for Materials Science in Tsukuba, Japan. The heat capacity of $Er_2Pt_2O_7$ contains a sharp peak, signifying that this material undergoes a long-range magnetic ordering transition at T_N = 0.3 K (Figure 1) [3]. This observation is noteworthy because other erbium pyrochlores, such as $Er_2Ti_2O_7$ and $Er_2Ge_2O_7$ where only the non-magnetic

---

[1] McMaster University, Hamilton, Ontario L8S 4M1, Canada
[2] NIST Center for Neutron Research, National Institute of Standards and Technology, Gaithersburg, MD 20899
[3] National Institute for Materials Science, 1-1 Namiki, Tsukuba 305-0044, Ibaraki, Japan
[4] University of Winnipeg, Winnipeg, Manitoba R3B 2E9, Canada
[5] Canadian Institute for Advanced Research, 661 University Avenue, Toronto, Ontario M5G 1M1, Canada
[6] Brockhouse Institute for Materials Research, Hamilton, Ontario L8S 4M1, Canada

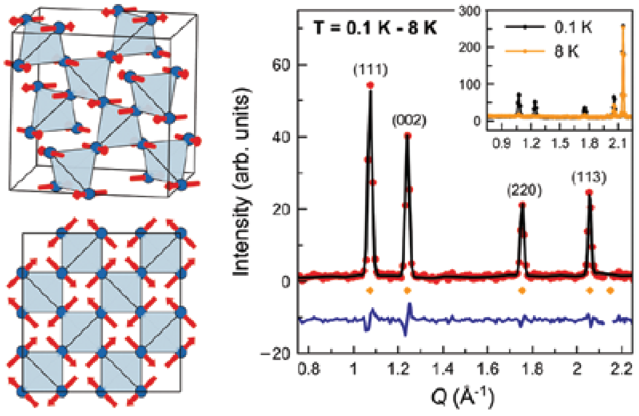

FIGURE 2: The diffraction pattern of $Er_2Pt_2O_7$ was isolated by taking an integration over the elastic channel of the DCS data, shown in Fig. 1. Below $T_N = 0.3$ K, $Er_2Pt_2O_7$ undergoes a long-range magnetic ordering transition and magnetic Bragg peaks are observed to form, as shown in the inset. The magnetic structure was solved using symmetry analysis and a Rietveld refinement. The resulting structure is a $k = 0$ antiferromagnetic state referred to as Γ_7 or the Palmer-Chalker state.

element is varied, order at significantly higher temperatures. While these non-magnetic substitutions do slightly alter the size of the crystal lattice, one would generally expect their effect to be rather minimal. Therefore, the more than 75 % suppression of ordering temperature in $Er_2Pt_2O_7$ is anomalous and hints that this system may be at the cusp of a quantum spin liquid state.

In Figure 1 (a-d) we present the temperature dependence of the spin excitations in $Er_2Pt_2O_7$ measured on the Disc Chopper Spectrometer (DCS), where the temperature of each panel is labelled for convenience in the heat capacity. Above $T_N = 0.3$ K, one can observe a broad shoulder in the heat capacity centered at $T^* = 1.5$ K. Inspection of the corresponding inelastic neutron scattering spectra reveals that this broad anomaly is correlated with developing short-range quasi-static spin correlations. These correlations are peaked near $Q = 1.1$ Å^{-1}, an antiferromagnetic zone center. When $Er_2Pt_2O_7$ is cooled below $T_N = 0.3$ K, this scattering is observed to segregate into resolution-limited magnetic Bragg reflections and a flat, well-defined inelastic mode centered at 0.2 meV, as could be expected for a magnetically ordered state. In the remainder of this report, our analysis will focus on the data presented in Figure 1(d), first starting with the elastic scattering and then moving on to the inelastic scattering.

The elastic scattering from $Er_2Pt_2O_7$ can be isolated by performing an integration in energy from -0.05 meV to 0.05 meV. The resulting diffraction patterns are presented in Figure 2. In the inset, a comparison of spectra collected at $T = 8$ K and 0.1 K is presented where one can clearly observe that additional intensity is present in the 0.1 K spectra. This additional intensity is located on symmetry positions allowed by the pyrochlore crystal structure, signifying that the symmetry group for the magnetic order is identical to that of the crystal structure. In order to determine the nature of the magnetically-ordered state, we can isolate the magnetic diffraction pattern by subtracting the two data sets, which is shown in the main panel of Figure 2. Using symmetry analysis and Rietveld refinement we determined that the magnetically ordered state of $Er_2Pt_2O_7$ belongs to the Γ_7 irreducible representation, which is often dubbed the Palmer-Chalker state [4]. The spin configuration for this antiferromagnetic state is also

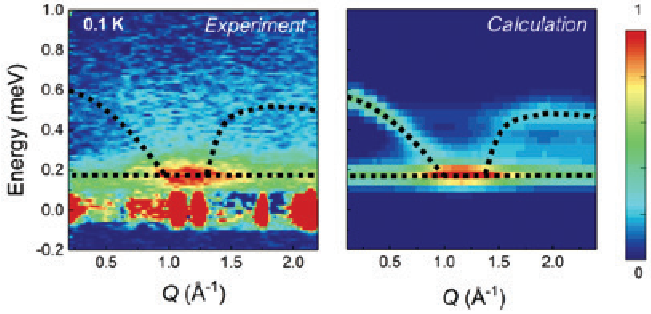

FIGURE 3: Linear spin wave theory was used to refine the exchange couplings for $Er_2Pt_2O_7$. The resulting powder averaged spin wave calculation describes well the flat band centered at 0.2 meV observed in the experimental spectrum. However, the calculation also predicts two dispersive branches at higher energies that are strikingly absent from the experimental data. The spectral weight associated with these upper branches is instead smeared out into a continuum of scattering, reminiscent of the expected behavior of a quantum spin liquid.

presented in Figure 2 where on a single tetrahedron the spins are oriented in two orthogonal pairs of anti-parallel spins.

Having solved the magnetic structure for $Er_2Pt_2O_7$ we can next turn to the inelastic spectra at $T = 0.1$ K, presented in Figure 3, where the intensity range has been modified to enhance the features of the inelastic signal. Using linear spin-wave theory, we refined the exchange couplings in $Er_2Pt_2O_7$ and the resulting calculated spin wave spectrum is presented in Figure 3. This calculation provides a very good description of the flat band centered at 0.2 meV, reproducing both its lack of dispersion and its Q-dependence. However, there is a striking discrepancy between the calculation and the experimental spectrum at higher energies: two dispersive bands are predicted that are absent in the measured data. Instead, the spectral weight associated with these branches is smeared out into a continuum of scattering reminiscent of our earlier description of what can be expected for a quantum spin liquid.

In this work, we demonstrate that $Er_2Pt_2O_7$ has the characteristics of proximity to a quantum spin liquid state: strong suppression of magnetic order and a spin excitation continuum [4]. The quantum spin liquid state is of significant interest because of its quantum entangled nature, which places it at odds with our classical intuition about matter. Related theoretical work provides a framework through which we can understand the origin of this behavior [5, 6]. Having identified a material that is close to the boundary of a quantum spin liquid state, we can next explore perturbations such as pressure or chemical substitution that might push this system ever closer to the quantum limit.

References

[1] L. Balents, Nature **464**, 199-208 (2010).

[2] J. S. Gardner, M. J. P. Gingras, and J. E. Greedan, Rev. Mod. Phys. **82**, 53 (2010).

[3] Y. Q. Cai et al., Phys. Rev. B **93**, 014443 (2016).

[4] A. M. Hallas et al., Phys. Rev. Lett. **119**, 187201 (2017).

[5] H. Yan, O. Benton, L. Jaubert, and N. Shannon, Phys. Rev. B **95**, 094422 (2017).

[6] A.M. Hallas, J. Gaudet, and B.D. Gaulin, Annu. Rev. Cond. Matter Phys. **9**, 105 (2018).

Amplitude mode in the planar triangular antiferromagnet $Na_{0.9}MnO_2$

R. L. Dally,[1,2] Y. Zhao,[3,4] Z. Xu,[3,4] R. Chisnell,[3] M. B. Stone,[5] J. W. Lynn,[3] L. Balents,[6] and S. D. Wilson[1]

Amplitude modes reflect an oscillation in the magnitude of a complex order parameter, and in condensed matter systems, they are often sought to be studied as potential solid-state physics proxies of the Higgs boson. Detecting amplitude modes is difficult, as they are typically unstable to decay, and observations have generally been limited to low-dimensional and highly quantum spin lattices close to instabilities, such as in chemically one-dimensional antiferromagnetic chain systems where interchain coupling is close to the critical strength of driving the formation of long-range magnetic order [1]. This work reports α-$Na_{0.9}MnO_2$ single crystal neutron scattering results that show an alternate route to realizing amplitude modes in an anisotropic triangular lattice of conventional spins in a two-dimensional antiferromagnet [2].

Fig. 1(a) illustrates the three-dimensional antiferromagnetically ordered phase of the $S = 2$ (Mn^{3+}) spins in the *ac*-plane of α-$Na_{0.9}MnO_2$. The moments are ordered parallel along the *c*-axis, pointing along the elongated apical oxygen axis of the MnO_6 octahedra, and are fixed by a uniaxial single-ion anisotropy term in the spin Hamiltonian. Fig. 1(b) shows the anisotropic triangular lattice of a single Mn layer and the corresponding projection of the ordered spin state onto the *ab*-plane. Nearest-neighbor Mn ions form chains along the *b*-axis, and a strong exchange interaction between spins drives antiferromagnetic ordering. Each ion has four next-nearest neighbors, where a weaker antiferromagnetic exchange interaction introduces frustration and renders the system quasi one-dimensional. As is common for monoclinic crystals, the structure has a propensity to form twin boundaries; two crystallographic twins (t_1 and t_2) plus two allowed magnetic domains ($\boldsymbol{q}_1$ and $\boldsymbol{q}_2$) form the basis for a four-domain model, which was needed to interpret the inelastic neutron scattering data.

Quantized coherent fluctuations of spins are quasi-particles called magnons, and inelastic neutron scattering is a powerful tool for studying the propagation of these excitations in reciprocal space. The neutron spectra reveal information about the strength of interactions within a system and are indicative of the underlying physics driving the observed static magnetic structure. The triple-axis spectrometer at BT-7 was used to study the inelastic magnetic spectra for single crystals of α-$Na_{0.9}MnO_2$. Fig. 2(a) follows the dispersion as it propagates with energy and momentum, and Fig. 2(b) shows the same data summarized as an intensity color map. Energy scans at the 3D zone center, $\boldsymbol{Q} = (0.5, 0.5, 0)$, in Fig. 2(c) reveal two gapped modes at approximately 6 meV and 11 meV. An additional scan at the 1D zone center, $\boldsymbol{Q} = (0, 1.5, 0)$, shows that both modes have very little dispersion along the interchain direction and are quasi one-dimensional.

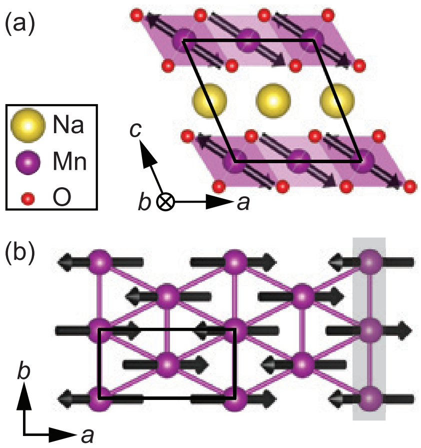

FIGURE 1: Summary of the crystal and magnetic structures of α-$NaMnO_2$. (a) The 3D magnetically ordered state with moments shown as black arrows in the *ac*-plane. The black rhombus denotes the chemical unit cell. (b) Projection of the 3D magnetically ordered state onto the *ab*-plane. The black rectangle denotes the chemical unit cell. The gray shaded region highlights the chain direction between nearest neighbor Mn atoms.

Linear spin-wave theory (LSWT) predicts two degenerate, transversely polarized magnons in α-$Na_{0.9}MnO_2$, which correspond to the 6 meV mode. The results of fitting to this model are shown as solid lines in Figs. 2(a) and 2(b), and the appearance of the additional excitation at 11 meV was unexpected. A polarized neutron scattering experiment was designed to further explore the physics behind this mode. Polarized neutrons can be utilized to determine if the nature of scattering intensity is nuclear or magnetic and can provide information about the orientation of magnetic structures

---

[1] Materials Department, University of California, Santa Barbara, CA 93106
[2] Boston College, Chestnut Hill, MA 02467
[3] NIST Center for Neutron Research, National Institute of Standards and Technology, Gaithersburg, MD 20899
[4] University of Maryland, College Park, MD 20742
[5] Oak Ridge National Laboratory, Oak Ridge, TN 37831
[6] Kavli Institute for Theoretical Physics, University of California, Santa Barbara, Santa Barbara, CA 93106

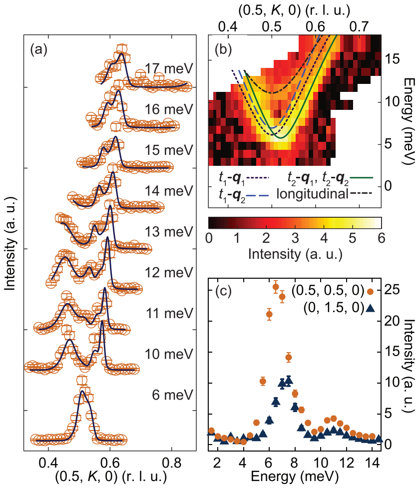

FIGURE 2: Inelastic neutron scattering data at $T = 2$ K. (a) Momentum scans at various energies through $Q = (0.5, 0.5, 0)$. Solid lines are resolution convolved fits to the data. (b) An intensity color map summarizing the scattering data from (a) along with dispersion of modes comprising the fits to the data in (a). Lines show fits to the expected transverse modes from the different crystallographic and magnetic domains within the sample: t_1-$\boldsymbol{q}_1$, t_1-$\boldsymbol{q}_2$, t_2-$\boldsymbol{q}_1$ and t_2-$\boldsymbol{q}_2$. The black dot-dashed curve highlights the longitudinal mode in the spectrum. (c) Constant energy scans at the 3D (0.5, 0.5, 0) and quasi-1D (0, 0.5, 0) antiferromagnetic zone centers. Error bars in (a) and (c) represent one standard deviation.

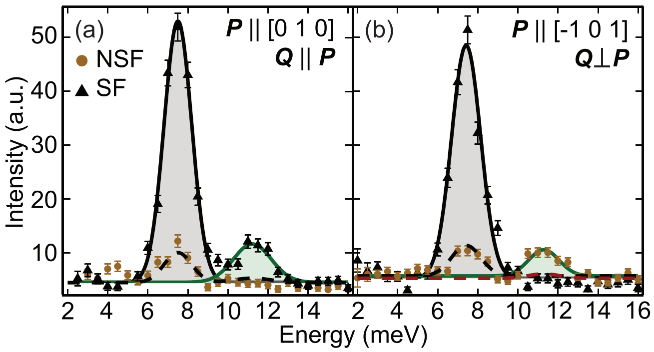

FIGURE 3: Polarized inelastic neutron scattering data about the quasi-1D zone center $\boldsymbol{Q} = (0, 1.5, 0)$. (a) Data collected with the neutron polarization $\boldsymbol{P}$ parallel to $\boldsymbol{Q}$. The two modes appear only in the SF channel and so are both magnetic in origin. (b) Data collected with the neutron polarization $\boldsymbol{P}$ parallel to the [−1, 0, 1] axis. Transverse spin fluctuations appear in the SF channel, and longitudinal fluctuations appear in the NSF channel. Data in both (a) and (b) were taken in the 3D ordered state at $T = 2.5$ K, and black dashed lines indicate the expected bleed through from the SF channel into the NSF channel due to imperfect neutron polarization. The red dashed line in (b) represents the expected bleed through from the NSF channel into the SF channel. Solid lines in (a) and (b) are Gaussian fits parameterizing each mode. Error bars represent one standard deviation.

and fluctuations. All nuclear scattering will appear in the non-spin-flip (NSF) scattering channel, and when the neutron polarization, $\boldsymbol{P}$, is parallel with respect to the scattering vector, $\boldsymbol{Q}$, all magnetic scattering will appear in the spin-flip (SF) channel. Fig. 3(a) shows that both the 6 meV magnon and the 11 meV excitations appear in the SF channel, indicating they are both magnetic in origin. When the neutron polarization, $\boldsymbol{P}$, is perpendicular with respect to the scattering vector, $\boldsymbol{Q}$, magnetic scattering can appear in the NSF or SF channel depending on the moment and fluctuation direction. The experimental results from this geometry are shown in Fig. 3(b), and because the moment direction is known in the α-$Na_{0.9}MnO_2$ samples, the scattering of the 11 meV mode into the NSF channel determined that this is an excitation resulting from fluctuations along the spin direction and thus is longitudinally polarized.

The higher energy mode's gap is not at the energy expected for a conventional two-magnon process involving two noninteracting magnons; at the zone center, the gap should be twice that of the transverse mode's gap. The difference in energy between this scenario and the data is $2E_{gap} - E_{long} = (1.2 \pm 0.1)$ meV, which implies an attractive potential between magnons. Theoretical calculations examined the problem of coupled magnons in the $T = 0$ K and large-spin limit for the 1D antiferromagnetic chain with single-ion anisotropy and found that a stable bound state of two magnons exists with a binding energy driven by the strong single-ion anisotropy of the material. The $T = 0$ K limit of this model is an ordered state, and the longitudinally polarized mode is reflective of a modulation of the order parameter magnitude, i.e., an amplitude mode.

Our neutron scattering results unambiguously reveal the presence of a longitudinally polarized mode. The geometrically-anisotropic triangular lattice of $S = 2$ spins with uniaxial single-ion anisotropy renormalize the spin interactions to be quasi-1D. This in turn drives the system into the limit where easy-axis (Ising-like) single-ion anisotropy within a Heisenberg spin chain stabilizes an amplitude mode comprised of bound magnons. This study motivates the search to find additional systems with similar lattice topologies and magnetic interactions, which were perhaps not considered in the past to be candidate materials where amplitude modes may be observed.

References

[1] D. Pekker, C. M. Varma, Annu. Rev. Conden. Mater. Phys. **6**, 269 (2015).

[2] R. L. Dally, Y. Zhao, Z. Xu, R. Chisnell, M. B. Stone, J. W. Lynn, L. Balents, S. D. Wilson, Nat. Commun. **9**, 2188 (2018).

Structural "delta-doping" to control magnetism in complex oxide heterostructures

E. J. Moon,[1] Q. He,[2] S. Ghosh,[3,4] B. J. Kirby,[5] S. T. Pantelides,[3] A. Y. Borisevich,[2] and S. J. May[1]

Delta-doping, in which a thin layer of dopants is inserted into a heterostructure to change the local charge density [Fig. 1(a)], has been an enabling strategy to realize new fundamental physical phenomenon in high mobility semiconductors and improve performance in electronic devices [1]. This charge-based, delta-doping approach has been applied to a range of material systems including silicon, compound semiconductors, and oxides. The important role played by the lattice degrees of freedom in complex oxides points to new strategies for delta-doping, namely a structural approach in which the local bond angles are the target of the "doping" and not the electron density. Within ABO_3 perovskite oxides, the B-O-B bond angles can deviate from 180° through collective rotations of the corner-connected BO_6 octahedra. Decreasing the B-O-B bond angles is known to decrease the electronic bandwidth, making carriers more localized and often suppressing magnetic ordering temperatures. In recent years, there has been significant interest in using thin films and superlattices to gain control of octahedral rotations through epitaxial strain and heterointerfaces as a means to engineer new functionality in oxide heterostructures [2]. In this work, we demonstrate a structural analogue to delta-doping by controlling octahedral rotations at the single unit cell level, thus providing a new means with which to engineer the local magnetism at the sub-nanometer length scale [3].

We demonstrate local control of octahedral rotations in a superlattice with repeated bilayers consisting of 20 unit cells of $La_{0.5}Ca_{0.5}MnO_3$ (LCMO) and 2 unit cells of $La_{0.5}Sr_{0.5}MnO_3$ (LSMO) grown by molecular beam epitaxy. These two manganites are isoelectronic, which mitigates charge transfer between the two materials, thus isolating the role of local structure on magnetic properties. In bulk form, the octahedral rotations in LCMO are larger than those in LSMO, with LCMO exhibiting Mn-O-Mn bond angles of 160.8° compared to 169.9° and 180° in LSMO. The implication of inserting thin LSMO layers within a thicker LCMO host is that the octahedral rotations will be suppressed within the ultrathin LSMO region, giving rise to a confined layer with increased electronic bandwidth compared to the LCMO regions [Fig. 1(b)].

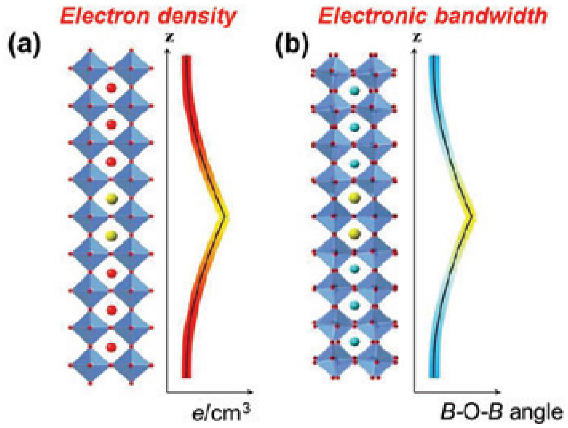

FIGURE 1: Schematic illustration of charge-based delta-doping (a) and structural "delta-doping" (b) in an ABO_3 perovskite oxide heterostructure. The BO_6 octahedra are shown in blue while the A-site cations are depicted as isolated spheres.

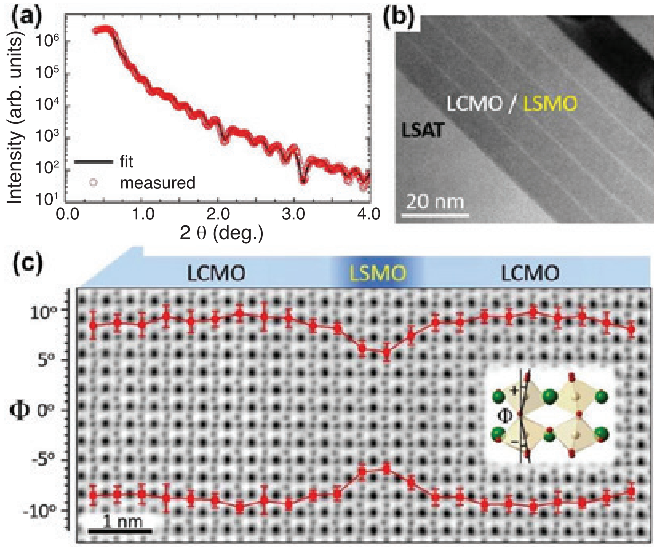

FIGURE 2: Structural confirmation of the $(LCMO)_{20}/(LSMO)_2$ superlattice obtained from (a) X-ray reflectivity and (b) scanning transmission electron microscopy. (c) The layer-resolved projected inclination angles of the MnO_6 octahedra, overlaid on an annular bright field image, reveal an increased Mn-O-Mn bond angle consistent with suppressed octahedral rotations within the two unit cell thick LSMO layers.

---

[1] Drexel University, Philadelphia, PA 19104
[2] Oak Ridge National Laboratory, Oak Ridge, TN 37831
[3] Vanderbilt University, Nashville, TN 37235
[4] SRM Research Institute and Department of Physics and Nanotechnology, SRM University, Kattankulathur, Tamil Nadu 603203, India
[5] NIST Center for Neutron Research, National Institute of Standards and Technology, Gaithersburg, MD 20899

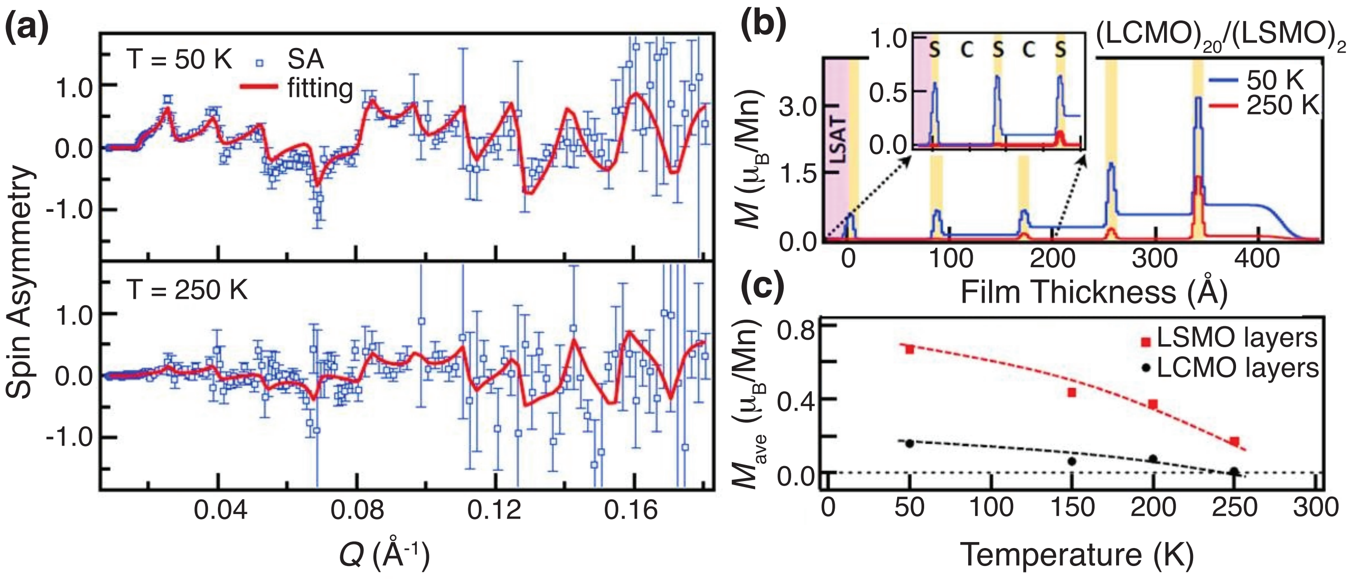

FIGURE 3: (a) Data and fits to the spin asymmetry measured at 50 K and 250 K from a $(LCMO)_{20}/(LSMO)_2$ superlattice. (b) The magnetization depth profile obtained from the PNR measurement and fits. (c) The average magnetization within the LSMO (red squares) and LCMO (black circles) layers demonstrates that both the magnetization and ordering temperatures are enhanced in the structurally "delta-doped" regions of the superlattice.

The presence of chemically distinct LSMO and LCMO layers within the superlattice was confirmed by X-ray reflectivity [Fig. 2(a)] and scanning transmission electron microscopy measurements [Fig. 2(b)]. The rotations of the MnO_6 octahedra across the LCMO/LSMO interfaces was mapped out using annular bright field imaging within the scanning transmission electron microscope, a technique that allows for the metal cations and oxygen sub-lattices to be directly visualized. As shown in Fig. 2(c), the MnO_6 octahedral inclination angle (Φ), which is a relative measure of the octahedral rotations, is suppressed within the thin LSMO layers. This result confirms that octahedral rotations can be controlled over sub-nanometer length scales using this structural "delta-doping" approach by altering the local *A*-site cation composition.

To probe the magnetic effects of the structural "delta-doping," we carried out polarized neutron reflectometry (PNR) at several temperatures on a $(LCMO)_{20}/(LSMO)_2$ and $(LCMO)_{20}/(LSMO)_4$ superlattice. The PNR measurements were performed on the PBR beamline and are summarized in Figure 3. Fits to the reflectivity and spin asymmetry confirm the presence of a modulated magnetic profile, in which the net magnetization within the LSMO layers is enhanced compared to the adjacent LCMO layers. Comparing the temperature dependence of the average magnetization within the LSMO and LCMO layers, we find that magnetization is quenched in LCMO at 250 K, while still persisting in LSMO, indicating a higher ordering temperature in the regions of reduced octahedral rotations. This behavior is consistent with enhanced electronic bandwidth in the ultrathin layers hosting increased Mn-O-Mn bond angles.

The implications of this work extend beyond manganite superlattices, as the observed design strategy can be broadly applied to confine bandwidth-controlled electronic and ferroic properties spatially in perovskite superlattices. As such, this same approach will be operable for perovskites that exhibit metal-insulator transitions and a variety of ordered magnetic states, as both ferromagnetic double-exchange and antiferromagnetic superexchange are strongly coupled to the local bonding environments. Additionally, the ability to confine magnetic states spatially without altering the local charge density or truncating the crystal offers a new means with which to study magnetism in the ultrathin two-dimensional limit without introducing surface perturbations. We therefore anticipate that this study will catalyze future experimental and theoretical work focused on structure-driven confinement of functional properties in complex oxide heterostructures.

References

[1] E. F. Schubert, Journal of Vacuum Science & Technology A, **8**, 2980 (1990).

[2] J. M. Rondinelli, S. J. May, J. W. Freeland. MRS Bulletin **37**, 261 (2012).

[3] E. J. Moon, Q. He, S. Ghosh, B. J. Kirby, S. T. Pantelides, A. Y. Borisevich, and S. J. May, Physical Review Letters **119**, 197204 (2017).

Applying nuclear methods to learning the secrets of ancient Chinese jade and bronze dagger-axes

R. Livingston,[1] A. O'Connor,[2] J. LaManna,[3] H. Chen-Mayer,[4] L. King,[4] and D. Turkoglu[5]

During the Shang dynasty in ancient China, ca. 1600 BCE - 1046 BCE, jade and bronze dagger-axes (*ge*) were made and used by the elite as ritual symbols of power and prestige. These ceremonial weapons consist of a nephrite jade [$Ca_2(Mg, Fe)_5Si_8O_{22}(OH)_2$] blade mounted in a bronze haft. Several examples of these dagger-axes are included in collections in the United States. Neutron radiography provides a potential method to image the jade tang hidden within the bronze haft and uncover early manufacturing techniques. As a preliminary feasibility test, a simulated dagger-axe was made using a modern replica blade carved from nephrite from Wyoming and copper alloy plates. After imaging the mockup dagger-axe, it was also examined using cold neutron prompt gamma activation (PGAA) and alpha/beta radiation autoradiography to evaluate the ability of these techniques to identify the nephrite source.

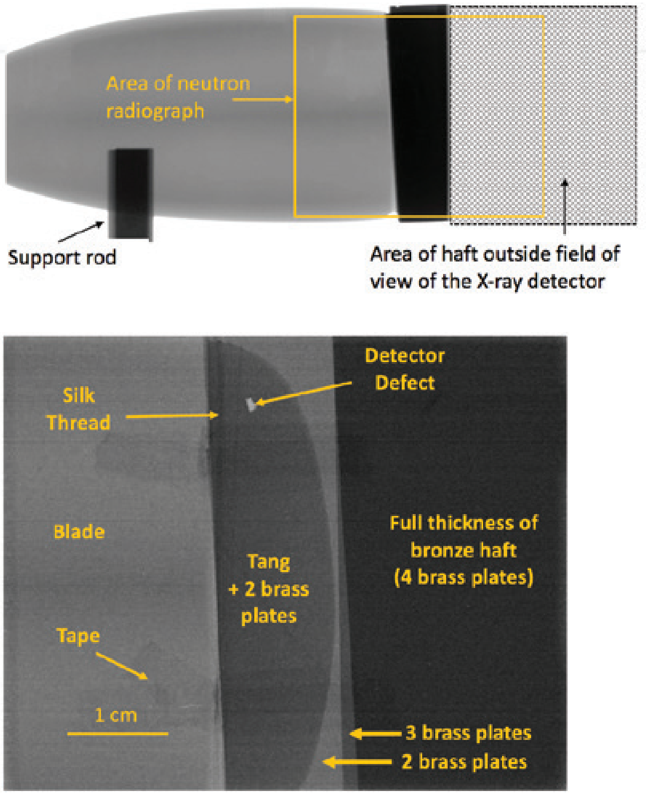

FIGURE 1: a) X-ray radiograph of the dagger blade and haft. b) Neutron radiograph of blade tang and haft area. See Fig. 1a for the position of this image on the dagger.

The simulated dagger was first imaged by X-ray and neutron radiography at the NIST Neutron Imaging Facility [1]. The details of the jade tang within the copper alloy haft were clearly visible (Fig. 1). Subsequently, the nephrite blade and the copper alloy plates were analyzed by PGAA at the Cold Neutron PGAA station at NIST. Three nephrite specimens in the Smithsonian collection from China, Siberia and Taiwan, characterized previously by electron microprobe analysis, were used as comparative standards. For the blade, three positions along the long axis were measured to evaluate the effect of variations in blade thickness on the PGAA results. The values for the three spots on the blade are the same within experimental uncertainties. The major nephrite elements – Ca, Mg, Fe and Si – were analyzed with uncertainties in the range of 0.3 % - 0.4 %. Three of the trace elements conventionally used for sourcing nephrite, Cr, Mn and Ni, were analyzed with similar uncertainties, as shown in Fig. 2, where the mean value of Fe, Cr, Mn and Ni from the three spots from the blade are compared with the results from the various nephrite sources. The results are given as molar ratios to Si, because the PGAA data are typically normalized by a characteristic element, in this case Si, to compensate for beam hardening and self-shielding in the sample. The variations in the elemental ratios between the different regions are much larger than the uncertainties, which indicates that the PGAA would be a suitable method for sourcing nephrite. Nephrite #2 from Xinjiang, China, has the lowest ratios across all elements and no measurable Ni, which implies a low content of accessory minerals. This was corroborated by the higher Mg content for this specimen. In addition, it was found that the Ca ratios for all the samples show good agreement with nephrite stoichiometry.

---

[1] University of Maryland, College Park, MD 20742
[2] Smithsonian American Art Museum, Washington, DC 20013
[3] Physical Measurement Laboratory, National Institute of Standards and Technology, Gaithersburg, MD 20899
[4] Material Measurement Laboratory, National Institute of Standards and Technology, Gaithersburg, MD 20899
[5] NIST Center for Neutron Research, National Institute of Standards and Technology, Gaithersburg, MD 20899

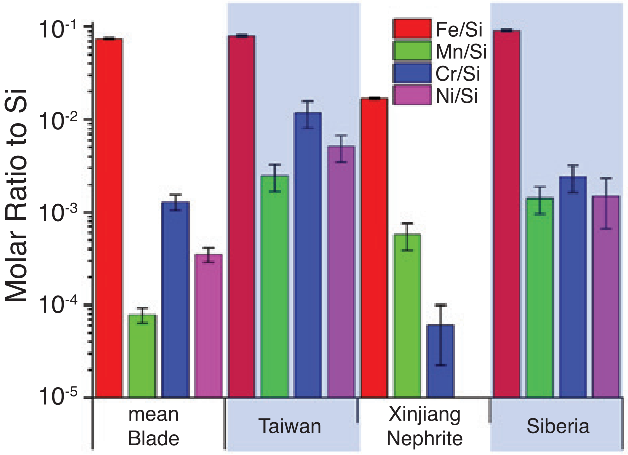

FIGURE 2: Major (Fe) and minor (Mn, Cr, Ni) elemental ratios in the nephrite blade compared to nephrite standards sourced from various regions. No Ni was detected in the Xinjiang sample.

The residual radioactivity of the objects was below the NRC exempt limits 3 months post irradiation. The samples were previously determined to have a natural gamma radioactivity level of ^{226}Ra and ^{235}U in the (10-20) Bq range. Post PGAA analysis, the blade was imaged by autoradiography for alpha and beta particle activity using a storage phosphor image plate which is sensitive to both alpha and beta radioactivity. An image plate exposed to the blade for roughly 22 days, and then it was scanned in a reader to obtain a spatial map of the activities (Fig. 3). The three regions of induced beta radioactivity from the neutron beam used for PGAA are clearly shown. In the area between these regions, possible hits by alpha radiation from the natural sources ^{226}Ra and ^{235}U are highlighted in red. This radiation is actually emitted all over the blade, but it is obscured in the irradiated areas by the much more intense induced beta activity. This natural alpha radiation, produced by the decay of uranium and thorium daughter products, could provide another set of elemental data that may be used to source the nephrite.

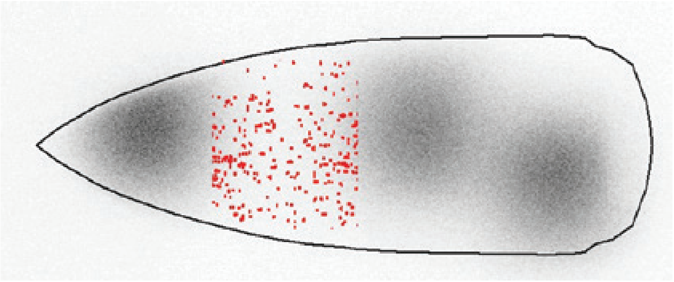

FIGURE 3: Storage phosphor autoradiography image of alpha and beta radiation of the nephrite blade. The shape of the blade is outlined in black; the gray areas are induced beta radiation from the PGAA neutron irradiation and the red symbols indicate possible alpha or beta particle hits from natural radioactivity.

We have applied neutron beam techniques to the nondestructive examination of cultural artifacts. While neutron and X-ray imaging revealed hidden structural information, prompt and delayed gamma ray emission and spectral analysis provided quantitative elemental information aiding the classification of the sources. In addition, natural and induced alpha/beta emission measured by the highly sensitive imaging plate can provide further information about these artifacts. As a result of this study a collaboration has been established with Chinese researchers to identify jade sources in Dunhuang region in Gansu Province in northwestern China.

Reference

[1] R.A. Livingston et al., Journal of Archaeological Science: Reports **21**, 99 (2018).

Residual stress in additive manufactured nickel alloy 625 parts

T. Gnäupel-Herold,[1] L. Bass,[2,3] J. Milner,[1] and S. Moylan[3]

While additive manufacturing (AM) has increased in popularity for efficiently manufacturing customizable parts through the layer-by-layer fabrication approach, the potential to build-up residual stress in metal parts limits design capabilities and product robustness. In fact, the dimensional distortions caused by residual stresses are one of the biggest obstacles to the wider adoption of AM based production of metal parts. In the laser-based, powder-bed fusion process, a laser selectively fuses unheated metal powder layer by layer generating residual thermal stresses from the temperature gradients, which can lead to severe deformations and losses of part tolerances. Residual stresses are 'frozen' in through the cooling conditions during the build process in which a spot (≈ 100 µm) of rapid melting and solidification moves at speeds of 8 m/s to 9 m/s in specific patterns (Figure 1). The resulting stresses are generally strongly compressive in the interior of an AM part, with stress balance provided by tensile stresses near the surface. The size of the build and features such as wall thickness, aspect ratios, and proximity to free surfaces strongly affect heat flow and cooling rate, both of which strongly affect the magnitude of the final residual stresses. It is notable that residual stresses from successive "micro-quenching" in laser-based AM are the opposite of what would be found if the same part were heated and quenched as a whole, resulting in compressive stresses near the surface and tensile stresses in the interior.

Post-build heat treatments largely eliminate residual stresses; however, the process increases cost, and in some of the frequently used materials, it may lead to the formation of unwanted phases that have inferior mechanical properties. The metal powders most often used for laser-based AM are either of the Inconel type or stainless steels, both of which may form other phases due to heat treatments.

In order to develop strategies that provide some control over the stress build-up during the AM process, the stresses first need to be quantified and correlated to intrinsically linked dimensional parameters such as thickness and aspect ratio. This study [1] explores what stresses are present in a simple part design and how geometric changes affect the amount of stress in three dimensions.

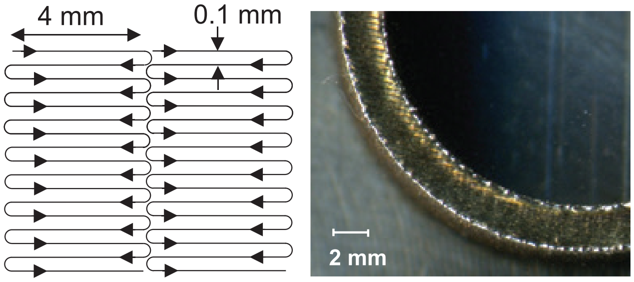

FIGURE 1: Progression of the laser beam in skin exposure.

Cylindrical Inconel 625 samples were designed with varied outer diameters, inner diameters, and heights, and samples were extracted with the base of the build plate still attached (Figure 2). Due to its high mechanical strength, Inconel 625 is widely used in laser-sintering based additive manufacturing. High strength, particularly at elevated temperatures, virtually guarantees high levels of residual stresses at the yield level in the finished build, thus providing good sensitivity due to large stress changes from the effect of geometric features. Stresses in laser-based AM are strongly triaxial in nature, which mostly excludes surface-based measurement methods, and it favors neutron diffraction as a method for non-destructive evaluation.

The principal stresses in cylindrical coordinates are shown in Figure 3 with the principal features of stresses on display, such as compressive stresses in the bulk and tensile stresses near the outer surfaces. The highest magnitudes are found in the axial direction.

The axial stresses near the top show a transition region that indicates a length scale of about 5 mm at which axial stresses go from zero directly at the surface to the plateau region of ≈ -850 MPa in the center. The radial stresses are by far the smallest in magnitude due to the proximity of a free surface, which forces a reduction in the stress component parallel to the surface normal. The effects of inner and outer diameter for the axial stresses are shown in Figure 4.

The introduction of an inner bore not only reduces the radial stress to near zero (stress component normal to this surface),

---

[1] NIST Center for Neutron Research, National Institute of Standards and Technology, Gaithersburg, MD 20899
[2] Virginia Polytechnic Institute and State University, Blacksburg, VA 24061
[3] Intelligent Systems Division, National Institute of Standards and Technology, Gaithersburg, MD 20899

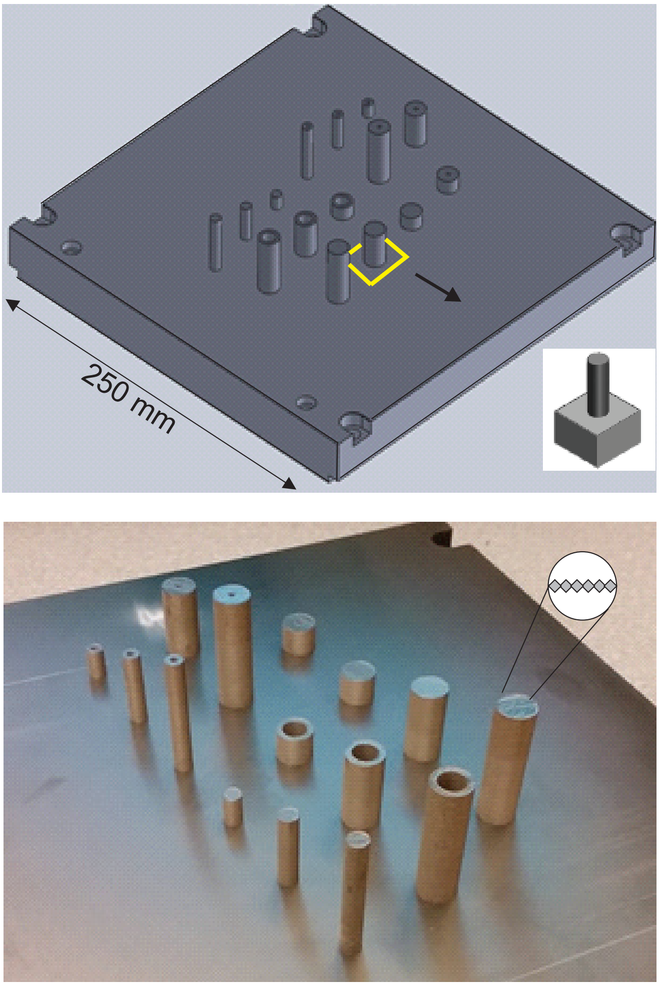

FIGURE 2: Samples a) as displayed from a CAD model and b) as built. After fabrication, the build plate was cut (yellow lines left) to isolate each specimen for stress measurements. The upper right corner shows the arrangement of neutron gage volumes.

but also it also decreases the axial stresses (Figure 4, middle, wall thickness 5 mm). The steep drop in the axial stresses for the 2 mm wall thickness (6 mm diameter, 2 mm wall thickness) indicates that a minimum dimension exists that is critical for maximum stress build-up. In comparison, the reduction of axial length has an effect on the magnitude of the stresses (Figure 5) only once the height reaches the diameter ($d = h = 12$ mm) for which maximum stresses are 20 % lower.

Most efforts to predict the outcomes of additive manufacturing focus on residual stress as the quantity responsible for part distortions. While distortions can be measured very accurately to compare with calculations, the models actually predict elastic strain, wherein distortions are the result of an integration over the entire 3D strain distribution. With elastic strain being the quantity measured in neutron diffraction, the value of the results presented here lies in the ability to compare and evaluate model predictions directly, thus aiding the ongoing improvement of finite-element models.

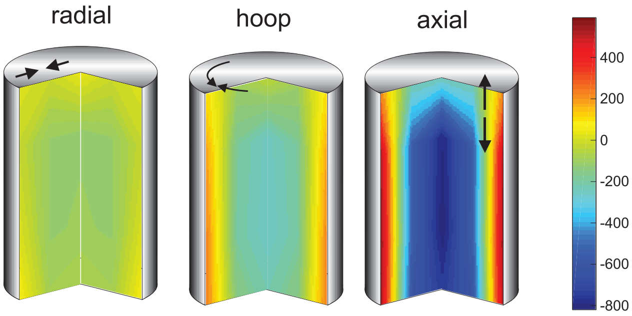

FIGURE 3: Stresses in MPa for cylinders with 12 mm diameter and 25 mm height.

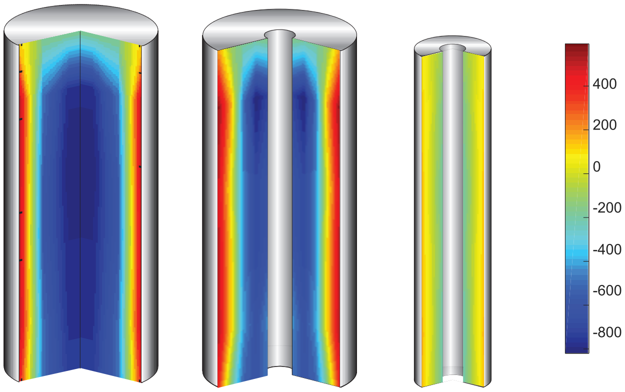

FIGURE 4: Stress reducing effect of outer and inner diameters at constant height of 40 mm. The bore diameter was 2 mm and outer diameters were 12 mm and 6 mm, respectively.

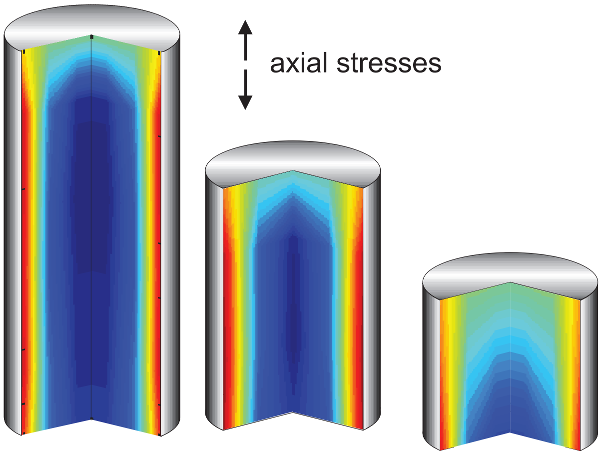

FIGURE 5: Axial stresses for solid cylinders of different height (left to right: 40 mm, 25 mm, and 12 mm; diameter: 12 mm).

Reference

[1] L. Bass, J. Milner, T. Gnäupel-Herold, S. Moylan, Journal of Manufacturing Science and Engineering **140**, 0610041-11 (2018).

Burial diagenesis and multiscale porosity in the St. Peter sandstone

L. M. Anovitz,[1] J. T. Freiburg,[2,3] M. Wasbrough,[4] D. F. R. Mildner,[4] K. C. Littrell,[5] V. Pipich,[6] and J. Ilavsky[7]

Sandstones are defined as indurated sands of siliceous character, rocks largely composed of sand-sized grains of silicate minerals such as quartz and feldspars, although non-silicates can also be present. They are extremely important rocks, both in terms of their regional extent and applications. Large sandstone formations may cover thousands of square kilometers and be thousands of feet thick. For instance, the Navajo Sandstone, which forms much of the scenic geology national parks and monuments in southern Utah covers about 265,000 km^2 in parts of Arizona, Colorado, Nevada and Utah, and is up to 700 m thick, and the St. Peter sandstone, covers over 600,000 km^2 in parts of Arkansas, Illinois, Indiana, Minnesota, Missouri and West Virginia, and averages 30 m to 60 m thick. Sandstone provides key properties to dimension stone, flagstone, and crushed stone; its porosity and permeability make it important as natural aquifers and oil and gas reservoirs; and it has significant potential for geological CO_2 sequestration. Understanding the nature of the pore structures of sandstones, and how they evolve when subjected to both geological and anthropogenic process is, therefore, critical to understanding how these geologic environments evolve and how these resources can be utilized.

The focus of this study [1] was to evaluate changes in the pore structure of the St. Peter Sandstone from the Illinois and Michigan Basins with burial diagenesis, in which slow burial over geologic time has subjected the original sand sediments to increasing pressure and temperature and fluid-mediated chemical transport. To do so we obtained 36 rock samples from five wells at depths from 2703 feet to 10,835 feet (820 m to 3300 m) and combined image analysis at larger scales, with small, very-small and ultra-small angle neutron scattering data to characterize pore dimensions over a seven order of magnitude range, from the centimeter to the nanometer scale.

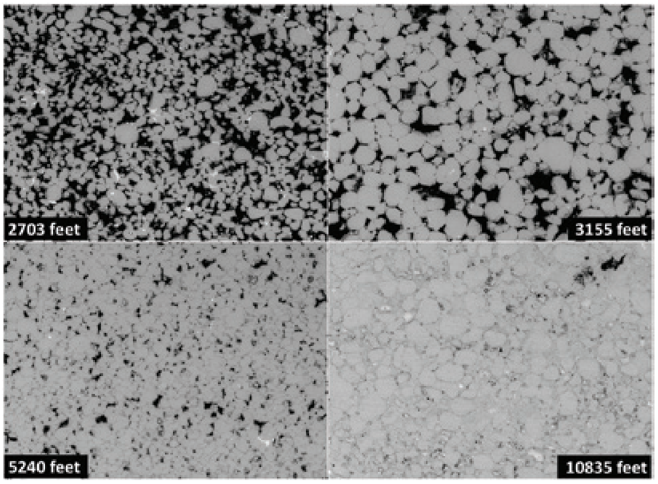

FIGURE 1: Backscattered electron images, high- and low-porosity samples versus depth. Each image is 6.35 mm across. All four samples consist largely of quartz grains, although small percentages of other materials are apparent, and significant dolomite cement is present in the sample from 10,835 feet.

Figure 1 shows backscattered electron (BSE) images of four of the samples studied. These images clearly show a decrease in overall porosity at the SEM image scale with increasing depth and indicate that this decrease is attributable to a combination of compaction and cementation. Most grains are at least moderately well-sorted and rounded, and a transition occurs with depth from a grain-supported to a more cement-supported structure. The latter, however, only dominates one of two deep samples from the Michigan Basin. Image-scale grain boundary contacts become more common with depth as do sutured, fractal-appearing grain boundaries. These images were analyzed for total porosity, multifractal behavior and lacunarity, and two-point autocorrelation analysis was used to combine the imaging results with those from neutron scattering to quantify the pore structures from scales ranging from several nm to ≈ 1 cm or larger [2-5].

From two to 19 samples were examined from each drill core (each core covering a relatively restricted depth range). As expected from Figure 1 the average total porosity decreased approximately logarithmically with depth. Figure 2, however, shows the Porod-transformed scattering data (including the image results) for the lowest and highest porosity samples at each depth. While standard $\log(I)$ vs. $\log(Q)$ plots suggest a near linear relationship that can be modeled as a surface fractal, greater complexity is apparent in this projection. The high-Q data are composed of a series of steps or peaks, often at similar Q values.

---

[1] Chemical Sciences Division, Oak Ridge National Laboratory, Oak Ridge, TN 37831-6110
[2] Illinois State Geological Survey, University of Illinois, Champaign, IL 61820
[3] Ernst-Moritz-Arndt-University, Institute of Geography and Geology, Friedrich-Ludwig-Jahn Str. 17a, D-17489 Greifswald, Germany
[4] NIST Center for Neutron Research, National Institute of Standards and Technology, Gaithersburg, MD 20899
[5] Chemical & Engineering Materials Division, Oak Ridge National Laboratory, Oak Ridge, TN 37831-6393
[6] Jülich Centre for Neutron Science (JCNS) at Heinz Maier-Leibnitz Zentrum (MLZ), Forschungszentrum Jülich GmbH, Lichtenbergstraße 1, D-85748 Garching, Germany
[7] Argonne National Laboratory, Argonne, IL 60439

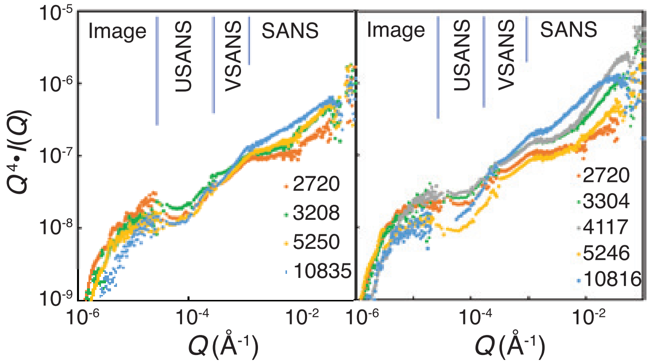

FIGURE 2: Porod-transformed scattering curves with calculated additions from backscattered electron images for the four lowest porosity samples (left) and the for the five highest porosity samples (right) at each depth (in feet). Approximate ranges of data for each instrument are shown, although some overlap exists.

The data show a distinct pattern of changes with depth. At larger scales (near $Q = 10^{-5}$ Å^{-1}), the intensity of the scattering curve, and therefore the porosity of the sample in that size range, decreases with depth. This is as expected and reflects the loss of the larger pores with depth due to compaction and cementation. At smaller scales (near $Q = 10^{-2}$ Å^{-1}), however, the deepest samples have the largest intensity, implying increased nanoscale porosity with increasing depth.

Increasing depth and decreasing overall porosity decreases absolute porosity only at scales larger than 10^6 Å; when normalized to 100 %, however, all fractions at scales larger than 10^4 Å increase, although only a slight decrease occurs in the absolute porosity between 10^4 and 10^6 Å. In both the normalized and the absolute cases, the fractions of pores with radii below 10^4 Å increase with depth. Although changes in the absolute pore fraction are small, this ratio increases significantly, by a factor of nearly seven, which implies a large increase in the number of such small pores. Assuming this is connected or that these represent pore throats, this result may have a dramatic impact on available reactive surface area.

In addition to changes in total and relative pore volumes, the fractal dimensions of the pore surfaces and pore structure also change with depth. Figure 3 shows the fractal dimensions of the pore structure at smaller scales derived from the average slope of the scattering curve (left) and at larger scales from the BSE images (right). Fig. 3 (left) shows the surface fractal dimension D_s as a function of depth from the average slope of the scattering data. These increase as a function of depth, reflecting a roughening of the grain boundaries from projected values of 2.34 at the surface to 2.67 at 12,000 feet. This is consistent with the presence of grain suturing in the more compacted materials. The change in D_s also reflects changes in the pore-size distribution. Since the intensity $I(Q) \sim cQ^{D-6}$, then $dI/dD = I \log Q$. This is necessarily negative since $\log Q$ is negative over the range of measurements. Thus, as D_s increases, $I(Q)$ decreases and, therefore, an increase in the surface fractal dimension reflects a decrease in the pore size number distribution.

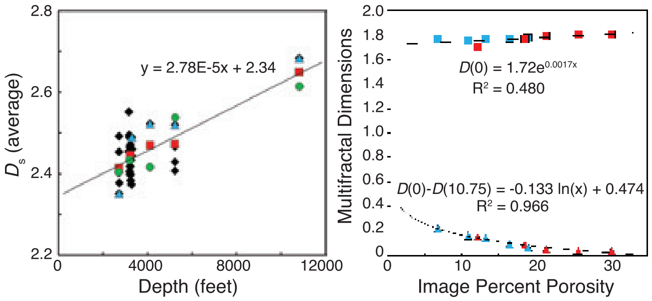

FIGURE 3: (left) Surface fractal dimension, D_s, derived from the overall slope of the scattering data as a function of depth for all analyzed samples (black diamonds), averages for each depth (red squares), the highest porosity samples for each depth (blue triangles), and the lowest porosity samples for each depth (green circles). (right) Monofractal dimension $D(0)$ (squares) and multifractality $D(0) - D(10.75)$ (triangles) derived from the SEM images as a function of porosity for both the highest porosity (red) and lowest porosity (blue) samples at each depth.

At the image scale results are somewhat different. Fig. 3 (right) shows the monofractal value [$D(0)$] and the multifractality [$D(0) - D(10.75)$] of the highest and lowest porosity samples from each drill hole calculated from the SEM images. Values for $D(0)$ decrease with decreasing porosity, and therefore with depth. This is opposite the trend observed at smaller scales from the scattering data. The multifractality of the pore structures, however, increases with decreasing porosity. Thus, the differences in fractal dimension between the low-concentration and high-concentration parts of the image increase as porosity decreases with depth, but the fractality of the system decreases overall (the pore system becomes smoother).

This study showed that changes in pore structure with burial diagenesis are significantly scale-dependent. Whereas overall porosity decreases with depth due to the combined effects of compaction and cementation, smaller-scale pores become a significantly larger fraction of the whole. Fractal dimensions decrease at larger scales (surfaces smooth) with increasing depth but increase at smaller scales (surfaces roughened) and pores become more isolated (higher lacunarity). Thus, evaluation of changes in the pore structures of sandstones appears to be an inherently multi-scale problem well addressed by a combination of small angle scattering and imaging techniques.

Reference

[1] L. M. Anovitz, J. T. Freiburg, M. Wasbrough, D. F. R. Mildner, K. C. Littrell, V. Pipich, J. Ilavsky, Marine and Petroleum Geology, **92**, 352 (2018).

[2] L. M. Anovitz, D. R. Cole, G. Rother, L. F. Allard, A. J. Jackson, K. C. Littrell, Geochimica et Cosmochimica Acta, **102**, 280 (2013).

[3] L. M. Anovitz, D. R. Cole, A. J. Jackson, G. Rother, K. C. Littrell, L. F. Allard, A. D. Pollington, D. J. Wesolowski, Geochimica et Cosmochimica Acta, **158**, 199 (2015).

[4] H.-W. Wang, L. M. Anovitz, A. Burg, D. R. Cole, L. F. Allard, A. J. Jackson, A. G. Stack, G. Rother, Geochimica et Cosmochimica Acta, **121**, 339 (2013).

[5] L. M. Anovitz, D. R. Cole, J. M. Sheets, A. Swift, H. W. Elston, S. Welch, S. J. Chipera, K.C. Littrell, D.F.R. Mildner, M. J. Wasbrough, Interpretation, SU59 (2105).

A neutron far field interferometer

D. Sarenac,[1,2] D. A. Pushin,[1,2] M. G. Huber,[3] D. S. Hussey,[3] H. Miao,[4] M. Arif,[3] D. G. Cory,[2,5,6,7] A. D. Cronin,[8] B. Heacock,[9,10] D. L. Jacobson,[3] J. M. LaManna,[3] A. J. Brooks,[11] L. G. Butler,[11] S. Guo,[11] M. M. Khonsari,[11] and H. Wen[4]

Interferometers are sensitive probes of nature; the recent detection of gravity waves by LIGO was only possible using an exquisitely stable, sensitive, and very long baseline interferometer. The neutron, a quantum particle, can also be "split" so that it can be made to interfere with itself after having sampled one of two paths. A conventional neutron interferometer employs a monolithic, perfect single crystal of silicon that through Laue diffraction by three blades, creates a beam splitter, mirror, and combiner, i.e., an analog of a Mach-Zehnder interferometer (Figure 1). This geometry creates well-separated paths (of order several centimeters) through the interferometer and enables measurements of the potential differences between the two paths. This has made possible precise measurements of the coherent scattering lengths of light nuclei, which inform the binding energies needed in many-body calculations, searches for exotic forces and particles, fundamental studies of quantum information theory, and the first demonstration of the equivalence principle wherein a quantum particle experiences a gravitational potential [1].

While highly sensitive, the perfect single crystal interferometer has some limitations. The first is that the single crystal only accepts a very narrow neutron energy bandwidth so that the count rate is low. Diffraction from the lattice planes requires alignment of the blades at the sub-nm scale. Vibrations or temperature gradients can easily spoil the contrast, requiring instruments with large vibration isolation and excellent temperature control. It is difficult to fabricate a new interferometer with highly visible interference fringes. One starts with an ingot of silicon (which limits the length to about 10 cm), and then machines the blades into the crystal. The machining process leaves surface defects and dislocations that irreversibly dephase the wavefunction as it transmits through the blade and consequently reduces fringe visibility. Etching can remove many of these imperfections, but experience shows that this is far from a repeatable process. The length limit of 10 cm constrains the kinds of samples and sample environments that can be used within the interferometer. The low intensity demands long counting times and generally prohibits acquiring phase images, which is undesirable as having access to the neutron phase can increase the sensitivity to density variations 1000-fold.

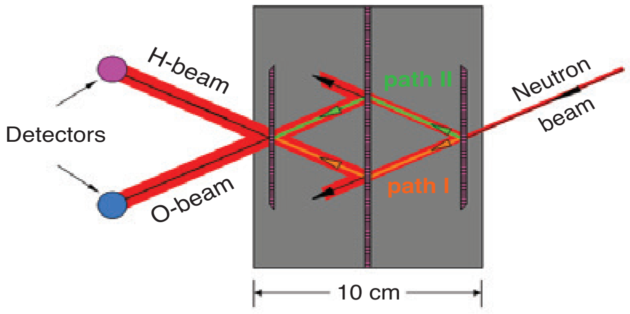

FIGURE 1: Top view of a conventional neutron interferometer. The first blade (shown in purple) on the right splits the neutron wavefunction via Bragg diffraction in the Laue geometry. The middle blade acts as the mirror in the Mach-Zehnder geometry, while the left blade recombines the neutron paths. Interference between the paths is measured as intensity oscillations in the two detectors.

The recently realized far-field interferometer using X-rays uses a potential geometry that would alleviate the fabrication woes, the low intensity, and space constraints [2]. There are two variants of the far-field interferometer: the two- and three-phase grating interferometer [3, 4] (Figure 2). In the two-grating version, two $\pi/2$-phase shifting gratings with nominally the same period (P_g) are placed close ($D \approx 1$ cm) to one another. When illuminated by a divergent beam, one can view the pair of gratings as a single grating composed of highly diffracting regions and non-diffracting regions that produce a diffraction pattern in the far-field. The period of the diffraction pattern is $P_d = P_g L / D$, where L is the distance from the source slit to the detector. With $L \approx 10$ m and $P_g \approx 1$ µm, the period of the diffraction pattern is $P_d \approx 1$ mm, which is readily resolvable by a neutron imaging detector (spatial resolution of 20 µm is routine). In the three-grating version, a π-phase-shifting grating is placed between the two $\pi/2$ gratings. The first $\pi/2$ grating and the π grating are separated by a distance $D_1 \approx 1$ m, which creates a virtual grating a distance D_1 from the π grating. Placing the second $\pi/2$ grating a distance $D_2 = D_1 + D$ creates an analogous geometry to the two-grating interferometer.

There are several remarkable features of the family of far-field interferometers. The use of phase gratings allows one to use a

---

[1] Department of Physics, University of Waterloo, Waterloo, Ontario, Canada N2L3G1
[2] Institute for Quantum Computing, University of Waterloo, Waterloo, Ontario, Canada N2L3G1
[3] National Institute of Standards and Technology, Gaithersburg, MD 20899
[4] National Institutes of Health, Bethesda, MD 20892
[5] Department of Chemistry, University of Waterloo, Waterloo, Ontario, Canada N2L3G1
[6] Perimeter Institute for Theoretical Physics, Waterloo, Ontario, Canada N2L2Y5
[7] Canadian Institute for Advanced Research, Toronto, Ontario, Canada M5G1Z8
[8] University of Arizona, Tucson, AZ 85721
[9] North Carolina State University, Raleigh, NC 27695
[10] Triangle Universities Nuclear Laboratory, Durham, NC 27708
[11] Louisiana State University, Baton Rouge, LA 70803

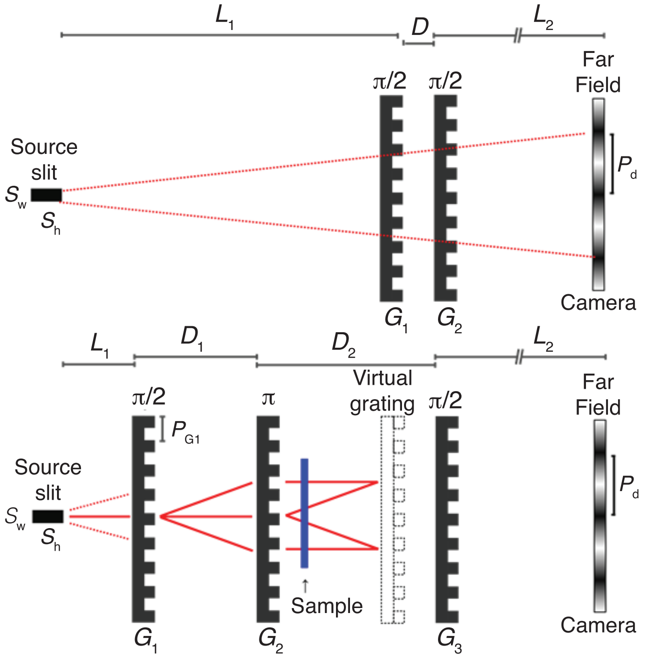

FIGURE 2: Geometry of the two grating (top) and three-grating (bottom) far-field interferometers.

large beam with a much broader energy bandwidth so that one has an imaging interferometer. Also, since the interferometer is constructed of trenches etched in silicon wafers, the development cost to realize a new interferometer is much reduced and nanofabrication procedures are more repeatable. The grating period is 10^4 times larger than the lattice spacing in silicon, and these interferometers are significantly less susceptible to vibrations while the overall geometry requirements to realize good contrast are much relaxed compared to those for the perfect crystal instrument.

In the two-grating version, the period of the interference pattern can be changed over many orders of magnitude by changing the separation, D, of the two gratings. Since the autocorrelation length in the sample probed by the interferometer is $\xi = \lambda\, Z / P_d$ (where λ is the wavelength and Z is the sample to detector distance), one can easily vary ξ by orders of magnitude. Since the change in visibility as a function of ξ is a measure of the system's pair correlation function, one can obtain spatially resolved small angle scattering data – and in three dimensions. As an example, the porosity and pore radius of additively manufactured steel dog bones subjected to fatigue has been measured, which showed (see Fig. 3) that there was pore migration and pore radius reduction as a function of fatigue [5].

The three-grating interferometer allows one to create a meters-long interferometer, allowing for bulky sample environments and an increased path length for interaction. As a first demonstration with neutrons, the visibility of the three-grating interferometer was measured for several total interferometer lengths, as shown in Figure 4. As claimed, the three-grating far field interferometer has measurable contrast for a 4 m total length. However, the measured contrast is about a factor 10 less than expected based on the analysis developed by Miao et al [2]. We are actively pursuing the source of this low visibility and believe it is most likely due to the π grating being imperfect, so that there was a significant intensity in the zero-order diffraction whereas for an ideal π grating there should be none.

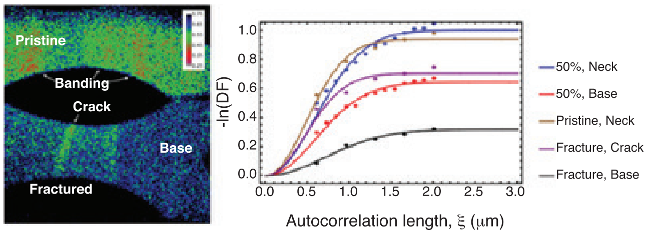

FIGURE 3: Far-field analysis of printed stainless steel plates subjected to fatigue. The dark field image at ξ = 607 nm of a fractured and pristine specimen (left) and fringe visibility variations (right) taken from all the dark field images. The change in visibility is modeled by dilute, monodisperse spheres to obtain a pore radius and porosity.

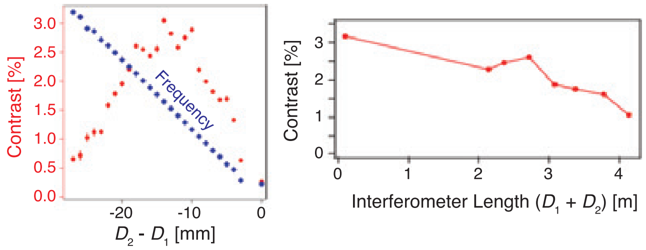

FIGURE 4: Measured visibility or contrast as a function of difference in position from the echo for overall L = 10 cm (left) and the maximum observed contrast for instrument length 10 cm to 4 m (right).

We have demonstrated a novel grating-based neutron interferometer [3, 4] capable of long path lengths, accepting higher intensities, increased sensitivity, and better robustness with the ability to perform dark-field neutron imaging. This new interferometer has 10^6 greater intensity than conventional neutron interferometers, can have a total length of 10 m allowing for a wholly unique measurement of Newton's gravitational constant, and enable phase imaging applications to realize a factor 10^3 increase in sensitivity to material density variations. Although there remains work to be done to improve aspects of the device, such as contrast, this technique has potential in measuring density variations and boundaries at intriguing lengths scales of materials and for fundamental physics applications such as Newton's Gravitational Constant. We see the far-field interferometer as being a key addition to the NCNR's instrument library.

References

[1] H. Rauch and S. A. Werner, "Neutron Interferometry: Lessons in Experimental Quantum Mechanics, Wave-particle Duality, and Entanglement," Oxford University Press, 2015.

[2] H. Miao et al., Nature Physics **12** (9), 830 (2016).

[3] D. Sarenac et al., Phys. Rev. Lett. **120**, 113201 (2018).

[4] D. A. Pushin Phys. Rev. A **95**, 043637 (2017).

[5] A. J. Brooks et al., Materials and Design **140**, 420–430 (2018).

Relationship between segmental dynamics and conductivity in polymer electrolytes

K. I. Mongcopa,[1] M. Tyagi,[2,3] J. P. Mailoa,[4] G. Samsonidze,[4] B. Kozinsky,[4,5] S. A. Mullin,[6] D. A. Gribble,[1]
H. Watanabe,[7] and N. P. Balsara[1,8,9]

Quasi-elastic neutron scattering (QENS) experiments on mixtures of poly(ethylene oxide) (PEO) and lithium bis(trifluoromethane)sulfonimide (LiTFSI) salt, a standard polymer electrolyte, led to the quantification of the effect of salt addition on segmental dynamics in the 1 Å to 10 Å length scale. The monomeric friction coefficient characterizing segmental dynamics on these length scales increases exponentially with salt concentration. More importantly, we find that this change in monomeric friction alone is responsible for all of the observed non-linearity in the dependence of ionic conductivity on salt concentration. Our analysis leads to a surprisingly simple relationship between macroscopic ion transport in polymers and dynamics at monomeric length scales.

The mechanism of ion conduction in conventional liquid electrolytes, e.g., mixtures of solvents with high dielectric constants such as alkyl carbonates and salts such as $LiPF_6$ used in current lithium-ion batteries, is well established. At low salt concentrations, ionic conductivity increases linearly with salt concentration due to an increase in charge carrier concentration. Charge screening, usually modeled using the Debye-Hückel theory, results in deviation from this linear dependence. At high enough concentration, the viscosity of the solution increases significantly and conductivity decreases with increasing concentration. The dependence of conductivity on salt concentration is thus characterized by a maximum.

One approach for improving the performance of rechargeable lithium batteries is to replace the flammable liquid electrolyte with a high molecular weight polymer. The prototypical polymer electrolytes are mixtures of polyethers such as PEO and LiTFSI salt. Similar to the case of liquid electrolytes, conductivity versus salt concentration also exhibits a maximum. However, the conductivity of polymer electrolytes is independent of viscosity; the viscosity of polymers, η, increases sharply with molecular weight, M, as $\eta \sim M^{3.4}$, while ionic conductivity at a fixed salt concentration is independent of M (for $M \geq 4$ kg/mol). Instead, the conductivity of high molecular weight polymers is determined by segmental dynamics which slow down due to associations between polymer chains and salt molecules. In this highlight, we clarify the origin of the conductivity maximum observed in polymer electrolytes. We particularly address the relative importance of screening and segmental dynamics. We quantify the underlying segmental dynamics at 363 K in polymer electrolytes consisting of PEO (35 kg/mol) and LiTFSI salt concentrations, r_s = 0, 0.08, 0.15 and 0.20 (r_s is the molar ratio of Li+ to ethylene oxide monomers) and establish the quantitative relationship between segmental dynamics and ionic conductivity. We characterize segmental dynamics measured by QENS using the monomeric friction coefficient, first introduced by Ferry [1], and show its direct correspondence with ionic conductivity. Data are collected using the CHRNS high-flux backscattering spectrometer over timescales ranging from 0.1 ns to 2 ns, and reciprocal space ranging from Q = 0.25 Å^{-1} to 1.75 Å^{-1}. Due to the large incoherent scattering cross section of hydrogen, the scattering intensity is primarily dominated by the incoherent scattering from the polymer backbone.

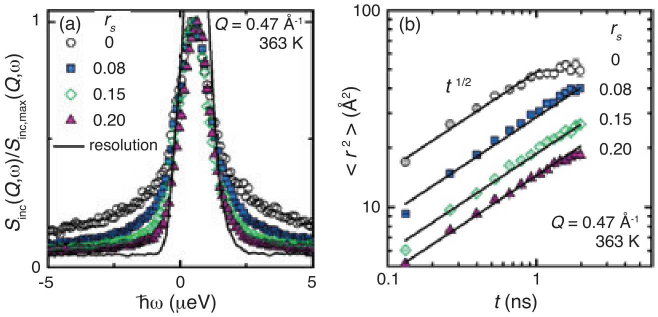

FIGURE 1: (a) Normalized incoherent structure factor, $S_{inc}(Q,\omega)/S_{inc,max}(Q,\omega)$, in the frequency domain, plotted as a function of energy, ħω, at Q = 0.47 Å^{-1} and 363 K measured by QENS. (b) Mean-square displacement, $< r^2 >$, as a function of time, t, with solid lines representing fits to the Rouse model scaling, $< r^2 > \sim t^{1/2}$.

The dependence of the normalized incoherent structure factor $S_{inc}(Q,\omega)$ on energy, ħω, obtained at a representative scattering vector Q = 0.47 Å^{-1} from these electrolytes is shown in Figure 1a. The instrumental resolution is obtained by measuring the sample at 20 K and appears as a purely elastic signal (solid black line) in the QENS spectra. The decreased width of the structure factor with increasing salt concentration is a signature of the slowing down of segmental dynamics due to associations between polymer segments and salt.

---

[1] University of California, Berkeley, Berkeley, CA 94720
[2] NIST Center for Neutron Research, National Institute of Standards and Technology, Gaithersburg, MD 20899
[3] University of Maryland, College Park, MD 20742
[4] Robert Bosch LLC, Cambridge, MA 02139
[5] Harvard University, Cambridge, MA 02138
[6] Seeo Inc., Hayward, CA 94545
[7] Kyoto University, Uji, Kyoto 611-0011, Japan
[8] Materials Sciences Division, Lawrence Berkeley National Laboratory, Berkeley, CA 94720
[9] Joint Center for Energy Storage Research, Lawrence Berkeley National Laboratory, Berkeley, CA 94720

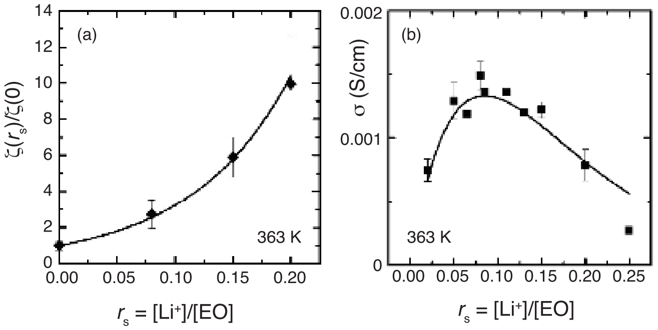

FIGURE 2: (a) Normalized friction coefficient, $\zeta(r_s)/\zeta(0)$, as a function of salt concentration, r_s. The solid curve represents eq 1. (b) Conductivity, σ, measured at 363 K from ac impedance spectroscopy plotted as a function of salt concentration, r_s. The solid curve represents eq 2.

The dependences of $< r^2(t) >$ obtained from the electrolytes at a representative value of $Q = 0.47$ Å^{-1} through the relationship, $S_{\mathrm{inc}}(Q,t) = \exp\left[\frac{-Q^2}{6} < r^2(t) >\right]$, are shown in Figure 1b. Over most of the available time window, $< r^2(t) >$ scales as $t^{1/2}$. This is a standard signature of segmental dynamics. The solid lines in Figure 1b represent the least squares fit through the data and are used to determine the Rouse parameter, $p_{\mathrm{R}} = < r^2(t) >/t^{1/2}$. We then use the Rouse model to relate p_{R} to the monomeric friction coefficient, $\zeta = (12 k_{\mathrm{B}} T l^2 / p_{\mathrm{R}}^2 \pi)$, where l is the statistical segment length. In our analysis, we neglect changes in l due to the presence of salt. Using the known value of l for PEO (5.8 Å), we obtain the dependence of ζ on salt concentration. In Figure 2a, we plot the normalized monomeric friction coefficient, $\zeta(r_s)/\zeta(0)$, as a function of salt concentration. It is evident that the monomeric friction coefficient increases exponentially with salt concentration: at $r_s = 0.20$, ζ of the electrolyte is a factor of 10 larger than that of neat PEO. The curve in Figure 2a quantifies the dependence of ζ on r_s according to

$$\frac{\zeta(r_s)}{\zeta(0)} = \exp\left[\frac{r_s}{0.085}\right] \qquad (1)$$

where the dimensionless constant 0.085 quantifies the exponential slowing of segmental relaxation due to the presence of salt in PEO/LiTFSI at 363 K. The values of ζ determined from p_{R} $(= < r^2(t) >/t^{1/2})$ reflect the friction experienced by a coarse-grained Rouse segment, and both glassy and rubbery relaxation processes contribute to this ζ. Experimental data indicate that at temperatures well above the glass transition temperature (true for systems examined in this study), the friction coefficients associated with these two processes exhibit similar temperature dependencies. Thus, at fixed temperatures, the ratio $\zeta(r_s)/\zeta(0)$ can be utilized to quantify the effect of salt on segmental dynamics.

In Figure 2b, we plot the conductivity of the electrolytes, measured by ac impedance spectroscopy, as a function of salt concentration. The data exhibit a maximum in the vicinity of $r_s = 0.08$, consistent with literature [2]. The curve in Figure 2b represents eq 2:

$$\sigma = 0.043 r_s \left[\exp\left(-\frac{r_s}{0.085}\right)\right] \text{ S/cm} \qquad (2)$$

where we have combined the expected effects of increasing r_s: a linear increase in charge carrier concentration and slowing of segmental dynamics measured by QENS. The pre-factor, 0.043 S/cm, is the specific conductivity of dilute PEO/LiTFSI electrolytes (with the electrolyte concentration, r_s, being a dimensionless quantity). To our knowledge, eq 2 represents the first attempt to quantify, on a purely experimental basis, the relationship between ionic conductivity and segmental relaxation. It is evident from Figure 2b that the data are consistent with the proposed relationship. The wide concentration range over which our result is valid is noteworthy; eq 2 applies to PEO/LiTFSI electrolytes with salt concentrations ranging from (0 to 4.5) mol/kg. While this expression applies to data at 363 K, we expect the same form to apply at other temperatures in which the conductive media forms a single phase. The reported dependence of conductivity on salt concentration in Figure 2b is consistent with the vast literature on PEO/LiTFSI mixtures. Likewise, our QENS data are also consistent with previous studies [3]. The main advance is that we conducted ac impedance and QENS on the same polymer samples, and sought to relate results from these separate experiments. While many have noted the correlation between ion transport and segmental motion, the direct connection between conductivity and monomeric friction that eq 2 embodies has not been recognized. It is important to realize that eq 2 is not a fit through the conductivity data. The agreement between eq 2 and the data in Figure 2b indicates that all of the non-linearity of the dependence of conductivity on salt concentration can be explained by monomeric friction coefficients measured independently by QENS. In other words, the slowing of ion transport of both Li^+ and TFSI^- ions due to salt-polymer interactions is accurately reflected in the motion of hydrogen atoms on the polymer backbone. Deviations from the linear scaling of conductivity with salt concentration thus do not arise due to charge screening, as is the case in conventional liquid electrolytes.

In summary, we have used QENS to quantify the effect of salt on segmental dynamics in a standard polymer electrolyte, PEO/LiTFSI. The Rouse model was used to determine the effect of salt addition on the monomeric friction coefficient. The deviation from linearity of the dependence of ionic conductivity on salt concentration is quantitatively consistent with changes in the monomeric friction coefficient determined by QENS. While the importance of segmental dynamics in polymer electrolytes has been noted by many, we are not aware of any previous study that suggests that it is the *only* effect that is responsible for the non-linear dependence of conductivity on salt concentration.

References

[1] J. D. Ferry, R. F. Landel, Kolloid-Zeitschrift **148**, 1 (1956).

[2] S. Lascaud, M. Perrier, A. Vallée, S. Besner, J. Prud'homme, M. Armand, Macromolecules **27**, 7469 (1994).

[3] A. Triolo, V. Arrighi, R. Triolo, S. Passerini, M. Mastragostino, R. E. Lechner, R. Ferguson, O. Borodin, G. D. Smith, Phys. B: Condens. Matter **301**, 163 (2001).

Structure and relaxation dynamics in the brush of polymer grafted nanoparticles

Y. Wei,[1] Y. Xu,[1] A. Faraone,[2] and M. J. A. Hore[1]

Polymers are attached to nanoparticle surfaces for a variety of purposes, including improving their dispersion within a material or to enhance compatibility with a solvent. When grafted to surfaces, the physical properties of the polymers, such as the size of the chains and time scales over which segments of the chain move, can be significantly altered relative to free chains due to the presence of the nanoparticle surface as well as the presence of nearby chains. At low polymer grafting densities on flat surfaces, individual polymer chains are far apart from one another, and the chains adopt a "mushroom" conformation in which the size of the chain scales with its length (N) as $R \sim N^{0.5}$ in a polymer melt or theta solvent or $R \sim N^{0.6}$ under good solvent conditions. In contrast, at high grafting densities, two regions of conformation emerge as shown in Fig. 1. Close to the nanoparticle surface, in the concentrated polymer brush (CPB) region, a high concentration of polymer causes the chains to become highly stretched. Farther away from the nanoparticle surface, the polymer density is lower in the semi-dilute polymer brush (SDPB) region and polymer chains have more free volume, allowing them to adopt more ideal conformations. The cutoff distance, r_c, between these two regions of conformation can be estimated from scaling theories and depends primarily on the size of the nanoparticle and the grafting density of the polymer chains [1]. We hypothesized that the portion of the chains in these two regions would exhibit different relaxation dynamics, which can affect quantities such as their mechanical properties. Using small-angle neutron scattering (SANS), a new scattering model, and neutron spin echo (NSE) spectroscopy, we *directly* measured both the structure and relaxation dynamics of the CPB and SDPB regions for the first time.

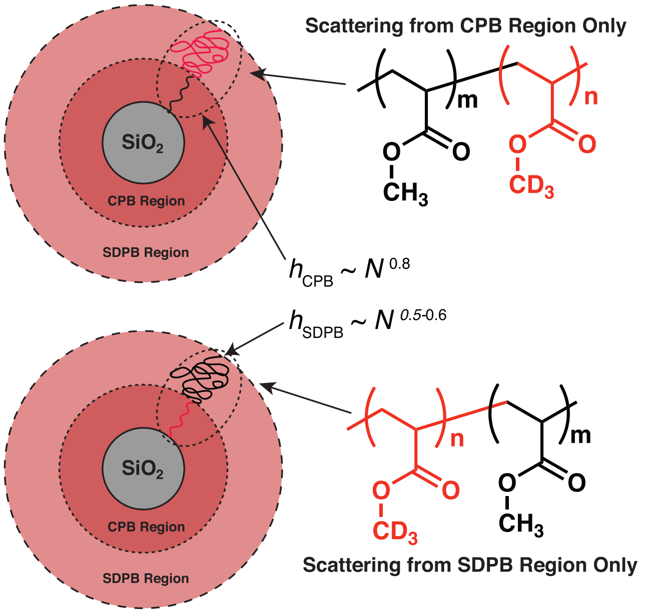

FIGURE 1: Illustration of the structure and deuteration scheme of a poly(methyl acrylate) chain grafted to a SiO_2 nanoparticle. In the concentrated polymer brush (CPB) region, a high concentration of polymer chains leads to highly stretched chains, and a thickness that scales with the length (N) of the chain as $h_{CPB} \sim N^{0.8}$. In the semi-dilute polymer brush (SDPB) region, a lower concentration of polymer chains causes the polymers to adopt more ideal conformations, with a size that scales as $h_{SDPB} \sim N^{0.6}$ in solution. For neutron scattering, the polymer is selectively deuterated. In the top figure, scattering from SDPB region is suppressed due to contrast matching with the solvent and nanoparticle core. In the bottom figure, scattering from the CPB region is suppressed when the deuteration scheme is reversed.

Neutron scattering presents a unique opportunity for polymer science because of the large difference in scattering length density of hydrogen and deuterium containing molecules, which allows us to selectively suppress scattering from different regions of a polymer sample. For this study, we polymerized methyl acrylate from the surface of SiO_2 nanoparticles (diameter ≈ 12 nm) using surface-initiated reversible addition-fragmentation chain-transfer polymerization (RAFT). As depicted in Fig. 1, we synthesized two systems of poly(methyl acrylate)-grafted SiO_2 nanoparticles. Partially deuterated methyl acrylate, SiO_2, and our solvent 1,1,2,2-tetrachloroethane-d_2 have similar scattering length densities, which allowed us to suppress scattering from either the CPB or SDPB region depending on the order of blocks of hydrogenated (PMA-h_6) and deuterated methyl acrylate (PMA-h_3d_3) on the grafted polymer. The molar mass of the polymer in the CPB region was approximately 17 kg/mol, and the molar masses of the SDPB region were 6 kg/mol (top system) and 20 kg/mol (bottom system). On the basis of scaling theories, we estimated that $r_c \approx 18$ nm.

We first performed SANS measurements on the two nanoparticle systems in Fig. 1 to ensure that our deuteration scheme/contrast matching conditions were successful, as well as to directly measure the conformation of the CPB and SDPB regions of the brush. Our measurements were performed at 25 °C and

---

[1] Case Western Reserve University, Cleveland, OH 44122

[2] NIST Center for Neutron Research, National Institute of Standards and Technology, Gaithersburg, MD 20899

analyzed using a core-chain-chain (CCC) model that we recently developed, which models the scattering from a spherical nanoparticle core that is grafted with polymers with two distinct regions of conformation. The results are shown in Fig. 2, along with illustrations of the structure of the nanoparticle systems that were inferred from fits to the SANS measurements. Our analysis confirmed that the portions of the polymer chains in the CPB region are highly stretched, that the chains transition to an ideal conformation in the SDPB region, and yielded a value of r_c close to our estimate. In the sample with the deuterated CPB region (Figure 2, bottom right), poor contrast between the CPB region, nanoparticle core, and solvent resulted in scattering that largely resembled that from free chains in solution. From our measurements [2], we confirmed that NSE measurements would be sensitive primarily to the dynamics of the portions of polymer chains that were fully hydrogenated. In addition, our measurements, for the first time, directly and simultaneously confirmed the local structure of the CPB and SDPB regions of grafted polymer chains.

NSE measurements were performed on the same set of samples at 80 °C, approximately 70 °C above the glass transition temperature of poly(methyl acrylate). The NSE measurements [2] were fit to the Zimm model of polymer dynamics to extract the characteristic relaxation times of the CPB and SDPB regions (τ_q) as a function of scattering vector q. The results are shown in Fig. 3. Qualitatively, from the NSE measurements we readily observe that the CPB region (dashed lines) relaxes more slowly than the SDPB region (solid lines), demonstrating that confinement in the CPB region significantly impacts the motions of the chains. The relaxation times we obtained from NSE measurements (Fig. 3b) show that dynamics in the CPB region are approximately three times slower than those in the SDPB region, even at high q (small length scales). The inset of Fig. 3b shows that the relaxation times scale as $\tau_q \sim q^{-2.5}$, indicating that, while the dynamics of the CPB region are slower than the SDPB region, the dynamics nevertheless obey the Zimm model due to the presence of solvent.

In conclusion, we used a combination of SANS and NSE to directly measure the local structure and relaxation dynamics of polymers grafted to a spherical nanoparticle core. Near the nanoparticle surface, a high concentration of polymer leads to stretched polymer chains and slower dynamics than portions of the chains farther away. Looking to the future, these measurements provide greater insight into polymer nanocomposites, and may lead to additional ways to tune the properties of such materials for a variety of applications.

References

[1] W. R. Lenart and M. J. A. Hore, Nano-Structures & Nano-Objects (2017).

[2] Y. Wei, Y. Xu, A. Faraone, and M. J. A. Hore, ACS Macro Letters **7** (6), 699 (2018).

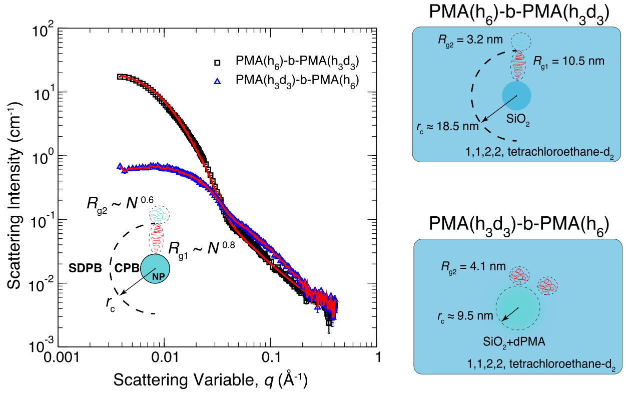

FIGURE 2: FIGURE 2: (Left) SANS measurements of poly(methyl acrylate)-grafted SiO$_2$ nanoparticles, along with fits to the CCC model (red). (Right) The structures of the two systems measured are illustrated, along with the sizes of the regions determined from fitting. The results are in excellent agreement with theory and previous measurements [1].

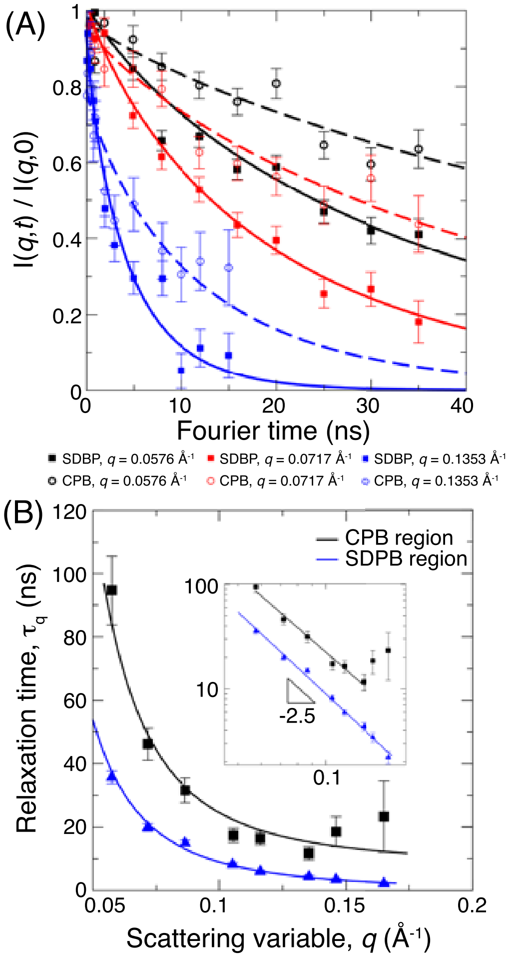

FIGURE 3: (a) NSE measurements of the CPB region (open points/dashed lines) and SDPB region (closed points/solid lines). (b) Relaxation times of the CPB and SDPB regions as a function of scattering variable q. The inset shows the data on a double logarithmic scale.

Conformational investigation of graft polymers as lubricant viscosity modifiers

M. T. Savoji,[1] D. Zhao,[1] R. J. Muisener,[3] K. Schimossek,[4] K. Schoeller,[4] T. P. Lodge,[1,2] and M. A. Hillmyer[1]

Polymeric oil additives have been commonly used in making “all season” engine oil since 1949. These large molecules (at a typical loading in oil of less than 10 wt %) undergo structural transformations with temperature and increase the oil viscosity relatively more at higher temperatures. This viscosity modification behavior is commonly attributed to polymer coil expansion with increasing temperature, as first proposed by Selby in 1958 [1]. Therefore, the oil viscosity variation decreases over the engine working temperature range, resulting in less wear for the metallic parts of the engine at elevated temperatures and easier engine startup at cold temperatures. Moreover, all-season oils containing polymeric viscosity modifiers do not necessarily require seasonal oil changes. In the past decades, polymeric oil additives with various compositions and architectures have been produced. Among these, poly(alkylmethacrylate)s (PAMAs) offer improved properties over a wide temperature range but are more expensive and thus are limited to high performance engine oils. Olefinic copolymers (OCPs) represent a breakthrough in terms of low cost and satisfactory performance. However, linear OCPs are susceptible to chain breakage under high shear conditions in an automobile engine, resulting in shorter lifetimes. Graft polymers combining PAMAs and polyolefins are of particular interest due to their typically high molar mass and low sensitivity to mechanical degradation, i.e., improved shear stability, resulting in improved performance.

In this work, we prepared a series of well-defined graft polymers with polyolefin backbone and PAMA side chains using controlled polymerization and studied their viscosification behavior in base oil by rheological measurements (the detailed description of polymer synthesis, characterization, and viscosity modification behavior can be found in the published work) [2]. Essentially, we have found that the graft polymers are promising candidates as viscosity modifiers. For instance, the graft polymer with the best viscometric behavior in our library, denoted as P9 (overall molar mass of 660 kg/mol), performs very similar to the optimized, state-of-the-art polymeric additive at a significantly reduced loading (Figure 1).

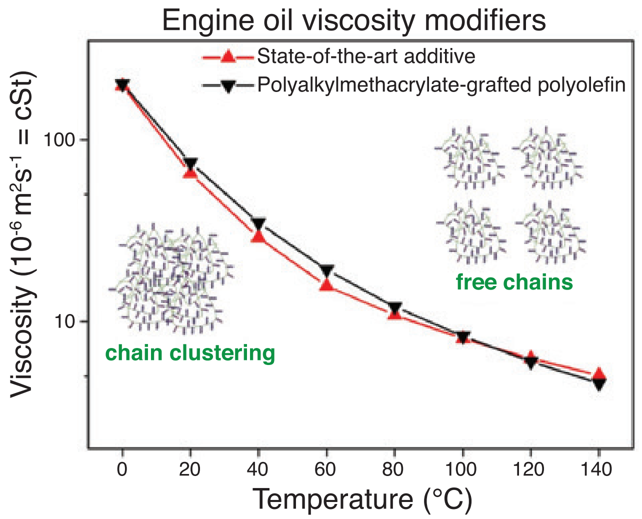

FIGURE 1: Zero shear viscosity vs temperature of the lubricant oil modified by the graft polymer P9 (0.8 %) and the optimized, state-of-the-art polymer additive (3.4 %), as indicated inside the graph. The solid lines are drawn as guides to the eye. The cartoons indicate the structure of the graft polymers at high (individually dispersed) and low temperatures (small aggregates).

To unravel the mechanism for the viscosity modification of the graft polymers, we measured the conformation of P9 in dilute solutions of deuterated dodecane (a surrogate aliphatic base oil) at varying temperatures using small angle neutron scattering (SANS) at NIST. As shown in Figure 2, there exists a shoulder in the lower scattering vector (q) regime in each SANS curve, reflecting the internal structure of the graft polymer. Also, in this q regime, the shape of the intensity trace changes with temperature, indicating some thermally-driven change in polymer structure. At high q, the scattering intensity, $I(q)$, scales approximately as q^{-2}, suggesting Gaussian chain statistics. Additionally, as the temperature decreases, the scattering intensity at lower q increases monotonically.

To better understand the molecular-level thermal response, we first fit the SANS data using a graft polymer form factor coupled with the random phase approximation (RPA, the full details of the model can be found in the reference) [2]. All the SANS traces at different temperatures are reasonably well represented by the proposed model, with three fitting parameters (the radius of gyration of one side chain, $R_{g,A}$, the backbone, $R_{g,B}$, and the effective Flory–Huggins interaction parameter, χ_{eff}). First, it is found that χ_{eff} decreases with increasing temperature,

---

[1] Department of Chemistry, University of Minnesota, Minneapolis, MN 55455
[2] Department of Chemical Engineering and Materials Science, University of Minnesota, Minneapolis, MN 55455
[3] Evonik Corporation
[4] Evonik Resource Efficiency GmbH

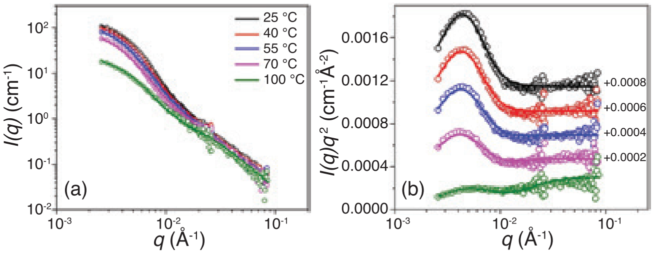

FIGURE 2: (a) The SANS scattering intensity $I(q)$ as a function of the scattering vector q for 2 mg/mL P9 in deuterated dodecane at varying temperatures. The incoherent scattering background has been subtracted, which was obtained from the fits and is comparable to the scattering level of the solvent. The symbols are experimental data, and the solid lines represent best fits to a graft copolymer form factor taking the polymer clustering into account. (b) The same data as in (a) plotted in the Kratky format, i.e., $I(q)q^2$ vs q. The data are vertically shifted for clarity, as indicated inside the graph.

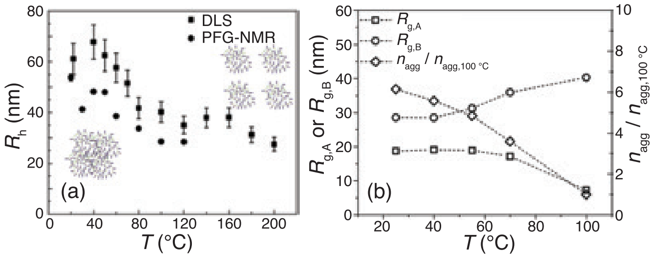

FIGURE 3: (a) The hydrodynamic radius (R_h) of 2 mg/mL P9 in dodecane measured by DLS and PFG-NMR as a function of temperature. The inset cartoons indicate the aggregation state of the graft polymer, i.e., well-dispersed at high temperatures vs clustering at lower ones. (b) Extracted parameters from Figure 2, radius of gyration ($R_{g,A}$ and $R_{g,B}$) and the degree of polymerization normalized by that at 100 °C ($n_{agg}/n_{agg,100\ °C}$) as a function of temperature.

while both $R_{g,A}$ and $R_{g,B}$ increase with temperature. These results collectively suggest the P9–dodecane system displays upper critical solution temperature (UCST) phase behavior and therefore the graft polymer coil expands as the temperature is elevated. Although this apparently agrees with the mechanism proposed by Selby, these results are not entirely consistent with those from dynamic light scattering (DLS) and pulsed field gradient NMR (PFG-NMR). As shown in Figure 3a, the hydrodynamic radius of P9 in dodecane *decreases* significantly with increasing temperature. For instance, there is a drop of ≈ 30 nm when the temperature is raised from 40 °C to 100 °C. This suggests that the RPA model might not be the most appropriate one to describe the SANS data. In fact, the extracted χ_{eff} from the fittings and the extrapolated reciprocal forward scattering intensity do not show a linear dependence on the reciprocal temperature. This likely indicates there might be some other changes in the solution properties with temperature.

One possibility is that there could be chain clustering at lower temperatures, which diminishes on heating. To examine this, we refit the SANS data by taking chain aggregation into account. Here, the graft polymers are assumed to interact athermally with the solvent over the temperature range studied. As shown in Figure 2, the SANS data are also well represented by this model, with the fitting parameters ($R_{g,A}$, $R_{g,B}$, and n_{agg}) summarized in Figure 3b. First, there is indeed a monotonic increase in n_{agg} (the number of graft polymer chains in one scattering object or cluster) as the temperature is reduced, consistent with the clustering hypothesis. Specifically, if the copolymers are assumed to be individually dispersed at 100 °C, they form clusters containing an average of ≈ 6 chains at 25 °C. On the other hand, $R_{g,B}$ increases with temperature (≈ 30 % from 25 °C to 100 °C), again reflecting the UCST phase behavior. In contrast, surprisingly, $R_{g,A}$ becomes progressively smaller as the temperature increases. On the basis of these results, a possible picture emerges: at higher temperatures, the copolymer chains are individually dissolved, but as the temperature decreases, chains aggregate into small clusters. As the graft polymers could act as surfactants, i.e., the PAMA side chains prefer to be embedded inside the cluster while the polyolefin backbone provides a miscible interface with the nonpolar oil, and the PAMA side chains could stretch to avoid contacts with the oil molecules as well as the polyolefin backbone. Accordingly, $R_{g,A}$ increases as the polymer chains become more clustered (i.e., as the temperature is reduced). Importantly, the chain aggregation hypothesis provides a consistent overall picture of the SANS, DLS and PFG-NMR results. On basis of this, a new mechanism for improved performance of graft polymers as viscosity modifiers can be proposed: progressive chain clustering at lower temperatures leads to gradual reduction in the net viscosity enhancement due to polymer clustering, which ultimately gives a smaller increase in oil viscosity at reduced temperatures.

In summary, we have developed a new class of lubricant additives based on graft polymers with polyolefin backbones and PAMA side chains. These graft polymers were demonstrated to be excellent candidates as viscosity modifiers. Size measurements by DLS and PFG-NMR indicated that the dominant mechanism of coil expansion upon increasing temperature cannot explain the viscosity improving behavior of these graft polymers in oil [3, 4]. Instead, the SANS results suggest that the chain clustering with decreasing temperature should reduce the overall hydrodynamic volume of the system, thus weakening the temperature dependence of the base oil viscosity. Finally, we highlight that the tunable chemistry given by this synthetic approach combined with the new mechanism revealed from the SANS experiments open the door to further optimization to meet all the requirements of viscosity modifiers, including permanent shear stability, and high-temperature high-shear (HTHS) behavior, which will greatly benefit the design of next-generation polymeric oil additives.

References

[1] T. Selby, ASLE Trans. **1** (1), 68 (1958).

[2] M. T. Savoji, D. Zhao, R. J. Muisener, K. Schimossek, K. Schoeller, T. P. Lodge, M. A Hillmyer, Ind. Eng. Chem. Res **57** (6), 1840 (2018).

[3] H. Müller, Tribol. Int. **11** (3), 189 (1978).

[4] D. LaRiviere, A.-F.A. Asfour, A. Hage, J. Z. Gao, Lubr. Sci. **12** (2), 133 (2000).

Clustering and percolation in suspensions of carbon black

J. J. Richards,[1] J. B. Hipp,[2] J. K. Riley,[3] P. D. Butler,[3] and N. J. Wagner[2]

"High-structured" carbon blacks, named for their large specific surface area, modify the electrical and mechanical characteristics of composites at vanishingly small volume fractions [1]. Recently, these particles have also been used in electrochemical flow applications [2]. In these emerging technologies, high-structured carbons facilitate electrochemical charging/discharging by maintaining an electrically percolated network under flow. While these technologies show promise for the scalable storage of renewable energy, their commercial success is challenged by pumping losses due to the large viscosity of typical working fluids [3]. While the origin of these undesirable rheological properties was not entirely understood, it was proposed that they arise due to the formation of a persistent mechanical network. Further, this mechanical network is thought to be critical to electrical transport through the electrically insulating fluids. To understand the link between the electrical and rheological properties of these slurries, a detailed microscopic mechanism was needed [4].

Carbon black filled materials exhibit a complex microstructural hierarchy. Neutron scattering is ideal for characterizing this structure as it provides access to a wide range of length scales. Therefore, we used neutron measurements to probe the structure during important rheological and electrical transitions as a function of volume fraction [5-7]. Prior to the small angle neutron scattering experiments, dynamic light scattering experiments (DLS), ac conductivity measurements, and viscoelastic testing were performed on a model high-structured carbon black, KetjenBlack EC-600JD, suspended in propylene carbonate. The results of these experiments are summarized in Figure 1. The DLS measurements probe the aggregation state of equilibrated samples after significant gentle dilution. If the particles were colloidally stable, then these experiments would show only the presence of primary aggregates leading up to the gel boundary. Instead, DLS reveals the formation of agglomerates that are stable against sedimentation and dilution. The formation of agglomerates occurs at a critical volume fraction, (ϕ_{fc}), where the weak surface charge on the primary aggregates is insufficient to maintain colloidal stability. Above ϕ_{fc}, a second population of large carbon agglomerates appears that is stable against dilution. While the formation of agglomerates is typical of gelation processes near the phase boundary, the suspensions do not settle with time and maintain fluidity. We therefore assert that these agglomerates are clusters with re-entrant stability formed with a preferred particle size (6 μm) whose concentration increases linearly with total carbon concentration above ϕ_{fc}.

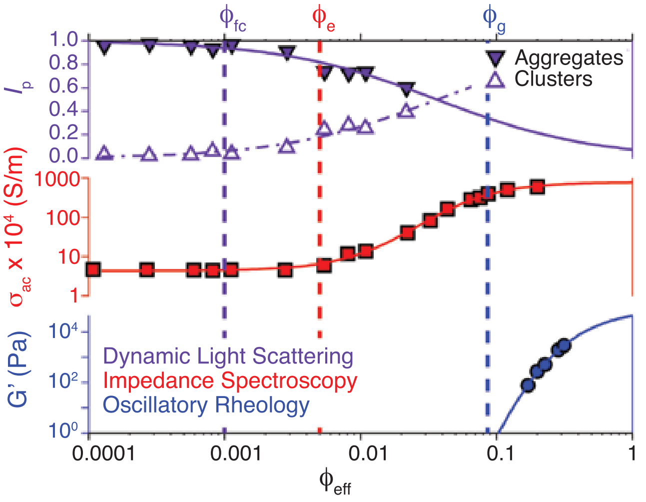

FIGURE 1: Top: relative intensity distribution of primary aggregates (closed triangles) and clusters (open triangles), Middle: ac conductivity measured at $f = 20$ kHz, and Bottom: elastic modulus, G', measured at $f = 1$ Hz and $\gamma_0 = 0.002$ vs. effective volume fraction of carbon black suspended in propylene carbonate. Vertical lines designate important transitions evident from the various techniques. From left to right: the fluid-clustered fluid phase transition, ϕ_{fc}, the electrical percolation threshold, ϕ_{e}, and the mechanical percolation threshold, ϕ_{g}. Lines are added to guide the eye.

Impedance spectroscopy measurements were performed to characterize the electrical properties of the suspension. The ac conductivity, σ_{AC}, measured at $f = 20$ kHz is plotted versus volume fraction and represents the sum of the ionic and electronic contributions to the electrical transport in the samples. The onset of electrical percolation is characterized by the critical volume fraction, ϕ_{e}, where the electrical conductivity of the suspension exceeds that of the ionic conductivity of the solvent. ϕ_{e} is greater than ϕ_{fc} where irreversible clusters form. Further, the power-law scaling of conductivity with increasing volume fraction indicates that the origin of the electrical transport is the disordered hopping of electrons between carbon particles.

---

[1] Northwestern University, Evanston, IL 60208

[2] University of Delaware, Newark, DE 19716

[3] NIST Center for Neutron Research, National Institute of Standards and Technology, Gaithersburg MD 20899

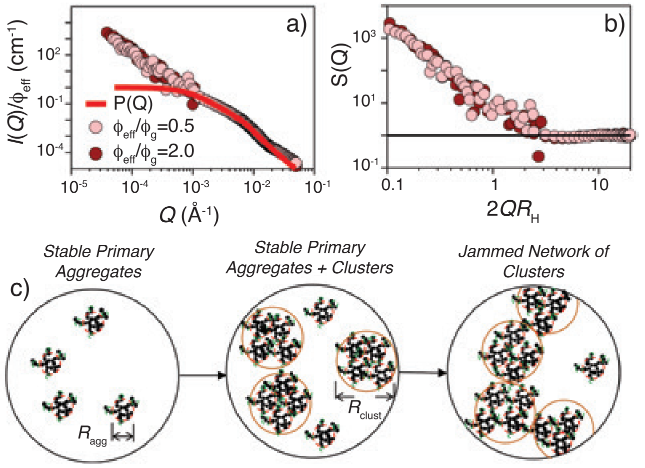

FIGURE 2: a.) Scattering intensity in absolute scale normalized to volume fraction vs. Q for samples spanning the gel boundary, b.) The static structure factor, $S(Q)$, vs. a normalized wavevector $2QR_H$ where R_H = 165 nm - it is evident that the primary aggregates are not in thermodynamic equilibrium, and c.) Schematic of structural transitions evident in suspensions of carbon black in propylene carbonate.

Finally, at a critical volume fraction, ϕ_g, the suspensions obtain a measurable elastic modulus, G', indicating that macroscopic gelation has occurred. Critically, the gelation boundary does not align with the onset of electrical percolation, suggesting that these two processes may not be directly linked.

While the macroscopic measurements imply that the electrical network is not the same as the stress bearing network, the dynamic measurements do not unequivocally rule out other structural transitions at higher volume fraction near the gel boundary. Carbon black suspensions prepared at elevated concentrations are opaque and therefore not suitable for DLS. Thus, ultra-small angle neutron scattering (USANS) and small angle neutron scattering (SANS) measurements were performed. Figure 2a shows the combined desmeared USANS and SANS scattering intensity normalized to volume fraction for samples below and above the gel boundary. The form factor of the primary aggregates, $P(Q)$, is also in Figure 2a. These data confirm that no structural transitions occur on the length scale of these clusters upon gelation. This is further emphasized by normalizing the scattering intensity to the primary aggregate form factor yielding the static structure factor $S(Q)$ (Figure 2b). The fact that $S(Q)>>1$ at low-Q confirms that the primary aggregates are not in an equilibrium aggregation state, despite indications from DLS that samples were in the fluid phase. Therefore, the low-Q scattering must arise from large clusters present in the sample that form at concentrations well below the gel boundary.

These USANS/SANS measurements confirm that the origin of the macroscopic rheological behavior is the formation of a re-entrant clustered fluid phase consisting of micron-sized agglomerates which arrest to form a system spanning stress-bearing network as shown in Figure 2c. However, the onset of gelation occurs at higher concentrations than the onset of clustering and electrical percolation. We are therefore left to conclude that the mechanical bonds that comprise the network are inter-cluster bonds and it is these bonds that are responsible for the deleterious increase in viscosity observed in electrochemical slurries. Interestingly, the electrical measurements show no indication of a change in the charge transport pathways when these inter-cluster bonds are formed. Therefore, we conclude that the stress-bearing network is not intrinsically linked with the network responsible for electrical transport. These results emphasize the diminished role that physical connectivity plays in determining the charge transport characteristics in such materials. Further, they suggest that while the clusters are responsible for the mechanical properties, the electrical properties arise instead from the aggregate and cluster dynamics (i.e., Brownian motion). These results emphasize the critical and yet unrecognized role that colloidal properties play in determining electrical transport in suspensions comprised of conducting particles and suggest new strategies for the design of slurry-based electrodes with optimized rheological performance [8].

References

[1] E. M. Spahr, R. Gilardi, D. Bonacchi, Encycl. Polym. Compos. 0–35 (2014).

[2] M. Duduta, et al., Adv. Energy Mater. **1**, 511 (2011).

[3] K. C. Smith, T.-M. Chiang, W. J. Carter, Electrochem. Soc. **161**, A486 (2014).

[4] J. Mewis, N. J.Wagner, J. Nonnewton. Fluid Mech. **157**, 147 (2009).

[5] P. Lindner, T. Zemb, (North-Holland, 2002).

[6] O. Glatter, (Academic Press Inc., 1982).

[7] L. A. Feigin, D. I. Svergun, (Akademie Verlag 1987).

[8] J. B. Hipp, J. J. Richards, N. J. Wagner, J. Rheol. *In preparation* (2018)

Viscoplastic fracture transition of a biopolymer gel

B. R. Frieberg,[1] R.-S. Garatsa,[1] R. L. Jones,[1] J. O. Bachert III,[2] B. Crawshaw,[2] X. M. Liu,[2] and E. P. Chan[1]

Gelatin is a thermoreversible gel, acting as an elastic solid at low temperatures and transitioning reversibly into a fluid at higher temperatures. The transition is key to its use in controlling the thickness and texture of foods, as a binding agent in paper products, and in soft gel capsules for vitamins and pharmaceuticals. However, in the case of gelatin based capsules, predictable fracture mechanics are required to facilitate a swelling-induced burst within the gastrointestinal system, delivering the active encapsulants. The capacity to tune the fracture energy with molecular structure could open gelatin applications to higher and lower temperature markets where performance reliability is currently prohibitive. Recent work [1] has suggested that gelatin fracture process is viscoplastic, a rate based inelastic regime dominated by disentanglement rather than chain scission. Using data from Small Angle Neutron Scattering (SANS), contact mechanical testing (CMT), and Cavitation Rheology (CR), we measure a transition from elastic to viscoplastic regimes as a function of the number density of mesh linkages. Understanding and manipulating this transition provides a route to enhance and better control performance through molecular structure.

Recently, we have reported data [2] from SANS that quantifies the mesh size, ξ_M, of the gel in the sold state that is the basis of elasticity. Using complimentary samples, The elastic modulus, E, is measured with CMT. With measured values of E, a simple relationship allows the extraction of the fracture energy, G_c, that describe the relevant mechanical state of the material from CR measurements. The result is a correlation of mesh size to fracture energy that reveals two regimes, below and above the entanglement concentration, ϕ_E.

The samples are mixtures of gelatin, derived from bovine hide, in deuterium oxide (D_2O). Gelatin powder, mixed with D_2O for contrast in the SANS measurement, is heated at 70 °C for several hours to achieve a homogeneous mixture. In the case of mechanical measurements, the solution is poured into a cylindrical mold and maintained under constant humidity until measurements are conducted. In the case of SANS, the solutions are syringed into titanium demountable cells with 1 mm path length and measured within hours of cooling. Gelatin/water ratios varied from 5 % to 40 % by mass gelatin.

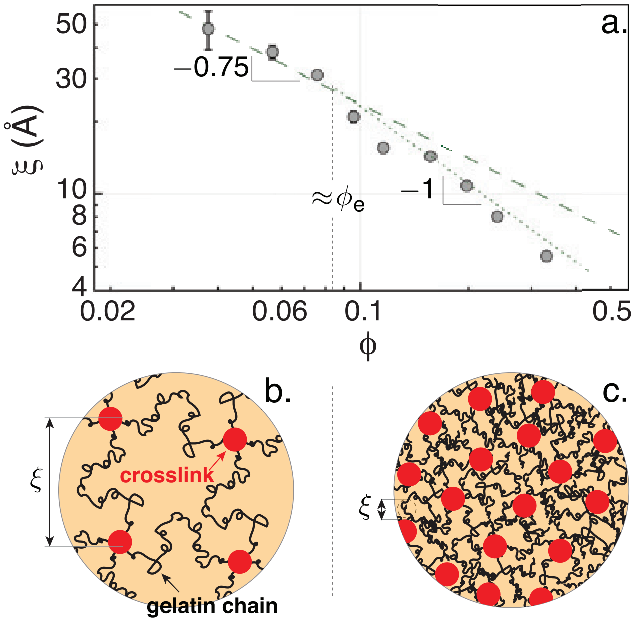

FIGURE 1: In (a), the measured correlation length, ξ, extracted from models of the SANS data as a function of the gelatin concentration by mass percentage, ϕ. Indicated in the plot are fits based on an expected slope of -0.75 below the entanglement concentration, consistent with theories of chains in good solvents, and -1.0 above the entanglement concentration that represent chains in a "theta" solvent. Schematics of the mesh are provided depicting structure (b) above and (c) below the entanglement concentration.

SANS was performed on the nSoft Small Angle Neutron Scattering instrument. Configurations used two wavelengths, λ, and two detector distances to measure the required range of momentum transfer, $|q| = 4\pi/\lambda \sin\theta$, where 2θ is the scattering angle. Using standard data reduction methods, the scattered intensity as a function of q is converted to differential cross section which is a measure of the probability of scattering from the average nuclei in a sample. Differential cross section is an intrinsic property of a material, and the form of the scattering reveals correlations in spatial structure. Here, in Figure 1, the correlation length extracted from SANS data reveals a transition in scaling near the estimated entanglement concentration of the fluid gelatin, ϕ_e.

---

[1] Materials Science and Engineering Division, National Institute of Standards and Technology, Gaithersburg, MD 20899

[2] Pfizer Consumer Healthcare, Richmond, VA 23220

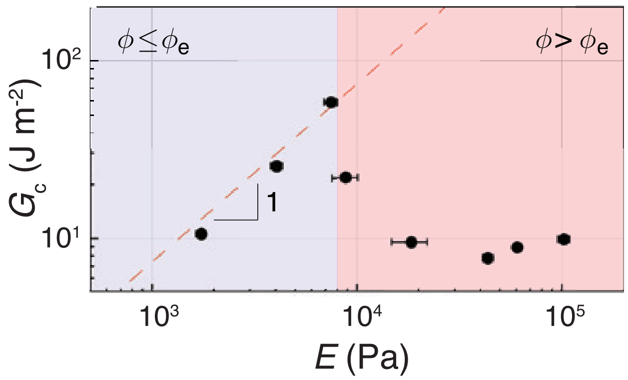

FIGURE 2: Comparison of the measured fracture energy (G_c) and the elastic modulus (E) of gels composed of gelatin and deuterium oxide. Two regions are highlighted, below (blue) and above (pink) the entanglement concentration, ϕ_E.

CMT measures the modulus by compressing the gel with a cylindrical punch. In this case, the punch has a diameter (2*a*) of 3 mm, and compresses at a fixed displacement rate. The stiffness in the limit of a semi-infinitely thick gel is obtained from the slope of the force, p, versus displacement, δ. The slope is then equated to the elastic modulus, E, by the equation $\Delta p/\Delta\delta - 2\,\bar{E}\,a$, where $\bar{E} = E/(1\text{-}\nu^2)$ and ν is Poisson's ratio.

The elastic modulus is key to understanding the fracture energy obtained by CR. Here, a syringe needle imposes a hydrostatic pressure, P_f, to create a bubble of radius r at a constant volumetric compression rate to cause neucleation of a cavity. At low energies, this process measures the elasticity and interfacial tension of the gel. Above a critical pressure, the pressure results in fracture. At this point, the fracture energy, G_c, is obtained from the relationship $P_f = (\pi G_c E/3r)^{1/2}$.

Using the measured values of E from CMT, the cavitation rheology data leads to values of G_c as a function of gelatin concentration (see Figure 2). Unsurprisingly, the data in Figures 1 and 2 show that the fracture energy of solid gelatin is strongly dependent on the volume fraction of the gelatin content. What is striking is the enhancement in the fracture energy as the entanglement concentration is approached, followed by a sharp dropoff at higher concentrations. While not shown here, the modulus, E, continues to increase with increasing concentration. Our study further indicates that this point represents a transition from fracture dominated by mechanical entanglement to a regime based on chain scission.

In conclusion, for soft gel capsules, $(G_c E)^{1/2}$ can be used as a descriptor of the rupture resistance due to this applied pressure. Although the highest gelatin content resulted in the highest measured value for the rupture resistance, our results indicate that viscoplasticity is a significant factor that can be tuned by modifying the elastic and fracture properties of the gel via addition of viscous fluids. As an example, the entanglement concentration is a tunable parameter with molecular weight, allowing the fracture energy to be adjusted for the needs of a specific application.

References

[1] T. Baumberger, C. Caroli and D. Martina, Nat. Mater. **5**, 552 (2006).

[2] B. R. Frieberg, R.-S. Garatsa, R. L. Jones, J. O. Bachert III, B. Crawshaw, X. Michael Liu, and E. P. Chan, Soft Matter **14**, 4696 (2018).

SANSDrop: a continuous approach to high-composition resolution structural characterization of multicomponent formulations

B. J. Bleier,[1] M. L. Davidson,[1] K. M. Weigandt,[2] and L. M. Walker[1]

We have been developing microfluidic and millifluidic approaches to characterize colloidal systems with the goal of high resolution in composition [1, 2]; important for characterizing a multicomponent formulation space and for searching for behaviors that occur abruptly in composition space. The use of droplet-based approaches results in small, discrete samples prepared in series with small, but controllable, variation in the composition between droplets. This approach has the advantages of using smaller amounts of material, limiting depletion to solid container walls, isolation of individual samples from each other and continuous flow.

Figure 1 demonstrates the generation of a train of droplets of varying composition in a continuous fluid. Here, the continuous fluid is a nonpolar oil (mineral, fluorinated or silicon oil) while the sample or droplet phase is an aqueous solution of varying composition. Droplets are millimeters in cross-section, set by the inner diameter of the tubing or capillary, and tens of millimeters in length, set by the relative flow rates of the dispersed and continuous phases. Overall flow rates are chosen so that the velocity of the droplets is mm to cm per minute, providing exposure times of minutes at a fixed point downstream. The neutron beam is shaped using a 6.3 mm x 1 mm horizontal slit; experiments were performed at a wavelength of 8 Å and sample-to-detector distances of 4.6 m. Scattering data are collected in event mode. Intensity is collected in 5 s bins and reported as neutron counts per bin.

Figure 2 shows results of a contrast variation experiment. In this case, streams A and B are the same concentration of silica nanoparticles (1.9 vol% Ludox HS-40) in D_2O or H_2O. The scattering and transmission are shown on the left, beginning with a region of steady flow (high H_2O), continuing through the gradient to another region of steady flow (high D_2O). The red points show plateaus from droplet scattering; the downward spikes are from the continuous phase oil spacers. A red dashed vertical line indicates the point of minimum scattering (the contrast match point for the particles). The figure on the right shows the comparison with macroscopic samples (5 discrete samples). The droplet data have not been corrected so they do not scale exactly, but the agreement is impressive demonstrating the higher compositional resolution that can be achieved with this technique. Note that this procedure exchanges resolution in intensity (now low) for resolution in composition (now high).

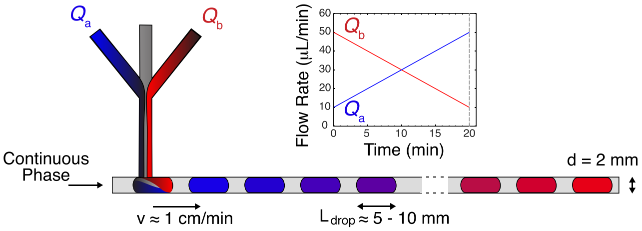

FIGURE 1: Droplet based approach to formation of a concentration gradient. Droplets produced in a glass capillary (25 cm long, 2 mm ID x 3 mm OD) providing 2 min of exposure time per droplet. Typical flow profiles for a linear gradient shown.

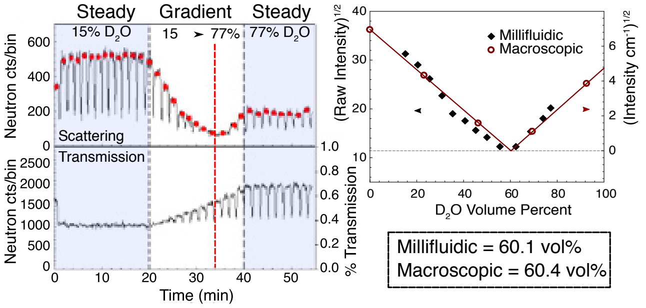

FIGURE 2: Results of a contrast variation experiment. Feed streams contain 1.9 vol% Ludox in heavy and light water. The contrast match point is found using scattered intensity and composition determined from flow rate calculations and verified with transmission. Results are compared to corrected data taken on five macroscopic samples.

A second feasibility study investigated the structure of an electrostatically stabilized nanoparticle system with added surfactant near a phase boundary. A large composition space was mapped and searched for regions of increased scattering from flocculation. These regions show significant structural peaks consistent with previous work [3], demonstrating the ability of the technique to quickly find regions of interest with limited sample and a consistent search [2].

In this preliminary study, we demonstrate that droplet-based continuous methods are compatible with SANS; intensity resolution is sacrificed for composition resolution providing a method to rapidly scan large regions of phase/structural behavior.

References

[1] B. J. Bleier, B. A. Yezer, S. L. Anna and L. M. Walker, J. Coll & Intf Sci **493**, 265 (2017).
[2] B. J. Bleier, PhD Thesis, Carnegie Mellon University, Pittsburgh PA (2017).
[3] S. R. Kline and E. W. Kaler, Langmuir, **10**, 412 (1994).

---

[1] Carnegie Mellon University, Pittsburgh, PA 15213
[2] NIST Center for Neutron Research, National Institute of Standards and Technology, Gaithersburg, MD 20899

In-situ ultrasound sample environment for small angle scattering studies

Y. Xi,[1] D. S. Li,[1,2] Y.-T. Lee,[1] and L. D. Pozzo[1]

Ultrasound is an important technique that has been widely utilized in various research fields, including biomedical imaging, disease treatments, as well as food processing and quality control [1-3]. In chemical laboratories, it also serves as a routine procedure for cleaning, emulsification and resuspension using sonication baths or 'horn' sonicators. [4]. More recently, cavitation induced by ultrasound has also been used to promote cystallization and chemical reactions [5, 6]. Yet, in many of these applications, the underlying physical mechanisms that are at play are not fully understood. In this work, a new sample environment has been developed to enable *in-situ* scattering characterization of structural evolution under well-characterized ultrasound fields.

A schematic of the new sample cell is shown in Figure 1. The sample is placed between two identical high intensity focused ultrasound (HIFU) transducers that are alternated to avoid sonophoresis depletion or enrichment of the sample due to the acoustic radiation force. A polyvinylidene difluoride (PVDF) broad range receiving transducer is placed orthogonal to the main acoustic field to detect and record cavitation signals. The cavitation probability reflects the likelihood that one acoustic pulse will result in at least one cavitation event. This allows for sample monitoring above and below cavitation thresholds. Transparent windows allow monitoring of structural changes using neutron or X-ray scattering.

An example application comes from the sono-crystallization of conjugated polymers, which is proposed to originate from nucleation sites induced by ultrasound fields. Figure 2 shows the effect of ultrasound on the polymer structures. Nanofibers are generated after ultrasound application. A clear increase in the intensity is observed from the SANS data at low-q range (0.003 Å$^{-1} < q < 0.01$ Å^{-1}), indicating the formation of nanofibers after 2 h of ultrasound application. USAXS also characterizes a lower q range (0.0001 Å$^{-1} < q < 0.0006$ Å^{-1}) corresponding to larger dimensions of the polymer structures. It is found that the scattering intensity increases as quickly as 5 min after insonation and the power law exponent decreases with extended sonication time. The increase in intensity can be rationalized by the formation of nucleation sites during sonication.

In summary, an *in-situ* ultrasound sample environment has been designed to allow for structural characterization using X-ray and neutron scattering experiments. With our newly developed sample environment [4, 6], the effect of acoustic frequency, pressure, and exposure time can be easily studied over a wide length scales from 0.1 nm to 1000 nm.

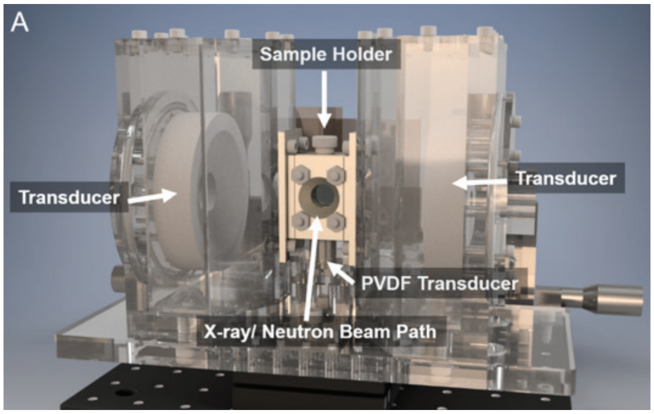

FIGURE 1: Schematic of the *in-situ* ultrasound sample environment.

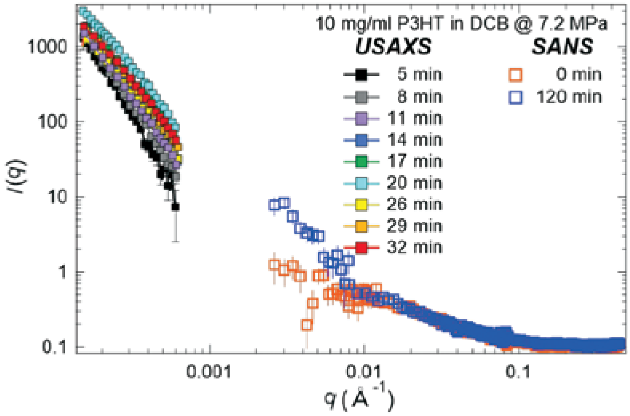

FIGURE 2: USAXS and small angle neutron scattering profiles of 10 mg/ml P3HT in DCB with various sonication time.

References

[1] A. Carovac, F. Smajlovic, D. Junuzovic, Acta Inform. Medica **19**, 168 (2011).

[2] T. S. Awad, H. A. Moharram, O. E. Shaltout, D. Asker, M. M. Youssef, Food Res. Int. **48**, 410 (2012).

[3] D. S. Li, S. J. Yoon, I. Pelivanov, M. Frenz, M. O'Donnell, L. D. Pozzo, Nano Lett. **17**, 6184 (2017).

[4] D. S. Li, Y.-T. Lee, Y. Xi, I. Pelivanov, M. O'Donnell, L. D. Pozzo, Soft Matter **14**, 5283 (2018).

[5] T. J. Mason, Chem. Soc. Rev. **26**, 443 (1997).

[6] Y. Xi, D. S. Li, G. M. Newbloom, W. K. Tatum, M. O'Donnell, C. K. Luscombe, L. D. Pozzo, Soft Matter **14**, 4963 (2018).

---

[1] Department of Chemical Engineering, University of Washington, Seattle, WA 98195

[2] Department of Bioengineering, University of Washington, Seattle, WA 98195

Spectral Compton imaging of prompt γ rays from neutron capture in bulk material

H. H. Chen-Mayer,[1] D. J. Turkoglu,[2] B. K. Riley,[3]
H. Chen,[4] E. Draeger,[5] and J. P. Polf[4]

The instrument for Prompt Gamma Activation Analysis (PGAA) at NGD makes use of the characteristic gamma rays emitted immediately following neutron capture events. The spectral analysis of these prompt gamma rays, typically in the 0.1 MeV to 10 MeV energy range yields quantitative compositional information of a bulk sample. However, this analysis currently lacks position information. We explore a novel tomographic approach to PGAA that is both quantitative and spatially resolved, based on coincidence measurements of Compton-scattered gamma rays in multi-detector arrays (Fig. 1a). The image reconstruction was performed by CORE software [1] based on a modified Stochastic Origin Ensemble technique to generate 3D images using selected gamma emission lines, enabling elemental identification with location information.

The PGAA instrument at NGD (Fig. 1b) [2] is equipped with a high purity germanium (HPGe) gamma-ray spectrometer. For this demonstration, a Compton camera (CC) was placed on the opposite side of the sample chamber (Fig. 1b) at the same detector-to-sample distance of 60 cm. The CC is based on pixelated CdZnTe detector technology [3] with two 8-module planes. Quantitative determination of H mass (proportional to the counts of the H peak) was performed by incrementing the number of wax disks placed in the neutron beam (1 to 6) and integrating the intensity of the 2.2 MeV peak which is due to the neutron absorption of H. In the Compton imaging mode, quantitative assessment was made with CORE tomographic reconstructions using an energy window around the 2.2 MeV emission line of H. The central slices of the reconstructed volumes containing the sample are shown in the inset of Fig. 1c. As expected, the intensity increases with the number of wax disks.

The reconstructed image has a full width at half-maximum of 5 mm with 1 mm resolution, in good agreement with the disk size of 4 mm in diameter. While spatial resolution has not yet been demonstrated experimentally with spatially discrete distributions, simulations were conducted using the Monte Carlo code GEANT4 to evaluate the feasibility. A stack of alternating disks of Ti and H (in the form of water) of 2 cm in diameter and 0.5 mm thick was placed perpendicularly to a set of two detector planes made with CdZnTe material. Prompt gamma rays produced by a beam of incident neutrons were tracked, and all interactions inside these two planes are recorded. The 5.5 mm spacing of the disks is fully resolvable, as are the individual H and Ti disks when each specific emission window is considered separately for the reconstruction.

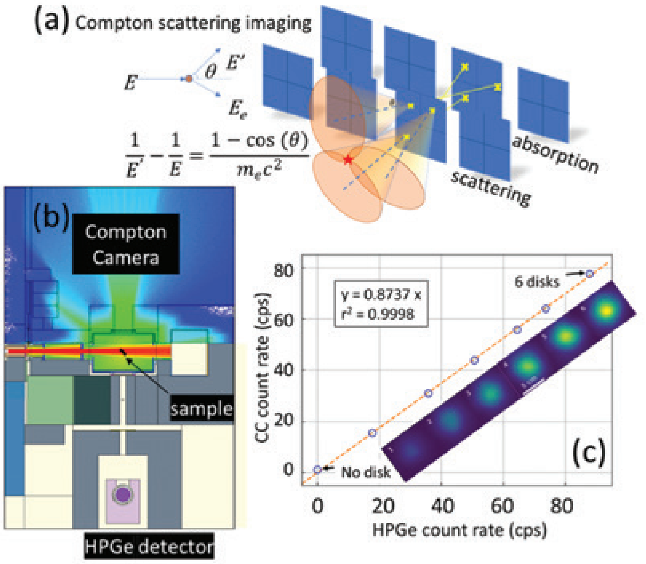

FIGURE 1: (a) Principle of Compton imaging with a two-stage pixelated detector: Compton cones are generated by the energy and location of the scattered gamma rays to determine the origin of the emission. (b) Top view of the NGD-PGAA instrument, with simulated neutron (red) and partial gamma field (green-blue) and detector locations shown. (c) Tomographically reconstructed images of the wax disks (inset) and H peak intensity obtained from the images vs HPGe count rate for the incremented number of wax disks. The uncertainty due to counting statistics is less than 1%.

Gamma rays from neutron absorption in H were used to demonstrate that quantitative 3D elemental imaging on a length-scale of several mm is achievable. Monte Carlo simulations were performed for a simple 4-plate stack of H and Ti, yielding promising results. These studies will facilitate improvement of the reconstruction process and provide ground work for a future optimized design of a Compton camera for PGAA imaging [4].

References

[1] J. C. Polf et al., Phys. Med. Biol. **60**, 7085 (2015).

[2] R. L. Paul et al., J Radioanal Nucl Chem **304**,189 (2015).

[3] F. Zhang, Z. He, C. E. Seifert, IEEE Trans Nucl Sci **54**, 843 (2007).

[4] H. Chen et al., J Radioanal Nucl Chem (2018) in press

---

[1] Material Measurement Laboratory, National Institute of Standards and Technology, Gaithersburg, MD 20899

[2] NIST Center for Neutron Research, National Institute of Standards and Technology, Gaithersburg, MD 20899

[3] University of Kentucky, Lexington, KY 40506

[4] University of Maryland School of Medicine, Baltimore, MD 21201

[5] Yale School of Medicine, New Haven, CT 06510

Precision counting of a cold neutron beam

M. S. Dewey,[1] E. S. Anderson,[2] D. M. Gilliam,[1] G. L. Greene,[3,4] A. B. Laptev,[5]
J. S. Nico,[1] W. M. Snow,[2] and A. T. Yue[1]

The Neutron Physics Group operates the Alpha-Gamma device on the monochromatic beam line NG-6M at the NCNR. It is a neutron detector that is designed to count the number of cold neutrons impinging on a thick boron target with sub-0.1 % relative uncertainty [1]. In the U.S., the NIST Radiation Physics Division is responsible for maintaining calibrated standards for each of the common forms of ionizing radiation. Whether it be neutrons, photons, electrons, or alpha particles, the ability to quantify the number of ionizing particles passing a point in space per unit time (flux) is an essential function in radiation physics.

In the U.S., the neutron standard is a spherically shaped radioactive source of neutrons called NBS-1 that is comprised of a small sealed capsule containing one gram of radium ($RaBr_2$) surrounded by a shell of beryllium 4 cm in diameter. The radium gives this source its 1600-year half-life, the sealed capsule insures that only gamma-rays escape the radium to enter the beryllium (alpha particles cannot penetrate the seal), and the beryllium converts a fraction of these gamma-rays into neutrons. This source emits about one million neutrons per second having energies ranging from 0 MeV to about 0.7 MeV. A device called a manganese bath (Mn bath) is used to compare the neutron emission rate of NBS-1 with other radioactive neutron sources [2]. If the neutron emission rate of NBS-1 is known (it is currently known to 0.85 % relative uncertainty), then the comparison provides the emission rate of the unknown source.

The Alpha-Gamma device was originally conceived to address a question in fundamental physics. A free neutron decays into a proton, an electron, and an electron antineutrino with a lifetime of 14.7 minutes. This lifetime can be predicted by the Standard Model of Particle Physics; therefore, precise measurements of this fundamental quantity can be used to test the Standard Model. In our beam-based measurement of the neutron lifetime, decays originating in a well-defined length of the beam are counted by counting the decay protons while simultaneously measuring the density of neutrons in that length of beam. The neutron lifetime is proportional to the neutron density divided by the rate of production of protons. To measure the density of neutrons in the beam, a flux monitor was constructed. In this device, a small fraction of the neutron beam is absorbed by a thin lithium-6 deposit leading to a measurable response for each neutron that is proportional to one over its velocity (the overall response is therefore proportional to neutron density). In 2012 the Alpha-Gamma device was used to recalibrate the flux monitor thereby allowing us to re-evaluate the lifetime and reduce its uncertainty [3]. The relative uncertainty achieved in that calibration was 0.07 %, which is about 50 times smaller than the state of the art.

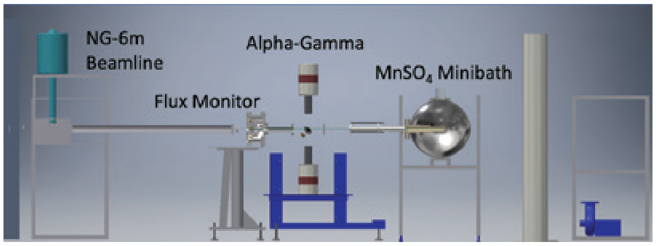

FIGURE 1: The experimental setup for calibrating the Mn bath on beam line NG-6M. In the first step, the Alpha-Gamma device calibrates the flux monitor; in the second step the Alpha-Gamma device is operated in pass-through mode, the calibrated beam passes into the bath, and its response is registered.

The calibrated flux monitor will be used to monitor and measure the flux of a neutron beam injected into a small portable Mn bath (see Fig. 1). This will serve to calibrate the bath. The calibrated bath will then be used to re-calibrate the national neutron standard NBS-1. The goal of the project is to reduce the uncertainty in NBS-1's emission rate by a factor of three. This technique for re-calibration does not rely on knowledge of any nuclear cross section. It is based solely upon the counting of ionizing particles with standard particle detectors. To our knowledge, this capability is unique in the world.

References

[1] A. T. Yue et al., Metrologia **55**, 460 (2018).

[2] J. M. Adams, Nuclear Instruments and Methods in Physics Research B **213**, 218 (2004).

[3] A. T. Yue et al., Phys. Rev. Lett. **111**, 222501 (2013).

---

[1] NIST Center for Neutron Research, National Institute of Standards and Technology, Gaithersburg, MD 20899

[2] Indiana University, Bloomington, IN 47408

[3] University of Tennessee, Knoxville, TN 37996

[4] Oak Ridge National Laboratory, Oak Ridge, TN 37831

[5] Los Alamos National Laboratory, Los Alamos, NM 87545

Peering inside heterogeneous pore surfaces with neutrons

W.-S. Chiang,[1,2,3] D. Georgi,[1] T. Yildirim,[2] J.-H. Chen,[1] and Y. Liu[2,3]

Surface heterogeneity is the variation of the structural or compositional properties on the surface and can significantly influence material properties. Although surface heterogeneity is ubiquitous in both natural and man-made materials, non-invasively probing it in bulk heterogeneous materials is still very challenging using existing techniques. Many techniques require flat and smooth surface and involve destructively pre-processing samples. It is especially difficult to probe the variation of compositional properties of the curved surface of pores that are deeply buried inside heterogeneous porous materials. A new scattering method, the Generalized Porod's Scattering Law Method (GPSLM) [1], has recently been developed to obtain quantitative information on the variation of the surface properties of porous materials by combining the well-known Porod's scattering law with the contrast variation method that is commonly used in small-angle neutron scattering (SANS) experiments. GPSLM can be directly applied to bulk materials without destructive sample preparation procedures providing an ensemble average of the surface properties of all pore surfaces within a sample. In particular, it gives the surface heterogeneity of the scattering length density (SLD), which is only related to the density and molecular formula of the components on the surfaces. GPSLM also shows that the average SLD obtained by the contrast variation method in the Porod's scattering region is the surface averaged SLD instead of the volume averaged SLD. This model-independent method requires no assumption of the size, shape, polydispersity, etc. for the pores.

We have applied GPSLM to kerogens isolated from natural shale rocks with different maturity [1]. Kerogens are the organic components of shale rocks whose pores are believed to be the main location of shale gas. It is important to know the variation of the pore surface in kerogens since it potentially influences the distribution of natural gas in shales. Figure 1(a) shows the typical image of Focused Ion Beam Scanning Electron Microscope (FIB-SEM) for kerogen and Figure 1(b) demonstrates the 2D cross section of heterogeneous porous materials, where solid matrices with different SLDs are drawn in different colors and the pores in between the solid matrices can be filled with fluid having an SLD of ρ_f. Changing ρ_f alters the contrast between the pores and the matrices and can be achieved by loading gas with different pressures or mixing hydrogenated and deuterated solvents with different ratios. With GPSLM, the surface-averaged SLD (ρ_A), the second moment of SLD ($\rho_{2M}{}^2$), the mean square deviation of surface SLD from ρ_A, i.e., the surface heterogeneity parameter ($\Delta_H{}^2$), and the surface to volume ratio (S/V) are quantitatively extracted for heterogeneous kerogen samples. Figure 1(c) and Figure 1(d) plot ρ_A and $\Delta_H{}^2$, respectively, as a function of hydrogen/carbon (H/C) ratio. The H/C ratio is determined from Prompt Gamma-Ray Activation Analysis (PGAA) and it decreases with increasing maturity of the kerogens. Figure 1(c) shows that ρ_f decreases with H/C while $\Delta_H{}^2$ increases with H/C. This is the first time that the surface heterogeneity of kerogens has been quantitatively determined.

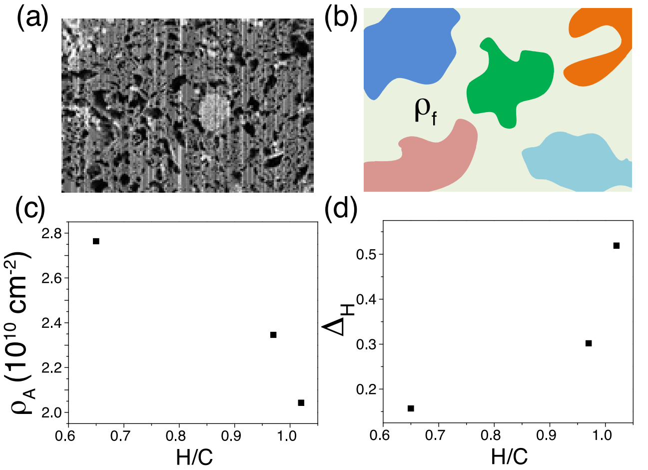

FIGURE 1: (a) FIB-SEM image of typical kerogen sample, (b) illustration of the 2D cross-section of a heterogeneous porous material, (c) the surface-averaged SLD, ρ_A *vs.* H/C ratio and (d) and the surface heterogeneity, Δ_H *vs.* H/C for three kerogen samples with different maturity.

Reference

[1] W.-S. Chiang, D. Georgi, T. Yildirim, J.-H. Chen, Y. Liu, Nat. Commun. **9**, 784 (2018).

---

[1] Aramco Services Company, Aramco Research Center-Houston, Houston, TX 77084

[2] NIST Center for Neutron Research, National Institute of Standards and Technology, Gaithersburg, MD 20899

[3] University of Delaware, Newark, DE 19716

Measurement of applied stress during shear deformation

T. Gnäupel-Herold and J. Milner

The optimization of sheet metal forming processes depends to a large degree on better materials data on stress and strain during multiaxial straining. However, the strain response to multi-axial stresses is generally not homogeneous [1], i.e., standard test methods that rely on sample averages cannot be used. Additionally, non-homogeneous deformation invariably induces residual stresses in the sample. These limitations can be overcome if regions with quasi-homogeneous strains can be identified and used for measurements of both stress and strain. Such data can be obtained from neutron diffraction measurements for stress determination in combination with digital image correlation (DIC) for the simultaneous measurement of plastic strain. There is also an important commonality between the two methods – both provide the spatial resolution necessary for the selection of a quasi-homogeneous measurement area. The combination of the two allows for the determination of the multiaxial yield function for a given straining mode.

DIC inherently captures the tensor character of strain, however, the determination of the stress tensor with neutron diffraction needs multiple specimen orientations, and all of this must be done while continuously deforming specimens made from some of the highest strength steels available. For this purpose, we have developed a device specifically for deployment on the BT-8 diffractometer that combines a rotational degree of freedom with two 40 kN actuators capable of any combination of uniaxial deformation (tension and compression) with shear deformation (Figure 1). Note that the ability to rotate the specimen during deformation is only useful in connection with the use of diffraction for stress determination. The angular range of rotation (135°) is both sufficient and necessary to uniquely identify the orientation of the principal stresses in all possible deformation modes. Examples for deformation modes important to the understanding of sheet metal forming are shown in Figure 2.

The device allows a great level of control over the orientation of principal axes through suitable magnitudes of vertical compression or tension superimposed to shear modes. One such application is the deformation with large magnitudes of shear strain. Such deformation modes exhibit significant changes in the orientation of the principal axes of both stress and strain. However, while the orientation of the principal strain axes is easily available from DIC virtually no data exist yet on the orientation of the principal stress axis system. The measurement of this orientation dependence requires both the rotation capability of the shear device and the spatial resolving power of neutron diffraction.

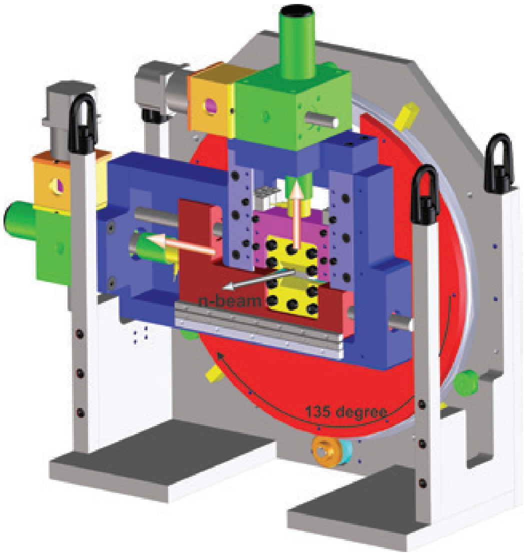

FIGURE 1: Generalized shear device dedicated for neutron diffraction allowing both general shear (horizontal actuation) and uniaxial deformation (vertical) as well as any combination of both. The rotational degree of freedom allows determination of the planar stress tensor as well as tracking of rotation of principal axes.

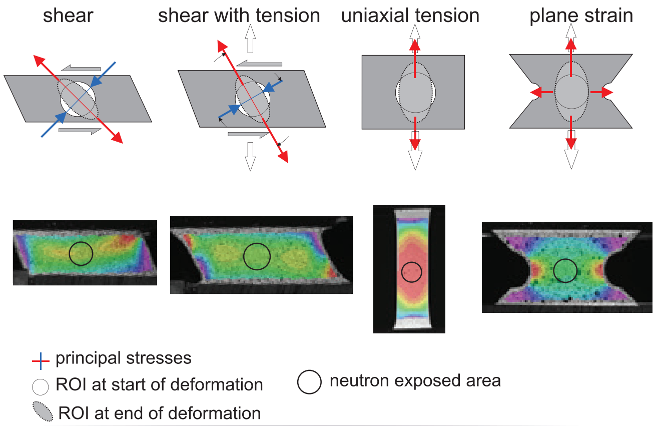

FIGURE 2: Deformations modes (top) with their respective von Mises strain maps (bottom) obtained by digital image correlation. Neutron exposed areas for stress measurements are indicated by the black circles (≈ 6 mm diameter). All multiaxial modes show pronounced inhomogeneity due to edge effects as indicated by large color gradients.

Reference

[1] S. Bouvier et al., Journal of Materials Processing Technology **172**, 96 (2006).

NIST Center for Neutron Research, National Institute of Standards and Technology, Gaithersburg, MD 20899

Neutron Source Operations

Reliability and Availability of the Reactor

The reactor operated for 182 days during FY 2018, achieving a reliability of 97.5 %. There were three unplanned shutdowns which resulted in 3.5 days lost, two days due to instrumentation failures for the cold source and one day due to a spurious instrument scram. Some of the lost time was made up by extending the reactor cycles.

New Underwater Saw for Shim Arms and Fuel

During FY 2018 Reactor Operations took delivery of a new underwater saw assembly. The new assembly is designed such that it can be permanently stationed in the fuel storage pool. The old assembly could not be permanently stored in the pool because the materials could not withstand exposure to water for longer than a couple of weeks. The function of the assembly is to remove the heads for used-up shim arms and separate the fueled regions from the non-fueled regions of spent fuel elements prior to shipment. Using the new assembly, we will be able to accomplish this task with considerably less effort. Key in the design effort was the establishment of proper saw-chip management, with the aim to keep the storage pool as clean as possible. The new assembly has been successfully tested with dummy fuel elements and will be used during the next spent fuel shipment.

Monitoring of Reactor Heavy Water

The NBSR's heavy water, D_2O, which serves as both the primary coolant and neutron moderator, has historically been replaced when its tritium concentration exceeds 2 Ci/L. This has occurred approximately every ten years. The reason for replacing the D_2O is a regulatory limit stating that the tritium concentration should not exceed 5 Ci/L.

FIGURE 1: Fuel saw assembly with Scott Slaughter looking on. The chip management system is on the left front side.

FIGURE 2: Fuel saw assembly submerged in test tank, which was designed to mimic the storage pool. Scott Slaughter is handling a dummy fuel element.

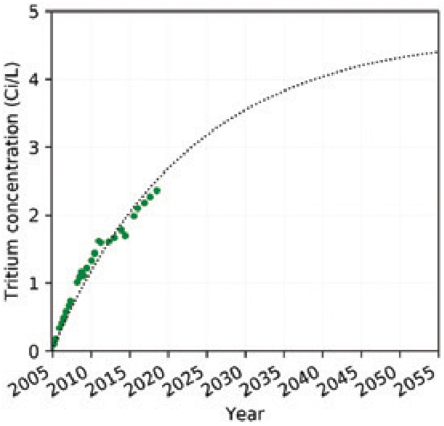

FIGURE 3: Tritium concentrations versus year.

Since the most recent replacement of the primary D_2O in October 2004, the tritium concentration has been measured at least once per year by Health Physics. Figure 3 shows measured tritium concentrations as well as non-linear regression analysis that projects the concentration until the year 2055. Although strategies were explored for reducing the tritium concentration without replacing the entire primary inventory, the projection of the concentration asymptotically approaches a value (4.65 Ci/L) that is lower than the 5 Ci/L limit. Additionally, analyses indicate that year-to-year values of personnel doses from tritium and effluent stack release of tritium are dependent on the nature of maintenance work rather than being correlated with the tritium concentration. For these reasons, the decision was made to delay – and possibly forego – the replacement of the ≈ 45,600 L of D_2O, saving a multi-million-dollar expense while reducing possible exposure risks.

The D_2O purity, or mass fraction D_2O, is another important factor to consider when assessing the "health" of the reactor D_2O. The D_2O purity affects reactivity, the determining factor for the NBSR cycle length: The reactivity of the NBSR is maximized with 100 % D_2O, while a degradation in purity to a mass fraction of 99.9 % results in reduction in reactivity that is equivalent to ≈ 2 days of operation. Because ingress of light water would make the NBSR inoperable below a mass fraction of 97.0 % D_2O due to lost reactivity, a positive pressure differential is maintained from the primary side to the secondary side of the main heat exchangers to prevent a light water leak into the primary D_2O. Although slowed by Helium cover gas, deuterium exchange with hydrogen in moist air could result in a very slow degradation in purity and reactivity. A recent recalibration of the densitometer is part of a new effort being made to monitor the long-term trend of the reactor D_2O purity. The purity of the primary D_2O was recently measured to be a mass fraction of 99.826 %.

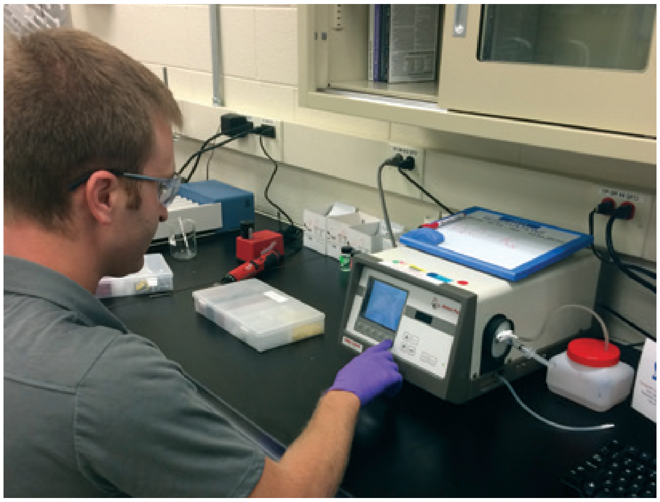

FIGURE 4: Danyal Turkoglu of Reactor Operations and Engineering prepares to begin a high precision density measurement using a U-Tube-Oscillation type densitometer. This instrument is located in the scientific laboratories of the NCNR. It was used to cross calibrate the instrument in use by Reactor Operations with the help of Liz Kelley of the Neutron Condensed Matter Science Group.

Cryogenic Refrigerator

A major milestone in the liquid deuterium cold source project was achieved in September 2017 with the commissioning of the new cryogenic helium refrigerator. The bankruptcy of the manufacturer delayed this accomplishment by about three years, as it fell upon the NCNR to gather the major components from various subcontractors and complete the installation. The final step was the installation and startup of the turbine ex pander. The new refrigerator has been operating since January cooling the existing liquid hydrogen cold sources. This larger refrigerator is needed in anticipation of the larger cooling requirements of the future LD_2 source.

FIGURE 5: The new cold source refrigerator, located in C200.

Conceptual designs for the LD_2 cryostat, condenser enclosure, transfer lines and support plug are complete. A pair (one spare) of 6 kW plate-and-fin type deuterium condensers have been delivered, tested and mounted inside their vacuum and helium containments. The deuterium gas management system (16 m^3 ballast tank and deuterium charging manifold) was installed in 2014. A contract for Phase 1 (engineering design/analysis of vessel prototypes) of the fabrication of the cryostat assembly was awarded in 2017, and Phase 2 (test prototypes, final design and fabrication) will commence this summer. The target date for installation is 2022.

Upgrade to Conventional Reactor Systems

Of all the work that was performed during the Fall 2017 reactor shutdown, two projects stood out has having been prepared for many years prior to fruition. These are the replacement of the primary cooling pump system and the replacement of the shim arm drive mechanism. Both projects were completed on schedule. Because of the work areas, these projects had the potential to be major drivers of the total radiological dose to the personnel involved in the work. Due to careful work planning, the total radiological dose remained below prediction. Below are two pictures of the completed assemblies.

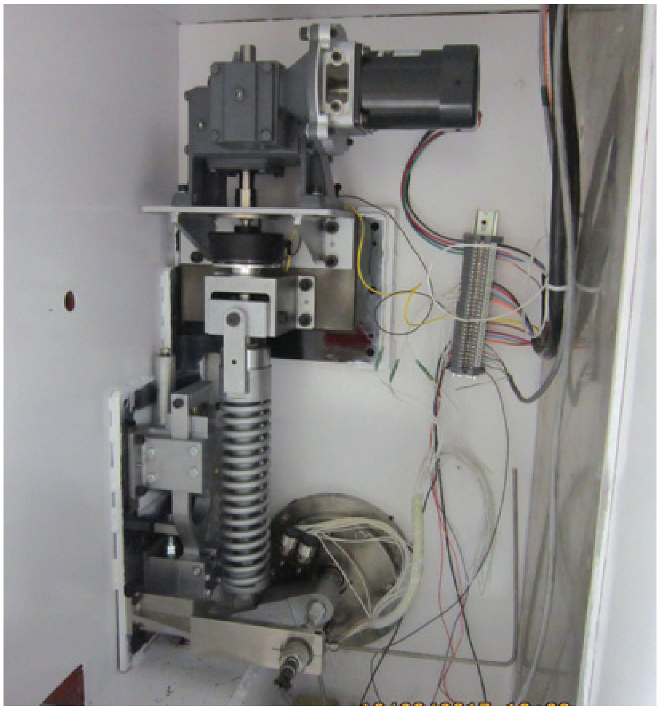

FIGURE 6: Shim arm mechanism positioned in place. The mechanism is reproducibly attached (with pinned connections) against a tooling plate that is welded to the biological shield. Skip welds in the left foreground and the back plane perform the permanent connection of the tooling plate to the biological shield. This construction will make it far easier to reconstruct the assembly in case of repair, because all hardware is permanently oriented against a reproducible datum. All necessary mechanical degrees of freedom have been fixed this way.

01/02/2018 15:35

FIGURE 7: New primary cooling pump assemblies. The new pumps are physically larger than the old pumps and as a result run cold to the touch, while the old pumps operated at ≈ 45 °C. What appear to be stainless-steel spool pieces (with the lifting lugs) are in fact the new nozzle check valves, which operate on flow (or lack thereof) alone as opposed to the old check valves, which operated on external air pressure.

Facility Development

Installations and Upgrades

VSANS on NG-3

The VSANS instrument has been commissioned and scientific experiments are now routinely completed. Over the last year a number of additional components were installed and tested. In May, the rear detector having high spatial resolution (0.9 mm fwhm) was installed. The detector uses a neutron scintillator with an intensifier and a Peltier-cooled CCD camera. Test measurements indicate the camera background is much higher than expected and dominates the weaker scattering from our test samples. A median filter applied to the 2D images is found to remove much of the intensifier background without distortion. Further testing of operating conditions are planned to attempt to further lower the observed background and thus extend the usable range of the detector.

The multi-hole collimators and MgF_2 lenses and prisms for the 18 converging beam collimation system were installed and aligned. Testing showed that the parasitic background from the new focusing optics is quite low and comparable to that seen with standard circular pinholes. The two-bounce highly oriented pyrolytic graphite (HOPG) monochromator was installed and found to produce a beam with wavelength resolution of 1 % fwhm, much higher wavelength resolution than what is available on the other SANS instruments at the NCNR. Three-inch-thick steel roofs and walls were installed around the vacuum vessel containing the beam collimation optics to lower the gamma ray background thus allowing the high flux/ low wavelength resolution "white beam" option of 40 % fwhm to be used. The radio frequency neutron spin flipper was installed and thus allows full beam polarization analysis experiments. Other neutron shielding modifications in the optics sections have been added to lower instrument background, which is now similar to that found on the other SANS instruments. The data reduction software is operational, allowing processing of Nexus data files containing all nine 2D detector histograms. The software can also process data taken in event mode where individual neutrons are time and location stamped.

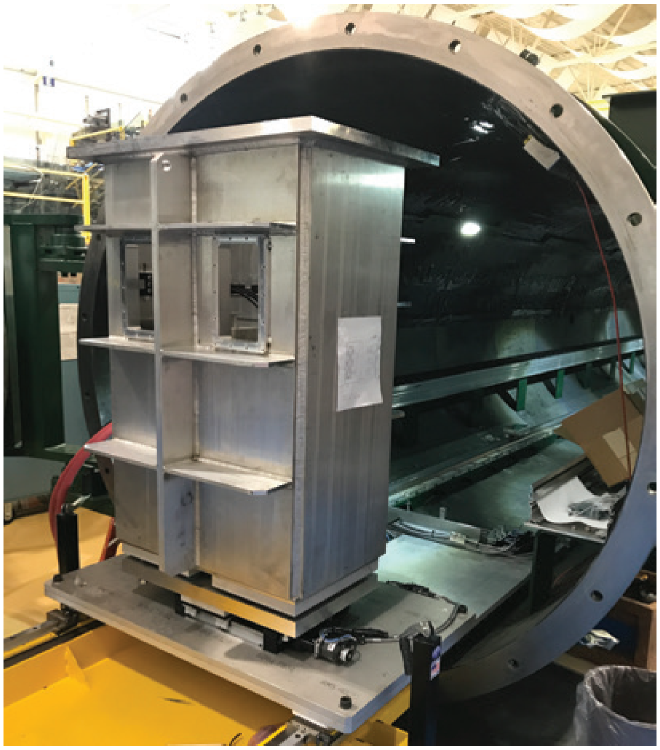

FIGURE 1: A back view of the housing for the high-resolution detector being installed on VSANS.

Currently, most VSANS experiments are run in a mode where the front and middle detector carriages are positioned to cover a single q-range much larger than what can be routinely accessed on the 30 m SANS instruments. In situ measurements of sample kinetics are now routine. White beam or HOPG wavelength selection options are routinely chosen to produce either higher beam flux or higher q-resolution than is available on the other SANS instruments.

CANDOR

There has been exciting progress toward the completion of the CANDOR instrument on NG-1 with the design, installation, and testing of several major assemblies. The primary instrument is essentially complete. This includes all of the components necessary for beam polarization including a 2 m long double V polarizer and an RF flipper. Another highlight is that the sample stage is fully operational, providing a highly accurate rotating base for the 4 m long detector arm. The sample stage also hosts a unique twin chain solution for compact cable management. The detector arm floor was poured and covered with anodized aluminum plates and the detector arm itself is installed and rotates smoothly around 150 degrees. Some of the assemblies have been installed on the detector arm including a 600 mm long removable diverging glass guide that can be replaced with a neutron spin filter to provide

^{3}He polarization during analysis. A 2.5 m long stationary diverging guide has also been installed. Both the removable and stationary diverging guides are encased in stainless-steel shielding. The data acquisition system NICE is functional and has begun testing. In the coming months, the prototype detector will be installed and tested before the final shielding is installed making CANDOR ready for its first neutrons.

Over this past year significant effort has been expended towards the simulation, design, and fabrication of a cryogenic detector for the CANDOR spectrometer. The energy analyzing HOPG crystals are to be cooled to ≈ 4K, largely eliminating the constant background in the detectors arising from thermal diffuse scattering. The scintillator-based neutron detectors will reside in a dry gas volume at constant, but non-cryogenic temperatures. Simulations guided the design of the cryogenic portions of a two-array prototype detector, which are expected to be assembled and tested in Q4 2018.

Development of the balance of the detector continues with contacts in place and in-house work to support the construction of both the two-array prototype and eighteen-array full detector. A single CANDOR detector array consists of 54 highly oriented pyrolytic graphite crystals set at different takeoff angles to diffract neutrons into ^{6}LiF:ZnS(Ag) neutron counters. The scintillator manufacturer has produced many small production runs of the 1.5 mm-thick neutron counters, which now consistently demonstrate > 93 % sensitivity for 3.27 meV (5 Å) neutrons. Front end electronics, including silicon photomultiplier carrier boards, preamps, lightbox passthroughs, and associated cabling have been designed and built to support the two-array prototype. The data acquisition electronics, high speed digitizers with field programmable gate arrays configured to process incoming waveforms with a pulse shape discrimination algorithm, have been procured and are undergoing testing and integration into the instrument control software.

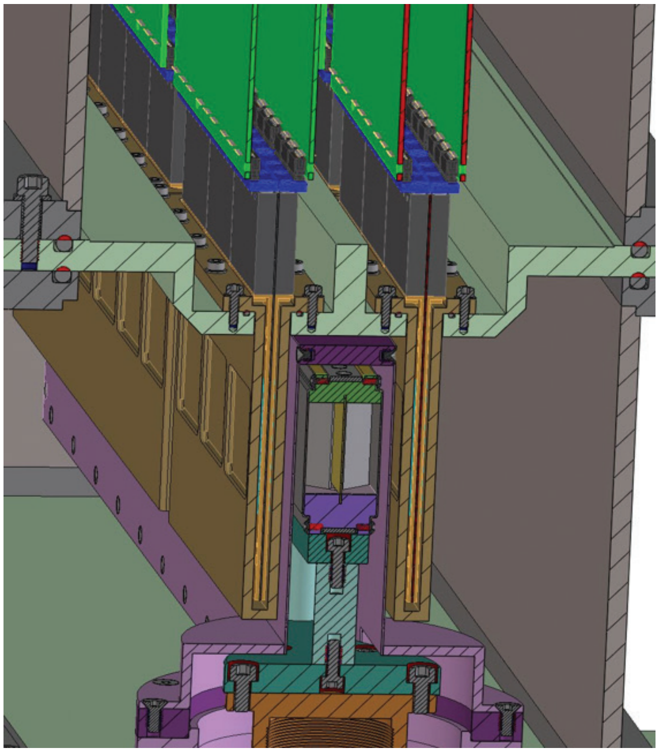

FIGURE 2: Cross section view of the cryogenically cooled energy analyzing detector for CANDOR. Highly oriented pyrolytic graphite crystals are cooled to 4K. The ultrathin neutron detectors, residing in pockets alongside the HOPG arrays, are in a dry gas at non-cryogenic temperatures along with the front-end electronics for the detector.

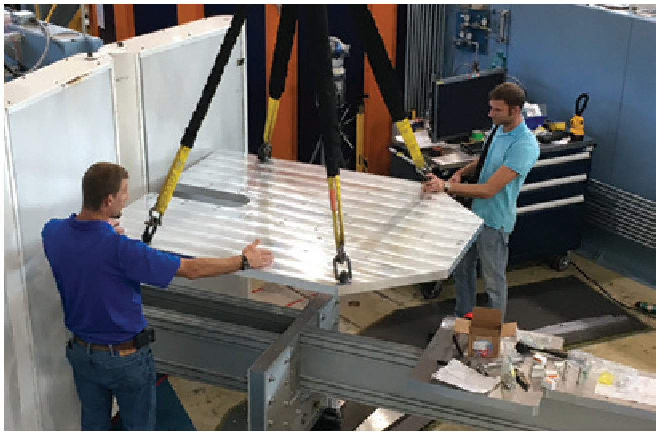

FIGURE 3: Danny Ogg (L) and Doug Ogg (R) installing part of the detector arm at CANDOR.

Electronics Updates

Over the course of 2018, the RFO electronics group has pursued upgrades to the air pad control system and double focusing monochromator (DFM) for the BT-7 triple axis spectrometer. The changes to the air pad controls enhanced stability and reliability. The new DFM controls are now based on the facility standard "VIPER" motor controls and demonstrate a speed up over the previous controls by nearly a factor of ten, dramatically reducing the time required for variable incident energy scans. A similar upgrade is planned for the MACS spectrometer in 2019.

Helium Spin Filters

The ^{3}He team has two primary missions, (i) development of new polarized neutron measurement capabilities including CANDOR (Chromatic Analysis Neutron Diffractometer or Reflectometer) and NSE (Neutron Spin Echo) instruments; (ii) service of the polarized neutron scattering experiments on NCNR instruments including the BT-7 thermal triple axis spectrometer, the small-angle neutron scattering instruments (SANS), the Multi-Axis Crystal Spectrometer (MACS), and Polarized ^{3}He And Detector Experiment Station (PHADES). It is notable that the NCNR runs the first SANS program in the U.S. that routinely operates with full polarization analysis, the first thermal triple axis spectrometer that routinely utilizes ^{3}He spin filters for polarization analysis, and MACS provides the highest polarized cold neutron flux with the largest scattering coverage for polarization analysis. During

FIGURE 4: The ^{3}He team and SURF student Hannah Burrall are testing a new polarizer for the intensity modulated neutron spin echo spectroscopy. In the picture Hannah is holding the compact ^{3}He polarizer that is inserted into the vacuum tube.

the past year, the NCNR's spin filter program serviced 24 user experiments, for a total of 79 days of beam time, 191 bar-liters of polarized ^{3}He gas, and 140 polarized ^{3}He cells.

For MACS, our focus has been on deploying infrastructure toward a routine, high flux wide angle polarization analysis capability and on expanding the capability to a wider incident energy range. Collaboration with the Sample Environment team has led to the development of a new cryostat dedicated for polarized MACS beam experiments that makes use of the horseshoe cell developed earlier for improvement of polarized neutronic performance and reliable operation.

For CANDOR, the ^{3}He team has designed and optimized a magnetically shielded solenoid to maintain the ^{3}He polarization on CANDOR. A nuclear magnetic resonance system is seamlessly integrated into CANDOR's data acquisition systems for all polarized beam experiments. A radio-frequency flipper was modeled, designed, and characterized to provide a large cross-sectional incident beam on CANDOR with one of the highest flipping efficiencies (better than 99.9 %).

For NSE, the ^{3}He team is exploring a new measurement capability, intensity modulated neutron spin echo (IMNSE) spectroscopy. IMNSE was demonstrated for applications in magnetic samples at ILL approximately 30 years ago, but never for soft matter applications. In a standard NSE setup, spectrometers are unable to separate coherent and spin incoherent nuclear scattering. IMNSE allows the separation of these NSE signals. Collective dynamics and single particle dynamics for chain-chain correlations in lipids, diffusion of gases within porous materials, and dynamics at the pre-peak of glass-forming liquids are some of the science that can be studied using IMNSE. A very compact ^{3}He polarizer and analyzer are being developed to fit into the limited space near the sample on NSE, and several ^{3}He NSE cells are being fabricated.

For BT-7, the ^{3}He team has developed a new ^{3}He polarizer that has yielded an improvement of the relaxation time of the ^{3}He polarization by a factor of 2.5. This has allowed polarized beam experiments on BT-7 to operate for 2 days without swapping the cells and a significant improvement in the time-averaged neutron polarization and transmission for user experiments. The University of Maryland and the ^{3}He team at the NCNR have made substantial progress in developing a compact CRYOPAD device for studies of complex magnetic structures and excitations.

Data Acquisition Software

The New Instrument Control Environment (NICE) is a Java-based data acquisition package that incorporates a highly versatile scripting capability to enable end user adaptations to be coded under all the major scientific programming languages. This year, much of the effort has focused on the two instruments in development, VSANS and CANDOR. NICE is currently operating the VSANS instrument full time, including external user experiments. The user interface has been streamlined to better support VSANS specific functionality. Support has been added for the high-resolution detector, and Nexus-compliant VSANS files are written and can be reduced and analyzed by the Igor-based data reduction software. In addition, event mode data can be collected and reduced as planned.

For CANDOR, nearly all of the NICE module has been written. NICE is able to operate all of the instrument that has currently been installed. Components that are in the process of installation are currently simulated and can be controlled as if they were present.

New features have been added to NICE to improve upon how the users can interact with instruments. A “trajectory wizard” is now available and in use on all reflectometers, including CANDOR. The wizard is a new system for setting up generalized reflectometry experiments where a user can create an entire series of measurements by entering a few pieces of information about their sample and the type of measurement they wish to perform. Also, a custom commands GUI feature has been added that makes command line features available visually in an interface which is customizable by instrument scientists. This allows new users to quickly use advanced features in NICE.

Data Analysis Software

Funded jointly by the NSF and EPSRC, the CCP-SAS project is focused on developing an easy-to-use open-source modeling package that enables users to generate physically accurate atomistic models, calculate scattering profiles and compare results to experimental scattering data sets in a single web-based software suite. SASSIE-web is available to the international scattering community. Workshop and training sessions at scattering centers and scientific meetings have expanded outreach and impact. SASSIE-web instances have been implemented on several domestic and international high-performance supercomputing centers. To date, over forty-eight manuscripts using our software products on a variety of structural biology and soft-matter problems have been published. With over six hundred registered users, the goals of the next year are to extend and enhance the user experience and work on providing stand-alone versions of the software.

FIGURE 5: The integrated polarized MACS setup with the newly developed dedicated cryostat is being tested for safe and reliable operation and performance evaluation on MACS.

Serving the Science and Technology Community

The mission of the NIST Center for Neutron Research is to assure the availability of neutron measurement capabilities to meet the needs of U.S. researchers from industry, academia and other U.S. government agencies. To carry out this mission, the NCNR uses several different mechanisms to work with participants from outside NIST, including a competitive proposal process, instrument partnerships, and collaborative research with NIST.

Proposal System

Most of the beam time on NCNR instruments is made available through a competitive, peer-review CHRNS proposal process. The NCNR issues calls for proposals approximately twice a year. Proposals are reviewed at several different levels. First, expert external referees evaluate each proposal on merit and provide us with written comments and ratings. This is a very thorough process where several different referees review each proposal. Second, the proposals are evaluated on technical feasibility and safety by NCNR staff. Third, we convene our Beam Time Allocation Committee (BTAC) to assess the reviews and to allocate the available instrument time. Using the results of the external peer review and their own judgment, the BTAC makes recommendations to the NCNR Director on the amount of beam time to allocate to each approved experiment. Approved experiments are scheduled by NCNR staff members in consultation with the experimenters.

The current BTAC members are:

- Pinar Akcora (Stevens Institute of Technology)
- Andrew Allen (NIST Materials Measurement Division)
- Jeffrey Allen (Michigan Technological University)
- Collin Broholm (The Johns Hopkins University)
- Leslie Butler (Louisiana State University)
- Mark Dadmun (University of Tennessee)
- Thomas Epps (University of Delaware)
- Kushol Gupta (University of Pennsylvania)
- Hubert King (ExxonMobil)
- Valery Kiryukhin (Rutgers University)
- Ramanan Krishnamoorti (University of Houston)
- Jennifer Lee (National Institutes of Health)
- Raul Lobo (University of Delaware)
- Steven May (Drexel University)
- Martin Mourigal (Georgia Institute of Technology)
- Lilo Pozzo (University of Washington)

Partnerships

The NCNR may form partnerships with other institutions to fund the development and operation of selected instruments. Partnerships are negotiated for a fixed period and may be renewed if there is mutual interest and a continued need. These partnerships have proven to be an important and effective way to expand the research community's access to NCNR capabilities.

Collaboration with NIST

Some time on all instruments is available to NIST staff in support of our mission. This time is used to work on NIST research needs, instrument development, and promoting the widespread use of neutron measurements in important research areas, particularly by new users. As a result of these objectives, a significant fraction of the time available to NIST staff is used collaboratively by external users, who often take the lead in the research. Access through such collaborations is managed through written beam time requests. In contrast to proposals, beam time requests are reviewed and approved internally by NCNR staff. We encourage users interested in exploring collaborative research opportunities to contact an appropriate NCNR staff member.

Research Participation and Productivity

The NCNR continued its strong record of serving the U.S. research community this year. Over the 2018 reporting year, the NCNR served 2742 researchers. (Research participants include users who come to the NCNR to use the facility as well as active collaborators, including co-proposers of approved experiments, and co-authors of publications resulting from work performed at the NCNR.)

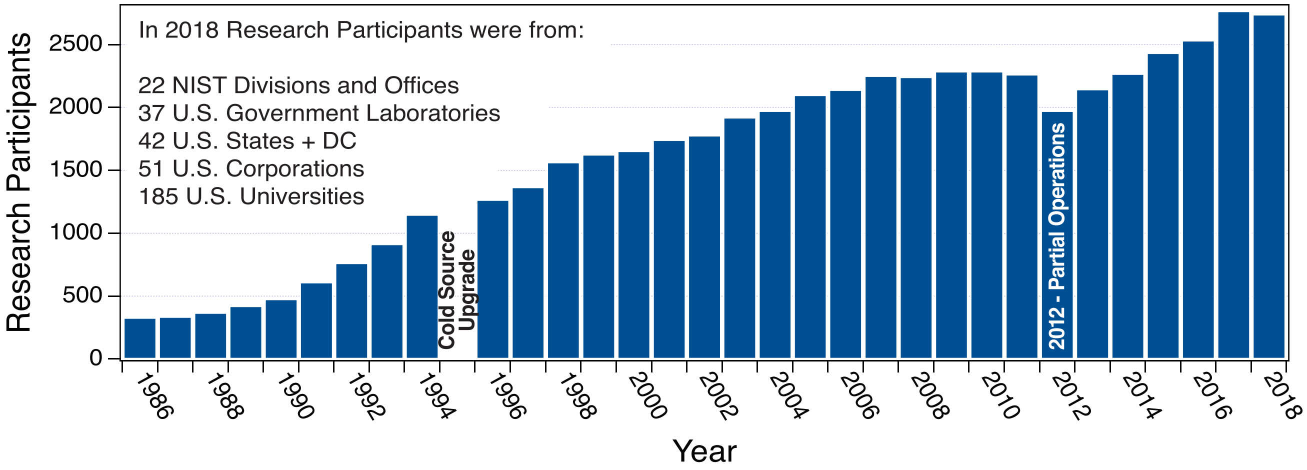

FIGURE 1: Research participants at the NCNR from 1986 - 2018.

2018 NCNR Proposal Program

In response to the last two calls for proposals for instrument time, we received 817 proposals, of which 373 were approved and received beam time. The following table shows the statistics for several instrument classes. The oversubscription, i.e., the ratio of days requested on all proposals to the days available, was 2.5 on average.

Instrument class	Proposals	Days requested	Days allocated
SANS and USANS	322	1111	421
Reflectometers	114	819	316
Spectrometers	324	2184	796
Diffraction	33	91	66
Imaging	24	130	102
Total	**817**	**4335**	**1701**

Users Group

The NCNR Users Group (NUG) provides an independent forum for all facility users to raise issues to NCNR management, working through its executive officers to carry out this function. The members of the NUG Executive Committee for 2018 are Megan Robertson (University of Houston), Michael Crawford (University of Delaware), Julie Hipp (University of Delaware, student/postdoc member), Carlos López-Barrón (ExxonMobil), Dmitry Reznik (University of Colorado), Rafael Verduzco (Rice University), and Igor Zaliznyak (Brookhaven National Laboratory).

Beginning this year, the NUG now regularly solicits user feedback via an email survey form that is sent to users approximately one week after the completion of their experiment. Issues identified by the NUG executive committee are regularly discussed with the NCNR and CHRNS management teams with a focus on resolving those requiring immediate action. The NUG also conducted a comprehensive user survey in the fall of 2015. There were more than 450 responses the majority of whom are CHRNS users. Overall the results, which are posted on the NUG website (www.indiana.edu/~lens/nug/nug.php), showed improvement relative to those from 2011 in 5 of the 6 general categories. Working closely with NUG, the NCNR and CHRNS management teams developed a comprehensive response/action plan designed to make the user experience more productive and enjoyable (Refer to ncnr.nist.gov/news/Response_to_survey_FINAL_19jul2016.pdf).

Panel of Assessment

The major organizational components of NIST are evaluated annually for quality and effectiveness by the National Research Council (NRC), the principal operating agency of both the National Academy of Sciences and the National Academy of Engineering. A panel appointed by the NRC convened at the NCNR on July 10-12, 2018. The panel members included Tom C. Lubensky (University of Pennsylvania, chair), Simon Billinge (Columbia University), Susan Coppersmith (University of Wisconsin, Madison), Aaron Eberle (ExxonMobil Chemical Company), Paul Fleury (Yale University), Dale Klein (University of Texas), Tonya Kuhl (University of California, Davis), Peter Moore (Yale University) and Thomas Russell (University of Massachusetts, Amherst). Their findings are summarized in a report published in December 2018. The report entitled "An Assessment of the National Institute of Standards and Technology Center for Neutron Research: Fiscal Year 2018" is available at https://www.nap.edu/catalog/25282/an-assessment-of-the-center-for-neutron-research-at-the-national-institute-of-standards-and-technology. A new panel is expected to convene at the NCNR in 2021.

The Center for High Resolution Neutron Scattering (CHRNS)

CHRNS is a national user facility that is jointly funded by the National Science Foundation and the NCNR. Its primary goal is to maximize access to state-of-the-art neutron scattering instrumentation for the research community. It currently operates six neutron scattering instruments at the NCNR, enabling users from around the nation to observe dynamical phenomena involving energies from ≈ 30 neV to ≈ 10 meV, and to obtain structural information on length scales from ≈ 1 nm to ≈ 10 μm. A more detailed account of CHRNS activities may be found on p. 62 of this report.

Partnerships for Specific Instruments

NG-7 SANS Consortium

A consortium that includes NIST, the ExxonMobil Research and Engineering Company, and the Industrial Partnership for Research in Interfacial and Materials Engineering (IPRIME) led by the University of Minnesota, operates, maintains, and conducts research at the 30m SANS instrument located on NG-7. Twenty-five percent of the beam time on this instrument is allocated to the general scientific community through the NCNR's proposal system. Consortium members conduct independent research programs primarily in the area of large-scale structure in soft matter. For example, ExxonMobil has used this instrument to deepen their understanding of the underlying nature of ExxonMobil's products and processes, especially in the fields of polymers, complex fluids, and petroleum mixtures.

The nSoft Consortium

Formed in August 2012, the nSoft Consortium allows member companies to participate with NIST in the development of advanced measurements of materials and manufacturing processes and develop their own expertise in state-of-the-art measurement technologies to include in their analytical research programs. nSoft develops new neutron-based measurement science for manufacturers of soft materials including plastics, composites, protein solutions, surfactants, and colloidal fluids. Members receive access to leading expertise and training support in neutron technology and soft materials science at NIST. Contact: Ron Jones, nSoft Director, rljones@nist.gov, 301-975-4624.

NIST / General Motors – Neutron Imaging

An ongoing partnership and collaboration between General Motors and NIST, which also includes Honda Motors through GM's partnership with Honda, continues to yield exciting results using neutron imaging. Neutron imaging has been employed to visualize the operation of fuel cells for automotive vehicle applications. Neutron imaging is an ideal method for visualizing hydrogen, the fuel of electric vehicle engines. These unique, fundamental measurements provide valuable material characterizations that will help improve the performance, increase the reliability, and reduce the time to market introduction of the next generation electric car engines. 25 % of the time on the BT-2 Neutron Imaging Facility is made available to the general scientific community through peer-reviewed proposals.

Interagency Collaborations

The Smithsonian Institution's Nuclear Laboratory for Archaeological Research is part of the Anthropology Department at the National Museum of Natural History. It has had a longstanding and productive partnership with the NCNR, during which time it has chemically analyzed over 43,100 archaeological artifacts by Instrumental Neutron Activation Analysis (INAA), drawing extensively on the collections of the Smithsonian, as well as on those of many other institutions in this country and abroad. Such chemical analyses provide a means of linking these diverse collections together in order to study continuity and change involved in the production of ceramic and other artifacts.

The Center for Food Safety and Applied Nutrition, U.S. Food and Drug Administration (FDA), maintains laboratory facilities at the NCNR providing agency-wide analytical support for food safety and food defense programs. Neutron activation and low-level gamma-ray detection techniques yield multi-element and radiological information about foods and related materials and provide a metrological foundation for FDA's field investigations and for radiological emergency response planning.

The Center for High Resolution Neutron Scattering (CHRNS)

The Center for High Resolution Neutron Scattering is a national user facility that is jointly funded by the National Science Foundation through its Division of Materials Research (grant number DMR-1508249) and by NIST. The CHRNS agreement was renewed for five years beginning on September 1, 2015. The primary purpose of this partnership is to maximize access for the scientific community to transformative neutron scattering instrumentation. The core mission of CHRNS is fourfold: (i) to develop and operate neutron scattering instrumentation, with broad application in materials research, for use by the general scientific community; (ii) to promote the effective use of the CHRNS instruments by having an identifiable staff whose primary function is to assist users; (iii) to conduct research that advances the capabilities and utilization of CHRNS facilities; and (iv) to contribute to the development of human resources through educational and outreach efforts. The scientific community provides essential input for new directions for CHRNS through a variety of mechanisms including post-experiment feedback and user surveys, the most recent of which was administered by the NCNR User Group (NUG) in the fall of 2015. The NUG Executive Committee also led a discussion for neutron users at the recent American Conference on Neutron Scattering (ACNS) held on June 24-28, 2018 in College Park, MD. A 2 ½ minute video, Getting Great Data with CHRNS, highlights and summarizes CHRNS' focus on advancing neutron scattering measurement capabilities and its prominent role in expanding, educating, and diversifying the community of researchers who use neutron methods. View the video on the NCNR website at https://www.ncnr.nist.gov/staff/dimeo/CHRNS_Animation_Final.mp4.

Scattering Instruments

The portfolio of instruments supported by CHRNS continues to evolve to ensure that the scientific capabilities exceed or are comparable to the best worldwide. Combined, CHRNS instruments can provide structural information on a length scale of ≈ 1 nm to ≈ 10 µm, and dynamical information on energy scales from ≈ 30 neV to ≈ 10 meV. During FY 2018 CHRNS continued to support operation of the High Flux Backscattering Spectrometer (HFBS), the Neutron Spin-Echo (NSE) spectrometer, and the Multi-Angle Crystal Spectrometer (MACS), which boasts the world's highest monochromatic cold-neutron flux and is now the premier instrument in the world for investigations of quantum magnetism. During the past year the instrument computer and drivers for the data acquisition on HFBS were upgraded to enhance reliability. In addition, event-mode data collection capabilities were developed and tested on MACS to facilitate time-dependence measurements. A new sample post was installed in the 10 T magnet to expand the accessible temperature range (> 40 K) for field-dependent MACS experiments. On NSE routine tuning and maintenance operations have continued. Preliminary tests and feasibility studies for the implementation of a modulated intensity option using ^{3}He cells have been undertaken with promising initial results.

Significant additions to the CHRNS facility include two innovative instruments, Very Small Angle Neutron Scattering (VSANS) instrument and Chromatic Analysis Neutron Diffractometer or Reflectometer (CANDOR). These instruments are currently being commissioned and installed, respectively, while the NG-B 30m Small Angle Neutron Scattering (SANS) instrument and the Ultra-Small Angle Neutron Scattering (USANS) instrument are simultaneously being phased out of the CHRNS suite. The versatile VSANS instrument is now functional and has many capabilities that match or exceed those of the NG-B 30m SANS. In parallel with user experiments, commissioning continues with the installation and testing of additional components. The apertures for the converging beam configuration and shielding of the pre-sample vessel were installed in the spring. The graphite monochromator, prisms for gravitational correction, and lenses for beam focusing were added and are now available. The third detector bank, with the high precision, scintillation detector, enabling the full Q range down to 0.0002 Å^{-1}, was recently installed and is currently being tested. With the addition of this detector, VSANS will cover extensive nano-to-meso length scales in a single measurement, eliminating the need for combined experiments on USANS and SANS in many cases. Time on the VSANS instrument has been offered in the last two calls for proposals and many successful experiments have been completed.

Since most components of the primary CANDOR instrument have arrived, installation is advanced despite delays introduced by detector design modifications involving cryogenic cooling of the analyzer crystals to reduce background and by the failure of a contractor to deliver electronic components of the detector system. The scintillation detectors are being tested, and the software for data acquisition and data reduction is also being tested. First neutrons are expected in the first quarter of 2019. We project that CANDOR will be included in the second call for proposals in 2019. When operational, CANDOR will be the only instrument of this type in the world with data rates provided by the multiplex detector that exceed those available elsewhere in the world by perhaps an order of magnitude or more.

FIGURE 1: VSANS staff, Cedric Gagnon, Elizabeth Kelley, Grethe Jensen and Yun Liu, in front of their new instrument.

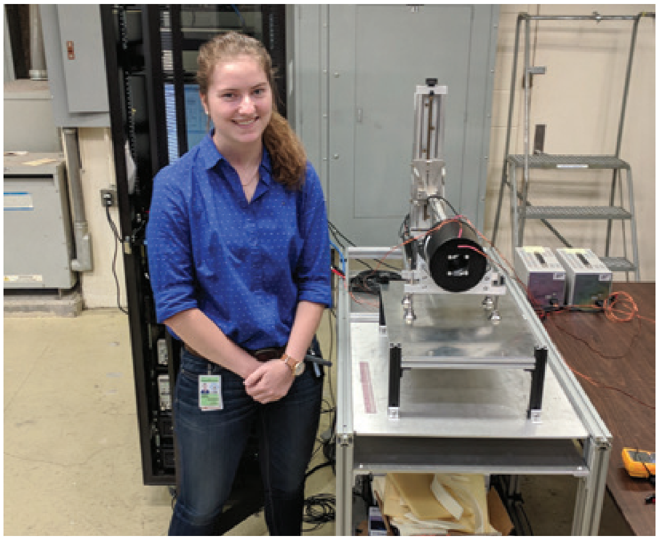

FIGURE 2: SURF student Hannah Burrall tests the new solenoid for NSE.

Research

The wide ranges of instrument capabilities available in CHRNS support a very diverse scientific program, allowing researchers in materials science, chemistry, biology, geosciences, and condensed matter physics to investigate materials such as polymers, metals, ceramics, magnetic materials, colloids, fluids and gels, rocks, and biological molecules. The research community can obtain access to the state-of-the-art CHRNS instrumentation using the NCNR's proposal system. Proposals to use the CHRNS instruments are critically reviewed on the basis of scientific merit and/or technological importance. In the previous Call for Proposals (call 37), 301 proposals requested CHRNS instruments, and 167 of these proposals received beam time. Of the 1394 days requested for the CHRNS instruments, 517 were awarded. Roughly half of the users of neutron scattering techniques at the NCNR employ CHRNS-funded instruments, and approximately one third of NCNR publications (see the "Publications" section on p. 70), over the current one-year period, are based on research performed using these instruments. This report contains several highlights of CHRNS publications. See the labeled highlights in the table of contents.

Scientific Support

CHRNS provides scientific support in three critical areas: sample environment, chemical laboratories and the production and delivery of polarized neutron beams. The accomplishments in each of these areas during FY 2018 are summarized below.

The laboratory staff continues to equip and maintain user laboratories and routinely assists users with sample preparations. The staff ensures that users have the tools, supplies and training they need for a successful experiment. In FY 2018 the Guide Hall Laboratory became available to users, providing CHRNS users an easily accessible laboratory to handle slightly activated materials.

The CHRNS Sample Environment team provides users with the equipment and training needed to make neutron measurements under external conditions of temperature, pressure, magnetic field, humidity, and fluid flow. CHRNS users have access to a variety of flow systems, rheometers, gas-loading systems, two superconducting magnets with fields of up to 11 Tesla, a new leak detector, and other

FIGURE 3: Participants and instructors in the 2018 CHRNS Summer School "Methods and Applications of Small Angle Neutron Scattering and Neutron Reflectivity."

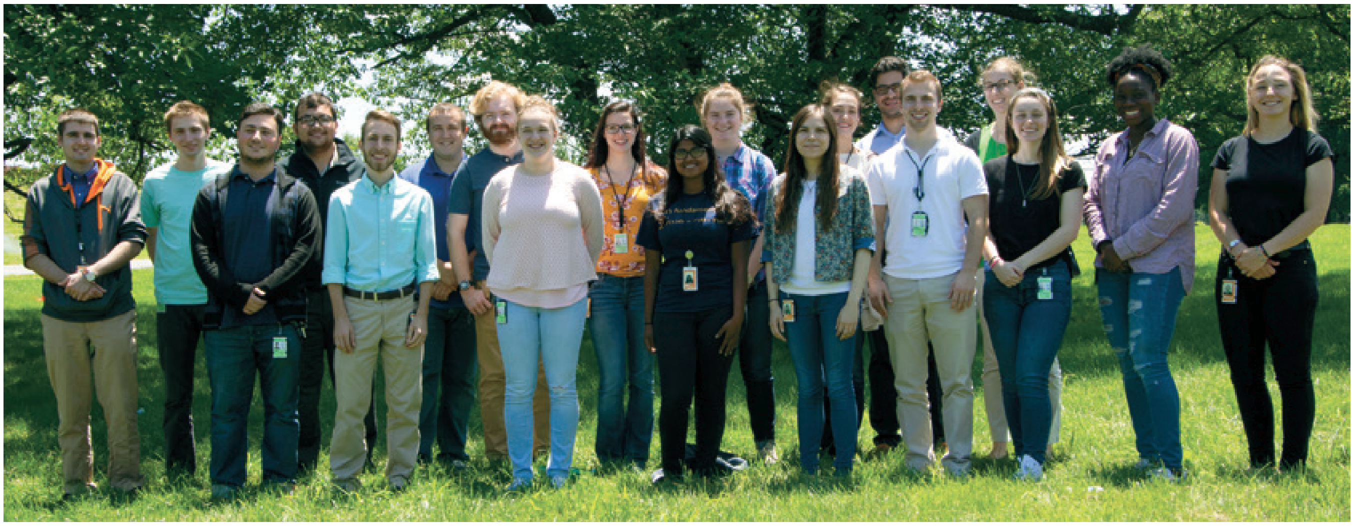

FIGURE 4: The 2018 SURF students.

complex equipment to control parameters such as pressure, humidity, and electric fields. During FY 2018 the team set up and operated a diverse range of complex sample environment equipment for more than 170 experiments. This total includes 42 experiments involving rheometers and shear cells, and 19 experiments that required access to mK temperatures, 12 of which simultaneously required magnetic fields up to 11.5 T. In addition, CHRNS has commissioned a new orange cryostat with a specially designed tail that is fully compatible with the use of ^{3}He spin filters on MACS. With complementary capabilities provided by a dedicated closed cycle refrigerator, MACS users regularly perform polarization experiments from the mK regime to room temperature. A new cylindrical silicon tailpiece (made from a single boule of silicon in lieu of aluminum) has been developed for use on closed cycle refrigerators in conjunction with a SANS electromagnet. The tailpiece allows for sample rotation in applied magnetic fields and reduces the background substantially. Improvements to the Liquid Injection Pressure System (LIPS) provide greater stability of pressures up to 400 MPa, and better temperature control in the range -20 °C $\leq T \leq$ 100 °C. LIPSS was used for 7 experiments on the CHRNS NG-B 30m SANS during FY 2018 and is available for usage on any upcoming SANS or USANS investigations.

CHRNS also enables polarized neutron scattering experiments on MACS and SANS instruments by providing of record-breaking ^{3}He spin analyzer cells with specialized geometries. During FY 2018, the ^{3}He Spin Filter team served a range of user experiments on both MACS and SANS. It is notable that CHRNS runs the only SANS program in the U.S. that routinely operates with full polarization analysis, and spin polarization and analysis will soon be available on VSANS following the recent installation of the guide field and RF flipper. The ^{3}He team focused on deploying infrastructure toward a routine, high flux wide angle polarization analysis capability on MACS and on expanding the capability to a wider incident energy range. MACS now provides the largest scattering angle coverage for polarization analysis.

For NSE, the ^{3}He team is exploring a new measurement capability, intensity modulated neutron spin echo (IMNSE) spectroscopy. IMNSE was demonstrated for applications in magnetic samples at ILL about 30 years ago, but never for soft matter applications. The IMNSE technique allows the separation of coherent and spin incoherent nuclear scattering, which is not possible in the standard NSE setup. Hence collective dynamics and signal particle dynamics can be simultaneously investigated for chain-chain correlations in lipids, diffusion of gases within porous materials, dynamics at the prepeak of glass-forming liquids. A very compact ^{3}He polarizer and analyzer are being developed to fit into the limited space near the sample on NSE, and several compatible ^{3}He NSE cells are currently being fabricated.

In the future, CANDOR will produce spin-polarized incident beams using a double-V supermirror polarizer (efficiency of > 95 %), along with an RF spin flipper (efficiency of 99.5 %) and will be spin-analyzed by a ^{3}He spin filter. The ^{3}He team has designed and optimized a magnetically shielded solenoid to maintain the ^{3}He polarization on CANDOR. The team has also developed a ^{3}He nuclear magnetic resonance system that is able to be seamlessly integrated into CANDOR's data acquisition systems for all polarized beam experiments. The ^{3}He team has modelled, designed, and characterized a radio-frequency flipper to flip a large cross-sectional incident beam on CANDOR with one of the highest flipping efficiencies (better than 99.9 %).

Education and Outreach

CHRNS sponsored a variety of educational programs and activities tailored to specific age groups and professions. The twenty-fourth annual summer school, held on June 19-23, 2018 was entitled "Methods and Applications of Small Angle Neutron

FIGURE 5: The 2018 SHIP interns.

Scattering and Neutron Reflectivity." Forty-two graduate and postdoctoral students from 32 universities and five industrial researchers participated in the school. Guest lecturers were Dr. Ingrid Hallsteinsen from the Advanced Light Source, Prof. Alexis Navarre-Sitchler from the Colorado School of Mines, and Dr. Ron Jones, Director of the nSoft consortium.

CHRNS co-sponsored several other workshops throughout the year including the second Fundamentals of Quantum Materials Winter school at the University of Maryland (January 8-11, 2018), the fifth Neutron Day at the University of Delaware (November 8, 2017) and the second biennial International Society for Sample Environment training course at NIST (November 13-17, 2017).

CHRNS staff scientists participated in teaching courses at nearby universities including the University of Maryland and University of Delaware. Some of the courses involve scattering lab practicals performed at the NCNR using CHRNS instruments. In the fall of 2017, Yun Liu (CHRNS staff member) and Yimin Mao were co-lecturers for an advanced graduate course entitled "Advanced Characterization of Soft Matter" at the University of Maryland. The course focused on both theories and experimental works of studying structure and dynamics of soft matter materials using scattering techniques (light, X-ray and neutron scattering). During that same semester, Boualem Hammouda taught an Honors Seminars Course entitled "Science in Current Events" at the University of Maryland for freshmen and sophomores.

As part of its expanding education and outreach effort, CHRNS offers to university-based research groups with BTAC-approved experimental proposals the opportunity to request travel support for an additional graduate student to participate in the experiment. This support is intended to enable prospective thesis students, for example, to acquire first-hand experience with a technique that they may later use in their own research. Announcements of this program are sent to all of the university groups whose experimental proposals receive beam time from the BTAC. Recipients of the announcement are encouraged to consider graduate students from under-represented groups for this opportunity. The program is also advertised on the NCNR's website at https://www.nist.gov/ncnr/arrange-visit-ncnr/financial-assistance#graduate.

As in previous years, CHRNS participated in NIST's Summer Undergraduate Research Fellowship (SURF) program. In 2018 CHRNS hosted 19 SURF students, including seven returning interns, one of whom previously participated in the SHIP program. The students participated in research projects such as exploration of the rheological properties of dense lipid vesicle solutions, characterization of adjuvant-protein interactions in vaccines, fabrication of crosslinked silica-based nanoporous networks, Monte-Carlo exploration of focused

FIGURE 6: Scott Hanna (center) from Winston Churchill High School works with mentors Richard Azuah (left) and Tim Prisk (right) on a DCS measurement.

neutron guide geometries, development of a virtual training simulator for reactor operators using a HoloLens technology. They presented their work at the NIST SURF colloquium in early August 2018 in sessions moderated by program officers from the National Science Foundation. The colloquium also featured an invited talk by Paul Neves from the University of Maryland on SANS characterization of skyrmions in chemically-substituted Cu_2OSeO_3. It is notable that Mr. Neves recently received a scholarship from the Barry Goldwater Foundation, in part, for his CHRNS SURF research, which he described in a recent NIST blog (https://www.nist.gov/blogs/taking-measure/surfing-susceptometers-skyrmions-making-neutron-maniac).

CHRNS initiated a Research Experiences for Teachers (RET) program in 2010. For the summer of 2018, the program hosted two teachers from Montgomery County, MD. Scott Hanna from Winston Churchill High School studied the microscopic dynamics of liquid and solid hydrogen using DCS under the guidance of Tim Prisk and Richard Azuah. Munna Chakrabarti from Watkins Mill High School investigated the rheological properties on an insulin analogue using SANS with mentor Grethe Jensen. Both Mr. Hanna and Dr. Chakrabarti highlighted their research in oral presentations in August.

Elementary, Middle, and High School Activities

The Summer High School Intern Program (SHIP) is a very successful, competitive NIST-wide program for students who are interested in performing scientific research during the summer. CHRNS hosted seven interns from local high schools. The students studied the environmental factors that contribute to glass aging and alteration, explored segmentation techniques for analysis of neutron images of meteorites, developed reinforcement learning algorithms for efficiently obtaining crystallographic measurements, and automated a slit rheometer for SANS and a neutron spin flipper. The results of the students' summer investigations were highlighted in a NIST-wide poster session, as well as in a well-attended symposium at the NCNR. Isabella DeClue from Montgomery Blair High School was honored to receive a 2nd place poster award from NIST's chapter of Sigma Xi.

A large number of specialized tours for middle school, high school, and university students were also offered throughout the year. At local schools CHRNS staff members also give science-based talks or lead hands-on demonstrations at local schools, participate in STEM events, and even volunteer as robotics coaches.

2018 Awards

Dr. **Kate A. Ross**, Assistant Professor, Department of Physics of Colorado State University is the winner of the 2018 **Lee Osheroff Richardson Science Prize** for North and South America. Kate is recognized for her research towards elucidation of exotic magnetic ground states and ground state selection in quantum frustrated magnets, using neutron scattering techniques at low temperatures and in high magnetic fields. Kate is a user of NCNR facilities and is the author of an article in NIST's "Taking Measure" blog.

Rebecca Dally of the University of California, Santa Barbara was awarded the American Physical Society's **GMAG Dissertation Award** for her work exploring magnetism in a series of transition metal oxides with intertwined spin and orbital degrees of freedom. The award carries with it a cash prize as well as an invited talk at the annual March Meeting of the American Physical Society in Los Angeles in 2018. Rebecca did much of her research at the NCNR. She has recently joined the NCNR as a post-doctoral researcher.

University of Maryland graduate student **Stephanie Gnewuch** won the **Margaret C. Etter Student Lecture Award** in Neutron Scattering at the American Crystallographic Association National meeting for her work on the synthesis and characterization of transition metal phosphates. The award was presented at the ACA meeting in Toronto, July 2018. Stephanie is a frequent user of the NCNR. She also was an SURF student during her undergraduate studies.

Yuyin Xi was selected for the **Graduate Excellence Award** in polymer science from the American Chemical Society at their meeting in San Francisco, CA. Yuyin is currently a post-doctoral researcher at the NCNR.

Thomas Gnäupel-Herold is a recipient of the 2018 **Henry Marion Howe Medal** by ASM International. The Henry Marion Howe Medal, established in 1923, honors the authors whose paper has been selected as the best of those published in Metallurgical Transactions. Thomas and his coauthors, Eric A. Lass, Mark R. Stoudt, Maureen E. Williams, Michael B. Katz, Lyle E. Levine, Thien Q. Phan, and Daniel S. Ng, (all from NIST) were recognized for their article entitled "Formation of the Ni_3Nb δ-Phase in Stress-Relieved Inconel 625 Produced via Laser Powder-Bed Fusion Additive Manufacturing."

Paul Neves, an undergraduate at the University of Maryland, was awarded a **Barry Goldwater Scholarship**, which encourages students to pursue advanced study and careers in the sciences, engineering and mathematics. Paul also received a **best poster award** for his sample environment development work at the 9th International Workshop on Sample Environment at Scattering Facilities. Paul has spent several years working at the NCNR both as a SURF student and during the school year.

Prof. **Norm Wagner** from the University of Delaware (and long-time user and associate of the NCNR) received the 2018 **Sustained Research Prize** by the Neutron Scattering Society of America for his "seminal and sustained contributions to our understanding of soft condensed matter physics using neutron scattering."

Dmitry Pushin from the University of Waterloo (and long-time user and associate of the NCNR & PML) received the 2018 **Science Prize** from the Neutron Scattering Society of America for the "invention and application, in particular to neutron holography, of the five blade, decoherence-free interferometer."

Bradley D. Olsen, Associate Professor in the Department of Chemical Engineering at MIT, has been awarded the 2018 **John H. Dillon Medal** from the American Physical Society, "for significantly expanding our understanding of the physics of polymers, including the self-assembly of block copolymers incorporating a fully folded protein, the influence of polymer shape on diffusion; for engineering novel gels; and for updating the theory of the modulus of a network." Brad's research makes extensive use of NCNR facilities.

University of Minnesota Regents Professor **Timothy Lodge** has received the 2018 **Paul J. Flory Polymer Education Award** from the American Chemical Society (ACS) Division of Polymer Chemistry, honored for his outstanding achievements in promoting undergraduate and graduate polymer education. He has mentored more than 160 undergraduate and graduate students in his research laboratory and taught more than 30 undergraduate and graduate courses in polymer science. Tim is also a long-time user of the NCNR.

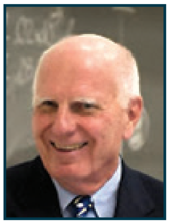

Prof. **Sam Werner** (long-time user and associate of the NCNR & PML) received the **Clifford G. Shull Prize in Neutron Science** by the Neutron Scattering Society of America. This prize is to recognize outstanding research in neutron science and leadership promoting the North American neutron scattering community. Sam is recognized for his contributions to the "observation of the fundamental quantum-mechanical nature of spins through the effects of rotation and the gravitational field, using neutron interferometry, including the observation of the Aharonov- Casher effect, for his extensive work with neutron scattering on the magnetic properties of transition metals and their alloys, for his critical role in the NSSA, particularly as its Founding President, and for his wide and lasting influence on the neutron community, including nurturing of many neutron scientists."

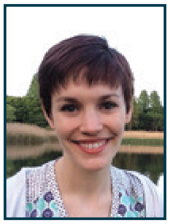

Alannah Hallas, from Rice University, received the 2018 **Prize for Outstanding Student Research** from the Neutron Scattering Society of America for her "exploration of new families of quantum pyrochlore magnets and elucidating their phase behavior and excitations using forefront neutron scattering techniques." Much of her award-winning research was performed at the NCNR.

Michael Hore, Assistant Professor of Macromolecular Science and Engineering and former NCNR post-doc, has received a **Young Investigator Award** from the American Chemical Society's Polymer Materials Science and Engineering Division (PMSE). This award recognizes scientists who have made significant contributions to their fields within polymer science and engineering. See an article describing some of his work on page 38 of this report.

Wesley Fuhrman, a graduate student in the physics department at Johns Hopkins University and a frequent NCNR user, was recognized as a **Schmidt Science Fellow** for his outstanding research into topological insulators. The fellowship, which is endowed by former Google CEO Eric Schmidt, includes a $100,000 award. See an article describing some of his work on page 20 of this report.

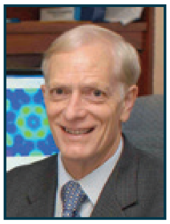

Jeff Lynn, NIST Fellow, will receive the **Albert Nelson Marquis Lifetime Achievement Award** by Marquis Who's Who, as announced in the Chicago Evening Post.

Scott Dewey of the PML was named an **American Physical Society Fellow** in recognition of "absolute measurements in neutron physics and ultra-high-resolution gamma spectroscopy."

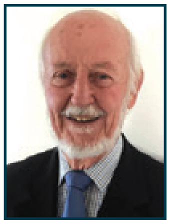

Dr. **Rolf L. Zeisler** was selected to receive the 2018 **Hevesy Medal Award** in recognition of his work for the development and application of nuclear analytical methods to biosciences as well as environmental studies, and for the promotion of certified reference materials at the highest level of metrological science. Unfortunately, Rolf passed away before he could accept this award.

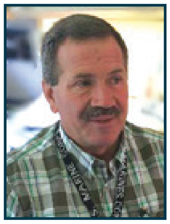

NCNR's **Don Pierce** received the 2018 **Sigma Xi Award for Outstanding Service** in Support of NIST Scientists. Don was recognized for his outstanding contributions to the development of neutron instruments at NIST and his sustained high-level service to NIST and NIST scientists.

Pat Connelly of the NCNR won the **Eugene Casson Crittenden Award** "for exceptional service to the NCNR user community, instrument scientists, and NIST laboratories that enables precision neutron measurement programs." Pat is an engineering technician who works behind the scenes in the NCNR's machine shop.

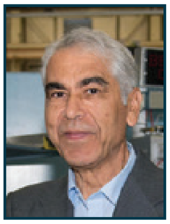

The NCNR's **Boualem Hammouda** won the **Department of Commerce Bronze Medal** "for development of the expansive SANS Toolbox, which has benefitted many hundreds of NCNR facility users and is freely available via the web."

Hui Wu of the NCNR won the **Department of Commerce Bronze Medal** "for producing an entirely new route to synthesizing hydrogen storage materials for fuel cells based on the complex chemistry of amines and boranes." Hui is an instrument scientist on the NCNR's powder diffractometer.

PML's **Eli Baltic** is a **Eugene Casson Crittenden Award** winner for "technical excellence and leadership in the development and operation of NIST neutron imaging facilities and advancing core metrology programs."

Publications: August 1, 2017 to July 31, 2018

Ahadi, K., Gui, Z., Porter, Z., Lynn, J.W., Xu, Z., Wilson, S.D., Janotti, A., Stemmer, S., "Carrier Density Control of Magnetism and Berry Phases in Doped $EuTiO_3$," APL Materials **6**(5), 056105 (2018).

Alam, K., Disseler, S.M., Ratcliff, W.D., Borchers, J.A., Ponce-Pérez, R., Cocoletzi, G.H., Takeuchi, N., Foley, A., Richard, A., Ingram, D.C., Smith, A.R., "Structural and Magnetic Phase Transitions in Chromium Nitride Thin Films Grown by rf Nitrogen Plasma Molecular Beam Epitaxy," Phys. Rev. B **96**(10), 104433 (2017).

Amon, A., Svanidze, E., Cardoso-Gil, R., Wilson, M.N., Rosner, H., Bobnar, M., Schnelle, W., Lynn, J.W., Gumeniuk, R., Hennig, C., Luke, G.M., Borrmann, H., Leithe-Jasper, A., Grin, Y., "Noncentrosymmetric Superconductor BeAu," Phys. Rev. B **97**(1), 014501 (2018).

Anovitz, L.M., Freiburg, J.T., Wasbrough, M., Mildner, D.F.R., Littrell, K.C., Pipich, V., Ilavsky, J., "The Effects of Burial Diagenesis on Multiscale Porosity in the St. Peter Sandstone: An Imaging, Small-Angle, and Ultra-Small-Angle Neutron Scattering Analysis," Mar. Petrol. Geol. **92**, 352 (2018). [CHRNS]

Asgari, M., Jawahery, S., Bloch, E.D., Hudson, M.R., Flacau, R., Vlaisavljevich, B., Long, J.R., Brown, C.M., Queen, W.L., "An Experimental and Computational Study of CO_2 Adsorption in the Sodalite-Type M-BTT (M = Cr, Mn, Fe, Cu) Metal-Organic Frameworks Featuring Open Metal Sites," Chem. Sci. **9**(20), 4579 (2018).

Baglioni, M., Montis, C., Chelazzi, D., Giorgi, R., Berti, D., Baglioni, P., "Polymer Film Dewetting by Water/Surfactant/Good-Solvent Mixtures: A Mechanistic Insight and Its Implications for the Conservation of Cultural Heritage," Angew. Chem. Int. Edit. **57**(25), 7355 (2018).

Bakaic, E., Smeets, N.M.B., Barrigar, O., Alsop, R., Rheinstädter, M.C., Hoare, T., "pH-Ionizable *In Situ* Gelling Poly(Oligo Ethylene Glycol Methacrylate)-Based Hydrogels: The Role of Internal Network Structures in Controlling Macroscopic Properties," Macromolecules **50**(19), 7687 (2017). [CHRNS]

Bao, Z., Xie, D., Chang, G., Wu, H., Li, L., Zhou, W., Wang, H., Zhang, Z., Xing, H., Yang, Q., Zaworotko, M.J., Ren, Q., Chen, B., "Fine Tuning and Specific Binding Sites with a Porous Hydrogen-Bonded Metal-Complex Framework for Gas Selective Separations," J. Am. Chem. Soc. **140**(13), 4596 (2018).

Barkley, D.A., Jiang, N., Sen, M., Endoh, M.K., Rudick, J.G., Koga, T., Zhang, Y., Gang, O., Yuan, G., Satija, S.K., Kawaguchi, D., Tanaka, K., Karim, A., "Chain Conformation near the Buried Interface in Nanoparticle-Stabilized Polymer Thin Films," Macromolecules **50**(19), 7657 (2017).

Bass, L., Milner, J., Gnäupel-Herold, T., Moylan, S., "Residual Stress in Additive Manufactured Nikel Alloy 625 Parts," J. Manuf. Sci. Eng. **140**(6), 061004 (2018).

Basutkar, M.N., Samant, S., Strzalka, J., Yager, K.G., Singh, G., Karim, A., "Through-Thickness Vertically Ordered Lamellar Block Copolymer Thin Films on Unmodified Quartz with Cold Zone Annealing," Nano Lett. **17**(12), 7814 (2017).

Bellur, K., Médici, E.F., Hermanson, J.C., Choi, C.K., Allen, J.S., "Determining Solid-Fluid Interface Temperature Distribution During Phase Change of Cryogenic Propellants using Transient Thermal Modeling," Cryogenics **91**, 103 (2018).

Bellur, K., Hussey, D., Jacobson, D., LaManna, J., Médici, E.F., Hermanson, J., Allen, J.S., Choi, C.K., "Neutron Attenuation Analysis of Cryogenic Propellants," J. Heat Transfer **140**(3), 030904 (2018).

Benedetto, A., Ballone, P., "An Overview of Neutron Scattering and Molecular Dynamics Simulation Studies of Phospholipid Bilayers in Room-Temperature Ionic Liquid/Water Solutions," Physica B, in press. [CHRNS]

Bentz, D.P., De la Varga, I., Muñoz, J.F., Spragg, R.P., Graybeal, B.A., Hussey, D.S., Jacobson, D.L., Jones, S.Z., LaManna, J.M., "Influence of Substrate Moisture State and Roughness on Interface Microstructure and Bond Strength: Slant Shear vs. Pull-Off Testing," Cement Concrete Comp. **87**, 63 (2018).

Bergeron, D.E., Mumm, H.P., Tyra, M.A., "Phase Stability and Lithium Loading Capacity in a Liquid Scintillation Cocktail," J. Radioanal. Nucl. Ch. **314**(2), 767 (2017).

Blach, T., Radlinski, A.P., Edwards, D.S., Boreham, C.J., Rehm, C., de Campo, L., Gilbert, E.P., "Fingerprint of Hydrocarbon Generation in the Southern Georgina Basin, Australia, Revealed by Small Angle Neutron Scattering," Int. J. Coal Geol. **186**, 135 (2018). [CHRNS]

Borodin, O., Suo, L., Gobet, M., Ren, X., Wang, F., Faraone, A., Peng, J., Olguin, M., Schroeder, M., Ding, M.S., Gobrogge, E., von Wald Cresce, A., Muñoz, S., Dura, J.A., Greenbaum, S., Wang, C., Xu, K., "Liquid Structure with Nano-Heterogeneity Promotes Cationic Transport in Concentrated Electrolytes," ACS Nano **11**(10), 10462 (2017).

Breidigan, J.M., Krzyzanowski, N., Liu, Y., Porcar, L., Perez-Salas, U., "Influence of the Membrane Environment on Cholesterol Transfer," J. Lipid Res. **58**(12), 2255 (2017).

Brok, E., Larsen, J., Varón, M., Hansen, T.W., Frandsen, C., "Induced Mesocrystal-Formation, Hydrothermal Growth and Magnetic Properties of α-Fe_2O_3 Nanoparticles in Salt-Rich Aqueous Solutions," Crystals **7**(8), 248 (2017).

Brooks, A.J., Hussey, D.S., Yao, H., Haghshenas, A., Yuan, J., LaManna, J.M., Jacobson, D.L., Lowery, C.G., Kardjilov, N., Guo, S., Khonsari, M.M., Butler, L.G., "Neutron Interferometry Detection of Early Crack Formation Caused by Bending Fatigue in Additively Manufactured SS316 Dogbones," Mater. Des. **140**, 420 (2018).

Brooks, A.J., Knapp, G.L., Yuan, J., Lowery, C.G., Pan, M., Cadigan, B.E., Guo, S., Hussey, D.S., Butler, L.G., "Neutron Imaging of Laser Melted SS316 Test Objects with Spatially Resolved Small Angle Neutron Scattering," J. Imaging **3**(4), 58 (2017).

Brown, K.L., Stockdale, C.P.J., Luo, H., Zhao, X., Li, J.-F., Viehland, D., Xu, G., Gehring, P.M., Ishida, K., Hillier, A.D., Stock, C., "Depth Dependant Element Analysis of $PbMg_{1/3}Nb_{2/3}O_3$ using Muonic X-rays," J. Phys.: Condens. Matter **30**(12), 125703 (2018).

Calabrese, M.A., Wagner, N.J., "Detecting Branching in Wormlike Micelles via Dynamic Scattering Methods," ACS Macro Lett. **7**(6), 614 (2018). [CHRNS]

Campbell, D.J., Eckberg, C., Wang, K., Wang, L., Hodovanets, H., Graf, D., Parker, D., Paglione, J., "Quantum Oscillations in the Anomalous Spin Density Wave State of FeAs," Phys. Rev. B **96**(7), 075120 (2017).

Cappelletti, R.L., Udovic, T.J., Li, H., Paul, R.L., "Glassy Carbon, NIST Standard Reference Material (SRM 3600): Hydrogen Content, Neutron Vibrational Density of States and Heat Capacity," J. Appl. Crystallogr., in press.

Cappelletti, R.L., Jach, T., Vinson, J., "Intrinsic Orbital Angular Momentum States of Neutrons," Phys. Rev. Lett. **120**(9), 090402 (2018).

Castellanos, M.M., Howell, S.C., Gallagher, D.T., Curtis, J.E., "Characterization of the NISTmAb Reference Material using Small-Angle Scattering and Molecular Simulation," Anal. Bioanal. Chem. **410**(8), 2141 (2018). [CHRNS]

Castellanos, M.M., Snyder, J.A., Lee, M., Chakravarthy, S., Clark, N.J., McAuley, A., Curtis, J.E., "Characterization of Monoclonal Antibody-Protein Antigen Complexes using Small-Angle Scattering and Molecular Modeling," Antibodies **6**(4), 25 (2017). [CHRNS]

Castellanos, M.M., Mattison, K., Krueger, S., Curtis, J.E., "Characterization of the NISTmAb Reference Material using Small-Angle Scattering and Molecular Simulation," Anal. Bioanal. Chem. **410**(8), 2161 (2018). [CHRNS]

Chen, X., Hwang, S., Chisnell, R., Wang, Y., Wu, F., Kim, S., Lynn, J.W., Su, D., Li, X., "Reversible Flat to Rippling Phase Transition in Fe Containing Layered Battery Electrode Materials," Adv. Funct. Mater., in press.

Chen, X., López-Barrón, C., Zeng, Y., Alamo, R.G., "Concentration Fluctuations in the Early Stages of LLPS and Partial Dissolution of Melt-Memory in Broadly Distributed Ethylene Copolymers," Polymer **148**, 181 (2018). [CHRNS]

Chiang, W.-S., Georgi, D., Yildirim, T., Chen, J.-H., Liu, Y., "A Non-Invasive Method to Directly Quantify Surface Heterogeneity of Porous Materials," Nat. Commun. **9**, 784 (2018). [CHRNS]

Chiang, W.-S., LaManna, J.M., Hussey, D.S., Jacobson, D.L., Liu, Y., Zhang, J., Georgi, D.T., Kone, J.R., Chen, J.-H., "Simultaneous Neutron and X-ray Imaging of 3D Structure of Organic Matter and Fracture in Shales," Petrophysics **59**(2), 153 (2018).

Chiang, W.-S., LaManna, J.M., Katsevich, A., Hussey, D.S., Jacobson, D.L., Frenkel, M., Georgi, D.T., Sun, Q., Liu, Y., Chen, J.-H., "Joint X-ray and Neutron Tomography of Shale Cores for Characterizing Structural Morphology," in "The Proceedings of the International Symposium of the Society of Core Analysts," edited by Society of Core Analysts, (International Symposium of the Society of Core Analysts, August 2017, Vienna, Austria) SCA2017-019 (2017).

Choi, K.-I., Kim, T.-H., Yuan, G., Satija, S.K., Koo, J., "Dynamics of Entangled Polymers Confined between Graphene Oxide Sheets as Studied by Neutron Reflectivity," ACS Macro Lett. **6**(8), 819 (2017).

Choi, K.-I., Kim, T.-H., Lee, Y., Kim, H., Lee, H., Yuan, G., Satija, S.K., Choi, J.-H., Ahn, H., Koo, J., "Perpendicular Orientation of Diblock Copolymers Induced by Confinement between Graphene Oxide Sheets," Langmuir **34**(4), 1681 (2018).

Cleveland, IV, T.E., He, W., Evans, A.C., Fischer, N.O., Lau, E.Y., Coleman, M.A., Butler, P., "Small-Angle X-ray and Neutron Scattering Demonstrates that Cell-Free Expression Produces Properly Formed Disc-Shaped Nanolipoprotein Particles," Protein Sci. **27**(3), 780 (2018). [CHRNS]

Collett, B., Bateman, F., Bauder, W.K., Byrne, J., Byron, W.A., Chen, W., Darius, G., DeAngelis, C., Dewey, M.S., Gentile, T.R., Hassan, M.T., Jones, G.L., Komives, A., Laptev, A., Mendenhall, M.P., Nico, J.S., Noid, G., Park, H., Stephenson, E.J., Stern, I., Stockton, K.J.S., Trull, C., Wietfeldt, F.E., Yerozolimsky, B.G., "aCORN: An Experiment to Measure the Electron-Antineutrino Correlation Coefficient in Free Neutron Decay," Rev. Sci. Instrum. **88**(8), 083503 (2017).

Connolly, M., Bradley, P., Slifka, A., Drexler, E., "*In Situ* Neutron Transmission Bragg Edge Measurements of Strain Fields near Fatigue Cracks Grown in Air and in Hydrogen," in "Proceeding of the International Hydrogen Conference 2016," edited by ASME, (International Hydrogen Conference (IHC2016): Materials Performance in Hydrogen Environments, September 2016, Jackson Hole, WY), 423 (2017).

Creuziger, A., Calhoun, C.A., Poling, W.A., Gnäupel-Herold, T., "Assessment of Bias Errors caused by Texture and Sampling Methods in Diffraction-Based Steel Phase Measurements," J. Appl. Crystallogr. **51**(3), 720 (2018).

Cudjoe, E., Khani, S., Way, A.E., Hore, M.J.A., Maia, J., Rowan, S.J., "Biomimetic Reversible Heat-Stiffening Polymer Nanocomposites," ACS Cent. Sci. **3**(8), 886 (2017). [CHRNS]

Dally, R.L., Zhao, Y., Xu, Z., Chisnell, R., Stone, M.B., Lynn, J.W., Balents, L., Wilson, S.D., "Amplitude Mode in the Planar Triangular Antiferromagnet $Na_{0.9}MnO_2$," Nat. Commun. **9**(1), 2188 (2018).

Danielsen, S.P.O., Sanoja, G.E., McCuskey, S.R., Hammouda, B., Bazan, G.C., Fredrickson, G.H., Segalman, R.A., "Mixed Conductive Soft Solids by Electrostatically Driven Network Formation of a Conjugated Polyelectrolyte," Chem. Mater. **30**(4), 1417 (2018). [CHRNS]

Dawn, A., Eisenhart, A., Mirzamani, M., Beck, T.L., Kumari, H., "Bowl-in-Bowl Complex Formation with Mixed Sized Calixarenes: Adaptivity Towards Guest Binding," Chem. Commun. **54**(52), 7131 (2018). [CHRNS]

DeCaluwe, S.C., Baker, A.M., Bhargava, P., Fischer, J.E., Dura, J.A., "Structure-Property Relationships at Nafion Thin-Film Interfaces: Thickness Effects on Hydration and Anisotropic Ion Transport," Nano Energy **46**, 91 (2018). [CHRNS]

DeCaluwe, S.C., Dura, J.A., "Finite Thickness Effects on Nafion Water Uptake and Ionic Conductivity at Hydrophilic Substrate Interfaces, and Implications for PEMFC Performance," ECS Transactions **80**(8), 619 (2017).

Deng, S., Sun, Y., Wu, H., Shi, Z., Wang, L., Yan, J., Shi, K., Hu, P., Diao, X., Huang, Q., Sürgers, C., Wang, C., "Phase Separation and Zero Thermal Expansion in Antiperovskite $Mn_3Zn_{0.77}Mn_{0.19}N_{0.94}$: An *in situ* Neutron Diffraction Investigation," Scripta Mater. **146**, 18 (2018).

Dennis, C.L., Jackson, A.J., Borchers, J.A., Gruettner, C., Ivkov, R., "Correlation between Physical Structure and Magnetic Anisotropy of a Magnetic Nanoparticle Colloid," Nanotechnology **29**(21), 215705 (2018). [CHRNS]

DiStefano, V.H., Cheshire, M.C., McFarlane, J., Kolbus, L.M., Hale, R.E., Perfect, E., Bilheux, H.Z., Santodonato, L.J., Hussey, D.S., Jacobson, D.L., LaManna, J.M., Bingham, P.R., Starchenko, V., Anovitz, L.M., "Spontaneous Imbibition of Water and Determination of Effective Contact Angles in the Eagle Ford Shale Formation using Neutron Imaging," J. Earth Sci.-China **28**(5), 874 (2017).

Dimeo, R., "Sketchnote Summary of 'The Backscattering Story: A Personal View,'" J. Neutron Res. **19**(3-4), 103 (2017).

Dimitrievska, M., Shea, P., Kweon, K.E., Bercx, M., Varley, J.B., Tang, W.S., Skripov, A.V., Stavila, V., Udovic, T.J., Wood, B.C., "Carbon Incorporation and Anion Dynamics as Synergistic Drivers for Ultrafast Diffusion in Superionic $LiCb_{11}H_{12}$ and $NaCB_{11}H_{12}$," Adv. Energy Mater. **8**(15), 1703422 (2018).

Dimitrievska, M., Stavila, V., Soloninin, A.V., Skoryunov, R.V., Babanova, O.A., Wu, H., Zhou, W., Tang, W.S., Faraone, A., Tarver, J.D., Trump, B.A., Skripov, A.V., Udovic, T.J., "Nature of Decahydro-*Closo*-Decaborate Anion Reorientations in an Ordered Alkali-Metal Salt: $Rb_2B_{10}H_{10}$," J. Phys. Chem. C **122**(27), 15198 (2018). [CHRNS]

Dishari, S.K., Rumble, C.A., Maroncelli, M., Dura, J.A., Hickner, M.A., "Unraveling the Complex Hydration Behavior of Ionomers under Thin Film Confinement," J. Phys. Chem. C **122**(6), 3471 (2018).

Du, E., Zhao, Q., Xiao, Y., Cai, L., Tao, R., "Electric Field Suppressed Turbulence and Reduced Viscosity of Asphaltene Base Crude Oil Sample," Fuel **220**, 358 (2018).

Du, E., Xu, X., Huang, K., Tang, H., Tao, R., "Bunker Diesel Viscosity is Dramatically Reduced by Electrorheological Treatment," Int. J. Mod. Phys. B **32**(2), 1850012 (2018).

Dupuy, F.G., Pagano, I., Andenoro, K., Peralta, M.F., Elhady, Y., Heinrich, F., Tristram-Nagle, S., "Selective Interaction of Colistin with Lipid Model Membranes," Biophys. J. **114**(4), 919 (2018).

Erwin, P., Dimitriou, M., Thompson, M.E., "Morphology of the D/A Interface in Vapor Deposited Bilayer Organic Photovoltaics," in "Proceedings of SPIE," edited by Bronstein, H.A., Deschler, F. and Bakulin, A.A., (Physical Chemistry of Semiconductor Materials and Interfaces XVI, August 2017, San Diego, CA) **10348**, 103480M (2017).

Etampawala, T., Tehrani, M., Nematollahi, A., He, L., Dadmun, M., "The Impact of Solvent Doping on the Morphology and Performance of Spray-Coated PEDOT:dPSS: A USANS and SANS Study," Org. Electron. **51**, 86 (2017). [CHRNS]

Fallarino, L., Riego, P., Kirby, B.J., Miller, C.W., Berger, A., "Modulation of Magnetic Properties at the Nanometer Scale in Continuously Graded Ferromagnets," Materials **11**(2), 251 (2018).

Faraone, A., Wagle, D.V., Baker, G.A., Novak, E.C., Ohl, M., Reuter, D., Lunkenheimer, P., Loidl, A., Mamontov, E., "Glycerol Hydrogen-Bonding Network Dominates Structure and Collective Dynamics in a Deep Eutectic Solvent," J. Phys. Chem. B **122**(3), 1261 (2018). [CHRNS]

Fobes, D.M., Zhang, S., Lin, S.-Z., Das, P., Ghimire, N.J., Bauer, E.D., Thompson, J.D., Harriger, L.W., Ehlers, G., Podlesnyak, A., Bewley, R.I., Sazonov, A., Hutanu, V., Ronning, F., Batista, C.D., Janoschek, M., "Tunable Emergent Heterostructures in a Prototypical Correlated Metal," Nat. Phys. **14**(5), 456 (2018).

Fobes, D.M., Lin, S.-Z., Ghimire, N.J., Bauer, E.D., Thompson, J.D., Bleuel, M., DeBeer-Schmitt, L.M., Janoschek, M., "Realization of the Axial Next-Nearest-Neighbor Ising Model in $U_3Al_2Ge_3$," Phys. Rev. B **96**(17), 174413 (2017). [CHRNS]

Frieberg, B.R., Garatsa, R.-S., Jones, R.L., Bachert, III, J.O., Crawshaw, B., Liu, X.M., Chan, E.P., "Viscoplastic Fracture Transition of a Biopolymer Gel," Soft Matter **14**(23), 4696 (2018).

Fuhrman, W.T., Chamorro, J.R., Alekseev, P.A., Mignot, J.-M., Keller, T., Rodriguez-Rivera, J.A., Qiu, Y., Nikolić, P., McQueen, T.M., Broholm, C.L., "Screened Moments and Extrinsic In-Gap States in Samarium Hexaboride," Nat. Commun. **9**(1), 1539 (2018). [CHRNS]

Gadipelli, S., Lu, Y., Skipper, N.T., Yildirim, T., Guo, Z., "Design of Hyperporous Graphene Networks and their Application in Solid-Amine Based Carbon Capture Systems," J. Mater. Chem. A **5**(34), 17833 (2017).

Gadipelli, S., Li, Z., Zhao, T., Yang, Y., Yildirim, T., Guo, Z., "Graphitic Nanostructures in a Porous Carbon Framework Significantly Enhance Electrocatalytic Oxygen Evolution," J. Mater. Chem. A **5**(47), 24686 (2017).

Gannon, W.J., Wu, L.S., Zaliznyak, I.A., Xu, W.H., Tsvelik, A.M., Qiu, Y., Rodriguez-Rivera, J.A., Aronson, M.C., "Local Quantum Phase Transition in YFe_2Al_{10}," P. Natl. A. Sci. USA **115**(27), 6995 (2018). [CHRNS]

García-Holley, P., Schweitzer, B., Islamoglu, T., Liu, Y., Lin, L., Rodriguez, S., Weston, M.H., Hupp, J.T., Gómez-Gualdrón, D.A., Yildirim, T., Farha, O.K., "Benchmark Study of Hydrogen Storage in Metal-Organic Frameworks under Temperature and Pressure Swing Conditions," ACS Energy Lett. **3**(3), 748 (2018).

Gartner, III, T.E., Morris, M.A., Shelton, C.K., Dura, J.A., Epps, III, T.H., "Quantifying Lithium Salt and Polymer Density Distributions in Nanostructured Ion-Conducting Block Polymers," Macromolecules **51**(5), 1917 (2018).

Gehring, P.M., Parshall, D., Harriger, L., Stock, C., Xu, G., Li, X., Luo, H., "Correspondence: Phantom Phonon Localization in Relaxors," Nat. Commun. **8**(1), 1935 (2017).

Genezini, F., Carbonari, A.W., Lynn, J.W., "International Workshop on Utilization of Research Reactors, São Paulo, Brazil," Neutron News **29**(1), 2 (2018).

Geng, L., Naderi, A., Mao, Y., Zhan, C., Sharma, P., Peng, X., Hsiao, B.S., "Rheological Properties of Jute-Based Cellulose Nanofibers under Different Ionic Conditions," in "Nanocelluloses: Their Preparation, Properties, and Applications, ACS Symposium Series, Vol. 1251," edited by Agarwal, U.P., Atalla, R.H., and Isogai, A., (American Chemical Society, Washington, DC) Chap. **6**, 113 (2017).

Geng, L., Peng, X., Zhan, C., Naderi, A., Sharma, P.R., Mao, Y., Hsiao, B.S., "Structure Characterization of Cellulose Nanofiber Hydrogel as Functions of Concentration and Ionic Strength," Cellulose **24**(12), 5417 (2017).

Geng, L., Chen, B., Peng, X., Kuang, T., "Strength and Modulus Improvement of Wet-Spun Cellulose I Filaments by Sequential Physical and Chemical Cross-Linking," Mater. Des. **136**, 45 (2017).

Gentile, T.R., Nacher, P.J., Saam, B., Walker, T.G., "Optically Polarized ^{3}He," Rev. Mod. Phys. **89**(4), 045004 (2017).

Giampaoli, G., Li, J., Hermann, R.P., Stalick, J.K., Subramanian, M.A., "Tuning Color through Sulfur and Fluorine Substitutions in the Defect Tin (II, IV) Niobate Pyrochlores," Solid State Sci. **81**, 32 (2018).

Giampaoli, G., Siritanon, T., Day, B., Li, J., Subramanian, M.A., "Temperature Independent Low Loss Dielectrics Based on Quaternary Pyrochlore Oxides," Prog. Solid State Ch. **50**, 16 (2018).

Gilbert, D.A., Burks, E.C., Ushakov, S.V., Abellan, P., Arslan, I., Felter, T.E., Navrotsky, A., Liu, K., "Tunable Low Density Palladium Nanowire Foams," Chem. Mater. **29**(22), 9814 (2017).

Gilbert, D.A., Ramírez, J.G., Saerbeck, T., Trastoy, J., Schuller, I.K., Liu, K., de la Venta, J., "Growth-Induced In-Plane Uniaxial Anisotropy V_2O_3/Ni Films," Sci. Rep. **7**(1), 13471 (2017).

Gilbert, T., Alsop, R.J., Babi, M., Moran-Mirabal, J., Rheinstädter, M.C., Hoare, T., "Nanostructure of Fully Injectable Hydrazone-Thiosuccinimide Interpenetrating Polymer Network Hydrogels Assessed by Small-Angle Neutron Scattering and dSTORM Single-Molecule Fluorescence Microscopy," ACS Appl. Mater. Interfaces **9**(48), 42179 (2017). [CHRNS]

Gómez-Gualdrón, D.A., Wang, T.C., García-Holley, P., Sawelewa, R.M., Argueta, E., Snurr, R.Q., Hupp, J.T., Yildirim, T., Farha, O.K., "Understanding Volumetric and Gravimetric Hydrogen Adsorption Trade-off in Metal-Organic Frameworks," ACS Appl. Mater. Interfaces **9**(39), 33419 (2017).

Gonzalez, M.I., Kapelewski, M.T., Bloch, E.D., Milner, P.J., Reed, D.A., Hudson, M.R., Mason, J.A., Barin, G., Brown, C.M., Long, J.R., "Separation of Xylene Isomers through Multiple Metal Site Interactions in Metal-Organic Frameworks," J. Am. Chem. Soc. **140**(9), 3412 (2018).

Gosselin, E.J., Lorzing, G.R., Trump, B.A., Brown, C.M., Bloch, E.D., "Gas Adsorption in an Isostructural Series of Pillared Coordination Cages," Chem. Commun. **54**(49), 6392 (2018).

Grebenkemper, J.H., Bocarsly, J.D., Levin, E.E., Seward, G., Heikes, C., Brown, C., Misra, S., Seeler, F., Schierle-Arndt, K., Wilson, S.D., Seshadri, R., "Rapid Microwave Preparation and Composition Tuning of the High-Performance Magnetocalorics $(Mn,Fe)_2(P,Si)$," ACS Appl. Mater. Interfaces **10**(8), 7208 (2018).

Grutter, A.J., Krycka, K.L., Tartakovskaya, E.V., Borchers, J.A., Madhukar Reddy, K.S., Ortega, E., Ponce, A., Stadler, B.J.H., "Complex Three-Dimensional Magnetic Ordering in Segmented Nanowire Arrays," ACS Nano **11**(8), 8311 (2017). [CHRNS]

Gu, X., Mildner, D.F.R., "Determination of Porosity in Anisotropic Fractal Systems by Neutron Scattering," J. Appl. Crystallogr. **51**(1), 175 (2018). [CHRNS]

Gunasekera, J., Dahal, A., Chen, Y., Rodriguez-Rivera, J.A., Harriger, L.W., Thomas, S., Heitmann, T.W., Dugaev, V., Ernst, A., Singh, D.K., "Quantum Magnetic Properties in Perovskite with Anderson Localized Artificial Spin-1/2," Adv. Sci. **5**(5), 1700978 (2018). [CHRNS]

Guo, H., Stan, G., Liu, Y., "Nanoparticle Separation Based on Size-Dependent Aggregation of Nanoparticles due to the Critical Casimir Effect," Soft Matter **14**(8), 1311 (2018). [CHRNS]

Guo, S., Dai, Q., Sun, X., Xie, X., "Neutron Scattering Measurement of Water Content and Chemical Composition of Alkali-Glass Powder Reacted Gel," Mater. Charact. **136**, 165 (2018).

Guo, Y., Zuo, X., Xue, Y., Zhou, Y., Yang, Z., Chuang, Y.-C., Chang, C.-C., Yuan, G., Satija, S.K., Gersappe, D., Rafailovich, M.H., "Enhancing Impact Resistance of Polymer Blends via Self-Assembled Nanoscale Interfacial Structures," Macromolecules **51**(11), 3897 (2018).

Guo, Z., Panda, D.K., Gordillo, M.A., Khatun, A., Wu, H., Zhou, W., Saha, S., "Lowering Band Gap of an Electroactive Metal–Organic Framework via Complementary Guest Intercalation," ACS Appl. Mater. Interfaces **9**(38), 32413 (2017).

Gupta, S., Bleuel, M., Schneider, G.J., "A New Ultrasonic Transducer Sample Cell for *in situ* Small-Angle Scattering Experiments," Rev. Sci. Instrum. **89**(1), 015111 (2018). [CHRNS]

Gupta, S., De Mel, J.U., Perera, R.M., Zolnierczuk, P., Bleuel, M., Faraone, A., Schneider, G.J., "Dynamics of Phospholipid Membranes Beyond Thermal Undulations," J. Phys. Chem. Lett. **9**(11), 2956 (2018). [CHRNS]

Habib, S.A., Khan, A.S., Gnäupel-Herold, T., Lloyd, J.T., Schoenfeld, S.E., "Anisotropy, Tension-Compression Asymmetry and Texture Evolution of a Rare-Earth-Containing Magnesium Alloy Sheet, ZEK100, at Different Strain Rates and Temperatures: Experiments and Modeling," Int. J. Plasticity **95**, 163 (2017).

Haddock, C., Amadio, J., Anderson, E., Barrón-Palos, L., Crawford, B., Crawford, C., Esposito, D., Fox, W., Francis, I., Fry, J., Gardiner, H., Holley, A., Korsak, K., Lieffers, J., Magers, S., Maldonado-Velázquez, M., Mayorov, D., Nico, J.S., Okudaira, T., Paudel, C., Santra, S., Sarsour, M., Shimizu, H.M., Snow, W.M., Sprow, A., Steffen, K., Swanson, H.E., Tovesson, F., Vanderwerp, J., Yergeau, P.A., "A Search for Possible Long Range Spin Dependent Interactions of the Neutron from Exotic Vector Boson Exchange," Phys. Lett. B, in press.

Haider, M.J., Zhang, H.V., Sinha, N., Fagan, J.A., Kiick, K.L., Saven, J.G., Pochan, D.J., "Self-Assembly and Soluble Aggregate Behavior of Computationally Designed Coiled-Coil Peptide Bundles," Soft Matter **14**(26), 5488 (2018). [CHRNS]

Hallas, A.M., Gaudet, J., Butch, N.P., Xu, G., Tachibana, M., Wiebe, C.R., Luke, G.M., Gaulin, B.D., "Phase Competition in the Palmer-Chalker *XY* Pyrochlore $Er_2Pt_2O_7$," Phys. Rev. Lett. **119**(18), 187201 (2017).

Hammouda, B., Kim, M.-H., "The Empirical Core-Chain Model," J. Mol. Liq. **247**, 434 (2017). [CHRNS]

Hasenmueller, E.A., Gu, X., Weitzman, J.N., Adams, T.S., Stinchcomb, G.E., Eissenstat, D.M., Drohan, P.J., Brantley, S.L., Kaye, J.P., "Weathering of Rock to Regolith: The Activity of Deep Roots in Bedrock Fractures," Geoderma **300**, 11 (2017). [CHRNS]

Hassan, M.T., Bateman, F., Collett, B., Darius, G., DeAngelis, C., Dewey, M.S., Jones, G.L., Komives, A., Laptev, A., Mendenhall, M.P., Nico, J.S., Noid, G., Stephenson, E.J., Stern, I., Trull, C., Wietfeldt, F.E., "The aCORN Backscatter-Suppressed Beta Spectrometer," Nucl. Instrum. Meth. A **867**, 51 (2017).

Haywood, A.D., Weigandt, K.M., Saha, P., Noor, M., Green, M.J., Davis, V.A., "New Insights into the Flow and Microstructural Relaxation Behavior of Biphasic Cellulose Nanocrystal Dispersions from RheoSANS," Soft Matter **13**(45), 8451 (2017). [CHRNS]

He, Q.L., Yin, G., Grutter, A.J., Pan, L., Che, X., Yu, G., Gilbert, D.A., Disseler, S.M., Liu, Y., Shafer, P., Zhang, B., Wu, Y., Kirby, B.J., Arenholz, E., Lake, R.K., Han, X., Wang, K.L., "Exchange-Biasing Topological Charges by Antiferromagnetism," Nat. Commun. **9**(1), 2767 (2018).

He, Y., Chen, F., Li, B., Qian, G., Zhou, W., Chen, B., "Porous Metal-Organic Frameworks for Fuel Storage," Coordin. Chem. Rev., in press.

He, Y., Zhou, W., Chen, B., "Current Status of Porous Metal-Organic Frameworks for Methane Storage," in "Metal-Organic Frameworks: Applications in Separations and Catalysis," edited by García, H.; and Navalón, S., (Wiley-VCH Verlag GmbH, Weinheim, Germany) Chap. **6**, 163 (2018).

Heacock, B., Arif, M., Cory, D.G., Gnäupel -Herold, T., Haun, R., Huber, M.G., Jamer, M.E., Nsofini, J., Pushin, D.A., Sarenac, D., Taminiau, I., Young, A.R., "Increased Interference Fringe Visibility from the Post-Fabrication Heat Treatment of a Perfect Crystal Silicon Neutron Interferometer," Rev. Sci. Instrum. **89**(2), 023502 (2018).

Healy, J., Knott, R., Edward, G., "Residual Orientation in Injection-Moulded Plaques of Atactic-Polystyrene I: The Effect of Processing Conditions," Polym. Eng. Sci., in press. [CHRNS]

Heikes, C., Lin, I.-L., Metz, T., Eckberg, C., Neves, P., Wu, Y., Hung, L., Piccoli, P., Cao, H., Leão, J., Paglione, J., Yildirim, T., Butch, N., Ratcliff, II., W., "Mechanical Control of Crystal Symmetry and Superconductivity in Weyl Semimetal $MoTe_2$," Phys. Rev. Mater. **2**(7), 074202 (2018). [CHRNS]

Helton, J.S., Jones, S.K., Parshall, D., Stone, M.B., Shulyatev, D.A., Lynn, J.W., "Spin Wave Damping Arising from Phase Coexistence below T_c in Colossal Magnetoresistive $La_{0.7}Ca_{0.3}MnO_3$," Phys. Rev. B **96**(10), 104417 (2017).

Hester, B.R., dos Santos, A.M., Molaison, J.J., Hancock, J.C., Wilkinson, A.P., "Synthesis of Defect Perovskites $(He_{2-x}\square_x)(CaZr)F_6$ by Inserting Helium into the Negative Thermal Expansion Material $CaZrF_6$," J. Am. Chem. Soc. **139**(38), 13284 (2017).

Higgins, J.S., Chan, M.K., Sarkar, T., McDonald, R.D., Greene, R.L., Butch, N.P., "Quantum Oscillations from the Reconstructed Fermi Surface in Electron-Doped Cuprate Superconductors," New J. Phys. **20**(4), 043019 (2018).

Hjelm, R.P., Taylor, M.A., Frash, L.P., Hawley, M.E., Ding, M., Xu, H., Barker, J., Olds, D., Heath, J., Dewers, T., "Flow-through Compression Cell for Small-Angle and Ultra-Small-Angle Neutron Scattering Measurements," Rev. Sci. Instrum. **89**(5), 055115 (2018). [CHRNS]

Hoffman, J.D., Wu, S.M., Kirby, B.J., Bhattacharya, A., "Tunable Noncollinear Antiferromagnetic Resistive Memory through Oxide Superlattice Design," Phys. Rev. Appl. **9**(4), 044041 (2018).

Hoogerheide, D.P., Gurnev, P.A., Rostovtseva, T.K., Bezrukov, S.M., "Real-Time Nanopore-Based Recognition of Protein Translocation Success," Biophys. J. 1**14**(4), 772 (2018).

Horkay, F., Basser, P.J., Hecht, A.-M., Geissler, E., "Microstructure and Dynamic Properties of Aggrecan Assemblies," MRS Advances **28**(3), 1589 (2018). [CHRNS]

Horkay, F., Basser, P.J., Hecht, A.-M., Geissler, E., "Ionic Effects in Semi-Dilute Biopolymer Solutions: A Small Angle Scattering Study," J. Chem. Phys., in press. [CHRNS]

Hu, J., Xiao, Y., Tang, H., Wang, H., Wang, Z., Liu, C., Zeng, H., Huang, Q., Ren, Y., Wang, C., Zhang, W., Pan, F., "Tuning Li-Ion Diffusion in α-$LiMn_{1-x}Fe_xPO_4$ Nanocrystals by Antisite Defects and Embedded β-Phase for Advanced Li-Ion Batteries," Nano Lett. **17**(8), 4934 (2017).

Hu, W.-T., Yang, H., Cheng, H., Hu, H.-Q., "Morphology Evolution of Polystyrene-Core/Polsy(*N*-Isopropylacrylamide)-Shell Microgel Synthesized by One-Pot Polymerization," Chinese J. Polym. Sci. **35**(9), 1156 (2017). [CHRNS]

Huang, K., Tan, C., Zhang, J., Ding, Z., MacLaughlin, D.E., Bernal, O.O., Ho, P.-C., Baines, C., Wu, L.S., Aronson, M.C., Shu, L., "Anomalous Quantum Critical Spin Dynamics in YFe_2Al_{10}," Phys. Rev. B **97**(15), 155110 (2018). [CHRNS]

Hung, L., Yildirim, T., "First-Principles Study of Magnetism, Lattice Dynamics, and Superconductivity in $LaFeSiH_x$," Phys. Rev. B **97**(22), 224501 (2018).

Hurst, A.M., Firestone, R.B., Sleaford, B.W., Bleuel, D.L., Basunia, M.S., Bečvář , F., Belgya, T., Bernstein, L.A., Carroll, J.J., Detwiler, B., Escher, J.E., Genreith, C., Goldblum, B.L., Krtička, M., Lerch, A.G., Matters, D.A., McClory, J.W., McHale, S.R., Révay, Z., Szentmiklosi, L., Turkoglu, D., Ureche, A., Vujic, J., "Developments in Capture-γ Libraries for Nonproliferation Applications," EPJ Web Conf. **146**, 09008 (2017).

Hussey, D.S., LaManna, J.M., Baltic, E., Jacobson, D.L., Stariha, S., Spernjak, D., Mukundan, R., Borup, R.L., "Membrane/Electrode Assembly Water Content Measured with 2 μm Spatial Resolution Neutron Imaging," ECS Transactions **80**(8), 385 (2017).

Hussey, D.S., Wen, H., Wu, H., Gentile, T.R., Chen, W., Jacobson, D.L., LaManna, J.M., Khaykovich, B., "Demonstration of Focusing Wolter Mirrors for Neutron Phase and Magnetic Imaging," J. Imaging **4**(3), 50 (2018).

Hussey, D.S., LaManna, J.M., Baltic, E., Jacobson, D.L., "Neutron Imaging Detector with 2 μm Spatial Resolution Based on Event Reconstruction of Neutron Capture in Gadolinium Oxysulfide Scintillators," Nucl. Instrum. Meth. A **866**, 9 (2017).

Ipek, B., Pollock, R.A., Brown, C.M., Uner, D., Lobo, R.F., "H_2 Adsorption on Cu(I)-SSZ-13," J. Phys. Chem. C **122**(1), 540 (2018).

Islam, M., Janssen, D., Romero-Talamas, C., Kostov, D., Wang, W., Liu, Z., Singh, N.B., Choa, F.-S., "Nuclear Radiation Monitoring using Plants," J. Nucl. Eng. Radiat. Sci., in press.

Iwamoto, T., Doi, Y., Kinoshita, K., Ohta, Y., Takano, A., Takahashi, Y., Nagao, M., Matsushita, Y., "Conformations of Ring Polystyrenes in Bulk Studied by SANS," Macromolecules **51**(4), 1539 (2018).

Jia, D., Muthukumar, M., Cheng, H., Han, C.C., Hammouda, B., "Concentration Fluctuations near Lower Critical Solution Temperature in Ternary Aqueous Solutions," Macromolecules **50**(18), 7291 (2017). [CHRNS]

Jiang, H., Beaucage, G., Vogtt, K., Weaver, M., "The Effect of Solvent Polarity on Wormlike Micelles using Dipropylene Glycol (DPG) as a Cosolvent in an Anionic/Zwitterionic Mixed Surfactant System," J. Colloid Interf. Sci. **509**, 25 (2018).

Jiang, M., Li, B., Cui, X., Yang, Q., Bao, Z., Yang, Y., Wu, H., Zhou, W., Chen, B., Xing, H., "Controlling Pore Shape and Size of Interpenetrated Anion-Pillared Ultramicroporous Materials Enables Molecular Sieving of CO_2 Combined with Ultrahigh Uptake Capacity," ACS Appl. Mater. Interfaces **10**(19), 16628 (2018).

Jiang, N., Cheung, J.M., Guo, Y., Endoh, M.K., Koga, T., Yuan, G., Satija, S.K., "Stability of Adsorbed Polystyrene Nanolayers on Silicon Substrates," Macromol. Chem. Phys. **219**(3), 1700326 (2018).

Jiang, N., Sen, M., Zeng, W., Chen, Z., Cheung, J.M., Morimitsu, Y., Endoh, M.K., Koga, T., Fukuto, M., Yuan, G., Satija, S.K., Carrillo, J.-M.Y., Sumpter, B.G., "Structure-Induced Switching of Interpolymer Adhesion at a Solid-Polymer Melt Interface," Soft Matter **14**(7), 1108 (2018).

Jiang, P., Huang, Q., Avdeev, M., Tao, F., Zhou, L., Gao, W., Cong, R., Yang, T., "Substitution-Induced Structure Evolution and Zn^{2+}/Ga^{3+} Ordering in '114' Oxides $MAZn_2Ga_2O_7$ ($M = CA^{2+}, Sr^{2+}$; $A = Sr^{2+}, Ba^{2+}$)," Inorg. Chem. **57**(13), 7770 (2018).

Jin, S., Fan, X., Wu, X., Sun, R., Wu, H., Huang, Q., Shi, C., Xi, X., Li, Z., Chen, X., "High-T_c Superconducting Phases in Organic Molecular Intercalated Iron Selenides: Synthesis and Crystal Structures," Chem. Commun. **53**(70), 9729 (2017).

Jones, S.Z., Bentz, D.P., Davis, J.M., Hussey, D.S., Jacobson, D.L., Molloy, J.L., Sieber, J.R., "Measurement and Modeling of the Ability of Crack Fillers to Prevent Chloride Ingress into Mortar," Cement Concrete Comp. **81**, 109 (2017).

Jouault, N., Kumar, S.K., Smalley, R.J., Chi, C., Moneta, R., Wood, B., Salerno, H., Melnichenko, Y.B., He, L., Guise, W.E., Hammouda, B., Crawford, M.K., "Do Very Small POSS Nanoparticles Perturb s-PMMA Chain Conformations?" Macromolecules **51**(14), 5278 (2018).

Kalonia, C.K., Heinrich, F., Curtis, J.E., Raman, S., Miller, M.A., Hudson, S.D., "Protein Adsorption and Layer Formation at the Stainless Steel-Solution Interface Mediates Shear-Induced Particle Formation for an IgG1 Monoclonal Antibody," Mol. Pharmaceut. **15**(3), 1319 (2018).

Kamiya, Y., Ge, L., Hong, T., Qiu, Y., Quintero-Castro, D.L., Lu, Z., Cao, H.B., Matsuda, M., Choi, E.S., Batista, C.D., Mourigal, M., Zhou, H.D., Ma, J., "The Nature of Spin Excitations in the One-Third Magnetization Plateau Phase of $Ba_3CoSb_2O_9$," Nat. Commun. **9**(1), 2666 (2018). [CHRNS]

Kan, W.H., Chen, D., Papp, J.K., Shukla, A.K., Huq, A., Brown, C.M., McCloskey, B.D., Chen, G., "Unravelling Solid-State Redox Chemistry in $Li_{1.3}Nb_{0.3}Mn_{0.4}O_2$ Single-Crystal Cathode Material," Chem. Mater. **30**(5), 1655 (2018).

Kharel, A., Lodge, T.P., "Coil Dimensions of Poly(Ethylene Oxide) in an Ionic Liquid by Small-Angle Neutron Scattering," Macromolecules **50**(21), 8739 (2017). [CHRNS]

Kim, H., Kim, J., Jeong, H.-S., Kim, H., Lee, H., Ha, J.-M., Cho, S.-M., Kim, T.-H., Nah, Y.-C., Shin, T.J., Bang, J., Satija, S.K., Koo, J., "Spontaneous Hybrids of Graphene and Carbon Nanotube Arrays at the Liquid-Gas Interface for Li-Ion Battery Anodes," Chem. Commun. **54**(41), 5229 (2018).

Kim, Y., Kim, J., Kim, D., Hussey, D.S., Lee, S.W., "Feasibility Evaluation of a Neutron Grating Interferometer with an Analyzer Grating Based on a Structured Scintillator," Rev. Sci. Instrum. **89**(3), 033701 (2018).

Kim, Y.H., Park, H., Kim, Y.K., Kim, J., Kang, J., "Reference Thermal Neutron Field at KRISS for Calibration of Neutron Detectors," Radiat. Meas. **107**, 73 (2017).

Kline, S.R., "2017 NCNR Annual Report," NIST SP **1216**, 1 (2017).

Kolesnikov, A.I., Reiter, G.F., Prisk, T.R., Krzystyniak, M., Romanelli, G., Wesolowski, D.J., Anovitz, L.M., "Inelastic and Deep Inelastic Neutron Spectroscopy of Water Molecules under Ultra-Confinement," J. Phys.: Conf. Ser. **1055**(1), 012002 (2018).

Koshari, S.H.S., Wagner, N.J., Lenhoff, A.M., "Effects of Resin Architecture and Protein Size on Nanoscale Protein Distribution in Ion-Exchange Media," Langmuir **34**(2), 673 (2018).

Krakowiak, K.J., Thomas, J.J., James, S., Abuhaikal, M., Ulm, F.-J., "Development of Silica-Enriched Cement-Based Materials with Improved Aging Resistance for Application in High-Temperature Environments," Cement Concrete Res. **105**, 91 (2018).

Krogstad, M.J., Gehring, P.M., Rosenkranz, S., Osborn, R., Ye, F., Liu, Y., Ruff, J.P.C., Chen, W., Wozniak, J.M., Luo, H., Chmaissem, O., Ye, Z.-G., Phelan, D., "The Relation of Local Order to Material Properties in Relaxor Ferroelectrics," Nat. Mater. **17**(8), 718 (2018).

Krueger, S., "Designing and Performing Biological Solution Small-Angle Neutron Scattering Contrast Variation Experiments on Multi-Component Assemblies," in "Biological Small Angle Scattering: Techniques, Strategies and Tips. Advances in Experimental Medicine and Biology," edited by Chaudhuri B., Muñoz I.G., Qian S., and Urban V.S. (Springer Nature, Gateway East, Singapore) Chap. **5**, 65 (2017).

Krycka, K.L., Dura, J.A., Langston, II, L.J., Burba, C.M., "Nanoconfinement-Induced Phase Segregation of Binary Benzene-Cyclohexane Solutions within a Chemically Inert Matrix," J. Phys. Chem. C **122**(14), 7676 (2018). [CHRNS]

Kwaambwa, H.M., Hellsing, M.S., Wasbrough, M.J., Bleuel, M., Rennie, A.R., "Salt Induced Polystyrene Latex Flocs Investigated by Neutron Scattering," J. Colloid Interf. Sci. **505**, 9 (2017). [CHRNS]

Kweon, K.E., Varley, J.B., Shea, P., Adelstein, N., Mehta, P., Heo, T.W., Udovic, T.J., Stavila, V., Wood, B.C., "Structural, Chemical, and Dynamical Frustration: Origins of Superionic Conductivity in *closo*-Borate Solid Electrolytes," Chem. Mater. **29**(21), 9142 (2017).

LaManna, J.M., Hussey, D.S., Baltic, E., Jacobson, D.L., "Neutron and X-ray Tomography (NeXT) System for Simultaneous, Dual Modality Tomography," Rev. Sci. Instrum. **88**(11), 113702 (2017).

LaManna, J.M., Hussey, D.S., Baltic, E., Jacobson, D.L., "Improving Material Identification by Combining X-ray and Neutron Tomography," in "Developments in X-ray Tomography XI," edited by Müller, B. and Wang, G., (SPIE Optical Engineering & Applications, September 2017, San Diego, CA) **10391**, 1039104 (2017).

Lang, X., Patrick, A.D., Hammouda, B., Hore, M.J.A., "Chain Terminal Group Leads to Distinct Thermoresponsive Behaviors of Linear PNIPAM and Polymer Analogs," Polymer **145**, 137 (2018). [CHRNS]

Lass, E.A., Stoudt, M.R., Williams, M.E., Katz, M.B., Levine, L.E., Phan, T.Q., Gnäupel -Herold, T.H., Ng, D.S., "Formation of the Ni_3Nb δ-Phase in Stress-Relieved Inconel 625 Produced *via* Laser Powder-Bed Fusion Additive Manufacturing," Metall. Mater. Trans. A **48A**(11), 5547 (2017).

Lee, C., Banerjee, R., Ge, N., Lee, J.K., Zhao, B., Baltic, E., LaManna, J.M., Hussey, D.S., Jacobson, D.L., Abouatallah, R., Wang, R., Bazylak, A., "The Effect of Cathode Nitrogen Purging on Cell Performance and *in operando* Neutron Imaging of a Polymer Electrolyte Membrane Electrolyzer," Electrochim. Acta **279**, 91 (2018).

Lee, J.K., Akgun, B., Jiang, Z., Narayanan, S., Foster, M.D., "Altering Surface Fluctuations by Blending Tethered and Untethered Chains," Soft Matter **13**(44), 8264 (2017).

Lehnert, R., Snow, W.M., Xiao, Z., Xu, R., "Constraining Spacetime Nonmetricity with Neutron Spin Rotation in Liquid ^{4}He," Phys. Lett. B **772**, 865 (2017).

Levin, I., Krayzman, V., Cibin, G., Tucker, M.G., Eremenko, M., Chapman, K., Paul, R.L., "Coupling of Emergent Octahedral Rotations to Polarization in (K,Na) NbO_3 Ferroelectrics," Sci. Rep. **7**(1), 15620 (2017).

Li, A.B., Kluge, J.A., Zhi, M., Cicerone, M.T., Omenetto, F.G., Kaplan, D.L., "Enhanced Stabilization in Dried Silk Fibroin Matrices," Biomacromolecules **18**(9), 2900 (2017). [CHRNS]

Li, B., Cui, X., O'Nolan, D., Wen, H.-M., Jiang, M., Krishna, R., Wu, H., Lin, R.-B., Chen, Y.-S., Yuan, D., Xing, H., Zhou, W., Ren, Q., Qian, G., Zaworotko, M.J., Chen, B., "An Ideal Molecular Sieve for Acetylene Removal from Ethylene with Record Selectivity and Productivity," Adv. Mater. **29**(47), 1704210 (2017).

Li, D.S., Lee, Y.-T., Xi, Y., Pelivanov, I., O'Donnell, M., Pozzo, L.D., "A Small-Angle Scattering Environment for *In Situ* Ultrasound Studies," Soft Matter **14**(25), 5283 (2018). [CHRNS]

Li, H., Yang, Z., Pan, C., Jiang, N., Satija, S.K., Xu, D., Gersappe, D., Nam, C.-Y., Rafailovich, M.H., "A New Strategy to Engineer Polymer Bulk Heterojunction Solar Cells with Thick Active Layers *via* Self-Assembly of the Tertiary Columnar Phase," Nanoscale **9**(32), 11511 (2017).

Li, K., Huang, Q.-Z., Zhang, Q., Xiao, Z., Kamiya, T., Hosono, H., Yuan, D., Guo, J., Chen, X., "$CsFe_{4-\delta}Se_4$: A Compound Closely Related to Alkali-Intercalated FeSe Superconductors," Inorg. Chem. **57**(8), 4502 (2018).

Li, L., Lin, R.-B., Krishna, R., Wang, X., Li, B., Wu, H., Li, J., Zhou, W., Chen, B., "Efficient Separation of Ethylene from Acetylene/Ethylene Mixtures by a Flexible-Robust Metal-Organic Framework," J. Mater. Chem. A **5**(36), 18984 (2017).

Li, M., Song, Q., Zhao, W., Garlow, J.A., Liu, T.-H., Wu, L., Zhu, Y., Moodera, J.S., Chan, M.H.W., Chen, G., Chang, C.-Z., "Dirac-Electron-Mediated Magnetic Proximity Effect in Topological Insulator/Magnetic Insulator Heterostructures," Phys. Rev. B **96**(20), 201301 (2017).

Li, W., Chiang, W.-S., LaManna, J., Kone, J., Chen, J.-H., Liu, Y., "3D Core-Scale Organic and Mineral Material Characterization of Source Rocks with Simultaneous Neutron and X-ray Imaging," Microsc. Microanal. **23**(S1), 2174 (2017).

Li, W., Fu, Z., Wang, X., Zhang, J., Liu, M., Zhao, J., Jin, M., Zhao, G., Dai, G., Deng, Z., Zhang, S., Feng, S., Hu, Z., Huang, Q., Lin, H., Chen, C.-T., Yang, Y., Jin, C., "Synthesis, Structure, and Properties of the Layered Oxyselenide $Ba_2CuO_2Se_2$," Inorg. Chem. **57**(9), 5108 (2018).

Lin, R.-B., Xiang, S., Li, B., Cui, Y., Zhou, W., Qian, G., Chen, B., "Reticular Chemistry of Multifunctional Metal-Organic Framework Materials," Israel J. Chem., in press.

Lin, R.-B., Xiang, S., Xing, H., Zhou, W., Chen, B., "Exploration of Porous Metal-Organic Frameworks for Gas Separation and Purification," Coordin. Chem. Rev., in press.

Lindstrom, R.M., Révay, Z., "Prompt Gamma Neutron Activation Analysis (PGAA): Recent Developments and Applications," J. Radioanal. Nucl. Ch. **314**(2), 843 (2017).

Lindstrom, R.M., "A Second-Generation Low-Background Gamma-Ray Spectrometer," Appl. Radiat. Isotopes **126**, 191 (2017).

Liu, I.-L., Pascale, M.J., Leão, J.B., Brown, C.M., Ratcliff, W.D., Huang, Q., Butch, N.P., "Pressure Tuning of Collapse of Helimagnetic Structure in Au_2Mn," Phys. Rev. B **96**(18), 184429 (2017).

Livingston, R., O'Connor, A., LaManna, J., Chen-Mayer, H., Turkoglu, D., "Investigation of a Simulated Chinese Jade and Bronze Dagger-axe by Neutron Radiography and Prompt Gamma Activation Analysis," J. Archaeol. Sci. Rep., in press.

López-Barrón, C.R., Zhou, H., Younker, J.M., Mann, J.A., "Molecular Structure, Chain Dimensions, and Linear Rheology of Poly(4-vinylbiphenyl)," Macromolecules **50**(22), 9048 (2017).

Lorzing, G.R., Trump, B.A., Brown, C.M., Bloch, E.D., "Selective Gas Adsorption in Highly Porous Chromium(II)-Based Metal-Organic Polyhedra," Chem. Mater. **29**(20), 8583 (2017).

Luhmann, A.J., Tutolo, B.M., Bagley, B.C., Mildner, D.F.R., Scheuermann, P.P., Feinberg, J.M., Ignatyev, K., Seyfried, Jr., W.E., "Chemical and Physical Changes during Seawater Flow through Intact Dunite Cores: An Experimental study at 150-200 °C," Geochim.Cosmochim. Ac. **214**, 86 (2017). [CHRNS]

Luzin, V., Spencer, K., Hill, M.R., Wei, T., Law, M., Gnäupel-Herold, T., "Stress Profiling in Cold-Spray Coatings by Different Experimental Techniques: Neutron Diffraction, X-ray Diffraction and Slitting Method," in "Materials Research Proceedings," edited MECA, (9th International Conference on Mechanical Stress Evaluation by Neutron and Synchrotron Radiation, September 2017, Skukuza, South Africa) **4**, 129 (2018).

Maliszewskyj, N.C., Osovizky, A., Pritchard, K., Yehuda-Zada, Y., Binkley, E., Ziegler, J., Tsai, P., Hadad, N., Baltic, G.M., Jackson, M., Hurlbut, C., Majkrzak, C.F., "An Energy Analyzing Detector for Cold Neutrons," Nucl. Instrum. Meth. A, in press.

Mamontov, E., Kolesnikov, A.I., Sampath, S., Yarger, J.L., "Hydrogen Mobility in the Lightest Reversible Metal Hydride, $LiBeH_3$," Sci. Rep. **7**(1), 16244 (2017).

Man, H., Shi, Z., Xu, G., Xu, Y., Chen, X., Sullivan, S., Zhou, J., Xia, K., Shi, J., Dai, P., "Direct Observation of Magnon-Phonon Coupling in Yttrium Iron Garnet," Phys. Rev. B **96**(10), 100406 (2017).

Manumpil, M.A., Leal-Cervantes, C., Hudson, M.R., Brown, C.M., Karunadasa, H.I., "Electronic Conductivity in a Porous Vanadyl Prussian Blue Analogue upon Air Exposure," Inorg. Chem. **56**(21), 12682 (2017).

Mao, Y., Bucknall, D.G., Kriegel, R.M., "Synchrotron X-ray Scattering Study on Amorphous Poly(Ethylene Furanoate) under Uniaxial Deformation," Polymer **139**, 60 (2018).

Mao, Y., Bucknall, D.G., Kriegel, R.M., "Simultaneous WAXS/SAXS Study on Semi-Crystalline Poly(Ethylene Furanoate) under Uniaxial Stretching," Polymer **143**, 228 (2018).

Mao, Y., Bleuel, M., Lyu, Y., Zhang, X., Henderson, D., Wang, H., Briber, R.M., "Phase Separation and Stack Alignment in Aqueous Cellulose Nanocrystal Suspension under Weak Magnetic Field," Langmuir **34**(27), 8042 (2018). [CHRNS]

Mao, Y., Zavalij, P.Y., "Two Furan-2,5-Dicarboxylic Acid Solvates Crystallized from Dimethylformamide and Dimethyl Sulfoxide," Acta Crystallogr. C, in press.

Marcus, G.G., Kim, D.-J., Tutmaher, J.A., Rodriguez-Rivera, J.A., Birk, J.O., Niedermeyer, C., Lee, H., Fisk, Z., Broholm, C.L., "Multi-q Mesoscale Magnetism in $CeAuSb_2$," Phys. Rev. Lett. **120**(9), 097201 (2018). [CHRNS]

Martin, H.J., White, B.T., Scanlon, C.J., Saito, T., Dadmun, M.D., "Tunable Synthetic Control of Soft Polymeric Nanoparticle Morphology," Soft Matter **13**(46), 8849 (2017). [CHRNS]

Martin, T.B., Gartner, III, T.E., Jones, R.L., Snyder, C.R., Jayaraman, A., "pyPRISM: A Computational Tool for Liquid-State Theory Calculations of Macromolecular Materials," Macromolecules **51**(8), 2906 (2018).

Masoomi, M., Shamsaei, N., Winholtz, R.A., Milner, J.L., Gnäupel-Herold, T., Elwany, A., Mahmoudi, M., Thompson, S.M., "Residual Stress Measurements via Neutron Diffraction of Additive Manufactured Stainless Steel 17-4 PH," Data in Brief **13**, 408 (2017).

McFarlane, J., Hale, R.E., DiStefano, V.H., Anovitz, L.M., Bilheux, H.Z., Cheshire, M.C., Daemen, L.L., Howard, R.L., Perfect, E., Hussey, D.S., Jacobson, D.L., LaManna, J.M., "Water Migration in Engineered Barrier Materials for Radioactive Waste Disposal," T. Am. Nucl. Soc. **118**, 217 (2018).

Méndez-Camacho, R., Cruz-Hernández, E., Castañeda-Priego, R., "Wigner Crystallization in Quantum Wires within the Yukawa Approximation," Phys. Rev. B **95**(8), 085437 (2017).

Meuse, C.W., Filliben, J.J., Rubinson, K.A., "Submultiple Data Collection to Explore Spectroscopic Instrument Instabilities Shows that Much of the 'Noise' is not Stochastic," Anal. Chem. **90**(8), 5066 (2018).

Meynell, S.A., Wilson, M.N., Krycka, K.L., Kirby, B.J., Fritzsche, H., Monchesky, T.L., "Neutron Study of In-Plane Skyrmions in MnSi Thin Films," Phys. Rev. B **96**(5), 054402 (2017).

Milner, J.L., Gnäupel-Herold, T., "Design of an Octo-Strain Specimen for Biaxial Tension Testing," in "Proceedings of the ASME 2018 International Manufacturing Science and Engineering Conference," edited by ASME, (ASME 2018 International Manufacturing Science and Engineering Conference, June 2018, College Station, Texas) 1 (2018).

Mineart, K.P., Kelley, E.G., Nagao, M., Prabhu, V.M., "Processing-Structure Relationships of Poly(Ethylene Glycol)-Modified Liposomes," Soft Matter **13**(31), 5228 (2017). [CHRNS]

Mineart, K.P., Venkataraman, S., Yang, Y.Y., Hedrick, J.L., Prabhu, V.M., "Fabrication and Characterization of Hybrid Stealth Liposomes," Macromolecules **51**(8), 3184 (2018).

Mongcopa, K.I.S., Poling-Skutvik, R., Ashkar, R., Butler, P., Krishnamoorti, R., "Conformational Change and Suppression of the Θ-Temperature for Solutions of Polymer-Grafted Nanoparticles," Soft Matter, in press. [CHRNS]

Mongcopa, K.I.S., Tyagi, M., Mailoa, J.P., Samsonidze, G., Kozinsky, B., Mullin, S.A., Gribble, D.A., Watanabe, H., Balsara, N.P., "Relationship between Segmental Dynamics Measured by Quasi-Elastic Neutron Scattering and Conductivity in Polymer Electrolytes," ACS Macro Lett. **7**(4), 504 (2018). [CHRNS]

Moon, E.J., He, Q., Ghosh, S., Kirby, B.J., Pantelides, S.T., Borisevich, A.Y., May, S.J., "Structural 'δ Doping' to Control Local Magnetization in Isovalent Oxide Heterostructures," Phys. Rev. Lett. **119**(19), 197204 (2017).

Morgan, B., Dadmun, M.D., "The Effect of Illumination on the Depth Profile of Thermally Annealed MEH-PPV/dPS Blends," J. Polym. Sci. Pol. Phys. **55**(15), 1142 (2017).

Moseley, D.H., Stavretis, S.E., Thirunavukkuarasu, K., Ozerov, M., Cheng, Y., Daemen, L.L., Ludwig, J., Lu, Z., Smirnov, D., Brown, C.M., Pandey, A., Ramirez-Cuesta, A.J., Lamb, A.C., Atanasov, M., Bill, E., Neese, F., Xue, Z.-L., "Spin-Phonon Couplings in Transition Metal Complexes with Slow Magnetic Relaxation," Nat. Commun. **9**(1), 2572 (2018).

Muckley, E.S., Naguib, M., Wang, H.-W., Vlcek, L., Osti, N.C., Sacci, R.L., Sang, X., Unocic, R.R., Xie, Y., Tyagi, M., Mamontov, E., Page, K.L., Kent, P.R.C., Nanda, J., Ivanov, I.N., "Multimodality of Structural, Electrical, and Gravimetric Responses of Intercalated MXenes to Water," ACS Nano **11**(11), 11118 (2017). [CHRNS]

Mueller, E., Alsop, R.J., Scotti, A., Bleul, M., Rheinstädter, M.C., Richtering, W., Hoare, T., "Dynamically Cross-Linked Self-Assembled Thermoresponsive Microgels with Homogeneous Internal Structures," Langmuir **34**(4), 1601 (2018). [CHRNS]

Mumm, P., "Resolving the Neutron Lifetime Puzzle," Science **360**(6389), 605 (2018).

Nagao, M., Kelley, E.G., Ashkar, R., Bradbury, R., Butler, P.D., "Probing Elastic and Viscous Properties of Phospholipid Bilayers using Neutron Spin Echo Spectroscopy," J. Phys. Chem. Lett. **8**(19), 4679 (2017). [CHRNS]

Nagao, M., "Structure and Dynamics of Lipid Bilayers Measured by Neutron Scattering Techniques," J. Pharm. Sci. Technol. **78**(1), 34 (2018). [CHRNS]

Nair, H.S., Brown, J.M., Coldren, E., Hester, G., Gelfand, M.P., Podlesnyak, A., Huang, Q., Ross, K.A., "Short-Range Order in the Quantum XXZ Honeycomb Lattice Material $BaCo_2(PO_4)_2$," Phys. Rev. B **97**(13), 134409 (2018).

Nakasone, M.A., Lewis, T.A., Walker, O., Thakur, A., Mansour, W., Castañeda, C.A., Goeckeler-Fried, J.L., Parlati, F., Chou, T.-F., Hayat, O., Zhang, D., Camara, C.M., Bonn, S.M., Nowicka, U.K., Krueger, S., Glickman, M.H., Brodsky, J.L., Deshaies, R.J., Fushman, D., "Structural Basis for the Inhibitory Effects of Ubistatins in the Ubiquitin-Proteasome Pathway," Structure **25**(12), 1839 (2017). [CHRNS]

Nanda, H., Garcia Sakai, V., Khodadadi, S., Tyagi, M., Schwalbach, E.J., Curtis, J.E., "Relaxation Dynamics of Saturated and Unsaturated Oriented Lipid Bilayers," Soft Matter, in press. [CHRNS]

Need, R.F., Isaac, B.J., Kirby, B.J., Borchers, J.A., Stemmer, S., Wilson, S.D., "Octahedral Tilt Independent Magnetism in Confined $GdTiO_3$ Films," Appl. Phys. Lett. **112**(13), 132407 (2018).

Need, R.F., Marshall, P.B., Kenney, E., Suter, A., Prokscha, T., Salman, Z., Kirby, B.J., Stemmer, S., Graf, M.J., Wilson, S.D., "Quasistatic Antiferromagnetism in the Quantum Wells of $SmTiO_3/SrTiO_3$ Heterostructures," npj Quantum Materials **3**(1), 7 (2018).

Nemoto, F., Kofu, M., Nagao, M., Ohishi, K., Takata, S.-I., Suzuki, J.-I., Yamada, T., Shibata, K., Ueki, T., Kitazawa, Y., Watanabe, M., Yamamuro, O., "Neutron Scattering Studies on Short- and Long-Range Layer Structures and Related Dynamics in Imidazolium-based Ionic Liquids," J. Chem. Phys., in press. [CHRNS]

Nieuwendaal, R.C., DeLongchamp, D.M., Richter, L.J., Snyder, C.R., Jones, R.L., Engmann, S., Herzing, A., Heeney, M., Fei, Z., Sieval, A.B., Hummelen, J.C., "Characterization of Interfacial Structure in Polymer-Fullerene Bulk Heterojunctions via ^{13}C {^2H} Rotational Echo Double Resonance NMR," Phys. Rev. Lett. **121**(2), 026101 (2018).

Nikitin, S.E., Portnichenko, P.Y., Dukhnenko, A.V., Shitsevalova, N.Y., Filipov, V.B., Qiu, Y., Rodriguez-Rivera, J.A., Ollivier, J., Inosov, D.S., "Doping-Induced Redistribution of Magnetic Spectral Weight in the Substituted Hexaborides $Ce_{1-x}La_xB_6$ and $Ce_{1-x}Nd_xB_6$," Phys. Rev. B **97**(7), 075116 (2018). [CHRNS]

Nolan, M.C., Fuentes Caparrós, A.M., Dietrich, B., Barrow, M., Cross, E.R., Bleuel, M., King, S.M., Adams, D.J., "Optimising Low Molecular Weight Hydrogels for Automated 3D Printing," Soft Matter **13**(45), 8426 (2017). [CHRNS]

Nouhi, S., Hellsing, M.S., Kapaklis, V., Rennie, A.R., "Grazing-Incidence Small-Angle Neutron Scattering from Structures below an Interface," J. Appl. Crystallogr. **50**(4), 1066 (2017). [CHRNS]

Nsofini, J., Sarenac, D., Ghofrani, K., Huber, M.G., Arif, M., Cory, D.G., Pushin, D.A., "Noise Refocusing in a Five-Blade Neutron Interferometer," J. Appl. Phys. **122**(5), 054501 (2017).

Oberdick, S.D., Abdelgawad, A., Moya, C., Mesbahi-Vasey, S., Kepaptsoglou, D., Lazarov, V.K., Evans, R.F.L., Meilak, D., Skoropata, E., van Lierop, J., Hunt-Isaak, I., Pan, H., Ijiri, Y., Krycka, K.L., Borchers, J.A., Majetich, S.A., "Spin Canting Across Core/Shell $Fe_3O_4/Mn_xFe_{3-x}O_4$ Nanoparticles," Sci. Rep. **8**(1), 3425 (2018). [CHRNS]

Omasta, T.J., Park, A.M., LaManna, J.M., Zhang, Y., Peng, X., Wang, L., Jacobson, D.L., Varcoe, J.R., Hussey, D.S., Pivovar, B.S., Mustain, W.E., "Beyond Catalysis and Membranes: Visualizing and Solving the Challenge of Electrode Water Accumulation and Flooding in AEMFCs," Energ. Environ. Sci. **11**(3), 551 (2018).

Omasta, T.J., Park, A.M., LaManna, J.M., Zhang, Y., Peng, X., Wang, L., Jacobson, D.L., Varcoe, J.R., Hussey, D.S., Pivovar, B.S., Mustain, W.E., "Correction: Beyond Catalysis and Membranes: Visualizing and Solving the Challenge of Electrode Water Accumulation and Flooding in AEMFCs," Energ. Environ. Sci. **11**(4), 995 (2018).

Orlandi, F., Aza, E., Bakaimi, I., Kiefer, K., Klemke, B., Zorko, A., Arčon, D., Stock, C., Tsibidis, G.D., Green, M.A., Manuel, P., Lappas, A., "Incommensurate Atomic and Magnetic Modulations in the Spin-Frustrated β-$NaMnO_2$ Triangular Lattice," Phys. Rev. Mater. **2**(7), 074407 (2018).

Osovizky, A., Pritchard, K., Yehuda-Zada, Y., Ziegler, J., Binkley, E., Tsai, P., Thompson, A., Hadad, N., Jackson, M., Hurlbut, C., Baltic, G.M., Majkrzak, C.F., Maliszewskyj, N.C., "Design of an Ultrathin Cold Neutron Detector," Nucl. Instrum. Methods Phys. Res., Sect. A **893**, 1 (2018).

Osovizky, A., Pritchard, K., Yehuda-Zada, Y., Ziegler, J.B., Tsai, P., Ghelman, M., Thompson, A.K., Ibberson, R.M., Baltic, G.M., Majkrzak, C.F., Maliszewskyj, N.C., "Selection of Silicon Photomultipliers for a $^6LiF:ZnS(Ag)$ Scintillator based Cold Neutron Detector," J. Phys. Commun. **2**(4), 045009 (2018).

Osovizky, A., Pritchard, K., Ziegler, J., Binkley, E., Yehuda-Zada, Y., Tsai, P., Thompson, A., Cooksey, C., Siebein, K., Hadad, N., Jackson, M., Hurlbut, C., Ibberson, R., Baltic, G.M., Majkrzak, C.F., Maliszewskyj, N.C., "^{6}LiF:ZnS(Ag) Mixture Optimization for a Highly Efficient Ultrathin Cold Neutron Detector," IEEE T. Nucl. Sci. **65**(4), 1025 (2018).

Osti, N.C., Dyatkin, B., Thompson, M.W., Tiet, F., Zhang, P., Dai, S., Tyagi, M., Cummings, P.T., Gogotsi, Y., Wesolowski, D.J., Mamontov, E., "Influence of Humidity on Performance and Microscopic Dynamics of Ionic Liquid in Supercapacitor," Phys. Rev. Mater. **1**(3), 035402 (2017). [CHRNS]

Palacios-Hernandez, T., Luo, H., Garcia, E.A., Pacheco, L.A., Herrera-Alonso, M., "Nanoparticles from Amphiphilic Heterografted Macromolecular Brushes with Short Backbones," Macromolecules **51**(8), 2831 (2018).

Pasco, C.M., Trump, B.A., Tran, T.T., Kelly, Z.A., Hoffmann, C., Heinmaa, I., Stern, R., McQueen, T.M., "Single-Crystal Growth of $Cu_4(OH)_6BrF$ and Universal Behavior in Quantum Spin Liquid Candidates Synthetic Barlowite and Herbertsmithite," Phys. Rev. Mater. **2**(4), 044406 (2018).

Pena-Francesch, A., Jung, H., Hickner, M.A., Tyagi, M., Allen, B.D., Demirel, M.C., "Programmable Proton Conduction in Stretchable and Self-Healing Proteins," Chem. Mater. **30**(3), 898 (2018). [CHRNS]

Perry, W.L., Clements, B., Ma, X., Mang, J.T., "Relating Microstructure, Temperature, and Chemistry to Explosive Ignition and Shock Sensitivity," Combust. Flame **190**, 171 (2018). [CHRNS]

Peryshkov, D.V., Bukovsky, E.V., Lacroix, M.R., Wu, H., Zhou, W., Jones, W.M., Lozinšek, M., Folsom, T.C., Heyliger, D.L., Udovic, T.J., Strauss, S.H., "Latent Porosity in Alkali-Metal $M_2B_{12}F_{12}$ Salts: Structures and Rapid Room-Temperature Hydration/Dehydration Cycles," Inorg. Chem. **56**(19), 12023 (2017).

Phelan, D., Han, F., Lopez-Bezanilla, A., Krogstad, M.J., Gim, Y., Rong, Y., Zhang, J., Parshall, D., Zheng, H., Cooper, S.L., Feygenson, M., Yang, W., Chen, Y.-S., "Structural Properties of Barium Stannate," J. Solid State Chem. **262**, 142 (2018).

Plumb, K.W., Stock, C., Rodriguez-Rivera, J.A., Castellan, J.-P., Taylor, J.W., Lau, B., Wu, W., Julian, S.R., Kim, Y.-J., "From Mean-Field Localized Magnetism to Itinerant Spin Fluctuations in the 'Nonmetallic metal' FeCrAs," Phys. Rev. B **97**(18), 184431 (2018). [CHRNS]

Poges, S., Jin, J., Guild, C., Li, W.-N., Birnkrant, M., Suib, S.L., "Preparation and Characterization of Aluminum Coatings via Electroless Plating onto Nickel Nanowires using Ionic Liquid Plating Solution," Mater. Chem. Phys. **207**, 303 (2018). [CHRNS]

Pokharel, G., May, A.F., Parker, D.S., Calder, S., Ehlers, G., Huq, A., Kimber, S.A.J., Arachchige, H.S., Poudel, L., McGuire, M.A., Mandrus, D., Christianson, A.D., "Negative Thermal Expansion and Magnetoelastic Coupling in the Breathing Pyrochlore Lattice Material $LiGaCr_4S_8$," Phys. Rev. B **97**(13), 134117 (2018).

Poling-Skutvik, R., Olafson, K.N., Narayanan, S., Stingaciu, L., Faraone, A., Conrad, J.C., Krishnamoorti, R., "Confined Dynamics of Grafted Polymer Chains in Solutions of Linear Polymer," Macromolecules **50**(18), 7372 (2017). [CHRNS]

Poudel, L., de la Cruz, C., Koehler, M.R., McGuire, M.A., Keppens, V., Mandrus, D., Christianson, A.D., "$LaCu_{6-x}Ag_x$: A Promising Host of an Elastic Quantum Critical Point," Physica B **536**, 479 (2018).

Prisk, T.R., Bryan, M.S., Sokol, P.E., Granroth, G.E., Moroni, S., Boninsegni, M., "The Momentum Distribution of Liquid ^{4}He," J. Low Temp. Phys. **189**(3-4), 158 (2017).

Prisk, T.R., Hoffmann, C., Kolesnikov, A.I., Mamontov, E., Podlesnyak, A.A., Wang, X., Kent, P.R.C., Anovitz, L.M., "Fast Rotational Diffusion of Water Molecules in a 2D Hydrogen Bond Network at Cryogenic Temperatures," Phys. Rev. Lett. **120**(19), 196001 (2018).

Provo, J.L., "History of Very Thick Film and Bulk Sample Group IIIB, IVB, VB, and Rare Earth Materials for Various Vacuum Applications," J. Vac. Sci. Technol. A **36**(4), 041602 (2018).

Pushin, D.A., Sarenac, D., Nsofini, J., Hincks, I., Miguel, P., Huber, M., Heacock, B., Arif, M., Clark, C.W., Cory, D.G., "Structured Waves: from Matter to Light," in "Imaging and Applied Optics 2018 (3D, AIO, AO, COSI, DH, IS, LACSEA, LSC, MATH, pcAOP)," edited by Optical Society of America, (Optical Society of America, June 2018, Orlando, FL) **SW2H**, SW2H.3 (2018).

Qiu, J., Mongcopa, K.I., Han, R., López-Barrón, C.R., Robertson, M.L., Krishnamoorti, R., "Thermodynamic Interactions in a Model Polydiene/Polyolefin Blend Based on 1,2-Polybutadiene," Macromolecules **51**(8), 3107 (2018). [CHRNS]

Qu, G., Zhao, X., Newbloom, G.M., Zhang, F., Mohammadi, E., Strzalka, J.W., Pozzo, L.D., Mei, J., Diao, Y., "Understanding Interfacial Alignment in Solution Coated Conjugated Polymer Thin Films," ACS Appl. Mater. Interfaces **9**(33), 27863 (2017). [CHRNS]

Rahalkar, A., Wei, G., Nieuwendaal, R., Prabhu, V.M., Srivastava, S., Levi, A.E., de Pablo, J.J., Tirrell, M.V., "Effect of Temperature on the Structure and Dynamics of Triblock Polyelectrolyte Gels," J. Chem. Phys., in press.

Reid, D.R., Jackson, N.E., Bourque, A.J., Snyder, C.R., Jones, R.L., de Pablo, J.J., "Aggregation and Solubility of a Model Conjugated Donor-Acceptor Polymer," J. Phys. Chem. Lett., in press.

Reimann, T., Schulz, M., Mildner, D.F.R., Bleuel, M., Brûlet, A., Harti, R.P., Benka, G., Bauer, A., Böni, P., Mühlbauer, S., "Domain Formation in the Type-II/1 Superconductor Niobium: Interplay of Pinning, Geometry, and Attractive Vortex-Vortex Interaction," Phys. Rev. B **96**(14), 144506 (2017). [CHRNS]

Rezhdo, O., Di Maio, S., Le, P., Littrell, K.C., Carrier, R.L., Chen, S.-H., "Characterization of Colloidal Structures During Intestinal Lipolysis using Small-Angle Neutron Scattering," J. Colloid Interf. Sci. **499**, 189 (2018). [CHRNS]

Richards, J.J., Hipp, J.B., Riley, J.K., Wagner, N.J., Butler, P.D., "Clustering and Percolation in Suspensions of Carbon Black," Langmuir **33**(43), 12260 (2017). [CHRNS]

Richards, J.J., Wagner, N.J., Butler, P.D., "A Strain-Controlled RheoSANS Instrument for the Measurement of the Microstructural, Electrical, and Mechanical Properties of Soft Materials," Rev. Sci. Instrum. **88**(10), 105115 (2017).

Richter, A.G., Dergunov, S.A., Kim, M.D., Shmakov, S.N., Pingali, S.V., Urban, V.S., Liu, Y., Pinkhassik, E., "Unraveling the Single-Nanometer Thickness of Shells of Vesicle-Templated Polymer Nanocapsules," J. Phys. Chem. Lett. **8**(15), 3630 (2017).

Riest, J., Nägele, G., Liu, Y., Wagner, N.J., Godfrin, P.D., "Short-Time Dynamics of Lysozyme Solutions with Competing Short-Range Attraction and Long-Range Repulsion: Experiment and Theory," J. Chem. Phys. **148**(6), 065101 (2018). [CHRNS]

Riley, J.K., Richards, J.J., Wagner, N.J., Butler, P.D., "Branching and Alignment in Reverse Worm-Like Micelles Studied with Simultaneous Dielectric Spectroscopy and RheoSANS," Soft Matter **14**(26), 5344 (2018).

Rostovtseva, T.K., Gurnev, P.A., Hoogerheide, D.P., Rovini, A., Sirajuddin, M., Bezrukov, S.M., "Sequence Diversity of Tubulin Isotypes in Regulation of the Mitochondrial Voltage-Dependent Anion Channel," J. Biol. Chem. **293**(28), 10949 (2018).

Salunke, N., Nallapaneni, A., Yuan, G., Stafford, C.M., Niu, H., Shawkey, M.D., Weiss, R.A., Karim, A., "Film Confinement Induced 'Jump-Percolation' Wetting Transition in Amphiphilic Block Copolymer Films," ACS Appl. Mater. Interfaces **9**(40), 35349 (2017).

Sarenac, D., Pushin, D.A., Huber, M.G., Hussey, D.S., Miao, H., Arif, M., Cory, D.G., Cronin, A.D., Heacock, B., Jacobson, D.L., LaManna, J.M., Wen, H., "Three Phase-Grating Moiré Neutron Interferometer for Large Interferometer Area Applications," Phys. Rev. Lett. **120**(11), 113201 (2018).

Sarte, P.M., Aczel, A.A., Ehlers, G., Stock, C., Gaulin, B.D., Mauws, C., Stone, M.B., Calder, S., Nagler, S.E., Hollett, J.W., Zhou, H.D., Gardner, J.S., Attfield, J.P., Wiebe, C.R., "Evidence for the Confinement of Magnetic Monopoles in Quantum Spin Ice," J. Phys.: Condens. Matter **29**(45), 45LT01 (2017).

Savoji, M.T., Zhao, D., Muisener, R.J., Schimossek, K., Schoeller, K., Lodge, T.P., Hillmyer, M.A., "Poly(Alkyl Methacrylate)-Grafted Polyolefins as Viscosity Modifiers for Engine Oil: A New Mechanism for Improved Performance," Ind. Eng. Chem. Res. **57**(6), 1840 (2018).

Schantz, A.B., Ren, T., Pachalla, A., Shen, Y., Hickey, R.J., Kumar, M., "Porous Vesicles with Extrusion-Tunable Permeability and Pore Size from Mixed Solutions of PEO-PPO-PEO Triblock Copolymers," Macromol. Chem. Physic. **219**(9), 1700620 (2018).

Scheie, A., Kindervater, J., Säubert, S., Duvinage, C., Pfleiderer, C., Changlani, H.J., Zhang, S., Harriger, L., Arpino, K., Koohpayeh, S.M., Tchernyshyov, O., Broholm, C., "Reentrant Phase Diagram of $Yb_2Ti_2O_7$ in a ⟨111⟩ Magnetic Field," Phys. Rev. Lett. **119**(12), 127201 (2017).

Senses, E., Tyagi, M., Natarajan, B., Narayanan, S., Faraone, A., "Chain Dynamics and Nanoparticle Motion in Attractive Polymer Nanocomposites Subjected to Large Deformations," Soft Matter **13**(43), 7922 (2017). [CHRNS]

Senses, E., Narayanan, S., Mao, Y., Faraone, A., "Nanoscale Particle Motion in Attractive Polymer Nanocomposites," Phys. Rev. Lett. **119**(23), 237801 (2017).

Shaffer, D.L., LaManna, J.M., Jacobson, D.L., Hussey, D.S., Elimelech, M., Chan, E.P., "Studying Water and Solute Transport through Desalination Membranes via Neutron Radiography," J. Membrane Sci. **548**, 667 (2018).

Shamblin, J., Dun, Z., Lee, M., Johnston, S., Choi, E.S., Page, K., Qiu, Y., Zhou, H., "Structural and Magnetic Short-Range Order in Fluorite Yb_2TiO_5," Phys. Rev. B **96**(17), 174418 (2017). [CHRNS]

Shen, F.-R., Kuang, H., Hu, F.-X., Wu, H., Huang, Q.-Z., Liang, F.-X., Qiao, K.-M., Li, J., Wang, J., Liu, Y., Zhang, L., He, M., Zhang, Y., Zuo, W.-L., Sun, J.-R., Shen, B.-G., "Ultra-Low Thermal Expansion Realized in Giant Negative Thermal Expansion Materials through Self-Compensation," APL Mater. **5**(10), 106102 (2017).

Sheridan, R.J., Orski, S.V., Jones, R.L., Satija, S.K., Beers, K.L., "Surface Interaction Parameter Measurement of Solvated Polymers via Model End-Tethered Chains," Macromolecules **50**(17), 6668 (2017).

Shu, S., Almirall, N., Wells, P.B., Yamamoto, T., Odette, G.R., Morgan, D.D., "Precipitation in Fe-Cu and Fe-Cu-Mn Model Alloys under Irradiation: Dose Rate Effects," Acta Mater., in press.

Shu, S., Wirth, B.D., Wells, P.B., Morgan, D.D., Odette, G.R., "Multi-Technique Characterization of the Precipitates in Thermally Aged and Neutron Irradiated Fe-Cu and Fe-Cu-Mn Model Alloys: Atom Probe Tomography Reconstruction Implications," Acta Mater. **146**, 1 (2018).

Siderius, D.W., Krekelberg, W.P., Chiang, W.-S., Shen, V.K., Liu, Y., "Quasi-Two-Dimensional Phase Transition of Methane Adsorbed in Cylindrical Silica Mesopores," Langmuir **33**(50), 14252 (2017). [CHRNS]

Silverstein, H.J., Sinclair, R., Sharma, A., Qiu, Y., Heinmaa, I., Leitmäe, A., Wiebe, C.R., Stern, R., Zhou, H., "Naturally Tuned Quantum Critical Point in the $S = 1$ Kagomé $YCa_3(VO)_3(BO_3)_4$," Phys. Rev. Mater. **2**(4), 044006 (2018).

Skripov, A.V., Isnard, O., Mushnikov, N.V., Terent'ev, P.B., Gaviko, V.S., Udovic, T.J., "Hydrogen Dynamics in the Hexagonal $Ho_2Fe_{17}H_4$ and $Y_2Fe_{17}H_{4.2}$: Inelastic and Quasielastic Neutron Scattering Studies," J. Alloy Compd. **720**, 277 (2017). [CHRNS]

Skripov, A.V., Skoryunov, R.V., Soloninin, A.V., Babanova, O.A., Stavila, V., Udovic, T.J., "Nuclear Magnetic Resonance Study of Anion and Cation Reorientational Dynamics in $(NH_4)_2B_{12}H_{12}$," J. Phys. Chem. C **122**(6), 3256 (2018).

Sowards, J.W., Hussey, D.S., Jacobson, D.L., Ream, S., Williams, P., "Correlation of Neutron-Based Strain Imaging and Mechanical Behavior of Armor Steel Welds Produced with the Hybrid Laser Arc Welding Process," J. Res. Natl. Inst. Stan. **123**, 123011 (2018).

Stariha, S., Wilson, M.S., LaManna, J.M., Jacobson, D.L., Hussey, D.S., Macauley, N., Rau, J.A., Borup, R.L., "Determining Water Content and Distribution in PEMFCs to Predict Aging While in Storage," ECS Transactions **80**(8), 377 (2017).

Steinbach, A.J., Allen, J.S., Borup, R.L., Hussey, D.S., Jacobson, D.L., Komlev, A., Kwong, A., MacDonald, J., Mukundan, R., Pejsa, M.J., Roos, M., Santamaria, A.D., Sieracki, J.M., Spernjak, D., Zenyuk, I.V., Weber, A.Z., "Anode-Design Strategies for Improved Performance of Polymer-Electrolyte Fuel Cells with Ultra-Thin Electrodes," Joule **2**(7), 1297 (2018).

Stimpson, L.J.V., Rodriquez, E.E., Brown, C.M., Stenning, G.B.G., Jura, M., Arnold, D.C., "Magnetic Ordering in a Frustrated Bow-Tie Lattice," J. Mater. Chem. C **6**(16), 4541 (2018).

Stock, C., Rodriguez, E.E., Lee, N., Demmel, F., Fouquet, P., Laver, M., Niedermayer, C., Su, Y., Nemkovski, K., Green, M.A., Rodriguez-Rivera, J.A., Kim, J.W., Zhang, L., Cheong, S.-W., "Orphan Spins in the $S = \frac{5}{2}$ Antiferromagnet $CaFe_2O_4$," Phys. Rev. Lett. **119**(25), 257204 (2017). [CHRNS]

Stock, C., Gehring, P.M., Ewings, R.A., Xu, G., Li, J., Viehland, D., Luo, H., "Spontaneous Decay of a Soft Optical Phonon in the Relaxor Ferroelectric $PbMg_{1/3}Nb_{2/3}O_3$," Phys. Rev. Mater. **2**(2), 024404 (2018).

Stock, C., Rodriguez-Rivera, J.A., Schmalzl, K., Demmel, F., Singh, D.K., Ronning, F., Thompson, J.D., Bauer, E.D., "From Ising Resonant Fluctuations to Static Uniaxial Order in Antiferromagnetic and Weakly Superconducting $CeCo(In_{1-x}Hg_x)_5$ ($x = 0.01$)," Phys. Rev. Lett. **121**(3), 037003 (2018). [CHRNS]

Strobel, T.A., Ramirez-Cuesta, A.J., Daemen, L.L., Bhadram, V.S., Jenkins, T.A., Brown, C.M., Chen, Y., "Quantum Dynamics of H_2 Trapped within Organic Clathrate Cages," Phys. Rev. Lett. **120**(12), 120402 (2018).

Summers, B., Chen, Y., Dahal, A., Singh, D.K., "New Description of Evolution of Magnetic Phases in Artificial Honeycomb Lattice," Sci. Rep. **7**(1), 16080 (2017).

Sun, X., Faraone, A., Dai, Q., Guo, S., "A New Approach of Quantitatively Analyzing Water States by Neutron Scattering in Hardened Cement Paste," Mater. Charact. **136**, 134 (2018). [CHRNS]

Sun, X., Guo, S., Dai, Q., Xiao, X., "Microstructure Characterization of Alkali-Glass Particle and Alkali-Glass Powder Reacted Gels with Neutron Scattering and Imaging Techniques," Mater. Charact. **131**, 98 (2017). [CHRNS]

Svanidze, E., Georgen, C., Hallas, A.M., Huang, Q., Santiago, J.M., Lynn, J.W., Morosan, E., "Band Jahn-Teller Structural Phase Transition in Y_2In," Phys. Rev. B **97**(5), 054111 (2018).

Sypek, J.T., Yu, H., Dusoe, K.J., Drachuck, G., Patel, H., Giroux, A.M., Goldman, A.I., Kreyssig, A., Canfield, P.C., Bud'ko, S.L., Weinberger, C.R., Lee, S.-W., "Superelasticity and Cryogenic Linear Shape Memory Effects of $CaFe_2As_2$," Nat. Commun. **8**(1), 1083 (2017).

Tabatabai, A.P., Weigandt, K.M., Blair, D.L., "Acid-Induced Assembly of a Reconstituted Silk Protein System," Phys. Rev. E **96**(2), 022405 (2017).

Tang, W.S., Dimitrievska, M., Stavila, V., Zhou, W., Wu, H., Talin, A.A., Udovic, T.J., "Order-Disorder Transitions and Superionic Conductivity in the Sodium *Nido*-Undeca(carba)borates," Chem. Mater. **29**(24), 10496 (2017). [CHRNS]

Tanino, Y., Syed, A., "*In-Situ* Imaging of Fractured Rock and Flow through Them using Simultaneous Neutron and X-ray Computed Tomography, EPSRC," Impact **2017**(7), 61 (2017).

Taylor, M.K., Runčevski, T., Oktawiec, J., Bachman, J.E., Siegelman, R.L., Jiang, H., Mason, J.A., Tarver, J.D., Long, J.R., "Near-Perfect CO_2/CH_4 Selectivity Achieved through Reversible Guest Templating in the Flexible Metal-Organic Framework Co(bdp)," J. Am. Chem. Soc., in press.

Tehrani, M., Etampawala, T.N.B., Dadmun, M., Hossain, M.A., "Resolving Hierarchical Structures in Carbon Nanotube Networks using Small- and Ultrasmall-Angle Neutron Scattering," J. Phys. Chem. C **121**(40), 22442 (2017). [CHRNS]

Teixeira, S.C.M., Leão, J.B., Gagnon, C., McHugh, M.A., "High Pressure Cell for Bio-SANS Studies under Sub-Zero Temperatures or Heat Denaturing Conditions," J. Neutron Res. **20**(1), 11 (2018). [CHRNS]

Telang, A., Gnäupel-Herold, T., Gill, A., Vasudevan, V.K., "Effect of Applied Stress and Temperature on Residual Stresses Induced by Peening Surface Treatments in Alloy 600," J. Mater. Eng. Perform. **27**(6), 2796 (2018).

Theis-Bröhl, K., Vreeland, E.C., Gomez, A., Huber, D.L., Saini, A., Wolff, M., Maranville, B.B., Brok, E., Krycka, K.L., Dura, J.A., Borchers, J.A., "Self-Assembled Layering of Magnetic Nanoparticles in a Ferrofluid on Silicon Surfaces," ACS Appl. Mater. Interfaces **10**(5), 5050 (2018).

Toft-Petersen, R., Abrahamsen, A.B., Balog, S., Porcar, L., Laver, M., "Decomposing the Bragg Glass and the Peak Effect in a Type-II Superconductor," Nat. Commun. **9**(1), 901 (2018).

Treiman, A.H., LaManna, J.M., Anovitz, L.M., Hussey, D.S., Jacobson, D.L., "Neutron Computed Tomography of Meteorites: Detecting Hydrogen-Bearing Materials," in "Proceedings of the 49th Lunar and Planetary Science Conference 2018," (49th Lunar and Planetary Science Conference 2018, March 2018, The Woodlands, TX) **49**, 1993 (2018).

Triadan, D., Carrera, E.G., Blackman, M.J., Bishop, R.L., "Sourcing Chihuahuan Polychrome Ceramics: Assessing Medio Period Economic Organization," Lat. Am. Antiq. **29**(1), 143 (2018).

Trinh, V., Xu, J., "An Experimental Study on Flow and Heat Transfer Characteristics of Ethanol/Polyalphaolefin Nanoemulsion Flowing through Circular Minichannels," Nanoscale Res. Lett. **12**(1), 216 (2017).

Trump, B.A., Koohpayeh, S.M., Livi, K.J.T., Wen, J.-J., Arpino, K.E., Ramasse, Q.M., Brydson, R., Feygenson, M., Takeda, H., Takigawa, M., Kimura, K., Nakatsuji, S., Broholm, C.L., McQueen, T.M., "Universal Geometric Frustration in Pyrochlores," Nat. Commun. **9**(1), 2619 (2018).

Turkoglu, D., Chen-Mayer, H., Paul, R., Zeisler, R., "Assessment of PGAA Capability for Low-Level Measurements of H in Ti Alloys," Analyst **142**(20), 3822 (2017).

Valadez-Pérez, N.E., Liu, Y., Castañeda-Priego, R., "Reversible Aggregation and Colloidal Cluster Morphology: The Importance of the Extended Law of Corresponding States," Phys. Rev. Lett. **120**(24), 248004 (2018). [CHRNS]

van Duijn, J., Kim, K.H., Hur, N., Ruiz-Bustos, R., Adroja, D.T., Bridges, F., Daoud-Aladine, A., Fernandez-Alonso, F., Wen, J.J., Kearney, V., Huang, Q.Z., Cheong, S.-W., Perring, T.G., Broholm, C., "Induced Quadrupolar Singlet Ground State of Praseodymium in a Modulated Pyrochlore," Phys. Rev. B **96**(9), 094409 (2017).

Vanegas, J.M., Heinrich, F., Rogers, D.M., Carson, B.D., La Bauve, S., Vernon, B.C., Akgun, B., Satija, S., Zheng, A., Kielian, M., Rempe, S.B., Kent, M.S., "Insertion of Dengue E into Lipid Bilayers Studied by Neutron Reflectivity and Molecular Dynamics Simulations," BBA - Biomembranes **1860**(5), 1216 (2018).

Varma, C.M., Gannon, W.J., Aronson, M.C., Rodriguez-Rivera, J.A., Qiu, Y., "Quantum Critical Singularities in Two-Dimensional Metallic XY Ferromagnets," Phys. Rev. B **97**(8), 085134 (2018). [CHRNS]

Vidyasagar, A., Ku, S.H., Kim, M., Kim, M., Lee, H.S., Pearce, T.R., McCormick, A.V., Bates, F.S., Kokkoli, E., "Design and Characterization of a PVLA-PEG-PVLA Thermosensitive and Biodegradable Hydrogel," ACS Macro Lett. **6**(10), 1134 (2017).

Vu, T., Tran, T.N., Xu, J., "Single-Phase Flow and Heat Transfer Characteristics of Ethanol/Polyalphaolefin Nanoemulsion Fluids in Circular Minichannels," Int. J. Mass Tran. **113**, 324 (2017).

Vural, D., Hu, X., Lindner, B., Jain, N., Miao, Y., Cheng, X., Liu, Z., Hong, L., Smith, J.C., "Quasielastic Neutron Scattering in Biology: Theory and Applications," Biochem. Biophys. Acta **1861**(1), 3638 (2017). [CHRNS]

Walter, J., Yu, G., Yu, B., Grutter, A., Kirby, B., Borchers, J., Zhang, Z., Zhou, H., Birol, T., Greven, M., Leighton, C., "Ion-Gel-Gating-Induced Oxygen Vacancy Formation in Epitaxial $La_{0.5}Sr_{0.5}CoO_{3-\delta}$ Films from *in operando* X-ray and Neutron Scattering," Phys. Rev. Mater. **1**(7), 071403 (2017).

Wang, C., Gong, Y., Dai, J., Zhang, L., Xie, H., Pastel, G., Liu, B., Wachsman, E., Wang, H., Hu, L., "*In Situ* Neutron Depth Profiling of Lithium Metal-Garnet Interfaces for Solid State Batteries," J. Am. Chem. Soc. **139**(40), 14257 (2017).

Wang, E., Lu, J., Bates, F.S., Lodge, T.P., "Effect of Corona Block Length on the Structure and Chain Exchange Kinetics of Block Copolymer Micelles," Macromolecules **51**(10), 3563 (2018).

Wang, F., Borodin, O., Gao, T., Fan, X., Sun, W., Han, F., Faraone, A., Dura, J.A., Xu, K., Wang, C., "Highly Reversible Zinc Metal Anode for Aqueous Batteries," Nat. Mater. **17**(6), 543 (2018).

Wang, H., Bao, Z., Wu, H., Lin, R.-B., Zhou, W., Hu, T.-L., Li, B., Zhao, J.C.-G., Chen, B., "Two Solvent-Induced Porous Hydrogen-Bonded Organic Frameworks: Solvent Effects on Structures and Functionalities," Chem. Commun. **53**(81), 11150 (2017).

Wang, H., Cao, H., Zhang, W., Chen, J., Wu, H., Pistidda, C., Ju, X., Zhou, W., Wu, G., Etter, M., Klassen, T., Dornheim, M., Chen, P., "Li_2NH-$LiBH_4$: A Complex Hydride with Near Ambient Hydrogen Adsorption and Fast Lithium Ion Conduction," Chem.- Eur. J. **24**(6), 1342 (2018).

Wang, J., Feng, Y., Agrawal, N.R., Raghavan, S.R., "Wormlike Micelles *versus* Water-Soluble Polymers as Rheology-Modifiers: Similarities and Differences," Phys. Chem. Chem. Phys. **19**(36), 24458 (2017). [CHRNS]

Wang, S., Zhao, W., Lee, T.S., Singer, S.W., Simmons, B.A., Singh, S., Yuan, Q., Cheng, G., "Dimethyl Sulfoxide Assisted Ionic Liquid Pretreatment of Switchgrass for Isoprenol Production," ACS Sustain. Chem. Eng. **6**(3), 4354 (2018). [CHRNS]

Wang, W., Song, Y., Hu, D., Li, Y., Zhang, R., Harriger, L.W., Tian, W., Cao, H., Dai, P., "Local Breaking of Fourfold Rotational Symmetry by Short-Range Magnetic Order in Heavily Overdoped $Ba(Fe_{1-x}Cu_x)_2As_2$," Phys. Rev. B **96**(16), 161106 (2017).

Wang, Z., Mao, Y., Jarumaneeroj, C., Thitisak, B., Tiyapiboonchaiya, P., Rungswang, W., Hsiao, B.S., "The Influence of Short Chain Branch on Formation of Shish-Kebab Crystals in Bimodal Polyethylene under Shear at High Temperatures," J. Polym. Sci. Pol. Phys. **56**(10), 786 (2018).

Weaver, J.L., Turkoglu, D., "Investigation of Alteration of ^{6}Li Enriched Neutron Shielding Glass," T. Am. Nucl. Soc. **117**, 1166 (2017).

Weaver. J.L., Pearce, C.I., Sjöblom, R., McCloy, J.S., Miller, M., Varga, T., Arey, B.W., Conroy, M.A., Peeler, D.K., Koestler, R.J., DePriest, P.T., Vicenzi, E.P., Hjärthner-Holdar, E., Ogenhall, E., Kruger, A.A., "Pre-Viking Swedish Hillfort Glass: A Prospective Long-Term Alteration Analogue for Vitrified Nuclear Waste," Int. J. Appl. Glass Sci., in press.

Weber, F., Parshall, D., Pintschovius, L., Castellan, J.-P., Kauth, M., Merz, M., Wolf, T., Schütt, M., Schmalian, J., Fernandes, R.M., Reznik, D., "Soft Phonons Reveal the Nematic Correlation Length in $Ba(Fe_{0.94}Co_{0.06})_2As_2$," Phys. Rev. B **98**(1), 014516 (2018).

Wei, G., Prabhu, V.M., Piunova, V.A., Carr, A.C., Swope, W.C., Miller, R.D., "Spatial Distribution of Hydrophobic Drugs in Model Nanogel-Core Star Polymers," Macromolecules **50**(24), 9702 (2017).

Wei, Y., Xu, Y., Faraone, A., Hore, M.J.A., "Local Structure and Relaxation Dynamics in the Brush of Polymer-Grafted Silica Nanoparticles," ACS Macro Lett. **7**(6), 699 (2018). [CHRNS]

Weinrich, M., Worcester, D.L., Bezrukov, S.M., "Lipid Nanodomains Change Ion Channel Function," Nanoscale **9**(35), 13291 (2017).

Weitzhandler, I., Dzuricky, M., Hoffmann, I., Garcia Quiroz, F., Gradzielski, M., Chilkoti, A., "Micellar Self-Assembly of Recombinant Resilin-/Elastin-Like Block Copolypeptides," Biomacromolecules **18**(8), 2419 (2017). [CHRNS]

Wen, H.-M., Li, L., Lin, R.-B., Li, B., Hu, B., Zhou, W., Hu, J., Chen, B., "Fine-Tuning of Nano-Traps in a Stable Metal-Organic Framework for Highly Efficient Removal of Propyne from Propylene," J. Mater. Chem. A **6**(16), 6931 (2018).

Wen, H.-M., Li, B., Li, L., Lin, R.-B., Zhou, W., Qian, G., Chen, B., "A Metal-Organic Framework with Optimized Porosity and Functional Sites for High Gravimetric and Volumetric Methane Storage Working Capacities," Adv. Mater. **30**(16), 1704792 (2018).

Weston, J.S., Harwell, J.H., Grady, B.P., "Rheological Characterization of Yield Stress Gels Formed *via* Electrostatic Heteroaggregation of Metal Oxide Nanoparticles," Soft Matter **13**(38), 6743 (2017). [CHRNS]

Weston, J.S., Seeman, D.P., Blair, D.L., Salipante, P.F., Hudson, Steven D., Weigandt, K.M., "Simultaneous Slit Rheometry and *In Situ* Neutron Scattering," Rheol. Acta **57**(3), 241 (2018). [CHRNS]

Wiechert, A.I., Liao, W.-P., Hong, E., Halbert, C.E., Yiacoumi, S., Saito, T., Tsouris, C., "Influence of Hydrophilic Groups and Metal-Ion Adsorption on Polymer-Chain Conformation of Amidoxime-Based Uranium Adsorbents," J. Colloid Interf. Sci., in press.

Worcester, D.L., Faraone, A., Zaccai, G., "The Summer of 1954 and Paths to the Institut Laue-Langevin," Neutron News **28**(3), 15 (2017).

Worthington, P., Drake, K.M., Li, Z., Napper, A.D., Pochan, D.J., Langhans, S.A., "Beta-Hairpin Hydrogels as Scaffolds for High-throughput Drug Discovery in Three-Dimensional Cell Culture," Anal. Biochem. **535**, 25 (2017).

Xi, Y., Li, D.S., Newbloom, G.M., Tatum, W.K., O'Donnell, M., Luscombe, C.K., Pozzo, L.D., "Sonocrystallization of Conjugated Polymers with Ultrasound Fields," Soft Matter **14**(24), 4963 (2018). [CHRNS]

Xiao, Y., Liu, T., Liu, J., He, L., Chen, J., Zhang, J., Luo, P., Lu, H., Wang, R., Zhu, W., Hu, Z., Teng, G., Xin, C., Zheng, J., Liang, T., Wang, F., Chen, Y., Huang, Q., Pan, F., Chen, H., "Insight into the Origin of Lithium/Nickel Ions Exchange in Layered Li $(Ni_xMn_yCo_z)O_2$ Cathode Materials," Nano Energy **49**, 77 (2018).

Xie, R., López-Barrón, C.R., Greene, D.G., Wagner, N.J., "Comicellization of Binary PEO-PPO-PEO Triblock Copolymer Mixtures in Ethylammonium Nitrate," Macromolecules **51**(4), 1453 (2018). [CHRNS]

Xie, R., Xie, Y., López-Barrón, C.R., Gao, K.-Z., Wagner, N.J., "Ultra-Stretchable Conductive Iono-Elastomer and Motion Strain Sensor System Developed Therefrom," Technol. Innovation **19**(3), 613 (2018).

Xie, R., López-Barrón, C.R., Wagner, N.J., "Self-Assembly of Block Copolymers in Ionic Liquids," in "Ionic Liquids: Current State and Future Directions, ACS Symposium Series, Vol. 1250," edited by Shiflett, M.B. and Scurto, A.M., (American Chemical Society, Washington, DC) Chap. **5**, 83 (2017). [CHRNS]

Xu, G., Li, B., Wu, H., Zhou, W., Chen, B., "Construction of ntt-Type Metal-Organic Framework from C_2-Symmetry Hexacarboxylate Linker for Enhanced Methane Storage," Cryst. Growth Des. **17**(9), 4795 (2017).

Xu, Z., Schneeloch, J.A., Wen, J., Winn, B.L., Granroth, G.E., Zhao, Y., Gu, G., Zaliznyak, I., Tranquada, J.M., Birgeneau, R.J., Xu, G., "Surprising Loss of Three-Dimensionality in Low-Energy Spin Correlations on Approaching Superconductivity in $Fe_{1+y}Te_{1-x}Se_x$," Phys. Rev. B **96**(13), 134505 (2017).

Xu, Z., Schneeloch, J.A., Yi, M., Zhao, Y., Matsuda, M., Pajerowski, D.M., Chi, S., Birgeneau, R.J., Gu, G., Tranquada, J.M., Xu, G., "Coexistence of Superconductivity and Short-Range Double-Stripe Spin Correlations in Te-Vapor Annealed $FeTe_{1-x}Se_x$ $(x \leqslant 0.2)$," Phys. Rev. B **97**(21), 214511 (2018).

Yamaguchi, T., Yoshida, K., Yamaguchi, T., Nagao, M., Faraone, A., Seki, S., "Decoupling between the Temperature-Dependent Structural Relaxation and Shear Viscosity of Concentrated Lithium Electrolyte," J. Phys. Chem. B **121**(37), 8767 (2017). [CHRNS]

Yamamoto, T., Shitara, K., Kitagawa, S., Kuwabara, A., Kuroe, M., Ishida, K., Ochi, M., Kuroki, K., Fujii, K., Yashima, M., Brown, C.M., Takatsu, H., Tassel, C., Kageyama, H., "Selective Hydride Occupation in BaVO$_{3-x}$H$_x$ ($0.3 \leq x \leq 0.8$) with Face- and Corner-Shared Octahedra," Chem. Mater. **30**(5), 1566 (2018).

Yang, F., Xu, G., Dou, Y., Wang, B., Zhang, H., Wu, H., Zhou, W., Li, J.-R., Chen, B., "A Flexible Metal-Organic Framework with a High Density of Sulfonic Acid Sites for Proton Conduction," Nature Energy **2**(11), 877 (2017).

Yang, J., Xu, F., "Synergistic Reinforcing Mechanisms in Cellulose Nanofibrils Composite Hydrogels: Interfacial Dynamics, Energy Dissipation, and Damage Resistance," Biomacromolecules **18**(8), 2623 (2017).

Yang, L., Cui, X., Yang, Q., Qian, S., Wu, H., Bao, Z., Zhang, Z., Ren, Q., Zhou, W., Chen, B., Xing, H., "A Single-Molecule Propyne Trap: Highly Efficient Removal of Propyne from Propylene with Anion-Pillared Ultramicroporous Materials," Adv. Mater. **30**(10), 1705374 (2018).

Yehuda-Zada, Y., Pritchard, K., Ziegler, J.B., Cooksey, C., Siebein, K., Jackson, M., Hurlbut, C., Kadmon, Y., Cohen, Y., Ibberson, R.M., Majkrzak, C.F., Maliszewskyj, N.C., Orion, I., Osovizky, A., "Optimization of ^{6}LiF:ZnS(Ag) Scintillator Light Yield using GEANT4," Nucl. Instrum. Meth. A **892**, 59 (2018).

Yu, L.L., Browning, J.F., Burdette, C.Q., Caceres, G.C., Chieh, K.D., Davis, W.C., Kassim, B.L., Long, S.E., Murphy, K.E., Oflaz, R., Paul, R.L., Sharpless, K.E., Wood, L.J., Yen, J.H., Zeisler, R., "Development of a Kelp Powder (*Thallus Laminariae*) Standard Reference Material," Anal. Bioanal. Chem. **410**(4), 1265 (2018).

Yu, L.L., Stanoyevitch, R.C., Zeisler, R., "SI Traceable Determination of Arsenic Species in Kelp (*Thallus Laminariae*)" Anal. Methods - UK **9**(29), 4267 (2017).

Yuan, G., Cheng, H., Han, C.C., "The Glass Formation of a Repulsive System with also a Short Range Attractive Potential: A Re-Interpretation of the Free Volume Theory," Polymer **131**, 272 (2017). [CHRNS]

Yuan, G., Han, C.C., "Glass Transition: from Interaction Potential Changes to the Corresponding Structural and Relaxation Responses along the Path of Reaching the Final Equilibrium," Sci. China Chem. **60**(1), 46 (2018). [CHRNS]

Yue, A.T., Anderson, E.S., Dewey, M.S., Gilliam, D.M., Greene, G.L., Laptev, A.B., Nico, J.S., Snow, W.M., "Precision Determination of Absolute Neutron Flux," Metrologia, in press.

Zarzar, J., Shatz, W., Peer, N., Taing, R., McGarry, B., Liu, Y., Greene, D.G., Zarraga, I.E., "Impact of Polymer Geometry on the Interactions of Protein-PEG Conjugates," Biophys. Chem. **236**, 22 (2018).

Zeisler, R., Cho, H., Souza Ribeiro, Jr., I., Shetty, M.G., Turkoglu, D., "On Neutron Activation Analysis with $\gamma\gamma$ Coincidence Spectrometry," J. Radioanal. Nucl. Ch. **314**(1), 513 (2017).

Zeng, Y., López-Barrón, C.R., Kang, S., Eberle, A.P.R., Lodge, T.P., Bates, F.S., "Effect of Branching and Molecular Weight on Heterogeneous Catalytic Deuterium Exchange in Polyolefins," Macromolecules **50**(17), 6849 (2017).

Zhai, X., Grutter, A.J., Yun, Y., Cui, Z., Lu, Y., "Weak Magnetism of Aurivillius-Type Multiferroic Thin Films Probed by Polarized Neutron Reflectivity," Phys. Rev. Mater. **2**(4), 044405 (2018).

Zhang, M., Corona, P.T., Ruocco, N., Alvarez, D., Malo de Molina, P., Mitragotri, S., Helgeson, M.E., "Controlling Complex Nanoemulsion Morphology using Asymmetric Cosurfactants for the Preparation of Polymer Nanocapsules," Langmuir **34**(3), 978 (2018). [CHRNS]

Zhang, M., Zhou, W., Pham, T., Forrest, K.A., Liu, W., He, Y., Wu, H., Yildirim, T., Chen, B., Space, B., Pan, Y., Zaworotko, M.J., Bai, J., "Fine Tuning of MOF-505 Analogues to Reduce Low-Pressure Methane Uptake and Enhance Methane Working Capacity," Angew. Chem. Int. Edit. **56**(38), 11426 (2017).

Zhang, Q., Kale, T.S., Plunkett, E., Shi, W., Kirby, B.J., Reich, D.H., Katz, H.E., "Highly Contrasting Static Charging and Bias Stress Effects in Pentacene Transistors with Polystyrene Heterostructures Incorporating Oxidizable *N,N'*-Bis(4-Methoxyphenyl)aniline Side Chains as Gate Dielectrics," Macromolecules, in press.

Zhang, W., Nguyen, N.A., Murray, R., Xin, J., Mackay, M.E., "A Comparative Study on the Morphology of P3HT:PCBM Solar Cells with the Addition of Fe$_3$O$_4$ Nanoparticles by Spin and Rod Coating Methods," J. Nanopart. Res. **19**(9), 315 (2017). [CHRNS]

Zhang, Z., Tao, J., Xiang, S., Chen, B., Zhou, W., "New Progress of Microporous Metal-Organic Frameworks in CO_2 Capture and Separation," in "Materials and Processes for CO_2 Capture, Conversion, and Sequestration," edited by Li, Lan et. al., (John Wiley & Sons, Hoboken, NJ) Chap. **3**, 112 (2018).

Zhang, Z., Schwanz, D., Narayanan, B., Kotiuga, M., Dura, J.A., Cherukara, M., Zhou, H., Freeland, J.W., Li, J., Sutarto, R., He, F., Wu, C., Zhu, J., Sun, Y., Ramadoss, K., Nonnenmann, S.S., Yu, N., Comin, R., Rabe, K.M., Sankaranarayanan, S.K.R.S., Ramanathan, S., "Perovskite Nickelates as Electric-Field Sensors in Salt Water," Nature **553**(7686), 68 (2018).

Zhang, Z., Orski, S., Woys, A.M., Yuan, G., Zarraga, I., Wagner, N.J., Liu, Y., "Adsorption of Polysorbate 20 and Proteins on Hydrophobic Polystyrene Surfaces Studied by Neutron Reflectometry," Colloid Surface. B, in press.

Zhao, B., Yuan, G., Chu, X., Yang, J., Zhao, J., "Response of a Permanently Charged Polyelectrolyte Brush to External Ions: The Aspects of Structure and Dynamics," Langmuir **34**(23), 6757 (2018).

Zhao, D., Ma, Y., Lodge, T.P., "Exchange Kinetics for a Single Block Copolymer in Micelles of Two Different Sizes," Macromolecules **51**(6), 2312 (2018).

Zhao, J., Jin, Z., Hu, Q., Jin, Z., Barber, T.J., Zhang, Y., Bleuel, M., "Integrating SANS and Fluid-Invasion Methods to Characterize Pore Structure of Typical American Shale Oil Reservoirs," Sci. Rep. **7**(1), 15413 (2017).

Zhao, Y., Lynn, J.W., Thakur, G.S., Haque, Z., Gupta, L.C., Ganguli, A.K., "Magnetic Structures of Rare Earth Intermetallic Compounds $RCuAs_2$ (R = Pr, Nd, Tb, Dy, Ho, and Yb)," J. Phys. Chem. Solids **111**, 1 (2017).

Zheng, W., Zeng, S., Bais, H., LaManna, J.M., Hussey, D.S., Jacobson, D.L., Jin, Y., "Plant Growth-Promoting Rhizobacteria (PGPR) Reduce Evaporation and Increase Soil Water Retention," Water Resour. Res. **54**(5), 3673 (2018).

Zhou, X., Wilfong, B., Liou, S.-C., Hodovanets, H., Brown, C.M., Rodriguez, E.E., "Proton and Ammonia Intercalation into Layered Iron Chalcogenides," Chem. Commun. **54**(50), 6895 (2018).

Zhou, Y., He, Q., Zhang, F., Yang, F., Narayanan, S., Yuan, G., Dhinojwala, A., Foster, M.D., "Modifying Surface Fluctuations of Polymer Melt Films with Substrate Modification," ACS Macro Lett. **6**(9), 915 (2017).

Zhou, Y., Josey, B., Anim-Danso, E., Maranville, B., Karapetrova, J., Jiang, Z., Zhou, Q., Dhinojwala, A., Foster, M.D., "*In Situ* Nanoscale Characterization of Water Penetration through Plasma Polymerized Coatings," Langmuir, in press.

Zimmermann, K., Eells, R., Heinrich, F., Rintoul, S., Josey, B., Shekhar, P., Lösche, M., Stern, L.J., "The Cytosolic Domain of T-Cell Receptor ζ Associates with Membranes in a Dynamic Equilibrium and Deeply Penetrates the Bilayer," J. Biol. Chem. **292**(43), 17746 (2017).

Instruments and Contacts

(name, tel. 301-975-xxxx, email)

High resolution powder diffractometer (BT-1):
- J. K. Stalick, 6223, judith.stalick@nist.gov
- H. Wu, 2387, hui.wu@nist.gov
- Q. Z. Huang, 6164, qing.huang@nist.gov
- C. M. Brown, 5134, craig.brown@nist.gov

Engineering diffractometer (BT-8):
- T. Gnäupel-Herold, 5380, thomas.gnaeupel-herold@nist.gov

VSANS instrument (NG-3) (CHRNS):
- C. Gagnon, 2020, cedric.gagnon@nist.gov
- G. Jensen, 4591, grethe.jensen@nist.gov
- Y. Liu, 6235, yun.liu@nist.gov
- E. Kelley, 8584, elizabeth.kelley@nist.gov
- J. G. Barker, 6732, john.barker@nist.gov

30-m SANS instrument (NG-B) (CHRNS):
- B. Hammouda, 3961, hammouda@nist.gov
- S. Krueger, 6734, susan.krueger@nist.gov
- C. Gagnon, 2020, cedric.gagnon@nist.gov
- P. D. Butler, 2028, paul.butler@nist.gov

10-m SANS instrument (NG-B) (nSoft):
- R. Jones, 4624, ronald.jones@nist.gov
- K. Weigandt, 8396, kathleen.weigandt@nist.gov
- T. Martin, 8866, tyler.martin@nist.gov

USANS, Perfect Crystal SANS (BT-5) (CHRNS):
- M. Bleuel, 5165, markus.bleuel@nist.gov
- P. D. Butler, 2028, paul.butler@nist.gov

30-m SANS instrument (NG-7):
- S. Teixeira, 4404 susana.marujoteixeira@nist.gov
- Y. Mao, 5250, yimin.mao@nist.gov
- J. G. Barker, 6732, john.barker@nist.gov
- J. R. Krzywon, 6650, jkrzywon@nist.gov

Polarized Beam Reflectometer/Diffractometer (NG-D):
- B. J. Kirby, 8395, brian.kirby@nist.gov
- J. A. Borchers, 6597, julie.borchers@nist.gov
- C. F. Majkrzak, 5251, cmajkrzak@nist.gov

MAGIK, Off-Specular Reflectometer (NG-D):
- B. B. Maranville, 6034, brian.maranville@nist.gov
- J. A. Dura, 6251, joseph.dura@nist.gov
- C. F. Majkrzak, 5251, cmajkrzak@nist.gov

Neutron reflectometer-horizontal sample (NG-7):
- S. K. Satija, 5250, satija@nist.gov
- G. Yuan, 5098, guangcui.yuan@nist.gov

HFBS, High-flux backscattering spectrometer (NG-2) (CHRNS):
- M. Tyagi, 2046, madhusudan.tyagi@nist.gov
- T. Prisk, 5010, timothy.prisk@nist.gov

NSE, Neutron spin echo spectrometer (NG-A) (CHRNS):
- A. Faraone, 5254, antonio.faraone@nist.gov
- M. Nagao, 5505, michihiro.nagao@nist.gov

MACS, Multi-angle crystal spectrometer (BT-9) (CHRNS):
- J. A. Rodriguez-Rivera, 6019, jose.rodriguez@nist.gov
- Y. Qiu, 3274, yiming.qiu@nist.gov

Double-focusing triple-axis Spectrometer (BT-7):
- Y. Zhao, 2164, yang.zhao@nist.gov
- Z. Xu, 8097, zhijun.xu@nist.gov
- J. W. Lynn, 6246, jeff.lynn@nist.gov

SPINS, Spin-polarized triple-axis spectrometer (NG-5):
- G. Xu, 4144, guangyong.xu@nist.gov

Triple-axis spectrometer (BT-4):
- W. Ratcliff, 4316, william.ratcliff@nist.gov

FANS, Filter-analyzer neutron spectrometer (BT-4):
- T. J. Udovic, 6241, udovic@nist.gov

DCS, Disk-chopper time-of-flight spectrometer (NG-4):
- N. Butch, 4863, nicholas.butch@nist.gov
- W. Zhou, 8169, wei.zhou@nist.gov
- C. M. Brown, 5134, craig.brown@nist.gov

Cold neutron depth profiling (NG-5):
- J. Weaver, 6311, jamie.weaver@nist.gov

Cold-neutron prompt-gamma neutron activation analysis (NG-D):
- R. L. Paul, 6287, rpaul@nist.gov
- H. H. Chen-Mayer, 5595, heather.chen-mayer@nist.gov

Thermal-neutron prompt-gamma activation analysis (VT-5):
- R. L. Paul, 6287, rpaul@nist.gov

Other activation analysis facilities:

- N. Sharp, 3926, nicholas.sharp@nist.gov
- R. L. Paul, 6287, rpaul@nist.gov

Thermal Neutron Imaging Station (BT-2):

- J. LaManna, 6809, jacob.lamanna@nist.gov
- D. Jacobson, 6207, david.jacobson@nist.gov
- E. Baltic, 4842, eli.baltic@nist.gov
- D. Hussey, 6465, daniel.hussey@nist.gov

Cold Neutron Imaging Station (NG-6):

- D. Hussey, 6465, daniel.hussey@nist.gov
- E. Baltic, 4842, eli.baltic@nist.gov
- D. Jacobson, 6207, david.jacobson@nist.gov
- J. LaManna, 6809, jacob.lamanna@nist.gov

Neutron interferometer (NG-7):

- M. Huber, 5641, michael.huber@nist.gov
- S. Hoogerheide, 8582, shannon.hoogerheide@nist.gov
- D. Pushin, 4792, dmitry.pushin@nist.gov

Quantum-based neutron interferometer facility (NG-7):

- M. Huber, 5641, michael.huber@nist.gov
- S. Hoogerheide, 8582, shannon.hoogerheide@nist.gov
- D. Pushin, 4792, dmitry.pushin@nist.gov

Fundamental neutron physics station (NG-C):

- S. Hoogerheide, 8582, shannon.hoogerheide@nist.gov
- M. S. Dewey, 4843, maynard.dewey@nist.gov

Fundamental neutron physics station (NG-6):

- NG-6M: M. S. Dewey, 4843, mdewey@nist.gov
- NG-6M: H. P. Mumm, 8355, hans.mumm@nist.gov
- MDM (NG-6A): M. Huber, 5641, michael.huber@nist.gov
- MDM (NG-6A): T. Gentile, 5431, thomas.gentile@nist.gov
- α–γ: H. P. Mumm, 8355, hans.mumm@nist.gov
- α–γ: A. Thompson, 4666, alan.thompson@nist.gov

Theory and modeling:

- J. E. Curtis, 3959, joseph.curtis@nist.gov
- T. Yildirim, 6228, taner@nist.gov

Neutron test station (PHADES):

- R. Erwin, 6245, ross.erwin@nist.gov
- K. Krycka, 8685, kathryn.krycka@nist.gov

Instruments under development:

CANDOR, White-beam reflectometer/diffractometer:

- A. Grutter, 4198, alexander.grutter@nist.gov
- D. Hoogerheide, 8839, david.hoogerheide@nist.gov
- F. Heinrich, 4507, frank.heinrich@nist.gov
- C. F. Majkrzak, 5251, charles.majkrzak@nist.gov

SPINS-II:

- L. Harriger, 8360, leland.harriger@nist.gov

NIST Center for Neutron Research Contacts

Copies of annual reports, facility information, user information, and research proposal guidelines are available electronically.

Please visit our website: http://www.ncnr.nist.gov

For a paper copy of this report:

Steve Kline
301-975-6243
steven.kline@nist.gov

For general information on the facility:

Rob Dimeo
301-975-6210
robert.dimeo@nist.gov

Dan Neumann
301-975-5252
dan.neumann@nist.gov

For information on visiting the facility and/or user access questions:

Julie Keyser
301-975-8200
julie.keyser@nist.gov

Mary Ann FitzGerald
301-975-8200
maryann.fitzgerald@nist.gov

Becky Ogg
301-975-8200
rebecca.ogg@nist.gov

For information on performing research at the facility:

Yamali Hernandez
301-975-5295
yamali.hernandez@nist.gov

Facility address:

NIST Center for Neutron Research
National Institute of Standards and Technology
100 Bureau Drive, Mail Stop 6100
Gaithersburg, MD 20899-6100 USA

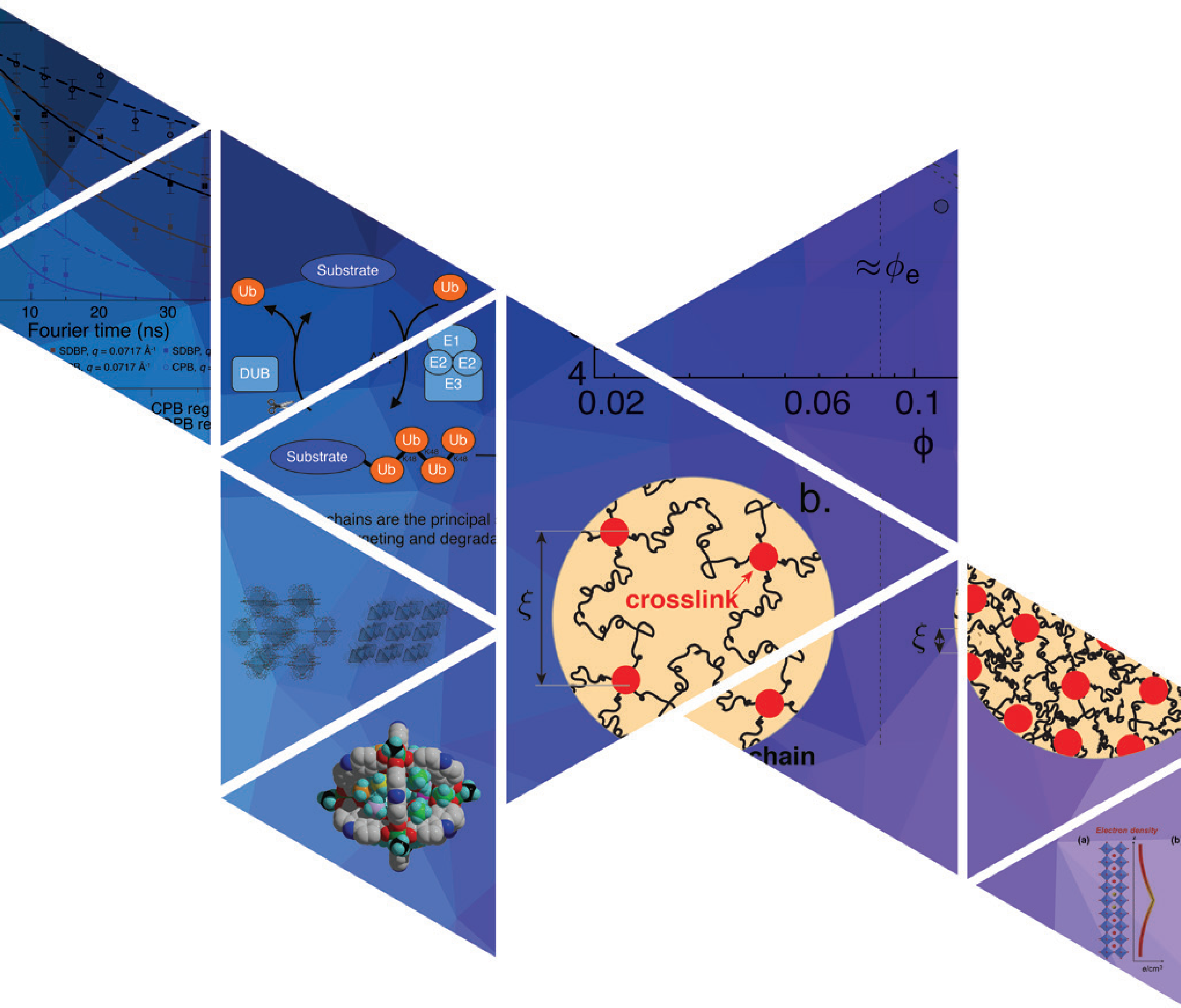

NIST CENTER FOR NEUTRON RESEARCH
National Institute of Standards and Technology
100 Bureau Drive, MS 6100
Gaithersburg, MD 20899-6100

www.ncnr.nist.gov